TIME-RESOLVED CRYSTALLIZATION OF DEEPLY COOLED LIQUID HYDROGEN ISOTOPES

von
Matthias Kühnel, Dipl.-Phys.
aus Hanau, Hessen

vorgelegt beim Fachbereich 13, Physik
der Johann Wolfgang Goethe-Universität
in Frankfurt am Main

Dissertation
zur Erlangung des Doktorgrades
der Naturwissenschaften
(D30)

ABSTRACT

This thesis serves two main purposes:

1. The introduction of a novel experimental method to investigate phase change dynamics of supercooled liquids

2. First-time measurements for the crystallization behaviour for hydrogen isotopes under various conditions

1) The new method is established by the synergy of a liquid microjet of $\approx 5\,\mu m$ diameter and a scattering technique with high spatial resolution, here linear Raman spectroscopy. Due to the high directional stability and the known velocity of the liquid filament, its traveling axis corresponds to a time axis static in space. Utilizing evaporative cooling in a vacuum environment, the propagating liquid cools down rapidly and eventually experiences a phase transition to the crystalline state. This temporal evolution is probed along the filament axis, ultimately resulting in a time resolution of $10\,ns$. The feasibility of this approach is proven successfully within the following experiments.

2) A main object of study are para-hydrogen liquid filaments. Raman spectra reveal a temperature gradient of the liquid across the filament. This behaviour can quantitatively be reconstructed by numerical simulations using a layered model and is rooted in the effectiveness of evaporative cooling on the surface and a finite thermal conductivity. The deepest supercoolings achieved are $\approx 30\%$ below the melting point, at which the filament starts to solidify from the surface towards the core. With a crystal growth velocity extracted from the data the appropriate growth mechanism is identified. The crystal structure that initially forms is metastable and probably the result of Ostwald's rule of stages. Indications for a transition within the solid towards the stable equilibrium phase support this interpretation.
The analog isotope ortho-deuterium is evidenced to behave qualitatively similar with quantitative differences being mass related.

In further measurements, isotopic mixtures of para-hydrogen and ortho-deuterium are investigated. It is found that the crystallization process starts earlier and lasts significantly longer compared to the pure substances with the maximum values between 20-50% ortho-deuterium content. A solely temperature based explanation for this effect can be excluded. The difference in the quantum character and hence effective size of the isotopes suggests a strong influence of the progressing liquid-solid-interface.
Small dilutions of each para-hydrogen and ortho-deuterium with neon show an even more extended crystallization process compared to above isotopic mixtures. Additionally, the crystal is strongly altered in favor of the equilibrium lattice structure of neon.

KURZBESCHREIBUNG

Die vorliegende Arbeit umfasst zwei Hauptanliegen:

1. Die Einführung einer neuartigen experimentellen Technik zur Untersuchung von Phasenübergangen stark unterkühlter Flüssigkeiten

2. Erste Messungen für das Kristallisationsverhalten der Wasserstoff Isotope unter diversen Experimentparametern

1) Das Fundament der neuen Technik ist die Kombination aus flüssigen Strahlen mit $\approx 5\,\mu m$ Durchmesser und Streumethoden mit hoher räumlicher Auflösung, hier Raman-Spektroskopie. Aufgrund der hohen Richtungsstabilität und errechenbaren Geschwindigkeit des flüssigen Filaments entspricht dessen Flugrichtung einer im Raum stationären Zeitachse. Durch Evaporation im Vakuum kühlt die propagierende Flüssigkeit rapide ab und kristallisiert schließlich. Diese Entwicklung wird entlang der Filamentachse mit einer zeitlichen Auflösung von $10\,ns$ vermessen. Die Durchführbarkeit dieses Ansatzes wird innerhalb der folgenden Experimente erfolgreich belegt.

2) Ein Hauptuntersuchungsobjekt sind flüssige para-Wasserstoff Filamente. Raman-Spektren zeigen, dass sich zunächst ein radialer Temperaturgradient ausbildet. Dieser kann quantitativ anhand einer numerischen Simulation rekonstruiert werden und ist in der Effektivität der Oberflächenverdampfung in Verbindung mit einer endlichen Wärmeleitung begründet. Die stärkste Unterkühlung liegt bei $\approx 30\%$ unterhalb des Schmelzpunktes, bei der das Filament beginnt von außen nach innen zu gefrieren. Mit der aus den Daten extrahierten Kristallwachstumsgeschwindigkeit wird der zugehörige Wachstumsmechanismus identifiziert. Die entstehende Kristallstruktur ist metastabil und ein Indiz für die Gültigkeit von Ostwalds Stufenregel. Hinweise auf einen Übergang zur Gleichgewichtsphase innerhalb des Kristalls bestätigen diese Interpretation.
Das analoge Isotop ortho-Deuterium verhält sich qualitativ ähnlich, wobei quantitative Unterschiede in Einklang mit der höheren Masse stehen.

In weiteren Untersuchungen werden Mischungen von para-Wasserstoff mit ortho-Deuterium untersucht. Im Vergleich zu den reinen Substanzen beginnt der Kristallisationsprozess hier früher und dauert deutlich länger an. Der stärkste Effekt wird zwischen $20-50\%$ ortho-Deuterium festgestellt. Eine rein auf Temperatur basierende Erklärung kann ausgeschlossen werden. Unterschiede im Quantencharakter und, daraus resultierend, der effektiven Größe der Isotope deuten auf einen starken Einfluss der flüssig-fest-Grenzfläche hin.
Geringe Verdünnungen von para-Wasserstoff bzw. ortho-Deuterium mit Neon zeigen einen noch längeren Kristallisationsprozess verglichen mit isotopischen Mischungen. Weiterhin ist die Kristallstruktur stark zugunsten jener von Neon im Gleichgewicht verschoben.

CONTENTS

Part I

FUNDAMENT

1 | INTRODUCTION

1.1 Motivation

Crystallization, a first order phase transition and the main issue in this thesis, is an ubiquitous phenomenon with essential implications on our every day lives. As an obvious example, freezing of liquid water on its way from clouds to the ground determines, if it rains, snows or hails. Also the circumvention of freezing is of paramount importance for biological systems in winter times.

Yet, the underlying mechanics for crystallization are still poorly understood [1, 2], as they are rooted in a complicated interplay between thermodynamic properties, particle dynamics and geometric effects. Crystallization itself usually is divided into the initial formation of embryos, i.e. the topic of nucleation, and the subsequent proceeding transformation of the liquid, i.e. referred to as crystal growth, but the link unifying these two concepts into one framework is missing. In fact, in a recently published paper [2] Kenneth F. Kelton, an expert in the research of nucleation effects, begins with "It is becoming increasingly clear that nucleation processes in liquids and glasses are more complicated than previously thought [...]", particularly highlighting that the current standard of knowledge becomes questionable with ongoing research.

Both nucleation and crystal growth critically depend on the particular microscopic details of the liquid, which due to statistical fluctuations additionally vary locally in the bulk. These local fluctuations and arrangements become increasingly important, when the liquid consists of several substances.
In this regard, an open question extensively debated these days is the connection between crystallization and its antagonist vitrification or glass formation, in which the final solid material exhibits an amorphous rather than an ordered lattice structure [3]. From empirical studies we know that vitrification strongly depends on the actual constitution of the liquid as well as thermodynamic properties like the cooling rate [4]. However up to now, no general theoretical framework is available to reliably predict, if, how and how fast a liquid is about to crystallize and only specialized empirical models for changes in certain parameters exist (e.g. [5]). Even more surprising, although glasses have been manufactured by mankind for thousands of years, the mechanisms that determine why the dynamics in such liquids drastically slow down and eventually form a glassy state, are known physically merely on a speculative basis [6].

Advances in this field do not only contribute to investigating the fundamental physical concepts, but of course have practical implications beyond. As mentioned in the beginning, atmospheric and biological physics can greatly benefit from new models regarding the nucleation of supercooled water under varied circumstances. Furthermore, manipulating the crystallization or vitrification behaviour, respectively, of metals and alloys is a key feature for controlling the properties of materials in terms of stiffness or electrical and thermal conductivity and can lead to entirely new characteristics [7].

As a last remark, polymorphism, i.e. the texture of multiple crystalline lattice structures depending on growth characteristics, plays a role in the efficacy of pharmaceuticals as well as in the perception and enjoyment of fat-based food like ice cream and chocolate [8, p.27].

As a first model system for this new experimental approach to elucidate crystallization phenomena, liquids of hydrogen molecules are chosen in this thesis. Not only is hydrogen the most abundant element in the universe and the third most common on earth's surface [9], but it also is a simple system with regard to its intermolecular potential and therefore a good candidate for the test of crystallization models. In addition, the hydrogen isotopes are appealing to study because due to the light mass their condensed phases are dominated by quantum effects. Experimental verification for the proposed superfluid phase in the bulk liquid is depending on whether it is possible to circumvent crystallization [10], to which this work delivers important results.
More technology oriented applications in the distant future may be the development of procedures to efficiently and safely store (condensed) hydrogen for fuel and energy purposes. For instance, manipulation of the crystalline structure through seeds or substrate materials might reduce the energy necessary to achieve densely packed hydrogen.

In conclusion, the unterstanding of crystallization and vitrification is still in a very early stage and considered a *hot topic* in condensed matter science, so that currently a lot of effort is put into new experimental and theoretical approaches. Not only will advances in this field shed light onto the fundamental physical mechanisms, but also enable technological applications in material sciences and biology.

1.2 Novelty of this work

In a nutshell, the aim of this experimental work is to establish a novel method to investigate dynamics and phase transitions in liquids on sub-μs time scales.
Up to the current date, a lot of knowledge about crystallization and vitrification comes from elaborate simulations of hard spheres [11], Lennard-Jones particles [12] or metals [13]. However, these model systems often use simplified interaction potentials, so that their validity is limited. Real atomar/molecular systems often are too complicated to be simulated in a dynamical way and only configurations of static liquid and solid states are retrievable.
An issue with gathering information about nucleation and crystal growth from the experimental point of view is that these effects happen on short time scales and on microscopic distances, yet require macroscopic samples, which are prone to disturbances and impurities due to the many particles involved. Measurements of the crystal growth rate in levitated metal droplets are capped to time resolutions in the order of 1 s and the interpretation is more complicated due to the chemical bonding between particles [14]. A different experimental route utilizes colloids, i.e. nano-sized hard spheres within a solvent, in which time scales of structural changes are stretched to days, months and even years [15]. Yet, effects like sedimentation, polydispersity and colloid-solvent interaction may distort the results and the applicability to atomar and molecular liquids is debatable [16, 17].
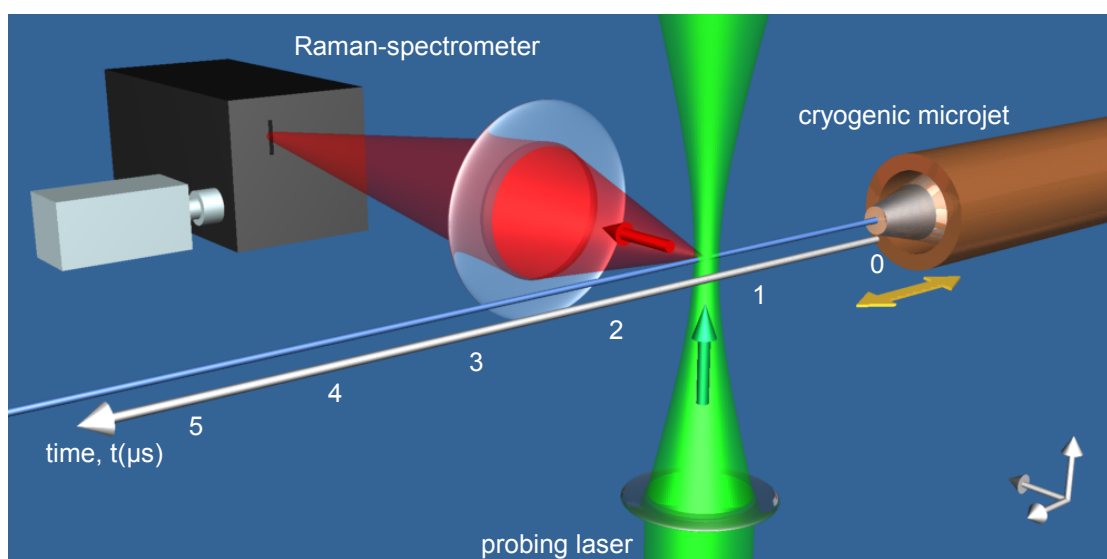
Figure 1: Schematic view of the new experimental approach.

The experimental approach reported in this work provides a new route to access crystallization effects largely unaffected from above criticism in a broad spectrum of real liquids. It relies on two established techniques, namely cryogenic microjets developed in our group e.g. applied as targets for laser-plasma interaction [18] and Raman spectroscopy e.g. already used on hydrogen cluster jets [19]. The combination of both, depicted in fig.1, creates a novel experimental technique, with which extremely fast cooling rates ($\approx 10^6$ K/s) are paired with a time resolution in the order of 10 ns to probe the crystallization behaviour of molecular liquids. The time resolution not only is orders of magnitude below current techniques, yet the self-replenishing nature of microjets guarantees that the samples are clean, i.e. without contaminations from other substances.

In the experiments reported in this thesis the pure samples are composed of hydrogen or deuterium, respectively, which represent the first measurements of the dynamics, i.e. supercooling and the transition to the crystalline state of these bulk liquids. Before, only the static liquid and crystalline bulk phases were available. In the further progress of this work, the crystallization behaviour of mixtures of hydrogen and deuterium as well as each of these with neon are presented, providing experimental data about the effects of particle size ratios, which is important information regarding crystallization and vitrification mechanics. Additionally, ramifications for the strongly supercooled, off-equilibrium grown crystal structure of these systems are measured for the first time. The hydrogen interaction potential is almost isotropic, Lennard-Jones-like and differences of the isotopes are introduced simply by the mass, altering the extent of quantum effects. Hence, our experimental results, particularly for mixtures, serve as an ideal basis to test models concerning the crystallization behaviour of quantum liquids.

1.3 Structure of this thesis

This thesis is divided into two main parts. The first part i *Fundament* covers basics and theoretical frameworks as well as elementary previous experiments.

The much longer part ii *Experiment* contains everything that is new, starting with the experimental *Setup* in chapter 3. As this work serves as a reference for future experiments, instructions are labeled in this setup chapter as *Manual:...*.
The first experimental chapter 4 evolves around filaments of liquid *pure para-hydrogen*, providing detailed analysis and the basis for the following data. In the next step *pure ortho-deuterium* is discussed in a shorter chapter 5 and compared to the previous data. *Mixtures of para-hydrogen and ortho-deuterium* are discussed in chapter 6 and represent another important part of this work. Afterward, thse findings are compared to *mixtures of para-hydrogen/ortho-deuterium with neon* in chapter 7.
For the reader with lack of time, the most important results from the experiments are condensed into sections labeled as *Summary:...* with references to important figures as a take away message.

In appendix A *additional measurements* are presented, whereas appendix B contains *calculations* that are used in the main thesis.

2 | BACKGROUND

2.1 Liquid Filaments

From a reductionist point of view the production of liquid jets seems pretty straight forward. At appropriate source conditions, a liquid, continuously pressed through a circular orifice, will emerge and travel in a long cylindrical shape, which we call a liquid filament (see fig. 2). In the technical application, however, the production of liquid filaments proves much more challenging, since it is very susceptible to the geometry of the nozzle and a variety of disturbances arising from deviations from ideal conditions. Because the nozzle system suitable for this experiment partially has been developed during this work, the particular nozzle design and its benefits will be introduced in the experiment section 3, while this chapter is dedicated to the general physical processes of a liquid injected into vacuum.
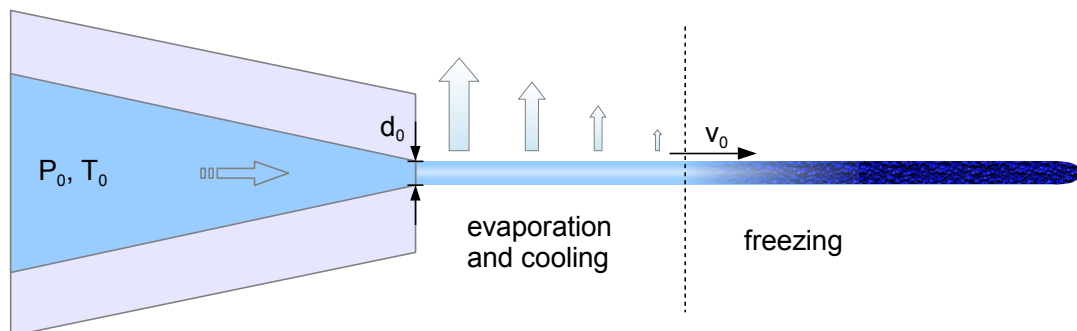
Figure 2: Schematic view of a liquid filament in vacuum. A liquid at temperature T_0 is pressed at pressure P_0 through a circular orifice with diameter d_0 and travels in shape of a long cylinder at constant velocity v_0. As soon as its surface is exposed to vacuum, the liquid starts evaporating molecules and cools down, until, in case of hydrogen, at some point the liquid filament begins to freeze.

One prerequisite for producing stable liquid filaments is to provide laminar flow conditions. Laminarity strongly depends on the geometry of the nozzle as well as the structure of its surfaces and edges in contact with the liquid, which will be discussed in chapter 3. The ultimate goal is to reduce geometrical features that promote the occurrence of turbulences, especially right before exiting the orifice.

Concerning the dynamic aspect of flow laminarity, each liquid behaves differently based on its thermodynamic properties. An important classical indicator for the flow conditions in pipes is the dimensionless Reynolds number Re, depending on the density ρ, velocity v_0 and kinematic viscosity μ of the liquid, as well as the nozzle diameter d_0.

Liquid parahydrogen at typical source conditions and a nozzle diameter used in this work yields

$$\text{Re} = \frac{\rho \cdot v_0 \cdot d_0}{\mu} = \frac{76\,\text{kg/m}^3 \cdot 200\,\text{m/s} \cdot 5 \cdot 10^{-6}\,\text{m}}{2 \cdot 10^{-5}\,\text{Pa} \cdot \text{s}} = 3800\,, \tag{2.1}$$

which is above the critical value $\text{Re}_{crit} \approx 2000$ at which turbulences start to occur [20]. For comparison, liquid water jets, established by our group in Frankfurt with $\rho = 1000\,\text{kg/m}^3$, $v = 50\,\text{m/s}$ and $\mu = 10^{-3}\,\text{Pa} \cdot \text{s}$, results in $\text{Re}_{water} = 250$. This already suggests that from the application oriented view it is not trivial to produce stable liquid filaments of parahydrogen as will be demonstrated in chapter 3.

Assuming we have found a nozzle sufficiently suitable for laminar flow, the next step to achieve liquid filaments is picking appropriate source conditions for the injection of the liquid. The two source parameters for tuning are the temperature of the nozzle T_0 and the inlet pressure P_0. Depending on the choice of these two values, the source conditions can correspond to different phases according to the phase diagram of the substance (see fig. 3) and one can produce different types of beams. Starting from higher values of T_0 one can expand either a gas, a supercritical fluid or liquid through the nozzle, resulting in supersonic gas jets, condensation in the gas, fragmentation of a liquid or liquid filaments, which was discussed in the diploma thesis [21, p.15 et seq]. For achieving stable liquid filaments, the source conditions T_0 and P_0 have to be deep in the liquid phase close to the melting line to avoid fragmentation due to the formation of cavitation bubbles during the expansion [22].

During the expansion process, the static, isotropic inlet pressure P_0 inside the nozzle is converted into a uniform, directed velocity v_0 after exiting. Mathematically this behaviour is described by the Bernoulli equation for an incompressible liquid [23]. As in our case we expand into vacuum, the potential energy on the left hand side of the equation is completely transformed into kinetic energy, yielding

$$\frac{P_0}{\rho} = \frac{v_0^2}{2}\,, \tag{2.2}$$

where ρ is the density of the liquid, assumed to be constant for P_0 in the range of a few bar. As P_0 and ρ are both known, equation 2.2 can be rewritten as one of the key formulas for this work:

$$v_0 = C \cdot \sqrt{\frac{2P_0}{\rho}} \tag{2.3}$$

with the additional $C \leqslant 1$ being an experimentally determined discharge coefficient accounting for natural losses due to friction. As there is no further friction in vacuum, equation 2.3 states that the emerging filament travels with a constant velocity v_0, which typically is in the order of $100\,\text{m/s}$ for hydrogen.
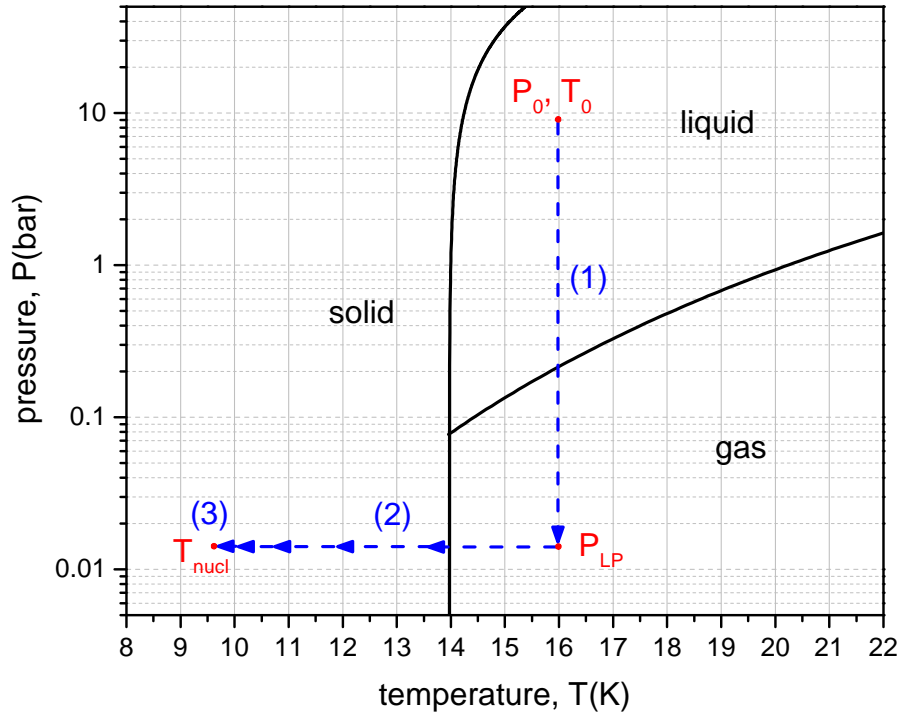
Figure 3: Phase diagram of hydrogen including conditions during different stages of expansion of a liquid. (1) A liquid at source conditions T_0 and P_0 is expanded through a nozzle and experiences a pressure drop to to its inherent Laplace pressure P_{LP} as soon as it is exposed to vacuum. (2) Through ballistic evaporation the temperature of the filament decreases according to its current vapor pressure, which is highest in the beginning and decreases rapidly. (3) At some temperature the nucleation rate is high enough to initiate the transition to the solid phase.

After exiting the nozzle orifice, the only pressure remaining in the cylindrical liquid with radius R_0 exposed to vacuum is the inherent Laplace pressure P_{LP}, caused by the surface tension γ:

$$P_{LP} = \frac{2\gamma}{R_0} \, , \tag{2.4}$$

which for liquid hydrogen in this experiment yields $P_{LP} \approx 12\,\text{mbar}$. During this rapid pressure drop from the initial P_0 to P_{LP}, the temperature can be considered constant, so that the corresponding trajectory in the equilibrium phase diagram is an isotherm (line (1) in fig. 3). Regardless of the initial conditions P_0 and T_0, the endpoint of this first process lies within the gas phase region, demonstrating the far off-equilibrium state of the liquid at this point.

In order to reach equilibrium, the liquid filament, propagating with v_0 through vacuum, tries to establish a vapor pressure above its surface according to the equilibrium vapor

pressure at its current temperature. At the vacuum exposed surface, the hot, high energy molecules are preferred to evaporate, as their momentum is high enough to overcome the binding force of the adjacent molecules in the liquid. This shifts the Boltzmann velocity distribution of the remaining molecules to lower energies, which effectively decreases the mean temperature of the liquid filament.

At dimensions of the liquid filaments used in this experiment, the evaporated molecules barely collide with each other and are diluted rapidly in the comparably huge vacuum chamber until finally removed via pumps. Therefore, the evaporation of molecules continues as if there was zero vapor pressure above the surface and the temperature of the filament steadily decreases. This process is known as ballistic evaporative cooling and can quantitatively be calculated via energy and mass conservation equations [23]. The equilibrium vapor pressure and hence the effectiveness of the cooling declines strongly with decreasing temperature so that the cooling rate also diminishes. For hydrogen a theoretical minimum temperature limit was found to be $T_{min} \approx 8\,K$ [23]. Because of the high thermal velocity of the light hydrogen molecules, the evaporation and cooling rate at the surface is quite fast and even at small filament diameters of $2R_0 = 5\,\mu m$ a dynamic temperature gradient with respect to the inner core is built up. To properly interpret the data in this work, the proposed model of [23] is enhanced to account for this temperature gradient by introducing a layered model, wherein the filament is divided into 100 equally mass weighted concentric hollow cylinders. The temperature exchange between these layers is governed by thermal conductivity at the current thermodynamic properties. The details of this method are described in appendix B.1 and compared to experimental data in chapter 4.1.1.2.

The cooling rate and theoretically lowest temperatures reachable for different substances mainly depend on their (extrapolated) liquid vapor pressure curves below the starting temperature T_0. A good indicator for the effectiveness of supercooling via ballistic evaporation is the vapor pressure at the triple point, which for both hydrogen and deuterium are comparably high. Correlated with the degree of supercooling is the probability of a transition to the solid phase (see nucleation theory in chapter 2.5.1).

If no extensive cooling is present, e.g. if the beam is injected into a warm buffer gas or inherently has a low triple point vapor pressure, source fluctuations propagating through the surface are enhanced by the surface tension and after some time the liquid beam finally is cut off into droplets, which is known as Rayleigh Breakup [21].

However, previous experiments have found that the cooling rate in a liquid hydrogen filament under stable flow conditions injected into vacuum is sufficient to start the nucleation and freezing process into a solid filament instead of breaking up into a stream of liquid droplets [18]. This feature is beneficial to this experiment, because the cylindrical geometry of the investigated volume roughly does not change, when the phase transition to the solid occurs. It is noteworthy that during and even after complete solidification, the filament still experiences cooling through evaporation down to its limit temperature discussed above.

Summary: Liquid filaments

The most critical part is to find nozzles suitable for laminar flow conditions, which is essential for producing stable liquid filaments. During the expansion process through the orifice, the static pressure P_0 is converted into a constant velocity v_0 of the cylindrical filament. When exposed to vacuum, the molecules at the surface evaporate ballistically according to the equilibrium vapor pressure at their current temperature, effectively cooling the filament. For hydrogen in this experiment the supercooling is strong enough to induce the transformation to the solid phase, keeping the same geometry of a propagating cylinder throughout the investigation time.

2.2 Raman scattering

Linear Raman scattering is an inelastic light scattering process, which means that the scattered photon differs in energy from the incident photon through the interaction with a molecule. The corresponding shift in energy within the molecule is accompanied by a transition between its vibrational, rotational or electronic states or even a combination of above. These shifts in energy of the molecule can be negative (Anti-Stokes scattering) or positive (Stokes scattering), whereas in this work only the latter is of interest as all the molecules are in their vibrational, rotational and electronic ground state. Raman scattering is always accompanied by the much more intense elastic light scattering, for which no exchange in energy occurs. This process is called Rayleigh scattering and responsible for the sky's blue color and beautiful sunsets.

The general description of the Raman effect [24] is quite complex and does not contribute significantly to understanding the observations and conclusions of this work. Though, it is worth looking at the interpretations arising from the two different approaches grounding in the wave-particle duality of light, because both pictures reveal different aspects of the phenomenon.

Let us imagine a free hydrogen molecule in its ground state inside a laser focus. In the first, classical scenario, the light acts as a wave and the molecule experiences an oscillating electromagnetic field. As typically the wavelength of the light ($\lambda \approx 500\,\mathrm{nm}$) is much larger than the size of the molecule (Hydrogen $d \approx 0.1\,\mathrm{nm}$) the electric field vector E can be assumed constant over the molecule at any moment.

In the adiabatic approximation [25], the hydrogen molecule is modeled by two stationary nuclei with equal mass surrounded by a rapidly responding electron distribution due to their huge mass difference. Through the time dependency of the external electric field, an oscillating electric dipole in the direction of the external field is induced in the molecule, in other words, the electron cloud itself oscillates as a response. The quantity governing the ability to oscillate is called polarizability and depends on the geometric and binding properties of a molecule.

This harmonic variation, however, can excite the two nuclei e.g. to periodically change their relative distance as well. In the quantum-mechanical description of the molecule only certain discrete values of these excitations are allowed, which are the vibrational states. Mathematically this is described as the wavefunction of the molecule being perturbed by the oscillating electromagnetic field provided by the light. The allowed transitions to excited states and their probabilities are governed by transition polarizability tensors.

The perturbed molecule can either go back to its initial state or, with a lower probability as the overlap between the initial and final wave function is smaller, to an excited state. In both cases, the oscillating electron cloud, which acts as a dipole, emits radiation; Either with the same frequency as the perturbation, resulting in the Rayleigh effect, or with a lower frequency due to the excited beat frequency of the nuclei motion, leading to the (Stokes) Raman effect [24, p.35]. The direction of the emitted light is not isotropic, but in a $\cos^2$-shape due to its dipole nature, with the dipole direction defined by the external electric field.

Unfortunately, in this light-as-a-wave-picture the limitations on rotational excitations cannot be satisfactorily explained. Therefore we now treat the light quantized, consisting of individual photons of energy $\Delta E_i = h\nu_0$, which can be absorbed by a molecule. For

linear Raman scattering this absorbed energy is significantly higher than the energy needed for a single vibrational or rotational excitation, but also well below the first electronic excitations, so that no resonance effects occur. Consequently the molecule is excited into a so-called virtual state, as it is not a stationary state, i.e. a solution of the time-independent Schroedinger equation [24, p.55].

As this virtual state is not stable, it decays into a final stationary state, which can be the same as the initial state (Rayleigh scattering, see a) in fig.4) or a vibrationally and/or rotationally excited state (Raman Stokes scattering, see b) in fig.4), accompanied by the emission of a photon according to the difference in energy. In case a) the energy of the emitted photon is the same as the initial one, $\Delta E_e = \Delta E_i$. In case b) the energy of the vibrational state $\Delta E_v = h\nu_v$ is subtracted, yielding $\Delta E_e = h(\nu_0 - \nu_v)$, in case c), which is not of relevance here, it is added.
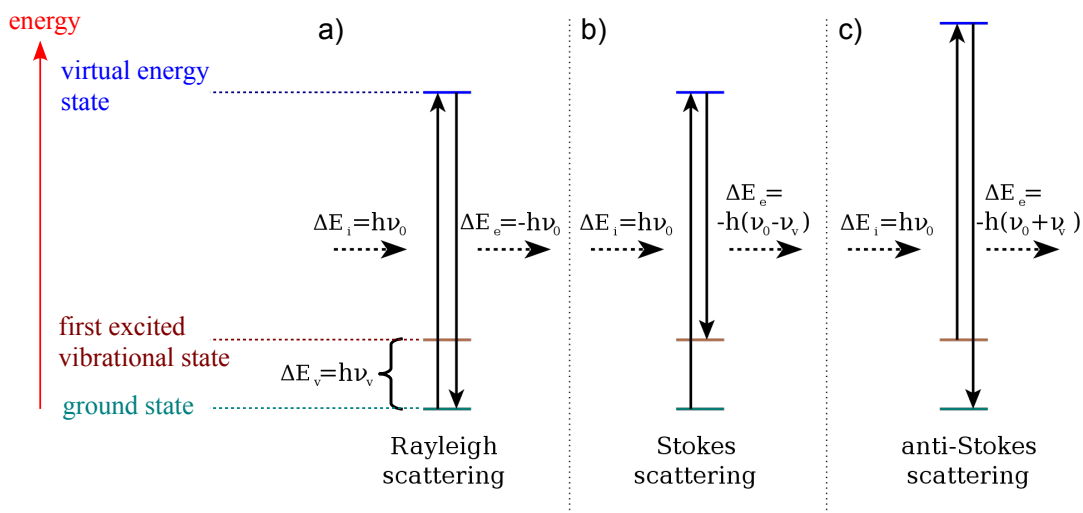
Figure 4: Schematic energy diagram of the Raman process in the light-as-a-particle view [26]. a) Rayleigh scattering. A molecule in the ground state absorbs a photon and is excited into a virtual energy state. Upon returning to the ground state, a photon with the same energy as the initial one is emitted. b) Stokes scattering. The absorption is identical, but this time the virtual state decays into the 1st vibrational state, emitting a photon with less energy. c) anti-Stokes scattering. A molecule in the 1st vibrational state absorbs a photon and decays into the ground state accompanied by the emission of a higher energy photon.

In this light-as-a-particle picture one can see that this process actually is a two photon process, since through the absorption the initial photon completely disappears and by the emission a new one is created. As each of the two photons carries a spin $s = 1$, for linear molecules like hydrogen only processes are allowed, for which the change in angular momentum is zero or $\Delta J = \pm 2$. Because a rotational excitation is accompanied by an integer change in spin, in Raman scattering of the hydrogen isotopes only double excitations of rotational states are allowed.

Furthermore, for a transation to be allowed it has to be Raman active. This means a change in the polarizability must occur based on the nuclear motion involved in

the transition. Fortunately, for the hydrogen isotopes both rotational and vibrational transitions are Raman active [24, p.39].

In the practical application of the effect, i.e. linear Raman spectroscopy, information about the irradiated matter is extracted by analyzing the wavelength of the scattered light λ_e. The probe is illuminated with a high intensity monochromatic continuous wave laser with fixed linear polarization. It is crucial to ensure that the wavelength λ_i of the laser is stable over time with high precision (here $\Delta\lambda_i/\lambda_i < 5\,\mathrm{ppm}$) because the Raman transition energies are measured as shifts from the reference wavelength.
The scattered light usually is collected by a spectrograph at a $90°$ angle with respect to the laser direction. Raman cross sections are extremely low, so that in the case of liquid hydrogen less than one in 10^{13} of the initial photons will contribute to the spectra. Therefore it is necessary to reduce the amount of Rayleigh scattered and stray light by filters blocking the wavelength of the laser. In the spectrograph, the remaining light is dispersed and the amount of light at a each wavelength is determined by a CCD camera or photomultiplier (discussed in detail in chapter 3.4).

Based on energy conservation one can calculate the shift in energy E for a particular transition from the shift of the scattered wavelength λ_e with respect to the initial wavelength λ_i by the Einstein equation

$$E = h \cdot c \left(\frac{1}{\lambda_i} - \frac{1}{\lambda_e} \right) , \tag{2.5}$$

where h is the Planck constant and c is the speed of light.
To give an estimate of the energy scales involved, the initial as well as the scattered light typically are in the visible to near-infrared region with a few eV, as the energy shifts in the molecule for vibrational and rotational excitations are comparably small in the order of 10^{-4} to $1\,eV$.
Usually, the shift in energy is expressed in wavenumbers ν in units cm^{-1}, defined as

$$\nu = \frac{1}{\lambda_i} - \frac{1}{\lambda_e} = \frac{E}{h \cdot c} , \tag{2.6}$$

so that $1\,eV \approx 8000\,cm^{-1}$.

Linear Raman spectroscopy has the great advantage for our experiment of being incoherent [24, p.10], which basically means that no correlation between two individual scattering processes exists (in contrast to e.g. the process of lasing, where this is the key aspect). As a consequence, there is a proportional relationship between the scattered light intensity I_e to both the total number of molecules N in the probed volume as well as the initial intensity I_i:

$$I_e \propto N \cdot I_i \tag{2.7}$$

So, additionally to the information about the energy for a particular Raman excitation, we obtain the amount of molecules experiencing this transition and can compare it to other transitions. A broad line in a Raman spectrum is constituted of many single Raman events, each with a sharp energy. Hence, the population of states can be probed, from which it is possible to draw further conclusions about macroscopic quantities like the temperature distribution of the sample (see later chapter 4.1.1).

The notation to describe a certain Raman transition of molecular hydrogen is $X_Y(Z)$, where $Y = v_f$ is the vibrational quantum number of the final state, $Z = J_i$ is the rotational quantum number of the initial state and $X = Q$ or S is a capital letter, stating the change in rotational quantum number with $\Delta J = 0$ or 2, respectively.

In this work only a few excitations of hydrogen are of interest:

- From the vibrational and rotational ground state (i.e. parahydrogen/orthodeuterium, see chapter 2.4) to the first pure vibrational state $J = 0 \rightarrow 0, v = 0 \rightarrow 1$, denoted as $Q_1(0)$.

- From the vibrational ground and rotational first excited state (i.e. orthohydrogen/-paradeuterium, see chapter 2.4) to the first vibrational state $J = 1 \rightarrow 1, v = 0 \rightarrow 1$, denoted as $Q_1(1)$.

- From the vibrational and rotational ground state to the second pure rotational state $J = 0 \rightarrow 2, v = 0 \rightarrow 0$, denoted as $S_0(0)$.

This very basic description of linear Raman scattering focuses on free molecules solely. More relevant for this work are phenomenons arising in the condensed phases of hydrogen, which will be discussed in the next chapter.

Summary: Raman scattering

A molecule can be excited into a virtual state through the absorption of a photon in the visible spectrum. The deexcitation can happen into the same state, i.e. the Rayleigh effect, or into state with a different vibrational and/or rotational quantum number, i.e. Raman scattering, while the photon emitted during this process carries the energy difference.

By analyzing these Raman scattered photons, linear Raman spectroscopy provides information about the energy of vibrational and rotational states of molecules in the sample as well as the population of these states.

2.3 The condensed phases of hydrogen

This chapter is dedicated to the condensed phases of hydrogen, namely the liquid and the solid. In the first part of this chapter the two spin isomers, ortho- and para-hydrogen, are explained. The second part covers effects of intermolecular interaction on vibrational and rotational excitations and their influence on Raman spectra.

2.3.1 Hydrogen spin isomers

As a prerequisite it is essential to distinguish between the two nuclear spin isomers of hydrogen, called para-hydrogen (p-H_2) and ortho-hydrogen (o-H_2). In para-hydrogen the two protons, which are fermions each carrying spin $I = 1/2$, are in an antiparallel configuration comprising to a total nuclear spin $I = 0$. Ortho-hydrogen on the other hand is defined by a parallel proton configuration, resulting in a $I = 1$ total nuclear spin, illustrated on the left side on fig. 5).
Surprisingly, this difference in the nuclear spin yields significant consequences in the condensed phases due to their intermolecular potential. Para-hydrogen in its ground state wirh angular momentum $J = 0$ does not exhibit a rotation and due to the uncertainty nature of the wave function the two protons can be modeled by a spherical positive charge density [25, p.8]. Hence, the electron distribution in the ground state surrounding the positive core and ultimately the whole molecule is spherically symmetric[1], comparable to the noble gases. In contrast, ortho-hydrogen with $J = 1$ in the ground state experiences a rotation and therefore generates an intrinsic preferential direction based on its rotation axis, which for the molecule lastly results in a shape of an elongated spheroid [27, p.399].
This difference in shape is crucial for our experiment as nucleation and crystal growth strongly depend on the intermolecular potential, which in $J = 1$ molecules is much more complicated than in the spherically symmetric $J = 0$ ones.

The nuclear spin magnetic quantum number m_I can take the $2I + 1$ values $m_I = -I, -I + 1, ..., I$ [25, p.25] resulting in a single state for p-H_2 ($I = 0$) and a triplet state for o-H_2 ($I = 1$). At room temperature, where all the states are approximately equally populated, this leads to a ratio of ortho to para-hydrogen of $3 : 1$, which is referred to as normal hydrogen (n-H_2, dashed line in fig. 5).
However, at low temperatures in the order of $20\,\mathrm{K}$, where the liquid is formed, the para-hydrogen $I = 0$ isomer is strongly favored due to its lower energy. The conversion rate of one isomer into the other is rather slow with about 1% per week [25, p.8] as the transition requires a strongly inhomogeneous magnetic field [27, p.416]. For an efficient conversion a catalytic material such as Ferric hydroxide oxide operated at low temperatures is used, speeding up the process down to several minutes and making continuous flow applications possible with a purity of para-hydrogen of $> 99.8\%$.
The uncatalyzed slow conversion rate yields the interesting feature that in the condensed

---

1 This is an astonishing feature and a nice example, where a classical interpretation reaches its limits. Therein, a diatomic molecule, which is not rotating, would have a fixed axis in space defined by the two atoms and obviously be not spherically symmetric
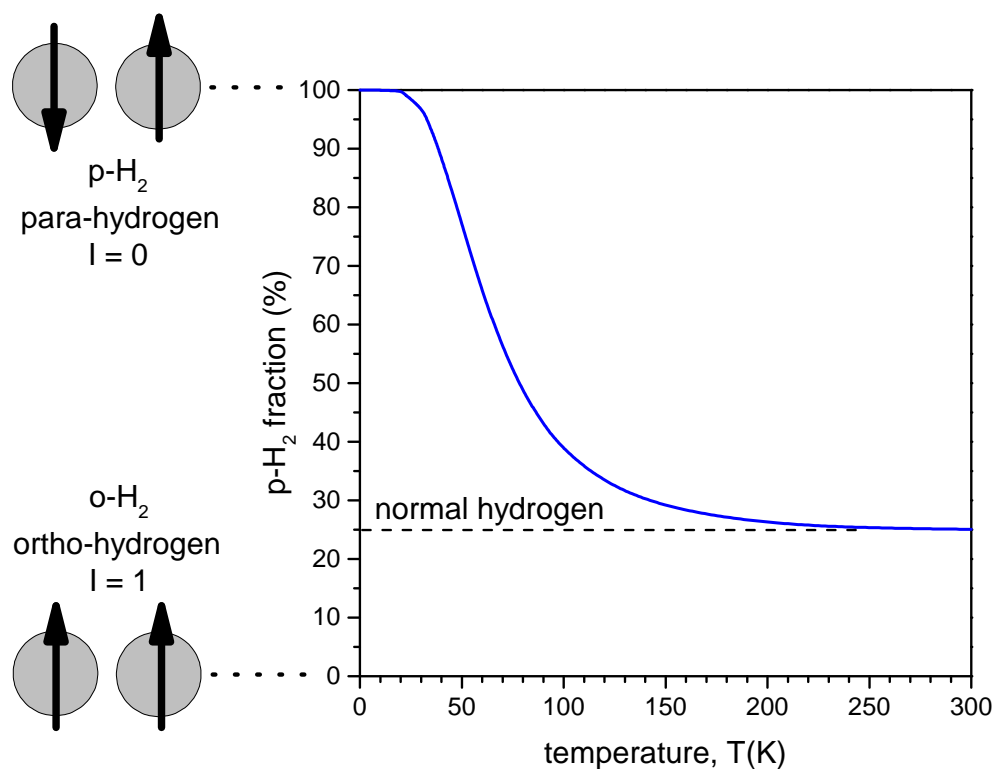
Figure 5: Equilibrium para-hydrogen fraction versus temperature. The dashed line marks the high temperature equilibrium ratio with 25 % para-hydrogen. On the left hand side the antiparallel and parallel nuclear spin constellations are illustrated for para- and ortho-hydrogen, respectively. Data from [28, p.6-291].

phases both isomers can be treated as separate species with their abundancies being conserved.

2.3.2 Raman effects in the condensed phases

Keeping the difference of the isomers in mind, we now take a look into the condensed phases and particularly how Raman scattering is influenced by the intermolecular forces. From the phase diagram (fig. 3) we see that at atmospheric pressure normal hydrogen liquefies at around 20 K and has a freezing/melting point $T_M \approx 14$ K. Variations in the thermodynamic properties of para-hydrogen compared to normal hydrogen are already measurable, but are relatively small with changes in the liquefying and melting points in the order of 0.1 K.
Both normal and para-hydrogen, when cooled close to equilibrium conditions, are found to freeze into an hcp lattice structure [27, p.423].

One of the most remarkable features of the condensed phases of hydrogen is that the rotational quantum number J and the vibrational quantum number v are good quantum numbers, i.e. conserved quantities. In classical words, hydrogen molecules, even in a

crystal at the lowest temperature, can almost freely vibrate and rotate as if they were in the gas phase. This is a unique feature of hydrogen and demonstrates its quantum nature in a striking way. The reason for this behaviour is the weak intermolecular interaction energy in comparison to the rotational and vibrational excitation energies, so that states of different J or ν do not mix [29, p.532].

As a consequence, in the mathematical approach of the condensed phases, the molecules are approximated as free and the intermolecular forces are introduced via perturbation theory. Most of the theoretical work was done in the solid phase [25] as the periodicity of a lattice offers a stricter, hence easier approach to the conditions of the environment, but the effects discussed below also occur in the liquid phase with minor changes.

A hydrogen molecule in a solid hcp lattice is surrounded by 12 partners, referred to as the nearest neighbors (nn). In comparison to the gas phase, the first vibrational excitation of both ortho- and para-hydrogen in the condensed phases are slightly lower in the order of $10\,\mathrm{cm}^{-1}$, $\approx 0.25\%$ of the excitation energy.

The main contribution to this shift can classically be interpreted as a stretching of the molecule due to the attractive forces of the adjacent nn molecules. Consequently, the nuclei vibrate at a slower pace and the associated energy is slightly reduced[2].

The second contribution to the energy shift is somewhat smaller, but more important because it gives rise to additional interesting effects. Beyond its isotropic interaction potential, para-hydrogen inheres a much weaker anisotropic electric quadrupole field, merely a factor 0.02 of the isotropic one [25, p.75]. In the condensed phases nn hydrogen molecules interact through this anisotropic part, manifesting in an electric quadrupole-quadrupole (EQQ) coupling.

We at first presume a hydrogen molecule is surrounded only by molecules of the same nuclear species. As all the particles are indistinguishable, the EQQ coupling leads to a delocalization of the vibrational excitation, because the surrounding molecules oscillate in phase as they all have the same resonance frequency. This in-phase vibration entails a lowering of the vibrational energy. Its motion can be interpreted as a traveling vibration, which is called a *vibron*, a quasiparticle mathematically described by a Bloch wave [25, p.36].

The EQQ coupling depends on the distance between molecules, which macroscopically is described by the density. The higher the (number) density, the stronger the EQQ coupling and the lower the energy of the vibron. For this reason the denser solid phase has a lower vibron energy than the liquid phase.

Owing to its shallow interaction potential, hydrogen is compressible in its condensed phases, with its density depending on pressure and temperature. For pure para-hydrogen Vilesov et al. [30] have constructed an empirical formula, connecting the temperature dependent density $\rho(T)$ at equilibrium vapor pressure with the excitation energy in wavenumbers ν:

$$\nu = \nu_0 - c\rho(T)^2 \,, \tag{2.8}$$

where the parameters $\nu_0 = (4157.1 \pm 0.1)\,\mathrm{cm}^{-1}$ and $c = (975 \pm 28)\,\mathrm{cm}^{-5}\mathrm{g}^{-2}$ are suitable for both the liquid and the solid phase, although the former is more interesting

---

2 The same explanation can also be utilized to understand the lower vibrational excitation $Q_1(1)$ of o-H_2 with respect to $Q_1(0)$ of p-H_2. The intrinsic rotation ($J = 1$) of the former results in a greater mean distance of the nuclei owing to the centrifugal force and therefore the vibration is slower [25, p.67].

for us. The density of the liquid at equilibrium pressure is known and was extrapolated [10] to values below the melting point, assuming the thermal expansion is proportional to the specific heat, yielding

$$\rho_L = 0.08277 - 3.01 \cdot 10^{-5} T^2 \ . \tag{2.9}$$

Combining equations 2.8 and 2.9 offers a direct relationship between wavenumber of the vibron in cm^{-1} and temperature of the liquid of pure p-H_2 in K:

$$T = \sqrt{(0.08277 - 3.01 \cdot 10^5 \cdot \sqrt{\frac{4157.1 - \nu}{975}}} \tag{2.10}$$

This formula is of importance, when analyzing pure p-H_2 in section 4.1.1.1.

However, equation 2.10 applies only for pure para-hydrogen with low ortho concentrations $c_{oH2} \leqslant 0.5\%$.

Vibrons strongly prefer traveling between same-species molecules, because their resonance frequency is equal. If substantial amounts of impurities (e.g. o-H_2) are inserted into the condensed phase, p-H_2 vibrons have less vicinal partners to hop to and hence their excitation energy is increased. On the other hand, more ortho-molecules now have partners with the same resonance frequency and the energy of o-H_2 vibrons decreases. This effect has been found to be linear with concentration [31] and will be discussed in chapter 6.1.1.

An additional effect with impurities in general is that vibrons of the main component are more localized the higher the amount of impurity particles is, as these act as scattering centers. In Raman spectra this can be noticed as a broadening of the line and an asymmetry towards higher wavenumbers, which can be interpreted as the lifetime of the vibron [32, 33].

Another interesting effect is, that the scattering cross sections of vibrons originating from o-H_2 in comparison to p-H_2 molecules behave differently, if not all the particles close-by are of the same species. Ortho-hydrogen has a slightly lower energy of the first vibrational excitation, in the order of $0.1 - 0.2\% \cong 5 - 10 \, cm^{-1}$, i.e. its vibrational frequency is smaller in comparison to para-hydrogen (see footnote 2). An excited ortho-molecule is still able to drive in-phase oscillations of adjacent para-molecules, yet below their natural vibrational resonance frequency [25, p.70].

On the other hand, it is not possible for an excited para-hydrogen molecule to force in-phase oscillation onto nn ortho-molecules, because they cannot be driven above their resonance. Instead, they respond with a 180° out-of-phase oscillation, dampening the motion [25, p.79].

In Raman spectra this expresses as a strong imbalance between the scattering cross sections and thus intensity of the vibrational lines of the two species. Kranendonk defines the enhancement factor ξ by the ratio of measured intensities to the actual content:

$$\xi = \frac{I_{J=1}/I_{J=0}}{c_{J=1}/c_{J=0}} \tag{2.11}$$

Depending on the ratio of ortho- to para-hydrogen and the density in a sample, the intensity of the ortho-molecules can be enhanced by a factor of up to $\xi = 3.5$ with

respect to their relative mol fraction [34, 35]. Mathematically, the intensity enhancement and repression, respectively, of the $J = 1$ and $J = 0$ species balance each other exactly, so that the overall intensity according to the number of particles is conserved.

The rotational excitation experiences nearest neighbors effects as well. Similar to the vibron, if a para-hydrogen molecule is surrounded only by its same-species nn, the rotation is delocalized and the adjacent molecules conduct in-phase movements on account of the EQQ intermolecular forces. The motion can be interpreted as traveling rotations called *rotons* and, likewise to vibrons, rotons have a slightly lower energy compared to the gas phase.

As stated at the end of chapter 2.2, the first Raman active excitation $S_0(0)$ is from the ground state into the second excited state $J = 0 \rightarrow 2$. The final state has $2J + 1 = 5$ magnetic sub-states, $m_J = \pm 2, \pm 1, 0$, which in the gas phase are degenerated and give rise to a single rotational line. In the liquid the degeneration is broken through the interaction between the particles, but due to the lack of order each molecule senses a varied environment leading to a Lorentz-shaped Raman band, when averaged over a lot of molecules.
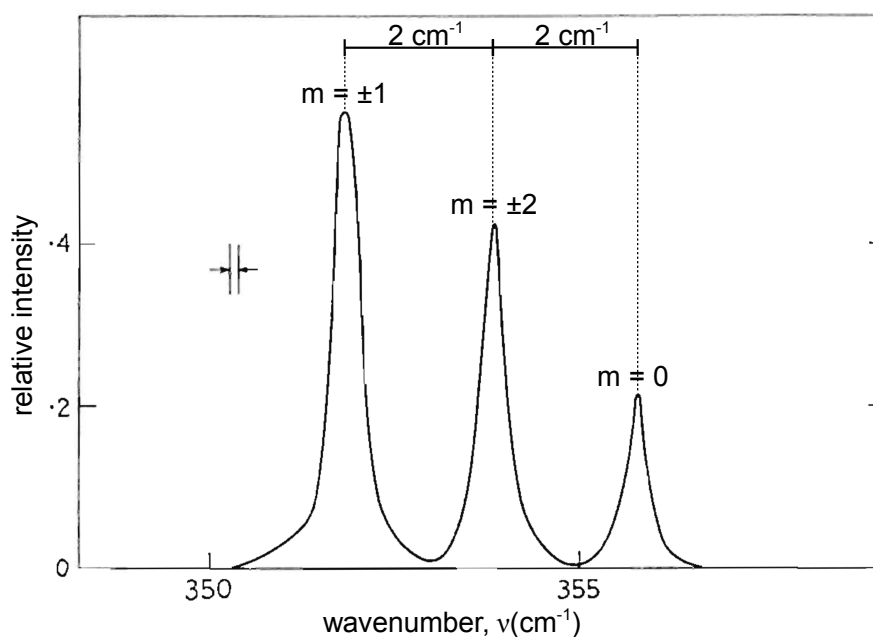
Figure 6: Splitting of the magnetic sub-levels of the $S_0(0)$ excitation in a pure p-H_2 hcp crystal at 2 K, measured in [36, p.15]. The splitting between between $m = \pm 1$ to $m = \pm 2$ and $m = \pm 2$ and $m = 0$ is even with $2\,cm^{-1}$.

In the ordered hcp structure in the solid, however, each para-hydrogen molecule experiences equal periodic conditions. The stacking of the layers in an hcp crystal defines a preferential axis c, which, classically, aligns all the rotational excitations and causes a splitting of the magnetic sub-levels (see fig 6). In pure para-hydrogen with a pure hcp structure, the splitting is almost equal with $2\,cm^{-1}$ between $m = \pm 1$ to $m = \pm 2$ and $m = \pm 2$ and $m = 0$, respectively.

Due to the defined c-axis, the scattered Raman light is sensitive to the orientation of the crystal in terms of the intensity ratio of the three peaks. In a powder, i.e. a randomly oriented polycrystal, the ratio from left to right is $2:2:1$ [25, p.121].

When ortho-hydrogen or other substances are mixed into the crystal, the periodicity is broken due to the random distribution of these impurity spots, hence rotons are more localized and experience varied surroundings. The sharp hcp structure gets blurred the more impurities are present up to a point, until a broad distribution similar to the liquid case remains.

An intensity enhancement of ortho-hydrogen, as observed in the vibrational bands, is not present in the rotational as the excitation energies of $J = 1$ and $J = 0$ differ significantly with $240\,\mathrm{cm}^{-1}$ in between and so do not drive each others motion.

Summary: Hydrogen condensed phases

Two spin isomers of hydrogen molecules exist, the favored p-H_2 carrying $J = 0$ and being spherically symmetric in the ground state whereas o-H_2 with $J = 1$ is not. In the condensed phases vibrational and rotational Raman excitations are extended into traveling vibrons and rotons onto adjacent same-species partners due to intermolecular quadrupole forces. Due to resonance effects the ortho-hydrogen peak intensity in the vibrational region is enhanced with respect to its relative mol fraction. In the rotational region the periodic hcp structure of at equilibrium frozen para-hydrogen results in a equal threefold splitting of the magnetic sub-states.

2.4 Comparison of Hydrogen, Deuterium, Neon and their mixtures

This chapter covers the knowledge necessary for interpreting the behavior of super-cooled mixtures of para-hydrogen with ortho-deuterium and of each of these with Neon. We start with comparing the properties of pure deuterium to pure hydrogen, figuring out their similarites and differences. Based on that comparison, we turn to mixtures of hydrogen with deuterium.
The same approach will then be used for the discussion of Neon.

2.4.1 Deuterium

2.4.1.1 Similarities to hydrogen

The deuterium atom is an isotope of hydrogen, defined by having an additional neutron in the nucleus. In the molecular state D_2 the two neutrons add a total of $I = 2 \cdot 1/2 = 1$ nuclear spin and therefore the deuterium molecule like the hydrogen molecule belongs to the boson family.
Likewise to hydrogen, for molecular deuterium two nuclear spin isomers exist, having either even ($I = 0$ or $I = 2$) nuclear spin with the rotational ground state $J = 0$ or odd spin ($I = 1$) with $J = 1$ as the ground state. Confusingly, due to their abundance at room temperature, the nomenclature is vice versa. Here, ortho-deuterium (o-D_2) in its ground state $J = 0$ is the spherically symmetric particle and para-deuterium (p-D_2) in the $J = 1$ state in shape of an elongated spheroid.
The nuclear spin magnetic sub-states yield a statistical distribution for normal deuterium at ambient pressure and temperature of o-D_2 : p-D_2 = 2 : 1 [37]. At low temperatures, again the o-D_2 $J = 0$ state is energetically favored. Yet, due to a lower energy of the rotational excitation and the higher melting point $T_M = 18.7\,\text{K}$ discussed below, statistically there is a higher population of the $J = 1$ state. Hence, the catalyzed conversion to the $J = 0$ state at around $20\,\text{K}$ is not as efficient as in hydrogen and typically remaining $J = 1$ contents in technical applications range between 2-3 %.

A very important feature that the $J = 0$ states p-H_2 and o-D_2 have in common, is the equality of their intermolecular interaction potential in good approximation, described by a Lennard-Jones or more accurately by a Silvera-Goldman model [27]. As the nuclei in the ground state in the adiabatic approach of both cases are non-moving, the mass difference classically does not make any difference and the repulsive core term in the intermolecular forces is the same. Also, the electron distribution, i.e. the attractive part, and ultimately the complete interaction potential is identical.

The Raman spectra of deuterium are qualitatively comparable to hydrogen in the condensed phases. Similarly, small EQQ interactions give rise to coupling between the molecules resulting in vibron and roton excitations. With the same reasoning as in chapter 2.3, in the vibrational bands of both liquid and solid an intensity enhancement of the lower energy $Q_1(1)$ excitation ($J = 1$ component) can be found. Yet, in D2 this effect is much more pronounced due to the smaller energy gap between the $Q_1(0)$ and $Q_1(1)$ bands, yielding enhancement factors of up to $\xi = 50$ for low p-D_2 concentrations [34].

Measurements of the rotational band $S_0(0)$ in pure o-D_2 reveal an hcp structure of the solid with the familiar splitting into 3 lines based on the magnetic sub-states [31].

	p-H_2	o-D_2	Ne
mass (u)	2	4	20
TP Temperature (K)[38]	13.8	18.7	24.6
TP Pressure (bar)[38]	0.07	0.17	0.43
LJ well depth ϵ (K)[39]	36.7	36.7	36.7
LJ well width σ (Å)[39]	2.96	2.96	2.788
De Boer param. λ_{db}[27]	0.28	0.20	0.07
molar vol. (cm^3/mol)[39]	22.83	19.86	13.31
J=1 content at 20K (%)	0.2	2.5	-
$Q_1(0)$ (cm^{-1})[40]	4162.06	2993.96	-
$S_0(0)$ (cm^{-1})[40]	354.38	179.06	-
crystal structure	hcp	hcp	fcc
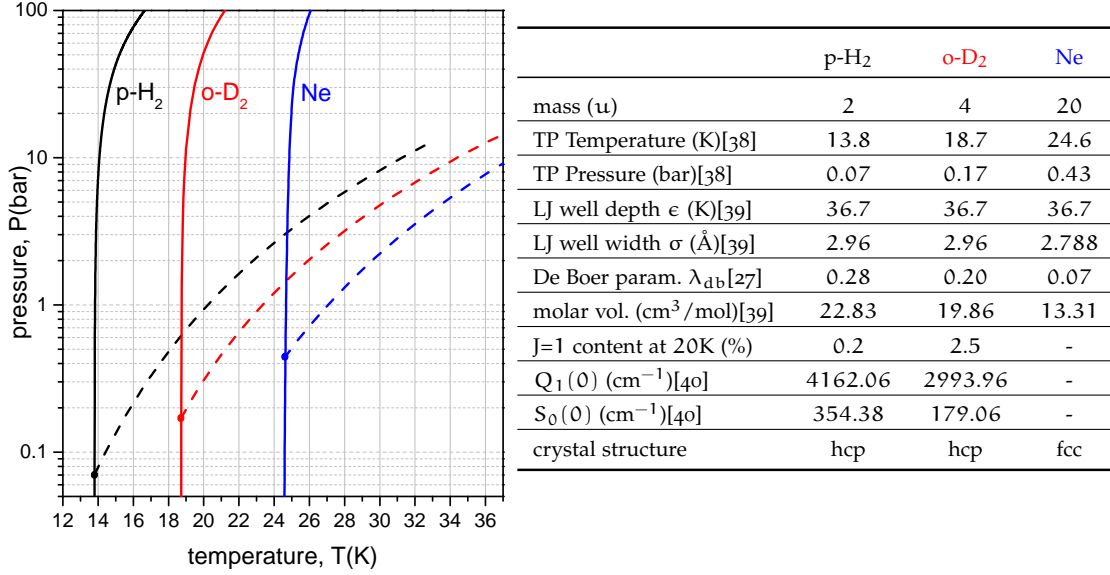
Figure 7: Phase diagrams and fundamental properties of p-H_2, o-D_2 and Neon. Melting curves and vapor pressure curves are represented by solid and dashed lines, respectively, the triple points TP by big dots.

2.4.1.2 Differences to hydrogen

When comparing H_2 and D_2 from the classical point of view, the most obvious difference between the two isotopes is the mass with a factor of 2, which entails the majority of distinctions. Starting at the thermodynamic properties one notices that the normal melting point is significantly higher for o-D_2 with $T_M(o\text{-}D_2) = 18.7\,$K with respect to $T_M(p\text{-}H_2) = 13.8\,$K (see fig. 7). In order to have the same kinetic energy

$$E_{kin} = 1/2mv^2 \, , \tag{2.12}$$

a deuterium molecule with double the mass has a velocity

$$v_{H_2}/v_{D_2} = \sqrt{m_{D_2}/m_{H_2}} = \sqrt{2} \approx 1.4 \tag{2.13}$$

times lower with respect to hydrogen, which is very close to the ratio of their melting points $T_M(o\text{-}D_2)/T_M(p\text{-}H_2)$. Hence, the higher inertia of D2 molecules results in phase transitions at higher (thermal) energies, i.e. temperatures.

A similar reasoning can be applied to the excitation energy required for the first vibrational $Q_1(0)$ and rotational $S_0(0)$ levels. Classically, the excited motion is determined by the higher (moment of) inertia of the nuclei, yielding a $\sqrt{m}$-dependency for the harmonic vibrational case and a m-dependency for the rotational case, so that

$$Q_1(0)(p\text{-}H_2)/Q_1(0)(o\text{-}D_2) \approx 1.4 \text{ and } S_0(0)(p\text{-}H_2)/S_0(0)(o\text{-}D_2) \approx 2.0 \tag{2.14}$$

in the gas phase [40].

However classical explanations do not suffice for comparing both isotopes, because at low temperatures in the condensed phases, quantum effects start to have an increasing impact. Previously it was stated that the intermolecular forces are identical for p-H_2 and o-D_2 in their ground state and can be modeled by a Silvera-Goldman potential with the same parameters. Thus, in the classical view the molar volume in the condensed phases for similar thermodynamic conditions (accounting for the inertia) should be equal.

Yet, comparing the molar volume at zero pressure at 4.2 K yields $V_{mol}(p\text{-}H_2) = 23.16\,cm^3/mol$ and $V_{mol}(o\text{-}D_2) = 19.95\,cm^3/mol$ [27, p.405/438], a difference of 16 %. The reason for this is the zero-point energy, which roots in Heisenberg's uncertainty principle and is another beautiful example for the quantum nature of hydrogen.

The "quantumness" of a particle can be described by the de Boer parameter λ_{db}, which represents the extent of its de Broglie wavelength relative to its Lennard-Jones interaction potential:

$$\lambda_{db} = \bar{h}\sigma\sqrt{m \cdot \epsilon} , \tag{2.15}$$

with σ and ϵ being the width and depth of the interaction potential. Both $J = 0$ hydrogen isotopes have the same potential and the de Boer parameter only differs in mass, yielding the familiar ratio $\lambda_{db}(p\text{-}H_2)/\lambda_{db}(o\text{-}D_2) = \sqrt{2} = 1.4$ [27, p.445].

The quantumness makes an appearance as the zero-point vibration, i.e. a delocalization of the molecule. Hence, in the quantum world the interaction potential does not have a definite center of mass, but is blurred according to the size of its wavefunction. In the condensed phases this delocalization leads to a partial overlap of the strongly repelling hard cores of the potential, which is compensated by greater distances of adjacent molecules.

As the de Boer parameter for hydrogen is greater than for deuterium, the wavefunction of the former extends to longer distances. For reference, the minimum of the Goldman-Silvera potential well is at 3.44 Å, whereas at zero pressure the separation of p-H_2 molecules in a 4.2 K solid is at 3.789 Å[27, p.437] and for o-D_2 at 3.605 Å[31, p.7]. Thus, effectively a p-H_2 molecule occupies more space than an o-D_2 molecule, despite having the same potential. This is an astonishing feature, especially when considering its origin solely is due to the difference in mass.

2.4.1.3 The hydrogen–deuterium system

Next, we turn to binary mixtures of p-H_2 with o-D_2 at equilibrium conditions. A main issue, contradictorily discussed in the literature, is if mixtures of these isotopes can be considered an ideal mixture, i.e. the substances mix perfectly without any favoring of local accumulation of one species or, macroscopically, phase separation [41, 42]. It has been found that substantial amounts of the $J = 1$ component appear to have an influence [41, p.282] due to their anisotropic interaction potential, hence, we will focus only on literature available for pure $J = 0$ mixtures.

The fundamental quantities governing the deviation from ideality are the heat of mixing H_E and the excess volume V_E. For the p-H_2−o-D_2 system these values have been determined both theoretically and experimentally to be small [41, 43] and no macroscopic phase separation has been observed for the pure liquid and solid phases

[42, p.110], endorsing the ideal behaviour. On the other hand, variational Monte Carlo simulations [44] have found a lower excess energy, i.e. likelihood, for o-D_2 clusters in solid p-H_2. Additionally, neutron diffraction experiments suggest a weak deviation from ideality even at $\approx 17\,$K with "concentration fluctuations in the short range order reflecting a probable tendency for the H2-D2 system to separate" [41, p.384].

In any case, as the deviations from ideality are quite small, we can conclude that the density ρ_x of a p-H_2—o-D_2 system in a pure phase, with x as the relative concentration of o-D_2, can be described by a linear equation combining the densities of the pure substances:

$$\rho_x = (1-x) \cdot \rho_{pH_2} + x \cdot \rho_{oD_2} \tag{2.16}$$
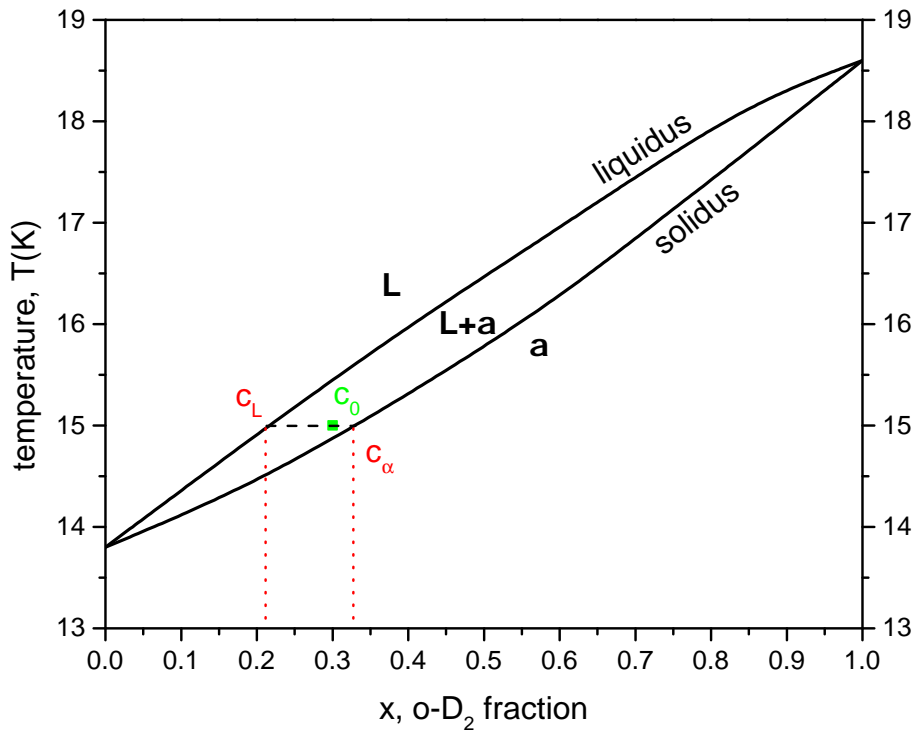
Figure 8: Binary phase diagram of the p-H_2—o-D_2 system at equilibrium vapor pressure. L and α denote the liquid and solid regions, respectively, whereas L $+ \alpha$ marks the coexisting phases. At arbitrary example conditions $T_0 = 15\,$K and overall concentrations $c_0 = 0.3$ a liquid phase with $c_L \approx 0.21$ and a solid phase with $c_\alpha \approx 0.32$ coexist. Data for liquidus and solidus line from [45].

An important remark is that the above statements about phase separation are only concerned with the pure liquid and pure solid states. Though, even in an ideal mixture, there are thermodynamic conditions at which a liquid and a solid phase coexist. The binary phase diagram for p-H_2 and o-D_2 is shown in figure 8 with temperature T vs. relative concentration of ortho-deuterium x, while the pressure is according to equilibrium conditions. The points at the left and right edges with $x = 0$ and 1

represent the melting points T_M or, more precisely, the triple points of pure p-H_2 and o-D_2, respectively. There are two lines connecting both points, the upper one being the so-called liquidus and the lower one the solidus, forming a "cigar"-shaped area. Conditions above the liquidus or below the solidus line represent the regular pure liquid, denoted as L, or pure solid, denoted as α, respectively. For points inside the cigar-shaped area, the thermodynamic equilibrium conditions lead to stable, coexisting liquid and solid phases $\alpha + L$. Yet, the concentration of isotopes within each phase differs.

For illustration, we choose an arbitrary point $c_0 = 0.3$, $T_0 = 15\,\text{K}$ inside the cigar. By drawing a horizontal dashed line we get the concentrations of the coexisting liquid and solid phases by the intersections with the liquidus and solidus line, respectively, resulting in $c_L = 0.21$ for the liquid phase and $c_\alpha = 0.32$ for the solid phase[3].

It is worth emphasizing that the coexisting phases with differing concentrations occur at equilibrium conditions ($t \to \infty$). If moving along a trajectory in the phase diagram, e.g. lowering the temperature T, the concentrations c_L and c_α have to adjust to the changing thermodynamic conditions. Because homogenization depends on the diffusion rate of the particles, especially in the solid phase the time to reach equilibrium of concentration can be quite extended and concentration gradients along the phases can arise.

2.4.2 Neon

Regarding mixtures with para-hydrogen, neon can be considered an augmented version of ortho-deuterium with a mass 10 times that of hydrogen. The melting point at atmospheric pressure is considerably higher with $T_M = 24.5\,\text{K}$, yet there still is overlap, so that the liquid phases of hydrogen and neon can be mixed.

Belonging to the noble gas family, the interaction potential of neon is spherically symmetric, too, and very close to that of hydrogen/deuterium, with the same well depth ϵ of the Lennard-Jones potential and just a 1.06 times smaller radius of the well minimum σ (see fig. 7). Furthermore, the higher mass results in a much smaller de Boer parameter $\lambda_{db} = 0.07$ and hence smaller zero point vibrations, so that the molar volume in the solid phase at 4.2 K and close to zero pressure is only $V_{mol} = 13.31\,\text{cm}^3/\text{mol}$, a factor of 1.7 less than hydrogen or 1.5 for deuterium, respectively [39, p.947]. Hence, at least from its interaction, neon can be considered an isotope of hydrogen, which makes it an ideal candidate for probing effects of a slightly changed interaction potential and influence of quantum behaviour based on the zero point energy. A significant difference emerges in the solid structure, as neon, like all noble gases, freezes into an fcc structure from the equilibrium melt, rather than an hcp for the hydrogen family.

Because of the greater microscopic differences in comparison to the p-H_2−o-D_2 system, mixtures of neon with para-hydrogen or ortho-deuterium differ more severely from an ideal mixture. The enthalpy of mixing is significantly higher, so that phase separations already occur at small dilutions and a homogeneous solubility in the liquid phase is limited to 5% at maximum for neon in H_2 and around twice that value for neon in D_2 depending on the temperature [48, 49].

---

3   The amounts of solid and liquid can also be calculated according to lever principles, but are not of relevance here. A nice introduction can be found in [46] and following pages.
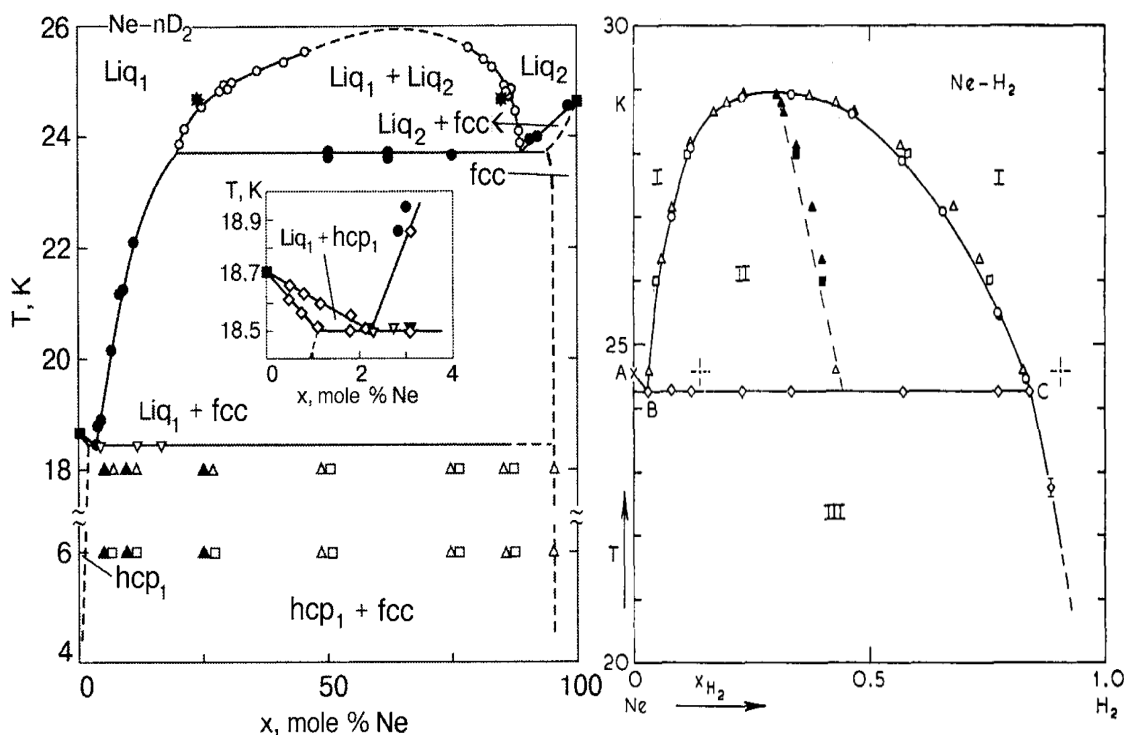
Figure 9: Left panel: Binary phase diagram of the n-D_2—Ne system at equilibrium vapor pressure [39]. The system is monotectic, with two liquid phases Liq1 + Liq2 of different concentration coexisting in a wide range. There are two triple points at Ne fractions x = 2.3% and 90.3%, which have lower freezing temperatures than the corresponding pure substances.

Right panel: Binary phase diagram of the Ne—p-H_2 system at equilibrium vapor pressure [47]. Regions I and III mark the homogeneous liquid and solid phases, respectively, whereas in II phase separation occurs.

The complicated binary phase diagram of n-D_2-Ne is of the monotectic type, i.e. that there are regions, where two liquid phases Liq1 + Liq2 with different concentrations coexist [39, p.949] (see left panel in fig.9). Depending on concentration and temperature, the solid exhibits either an fcc, an hcp or a mixed crystal structure, which all can be accompanied by a stable liquid with a different concentration. Additionally, two special triple points are present at high concentrations of one substance, which have a lower freezing temperature than the corresponding pure substances.

The binary phase diagram for mixtures of Ne—p-H_2 displayed in the right panel of fig.9 exhibits a similarly complex structure, including regions (II) in which phase separation occurs. Unfortunately, no binary phase diagrams for the pure J = 0 systems p-H_2-Ne and o-D_2-Ne are available so far, which may differ from the ones shown based on the differences in the intermolecular interaction of the J = 1 component.

As a last remark, we have to note that atomic neon does not have any vibrational or rotational states and, hence, exhibits no Raman activity.

Summary: Deuterium, neon and mixtures

The classical intermolecular interaction potentials of hydrogen and deuterium are equal. Yet, due to twice the mass of the latter the (moment of) inertia is greater, resulting in a higher melting point and lower Raman excitation energies. Additionally, lower zero point vibrations make deuterium molecules occupy less space compared to hydrogen. Mixtures of the spherically symmetric $J = 0$ isomers p-H_2 and o-D_2 behave ideal, i.e. are completely miscible.
Neon atoms exhibit a very similar interaction potential well depth, yet are smaller and 10 times heavier than p-H_2 molecules. The binary phase diagrams of neon with p-H_2 or o-D_2 are more complicated, so that only small dilutions are miscible.

2.5 Nucleation and Crystal growth

This chapter is dedicated to the phase transition from the microscopically disordered liquid to the periodically ordered crystal and discusses ideas how it can be frustrated. The necessary condition that this transition occurs is that at the current thermodynamic properties the solid has a lower free energy than the liquid state. In the equilibrium phase diagram the melting line represents this border, at which the free energy of both phases is equal. Yet, it is still possible, that a supercooled substance, with a temperature below the melting line, remains liquid for indefinite times. The reason for this is that, as an additional sufficient condition, an energy barrier similar to chemical reactions must be overcome to initiate the transition.
An easily reproducible example is supercooled water from the fridge slightly below 0°C staying liquid, but instantaneously starting to freeze, if a disturbance, e.g. a shockwave through a quick hit, is induced (Video: [50]).

From the theoretical description the process of crystallization is divided into two stages: Nucleation (section 2.5.1), in which first microscopic embryos with a crystal structure have to be formed against the counterplaying energy barrier and secondly crystal growth (section 2.5.2), which macroscopically governs the amount of the bulk transformed through the difference in free energy as the driving force. An additional third part offers a short introduction into the glass transition (section 2.5.3), for which nucleation and therefore crystallization is avoided.

2.5.1 Nucleation

In this section we will focus on homogeneous nucleation of a crystal structure in a liquid of a pure substance[4]. In its counterpart, heterogeneous nucleation, a foreign particle impurity acts as the nucleation seed for the solid. In contrast, the embryo in homogeneous nucleation exclusively arises from thermal fluctuations, i.e. rearrangement of particles, which underlies pure statistics.

The dominant theoretical description in the field is called classical nucleation theory (CNT). In the first, simple version of this model, molecules form a crystal structure in shape of a sphere separated by a sharp interface from the surrounding disordered liquid [51].
The basic assumption states that two opposing contributions to the Gibbs free energy Δg of this spherical solid embryo incorporating n molecules compete [52, p.1]: a negative term promoting the formation of the embryo depending on the chemical potential between the liquid and the solid $\Delta\mu(T) < 0$, scaling with the volume; Secondly a positive, surface term A, inhibiting the growth due to the interaction with the disordered liquid. The simple formula reads:

$$\Delta g(n) = -|\Delta\mu(T)|n + An^{2/3} \tag{2.17}$$

---

4 In general, nucleation is the main concept, when a new phase within a different one is generated. For example, the formation of cavitation bubbles leading to fragmentation of an expanded liquid also falls in this category.

As the terms differ in the scaling with n, by simply deriving eq.2.17 a critical size n^* is found, at which $\Delta g(n = n^*) \equiv \Delta g^*$ reaches its maximum (see fig. 10). At sizes $n > n^*$ clusters tend to grow because adding particles is energetically favorable and hence these clusters act as nucleation embryos initiating the growth of the solid, whereas smaller clusters with $n < n^*$ are likely to dissociate.
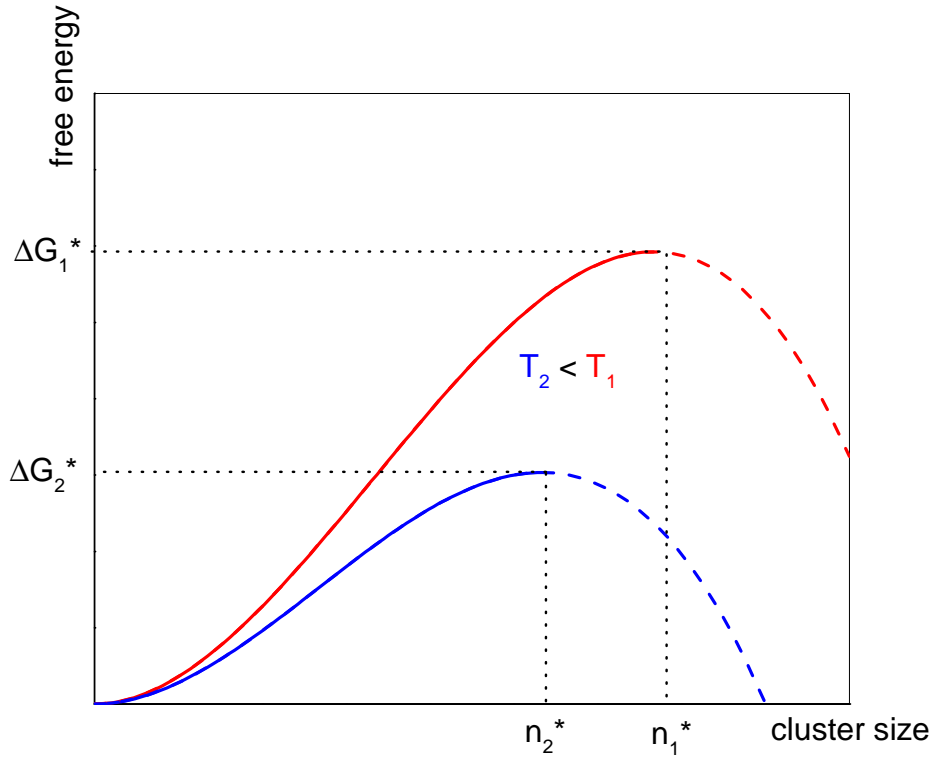
Figure 10: Schematic plot of eq. 2.17 for two different temperatures $T_2 < T_1$. Up to cluster sizes n^* adding particles demands energy (solid lines). Above that point, the energy balance is favorable and clusters tend to grow (dashed lines). Lowering the temperature (blue curve) decreases the energy barrier Δg^* as well as the critical cluster size n^*.

The value of Δg^* corresponds to the height of the energy barrier. The higher it is, the lower the probability that a critical cluster is spontaneously generated. This is expressed in the nucleation rate I, i.e. the number of critical clusters formed by thermal fluctuations in a given time and volume, which is written in the Arrhenius equation as [52, p.1]:

$$I(T) = I_0 \cdot exp\frac{-\Delta g^*(T)}{k_B T} \ , \tag{2.18}$$

where I_0 is a kinetic prefactor describing the rate, at which particles are added to the cluster, and k_B the Boltzmann constant. The nucleation rate strongly depends on temperature (see plot in fig. 11). With increased undercooling the difference in the chemical potential between the liquid and solid phase grows [10, p.478], lowering the number

of particles necessary for the critical nucleus and decreasing the energy barrier Δg^*. At a certain degree of undercooling (for pH2 $T \approx 7K$) the chemical potential difference becomes almost constant and the diminishing mobility of particles, represented by the denominator $k_B T$ in formula 2.18 leads to less frequent thermal fluctuations and an overall decrease in the nucleation rate.

As both these effects take place in the exponent, even slight changes in the temperature within 0.1 K cause dramatic variations with several orders of magnitude in $I(T)$ (compare fig. 11). The absolute values of the curve should not be trusted, as comparison to experimental data is usually only available in a small temperature range and fits with formula 2.18 are extremely prone to uncertainties.

In experimentalists' language, the nucleation rate is equivalent to how long the super-cooled liquid can survive without starting to freeze. As the appearance of a critical nucleus is a statistical process and due to its strong temperature dependence in combination with comparably huge liquid volumes used in experiments, generally a lot of critical nuclei are generated, starting the freezing process at different locations in the bulk. This circumstance is incorporated in the next section 2.5.2, where crystal growth is discussed.
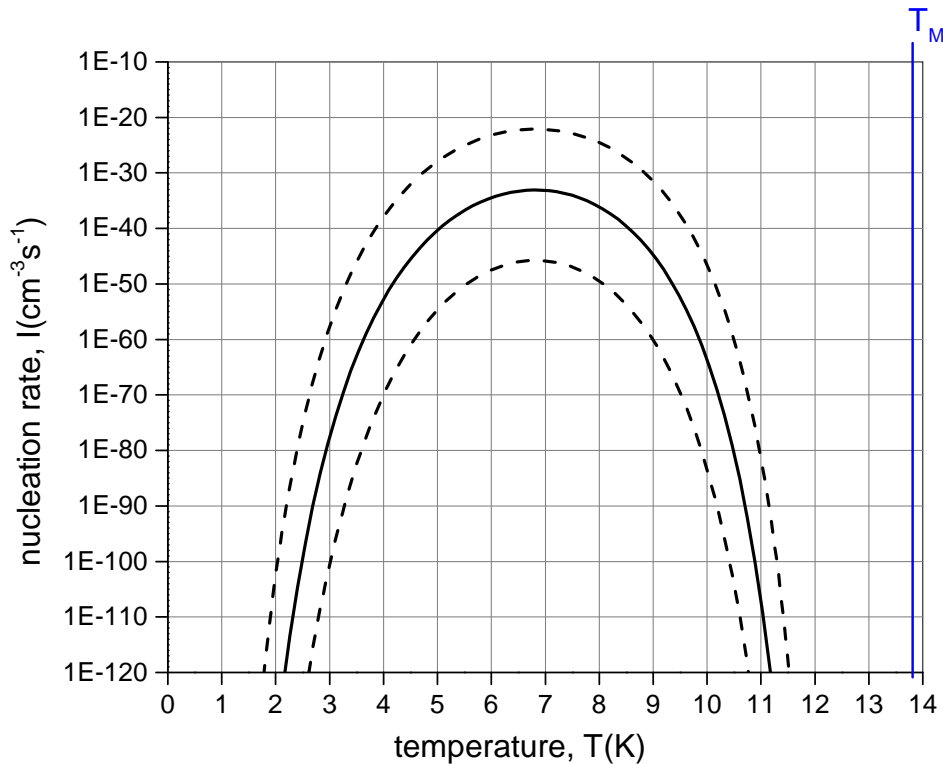

Figure 11: Nucleation rate, i.e. probability of freezing, of liquid $p-H_2$ with arbitrary parameters (solid line). Small changes in the temperature have a huge impact on the formation of nucleation embryos. Even small uncertainties of 10% in the liquid-solid surface energy contained in A in eq.2.17 change the absolute values of the curve dramatically (dashed lines). Data from [10].

The simple model introduced here implies several rough approximations. In recent years, enhancements have been made including deviations from a shape of a sphere for the embryo, a diffuse interface between the liquid and the solid core as well as the applicability of thermodynamic quantities to small clusters with just a few participating particles [52, p.1]. All these concepts deal with the nucleation rate at steady state, i.e. at fixed thermodynamic parameters. However it has been found [53], that the nucleation rate not only depends on the absolute temperature T, but also on the cooling rate Ṫ, changing the overall shape and position of the nucleation curve of fig.11.

However, as Raman spectroscopy is not sensitive to observing the initial nucleation process, mainly due to the marginal number of particles involved, we will not go into the mathematical subtleties of these descriptions.

Two further concepts of nucleation should be mentioned. Within the scope of the proposed superfluidity of hydrogen, the concept of quantum nucleation was discussed [10], in which hydrogen molecules can cross the energy barrier Δg^* via tunneling. This effect becomes stronger at lower temperatures, where quantum effects are more pronounced. Yet, as it is expected to occur merely at temperatures of $T < 8K$ or below, depending extremely on fit parameters, we don't expect it to play a role in this experiment.

The second aspect comes into play, when the liquid consists of more than one component. In this case, besides thermal fluctuations generating a solid core, there also can be local concentration fluctuations, severely altering the nucleation barrier [54]. Depending on the thermodynamic properties of the single components as well as on the interplay between them, local compositions can greatly lower the energy barrier and particles necessary for a critical nucleus, enhancing the overall nucleation rate (similar to lowering the temperature in fig.10) or, just the other way around, suppress crystalline nucleation giving rise to the formation of a glass [55].

The exact microscopic mechanisms behind nucleation are yet poorly understood [2]. Classical nucleation theory just states that an embryo has to overcome a critical size through thermal fluctuations in order to grow, but it does not explain, what these statistical fluctuation actually look like. As the crystal usually possesses a higher density than the liquid, density fluctuations towards higher values were thought to be the initiator for forming embryos [56].

However, in recent years by means of computer simulations and colloidal suspensions, another possible mechanism was found, accounting for structural rather than density precursors [57]. Within this *bond orientational ordering* theory, rearrangements of particles, which are compatible with a crystal structure, are the crucial configurations for triggering the nucleation process. Additionally, the topology of these clusters is proposed to determine the structure of the growing bulk crystal.

In this context Ostwald's rule of stages is of importance. It states that the structure that forms first from the melt does not necessarily have to be the energetically most stable final form. Rather, the transformation typically proceeds through several discrete metastable states [58]. The reason for this can be found in the amount of possible metastable forms, of which some can have a lower energy barrier, critical sizes demanding less particles or shapes already present in or compatible with the parent liquid phase.

2.5.2 Crystal growth

Crystal growth takes over, once the nucleation rate is high enough to allow the formation of critical nuclei, which are inevitably forced to increase in size.

The growth of the crystal can be described by the Avrami equation [59]. We start with a homogeneous, supercooled liquid at constant temperature in a fixed volume. As mentioned in the previous section, throughout the whole volume critical nucleation embryos are formed statistically corresponding to the nucleation rate I. A critical embryo grows isotropically in all directions, which results in a sphere linearly increasing in diameter with a constant growth velocity u. As critical embryos are created at random times, the sizes of the spheres at a given moment differ, yet each u is the same.
This first scenario is valid only for the beginning of the phase transformation to the crystal. After some time, when a significant part of the volume is already transformed, the growing spheres start to overlap and further growth at the intersections is disabled. This circumstance becomes more severe, the less remaining liquid volume is left, until everything has transformed to the crystalline phase.
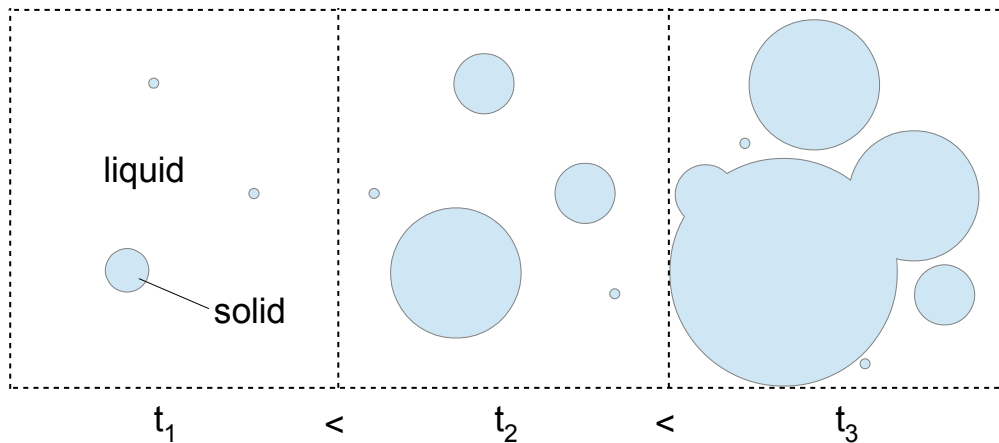
Figure 12: Three time steps of crystal growth according to the Avrami equation 2.19 in 2 dimensions. Continuously, critical solid embryos are formed at rate I throughout the volume, which grow at a constant velocity u. After some time (t_3) the solid spheres increasingly overlap until the whole volume is transformed.

The corresponding Avrami equation reads:

$$f(t) = 1 - exp(-\frac{\pi u^3 I t^4}{3}) \qquad (2.19)$$

The solid fraction $f(t)$ is the amount of solid already transformed and ranges between 0 before nucleation in the liquid phase up to 1, when the transformation is completed. The solid line in Fig.13 shows an example plot of the Avrami equation. The positive curvature in the beginning is associated with the over time increase of nucleation sites or growing spheres, respectively, whereas the negative curvature close to $f = 1$ represents the proceeding overlap of spheres. In the exponent of formula 2.19 the nucleation rate I and the linear, three-dimensional growth u^3 can be united with the

constants in a single parameter k, as well as the time dependency t^4 generalized to $(t - t_0)^n$, where t_0 denotes the time, at which the first critical nucleation embryos are formed, and n a variable exponent described later on:

$$f(t) = 1 - exp(k(t - t_0)^n) \tag{2.20}$$

This simplification is used for data fitting, because, as described in the previous section, the nucleation rate often is unknown.

Of course, the Avrami equation, stated in its simple version presented here, makes some approximations. Erukhimovitch and Baram [59] point out, that formula 2.19 does not take into account, that nucleation events can only take place in the untransformed, liquid volume instead of the total volume. This overestimates the solid fraction slope particularly at the end of the process and in their paper they offer an integral version, which later was proven to be wrong [60] and followed by a differential equation [61]. Hence, in a real system the increase of $f(t)$ at the end of the process is less pronounced as the original formula suggests. Unfortunately, the corrected equation is quite cumbersome for fitting data, because it must be solved numerically.

Another condition to obey is that the temperature and, associated with it, the crystal growth velocity as well as nucleation rate are assumed to be constant in time and throughout the whole volume, which experimentally is not always satisfied.

Keeping these restrictions in mind when fitting, the time exponent n can yield information about the growth details. Values of $n < 4$ signal that either the nucleation rate is not constant over time or homogeneous over the volume or the crystal growth does not proceed in 3 dimensions, is not isotropic or in some way frustrated. The effect of $n < 4$ on the fit is shown by the dashed and dotted line in fig.13. Basically, the whole process is stretched in time, with an earlier initial increase and a delay in reaching the final value $f = 1$.

Let us look more into the details of the actual growth mechanism, resulting in the macroscopic velocity u. In the model of an isotropically growing sphere, when zooming in onto microscopic scales, the proceeding interface between the liquid and the solid is a moving plane towards the liquid. Its velocity u is determined by the rate at which particles leave the melt and join the solid or, in another view, change their structure from the disordered to the periodically ordered state of the crystal. Mathematically this can be described as [4]

$$u(T) = f \cdot u_0(T) \cdot [1 - exp(-\frac{\Delta g}{k_B T})] \, , \tag{2.21}$$

where the part in brackets like in equation 2.18 is the free energy Arrhenius part, driving the transition and $u_0(T)$ is representing the growth mechanism. The attachment factor f, ranging between $0 \leqslant f \leqslant 1$ is the fraction of particles contributing to the growth and quite problematic as there is no way of experimentally determining this parameter, since it mainly depends on geometric arrangements.
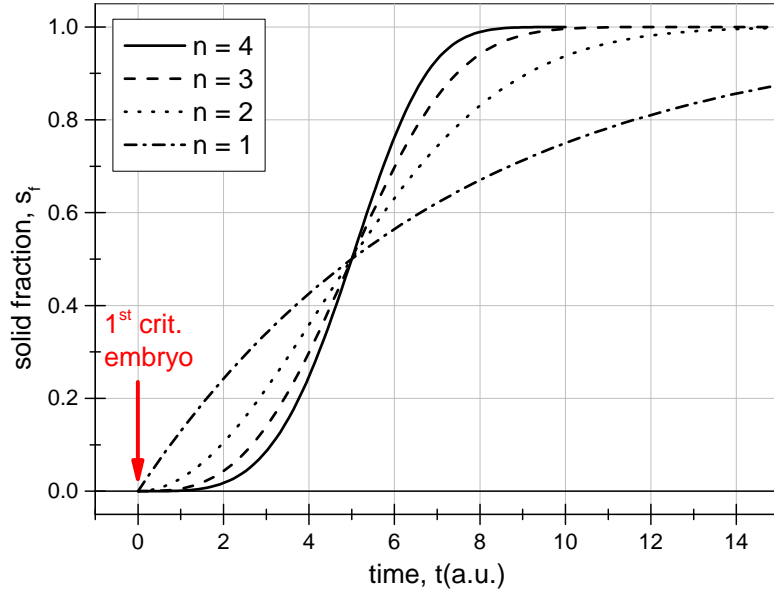
Figure 13: Plot of eq.2.20 with the standard exponent for time t with $n = 4$ (solid line), and smaller values $n = 3$ (dashed line), $n = 2$ (dotted line) and $n = 1$ (dashed+dotted line), representing crystal growth conditions deviating from ideality. The parameter k is chosen to cross the arbitrary common point $(x, y) = (5, 0.5)$.

There are two different concepts for $u_0(T)$: In the diffusion-limited model, the process is determined by the rate at which particles can diffuse into the interface and the solid, respectively. In this case

$$u_0^{dif} = \frac{D}{a} = \frac{D_0}{a} exp(-\frac{E}{k_B T}) \,, \tag{2.22}$$

with $D = D_0 exp(-E/(k_B T))$ the diffusion in Arrhenius form and a the interatomic distance. The majority of materials exhibits this kind of growth [12, p.1496].

The alternative process is the collision-limited model, in which the rate of particles colliding with the interface, determined by the thermal velocity, is predominant for the crystal growth:

$$u_0^{col} = \sqrt{\frac{3k_B T}{m}} \tag{2.23}$$

Typically, u_0^{col} is about three orders of magnitude greater than u_0^{dif} and more often present in monatomic liquids.

According to the literature available, there are no clear identifications to predict the growth mechanism in a substance or alloy. The "common wisdom" seems to be, that collision-limited growth will appear, if it is not hindered by a diffusion-dependent process [4]. These processes, where particle diffusion is mandatory, include:

- directionality/local structures involving the breaking of bonds

- a solute partitioning/phase segregation in an alloy

- chemical ordering enforcing certain sub-lattice structures

- the aspect ratio of big molecules demanding for reorientation

The list probably is incomplete, but it demonstrates, how poorly understood the mechanisms of crystal growth indeed are.

However, progresses have been made, especially regarding the first two items. Russo and Tanaka [57] state that icosahedral ordering in the liquid phase within hard sphere simulations can frustrate the growth of a crystal phase. They show that these local structures are energetically favorable at higher densities, but are incompatible with the crystal structure as their fivefold symmetry does not allow periodicity. This approach is closely connected to explaining the glass formation (see chapter 2.5.3). So far, only qualitative explanations have been proposed, a quantitative theoretical framework, unfortunately, is not yet available.

Regarding the second point on the list, Jackson et al. have constructed an analytical model [5], which can be applied to binary mixtures of metals and shall be elucidated now.

It should be emphasized that the concept of phase segregation only occurs in mixtures, which means more than one substance is present in the volume of interest. The main idea is that at the interface during solidification the relative concentration of the substances in the solid differs from that in the liquid, which requires diffusion of particles.

We consider a binary mixture with two substances A and B, whereas at equilibrium B is at low relative concentration $[C_B]_E < 0.1$ to be able to make some approximations. First a distribution coefficient k_e for the diluted B component at equilibrium is defined, which is the ratio of the relative concentration in the solid C_B^S to the relative concentration in the liquid C_B^L:

$$k_e \equiv \left[\frac{C_B^S}{C_B^L}\right]_e = \exp(-\frac{\Delta\mu_B^0}{k_B T}) \tag{2.24}$$

This is a theoretical value as it assumes an infinitely slow growth velocity of the crystal, so that k_e can be reached by diffusion. Yet in a realistic scenario, the time for diffusion is limited by the interface proceeding towards the liquid. The ratio of the distance the interface moves at velocity u to the mean distance a molecule can move by diffusion D is expressed in the parameter

$$\beta = \sqrt{\frac{a \cdot u}{D}[1 - \exp(-\frac{\Delta g^0}{k_B T})]} \ , \tag{2.25}$$

where a is the atomic distance and the part in brackets again the attachment rate to the solid driven by the chemical difference.

Connected to β, another quantity is defined as the energy transfer parameter P.

$$P = \frac{A\beta}{1 + A\beta} \ , \tag{2.26}$$

where A is a constant, unfortunately not specified more clearly.

Finally, the off-equilibrium segregation for small impurity concentrations can be approximated to

$$k \approx k_e^{1-P} \ . \tag{2.27}$$

For understanding the meaning of these new parameters, we look at their range of values in the limiting scenarios.

Relating to the definition of k_e we first choose an almost non moving interface $u \rightarrow 0$. By its definition, β, the ratio of interface velocity to diffusion, as well as the energy transfer parameter P become zero in that limit. The particles are free to diffuse away from the stagnating crystal and create two different concentration regions in the liquid and solid, respectively, the ratio being $k = k_e$ according to formula 2.24.

In the opposite scenario, the crystal grows very fast and particles do not have the time to diffuse. This is called *solute trapping* and its concept has been refined in [62]. Here, $\beta \rightarrow \infty$ and $P \rightarrow 1$, resulting in $k \rightarrow 1$. In this case, there is no segregation effect and all particles are "devoured" at their current position by the fast growing crystal interface. Finally, Jackson proposes a formula for calculating the crystal growth velocity u, which is valid for small concentrations of the B component, so that only the A component contributes to the crystal growth:

$$u \approx u_A = u_A^0 \left[C_A^l - C_A^s \exp \left(-\frac{(1-P)\Delta g_A^0 + P\Delta g_{mix}^0}{k_B T} \right) \right] , \qquad (2.28)$$

where u_A^0 is the growth velocity of the pure substance and Δg_{mix}^0 is the Gibbs free energy of mixing. Depending on the value of the energy transfer parameter P, the exponent can be dominated either by effects of the mixture ($P = 1$) or by segregation ($P = 0$).

Just recently, another approach for the slowing down of crystal growth in binary metal alloys has been presented [63]. Simulations reveal that the difference between a relatively fast and a slow growing crystal can be attributed to the factor f in eq.2.21, the attachment coefficient of particles. They further find that the liquid-crystal-interface for the faster growing alloy is significantly thicker and the compositional order is closer to that of the final crystal. Hence, they propose that the interface plays the fundamental role for crystal growth as well as the glass formation, because the slow growing alloy is, in contrast to the faster one, a good glass former.

All above concepts will be discussed in the light of our experimental results in chapter 6.1.6.

2.5.3 Glass transition

Another possibility for the fate of a supercooled melt is vitrification, i.e. the formation of a glass. In this case, no periodic crystal structure emerges, but instead around a critical temperature T_g the viscosity or relaxation time, respectively, increases by several orders of magnitude with the particles remaining as a disordered, yet "solid" system. Vitrification requires either big, complex molecules or in metals mixtures of at least two substances and it occurs only at fast cooling rates and/or deep quenches.

The microscopic details of the glass formation are even more unclear than for the crystal growth. Currently, there are several competing hypothesis, which are mainly backed up by computer simulations and often are more of qualitative than of quantitative character. Moreover, some of the ideas seem to be compatible with each other [64, p.623] and are as assumed to be closely related to nucleation and crystal growth, respectively. This interconnection, based on a huge amount of theoretical papers, in combination

with lack of experimental data makes it difficult to get a firm overview over this topic.

One major theory is the *random first-order transition theory* (RFOT) merged from three subcategories, including *mode-coupling theory*. Basically, its goal is to find a growing correlation length by means of minimizing the free energy landscape as a function of the order parameter. It assumes that the glassy state is a result of a real phase transition and hence a collective phenomenon based on the group statistics of all particles. Yet, due to the quite well understood limitations of this approach this phase transition is more likely to be related to a softened crossover through metastable states, which is slowed down by an increasing energy barrier [64, p.605, p.614].

An alternative approach proposes, that the origin of the glass formation is rooted within geometric frustration and the circumvention of the crystalline phase [57]. This concept has already been mentioned previously in section 2.5.2 as the occurrence of local structures. Starting from the mathematical issue of packing efficiency in 3 dimensions, one finds that, depending on the size ratios of (hard) spheres, certain local structures like icosahedral ordering are energetically favorable, but due to their fivefold symmetry can not be arranged into a periodic lattice structure. Other local symmetries are also identified to be incompatible with periodicity [65]. In a supercooled liquid these structures could hinder not only the growth of the crystal, but even suppress the formation of critical embryos at all. Hence, in this approach local short range order stabilizes against the long range order of the crystal.

Currently, these two theoretical statements presented here, phase transition vs. frustration of crystallization, are the main parties elucidating the glass formation. With our experiment we do not contribute directly to this topic, yet we can check the compatibility with our results.

Summary: Crystallization

Crystallization is divided into the two stages nucleation and crystal growth. Classical nucleation theory governs the generatation of critically-sized embryos with a crystalline structure in a supercooled liquid by statistical fluctuations, which can be of density, compositional or structural origin. The associated nucleation rate strongly depends on temperature and once critical embryos are formed the liquid is inevitably forced to freeze based on the positive energy balance.

In the subsequent crystal growth, these nucleation sites occur at random times throughout a volume at homogeneous temperature and grow radially at a constant velocity, the progess being described by the Avrami equation. Two models for the growth velocity exist, being determined either by the diffusion rate or the thermal velocity of particles. The crystal growth can be further influenced by geometric effects, compositional segregation or effects at the liquid-solid interface. Nucleation rate and crystal growth probably are closely related to the glass formation, in which the particles remain in their disordered state but the dynamics vanish.

Part II

EXPERIMENT

3 | SETUP

3.1 Overview

The experiments have been performed in a collaboration with the group of Prof. Salvador Montero Martin at the Department of Molecular Physics belonging to the Instituto de Estructura de la Materia, CSIC in Madrid. Hence, the experimental setup is a combination of two methods: the spectroscopy related assembly in Madrid united with the nozzle and cooling devices from our group in Frankfurt. As the latter is more robust and easier to transport than the Raman spectrometer, all main measurements were conducted in Madrid, whereas the concept and pretesting of nozzles took place in the laboratory in Frankfurt.

In fig.14 a schematic overview of the setup used for the Raman spectroscopy measurements in Madrid is displayed. The color code in the upper right corner will be the guide of sections to this chapter. Additionally to the technically oriented descriptions of the apparatus, subsections labeled as "Manual: ..." are added as instructions for future experiments.
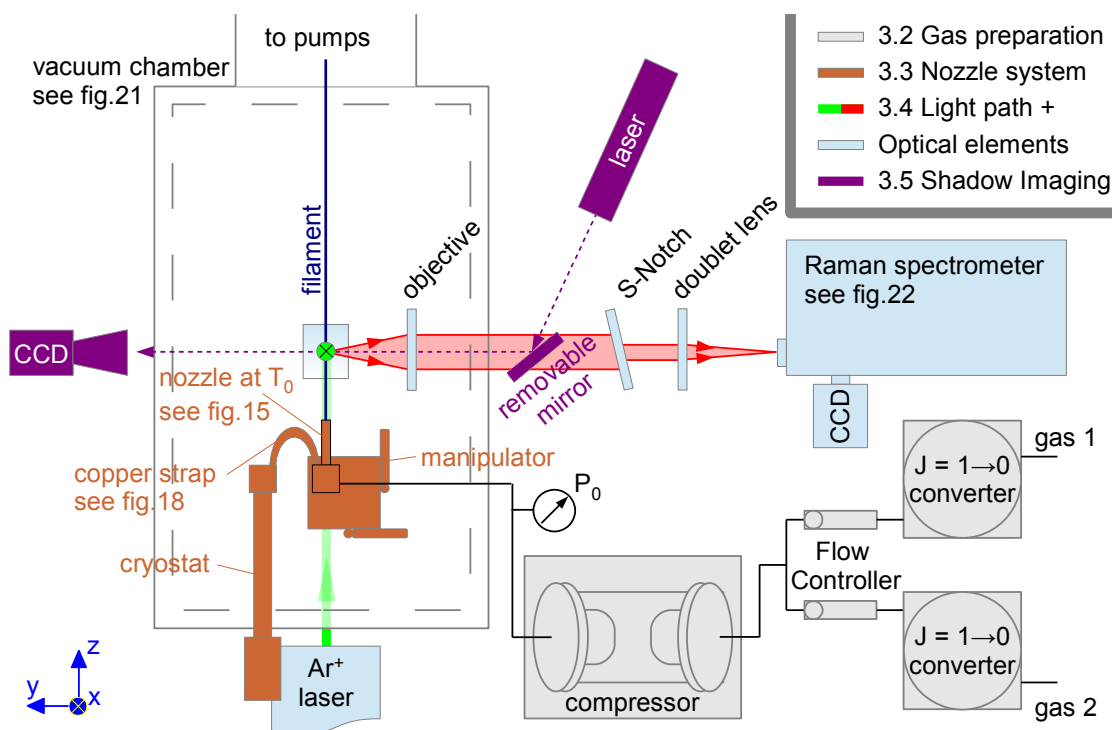

Figure 14: Schematic overview of the important components for the experiment in color code and the chapters, in which they are explained (top right).

3.2 Gas preparation

This section governs the setup for the preparation of the (mixed) gas samples and includes a subsection depicting the procedure to create filaments.

The associated parts are displayed in fig.14 in gray and connecting gas lines in black. We start in the lower right corner of the picture, marked with $Gas1$ and $Gas2$, respectively. For all experiments, commercial gas bottles from AirLiquide were used: n-H_2 N60 (99.9999% purity), n-D_2 N28 (99.8% purity, impurity mainly HD) and Ne N50 (99.999% purity). By pressure regulators (not shown) the bottle pressure is reduced to around $4\,bars$, which is the operating value of the $J = 1 \rightarrow 0$ converters used for producing p-H_2 and o-D_2, respectively. In case of neon, the converter is bypassed, yet pressure is also maintained at $4\,bar$.

The converters use commercial ferric hydroxide oxide (Fe(OH)O) powder with grain sizes of $300 - 600\,\mu m$ as catalyst material, which is cooled down to $20\,K$ by a closed-cycle cryostat, thermally isolated by vacuum. At this temperature, both hydrogen and deuterium are liquid (higher particle density) and the catalytic volume and active surface are large in comparison to the flow through the nozzle. Hence, molecules remain within catalytic conditions in the order of minutes, which allows for physically maximum $J = 1 \rightarrow 0$ conversions (see table 7 on p.23) in continuous flow operations. Due to the long initial cooling phase of the closed-cycle cryostats of a few hours, the converters are started and partially filled at least 12 hours prior to the experiments.

In the next step, the desired sample gas is prepared by means of (gaseous) mass flow controllers of type *F-201CV* from Bronkhorst. Several models with maximum flow values of 1000, 500, 200 and 20 nml/min were used in this experiment with the minimum flow of each being 2% of that value [1]. Depending mainly on the size of the nozzle d_0 and the target filament velocity v_0, associated with the expansion pressure P_0 via formula 2.3 on p.8, a total volume flow rate is determined in advance. Usually, these values are chosen through experience by previous values, but it can be estimated by comparing the mass flow (3.1) of the liquid through the nozzle having an exit surface $A = \frac{\pi}{4}d_0{}^2$ with the gaseous mass flow through the flowmeter (3.2).

$$\frac{dM}{dt} = A\rho_l v_0 = \frac{\pi}{4}d_0{}^2\rho_l v_0 \qquad (3.1)$$

$$\frac{dM}{dt} = \frac{dV}{dt}\rho_g \, , \qquad (3.2)$$

where ρ_l and ρ_g are the mass densities of the liquid and gas, respectively. The estimate for the total volume flow rate of the flow controllers then is

$$\frac{dV}{dt} = \frac{\pi}{4}\frac{\rho_l}{\rho_g}d_0{}^2 v_0 \, . \qquad (3.3)$$

Alternatively, this can be solved for d_0 to estimate the current nozzle diameter during a measurement:

$$d_0 = \sqrt{\frac{4}{\pi}\frac{dV}{dt}\frac{\rho_g}{\rho_l}\frac{1}{v_0}} \qquad (3.4)$$

---

1 nml = normal milliliter, volume of gas at $273\,K$ and $1013 mbar$

A typical value range of $\frac{dV}{dt}$ for a $5\,\mu m$ nozzle is $150 - 200\,nml/min$. For a single component sample, e.g. pure p-H_2, only one mass flow controller is used. If the flow controller is calibrated for a different gas, e.g. N_2, the desired volume flow rate first has to be multiplied by a gas conversion factor found in the manual, in this case 1.4 for p-H_2, and is afterward set as its operating value.

For mixtures, the total volume flow rate has to be split onto two flow meters according to their target ratio, again respecting their calibration factors. Formula 3.3 can also be applied to mixtures, yet one has to obey that the densities ρ_g and ρ_l change in a linear manner pertaining to the mixing ratio. Additionally, mind that ρ_l is contained in $v_0 = C \cdot \sqrt{\frac{2P_0}{\rho_l}}$ (p.8), so that e.g. for having the same velocity of a pure o-D_2 filament with respect to p-H_2, double the value of P_0 needs to be applied, which might exceed pressure gauge limits.

The exits of the flow controllers are conjoined and connected to a two-step membrane gas compressor. The compressor is vacuum leak tight and capable of maintaining underpressure (against atmosphere) on its entrance side, because its pumping speed is greater than the total volume flow rate $\frac{dV}{dt}$ through the nozzle. Therefore the flow controllers experience stationary conditions with $4\,bar$ coming from the $J = 1 \to 0$ converters against $\approx 0\,bar$ absolute at the entrance of the compressor. Behind the compressor, a liquid nitrogen cooled $0.5\,\mu m$ filter (not depicted) gets rid of possible dirt/water and an analogue as well as a digital gauge measure the final nozzle pressure P_0, before the tube is connected to the continuous flow cryostat, guiding the gas to the nozzle system inside of the vacuum chamber.

3.2.1 Manual: Establishing stable Filaments

In the first experiments, we used to control the nozzle pressure P_0 with a pressure regulator downstream the compressor (not pictured) and left the flow controller(s) completely open to just serve as a measure of the current flow. However, due to the high pressure between compressor and regulator of $\approx 140\,bar$ in that configuration, considerable back conversion of $J = 0 \to 1$ of H_2 and D_2 was detectable in the Raman spectra. To avoid this, the pressure regulator was virtually removed (= completely opened) and the flow controllers were set to maintain the total volume flow, as described in the previous section. With that procedure, the maximum pressure in all gas lines reached is P_0 with values $< 30\,bar$, what significantly reduces the back conversion.

Before starting a new measurement series, all gas lines are pumped out and flushed several times with the sample or sample ratio, respectively. This can be done after the initiation of the cooling process of the nozzle, as it takes some time until T_0 starts to decrease (see section 3.3.4). Yet, after the flushing is done, the flow controllers stay closed with a pressure of $P_0 < 1\,bar$ remaining in the lines to just have a little flow through the nozzle.

When the nozzle cryostat is at temperatures $T_0 \approx 20 - 26\,K$, depending on the mixture, both flow controllers with the previously by their ratio determined values are opened simultaneously, resulting in P_0 rising. At the beginning, the flow balance through the controllers is significantly larger than the current gas flow through the nozzle, so that at pressures $0 < P_0 < 1\,bar$ the increase of P_0 is quite fast and the gas sample

is accumulated in the lines behind the compressor. Exemplary for the case of pure p-H_2 at $T_0 = 20\,\mathrm{K}$, the vapor pressure line is reached at around $P_0 = 1\,\mathrm{bar}$ (see fig.7 on p.23) and the sample starts to liquefy inside the cold nozzle construction, during which P_0 maintains its value for about a minute. As soon as the interior of the nozzle volume is completely liquefied, P_0 again increases, yet more gradual as before, because at these conditions a spray with higher particle density, hence higher flow, is exiting the nozzle, which can be seen by the shadow imaging technique. Due to the ongoing rise in pressure, this beam becomes more narrow and eventually a slightly unstable filament, which gets straighter and more stable, the higher P_0 is. Due to the increase in velocity v_0 depending on P_0 (eq.2.3 on p.8), the liquid flow through the nozzle approximates the same value as the gas flow through the controllers and stable conditions with a steady P_0 are reached asymptotically. To accelerate this process of establishing equilibrium flow, double the values can be temporarily appointed to the flow controllers and switched back to normal values, until P_0 is constant over a few ten seconds, signaling that the flow is now balanced. If, through doubling the flow, one is overshooting this value and P_0 decreases after returning to the normal ratio, the line can also be carefully pumped out via a bypass to achieve equilibrium flow conditions.

Consider we have established a balanced flow situation. It can happen that the filament, monitored by shadow imaging, is not as stable as on previous days, even at similar P_0 and T_0 conditions. Reasons for this can be

- mixtures behaving differently than their pure constituents

- (partial) freezing of the nozzle orifice or surface

- clogging of the nozzle channel with an obstacle.

The first item can often be resolved by selecting different source conditions. The easiest and most successful way is lowering the temperature T_0, which significantly reduces the possibility of fragmentation and its preceding cavitation events (see chapter 2.1). Alternatively, P_0 can be altered, preferably increased, by changing the total volume flow of the controller(s), yet keeping their mixture ratio. This process is kind of trial and error and often is the main reason how (arbitrary) source conditions for measurement series are "chosen".

The second point of the list is an interesting effect itself. In some cases it was found that the equilibrium P_0 was higher than expected from the total volume flow, an indication that the flow through the nozzle is smaller than before. At other times at steady conditions, the vacuum in the chamber, measured by a change sensitive Pirani gauge, suddenly jumped to less than 10% smaller values and occasionally recovered to its previous reading after a few seconds. At the same moment as this value was lower, P_0 started to increase slightly, what also is a sign for a (temporary) shrinking of the flow through the nozzle, which can only be accounted for by a smaller effective nozzle diameter d_0 according to eq.3.1. The circumstance that the effect sometimes was only temporary, makes a clogging of the nozzle channel by an obstacle unlikely. It may be reasoned that small amounts of the liquid accumulate around the orifice and in nano cracks (compare section 3.3.1) and solidify through evaporation towards the vacuum, effectively reducing the nozzle diameter d_0.

Strong evidence for a partial freezing of the nozzle orifice was also found, when the nozzle regained its original size through heating. The safest way this can be done is

by increasing T_0 by a few $10\,K$ (e.g. for pure p-H_2 to $T_0 = 40\,K$) via the temperature controller and then pumping out the gas line up to the nozzle completely. Refilling of the lines can subsequently be done again at low temperatures, yet at a different T_0 as the previous filling (both higher and lower T_0 may work) or, more risky, by accumulating the sample gas with a closed valve after the compressor and opening it suddenly in order to cross the vapor pressure line instantly. A different method to get rid of a frozen orifice is briefly hitting the very nozzle tip with the Raman laser at $\approx 1\,W$ for $< 5\,s$. Due to this, the temperature rises rapidly and the filament widens into a spray, but recovers after the laser focus is gone. However, a recovery of the stable filament, if any, rarely lasted very long, as the nozzle was likely to freeze again. Additionally, though the nozzle did not take any obvious damage, it could suffer in the long-term.

If none of the above succeeds and the filament persists to be not optimally stable also in the next days, the last item on the list probably applies and the nozzle is clogged with an obstacle. To get rid of the dirt, the nozzle has to be dismounted and cleaned. Luckily, in the measurement campaigns done in this work, this has never been the case.

3.3 Nozzle system

In order to perform the experiments in this thesis, changes to the standard nozzle system typically used in Frankfurt had to be made. The new main requirements contain:

1. Nozzles capable of maintaining stable filaments over several hours

2. The possibility to get a laser focus of a few $Watt$ power close ($< 100\,\mu m$) to the nozzle orifice without influencing the filament

3. A positioning system of the nozzle with $< 1\,\mu m$ accuracy while retaining temperatures $< 20\,K$

Item one and two are covered by the new glass pipette system in sec.3.3.1 and point three by the positioning system in sec.3.3.2 of this chapter. Sections 3.3.3, 3.3.4 and 3.3.5 describe the procedures of mounting the nozzle, optimizing helium consumption and determining the zero position of the nozzle, respectively.

3.3.1 The glass pipettes

The first item on above list is fundamental and the search for suitable nozzles an ongoing research field for our whole group. Stable beams are a necessity for all experiments performed in our group, whether it is dense sprays for ion beam collision [66], a periodic droplet beam for laser plasma generation [18], supercooled water droplets or liquid filaments as in this work.

Previous to the new design, commercial electron microscopy apertures were used as nozzles, which are available with diameters down to $5\,\mu m$. Due to their initial purpose, they are metallic flat cylinders with $\approx 3\,mm$ diameter and a height of $1\,mm$ made of a platinum-iridium alloy, into which the orifice is drilled in a conic shape viewed from the inside part. The main problem for our application as a nozzle for liquids is that the
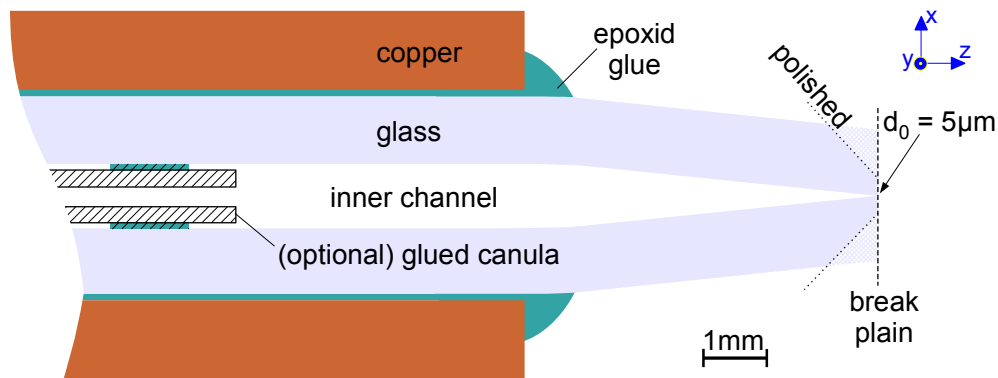
Figure 15: Schematic cross section of the glass pipette tip. Pipettes are prepared by cutting at the end of the converging inner channel (break plain). Suitable candidates are glued into a copper housing and tested. If the nozzle produces stable filament, its very tip is polished to reduce the outer diameter. Optional: The first nozzle series had a canula glued into their channel.

drilling process produces rough surfaces on the sub-μm scale. For liquid conditions with high Reynolds numbers, these irregularities act as sources for turbulences, which hinder laminar flow and ultimately stable filaments (see chapter 2.1). As even small differences in geometry and surface alter the flow, each nozzle is unique and very few of these aperture nozzles may perform better in establishing filaments, yet none was found to be outstanding. Additionally, in the current design these apertures are hold in place by a stainless steel cap with 6 mm diameter, which protrudes 600 μm with respect to the orifice and conflicts with the second point of the requirements list, i.e. probing close to the orifice.

For the new nozzle design, commercial, yet self-prepared glass pipettes are used. Their geometry is illustrated in fig.15. The purchased, ≈ 100 mm long glass tubes have an outer diameter of 3 mm and an inner diameter of 0.9 mm. They have already been heated and stretched in the middle into the shape of an hourglass, yet the inner channel converges to zero in about 8 mm length from both sides, accompanied by the outer diameter shrinking to ≈ 2 mm at this throat. Using a self-constructed microscope plus micro-positioning knife and turning the glass tube around its axis, its surface is cut perpendicularly at a position, at which the inner channel has converged to $\approx 5\,\mu$m in diameter. Thereafter, the pipette is broken at this predetermined point, resulting in an orifice with a diameter varying $\pm 20\,\mu$m, so that every 1 out of 10 to 20 nozzles produced this way exhibits a desirable value. The break plane is sharp, smooth and, in the best case, perpendicular to the axis of the inner channel. However, in most cases this surface (in parts) is slightly tilted or even curved (see fig.16).

The nozzle diameter is determined under a microscope with transmitting light. For this, the pipette is mounted with the channel parallel to the light, so that the orifice appears as a bright circular area, which is measured via calibrated scales inside the ocular. Suitable nozzle candidates are shortened to ≈ 25mm at the back end (not shown in fig.15) by a similar cut-and-break method, polished at that side to remove sharp edges and afterward cleaned with purified water.

nozzle name	method1	method2	method3	d_0 (µm)
X4-3	4.0	3.7	4.1	4.0 ± 0.3
XVII-06	-	5.1	5.5	5.3 ± 0.5
XVII-01	1.8	1.8	2.0	1.9 ± 0.1

Table 1: List of nozzles used for the experiments and their average diameter d_0 with standard derivative. The methods for determining the three single values are described in the list on p.47.

In the early stages of the new pipette concept, a hollow injection needle (canula) of 0.8 mm outer, 0.4 mm inner diameter and ≈ 30 mm length was glued with an epoxid resin from the back side into the inner channel of the nozzle to serve as an additional inner channel. This was mainly done to hinder Indium, which was used at that time to seal the connection with the nozzle holder, from reaching and clogging the nozzle orifice. At present, as the connection is tightened with a gold gasket, the canula is omitted. In the next step, the nozzle is glued at the cylindrical outer surface into a copper housing with the epoxid resin. After > 24 h hardening the nozzle is tested using water jets and, if successful, with hydrogen at cryogenic temperatures in the vacuum chamber.

If a nozzle is found to be capable of producing stable filaments of the desired gas sample(s), it can already be used for experiments, in which the interaction point with the probing beam is more than 1 mm away from the orifice, e.g. in droplet experiments. However, if the region very close to the nozzle exit shall be probed like in Raman measurements, the outer diameter of 2 mm of the very tip needs to be reduced to avoid overlaps with the probing (laser) beam. The present procedure is to mount the nozzle onto a self-made construction in a $\approx 45°$ angle with respect to a planar polishing disk with < 1 µm grain size. The nozzle is lowered carefully by a micrometer screw onto the rotating polishing disk, while the polishing progress is being observed from the side by a stereo microscope. This process is repeated several times with the nozzle being turned by $90°$ degrees around the channel axis, so that in the end the shape of the polished tip results in a square. It is essential to not have the orifice get in contact with the grinding plate as this is very likely to destroy its qualities. Hence, the reduction of the tip surface should be made iteratively and at times controlled from the front view by a microscope. Alternatively to the squared shape, the tip can also be polished into a circle or octagon by rotating the nozzle around its channel by smaller angles during the polishing phase. In any case, the final diameter of the tip should be $0.4 - 0.5$ mm.

All nozzles used in these experiments are listed in table 1. The final nozzle diameter is determined as a mean value of several methods:

1. Diameter of the circular area measured with a transmitting light microscope

2. Standard nozzle calibration with He gas flow at 10 bar into vacuum [21, eq.3.1]

3. Liquid flow through the nozzle measured by gas flow through flow controllers and using formula 3.4 on p.42
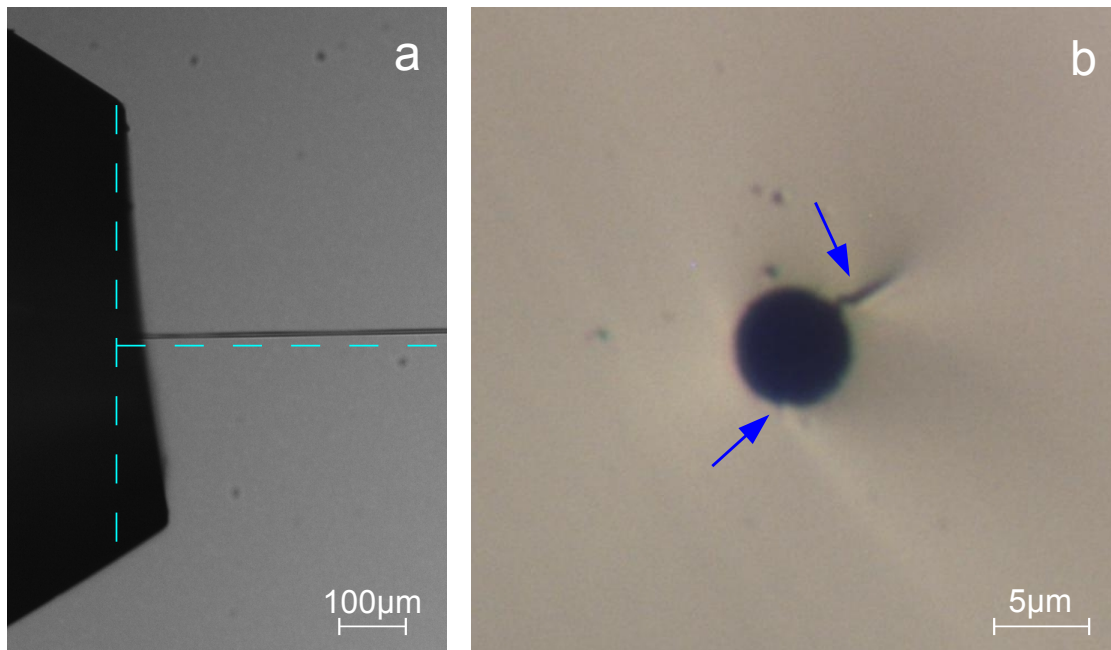
Figure 16: a) Shadow imaging picture of nozzle X4-3 made in Frankfurt. The nozzle surface clearly is tilted against the vertical axis, resulting in the beam pointing slightly upwards. Dashed teal lines are perpendicular guides to the eye. b) Front-illuminated microscope picture of the orifice of nozzle XVII-06. The blue arrows indicate cracks or bumps. A deviation from a perfectly plain surface can be suspected from the shadow spreading from the nozzle towards the lower right side.

This new nozzle design with glass pipettes has several benefits in comparison to the previous microscope aperture nozzles. The great advantage of glass as the material last in contact with the liquid before expansion is the smooth surface on sub-μm scales, which significantly reduces the probability of turbulences. Furthermore, the continuously slowly converging shape of the channel guiding the fluid does not possess any sharp transitions or edges. These two points make glass pipettes ideal candidates for laminar flow and enabled the first perfectly stable liquid filaments for our group. As the pipettes are glued at the sides (and not fixed with a cap from the front) and the tip is polished down to a small surface, it is possible to probe the filament with the laser focus being just $30\,\mu m$ away from the nozzle exit. Therefore item one and two from the requirements list on p.45 are fulfilled.

Other types of glass pipette concepts have also been tested, yet none of them has been able so far to serve as an alternative. An advantage of this current design is that the initial channel diameter d_i is big in comparison to the nozzle orifice ($d_i/d_0 \approx 200$), hence the velocity v_i of the liquid inside is low ($v_i = v_0/40000$). As the channel is also not too long ($l/d_i \approx 30$), a pressure drop due to frictional forces of the channel walls is limited and has been measured by induced periodic droplet beams [18] to be only 5%. On the other hand, other tested glass pipettes had channels of several mm length and a constant diameter equal to the nozzle orifice ($5\,\mu m$) so that $l/d_i > 10^3$, which resulted in high pressure losses.

Due to our cut-and-break procedure, the nozzle orifice usually possesses very sharp glass edges, which empirically has been found to have a positive effect on liquid filament stability. Its relatively thick glass walls of $1\,mm$ are another benefit of this particular pipette geometry, sincte this make it robust against light mechanical hits during mounting and transportation.

Though, the current nozzle design of course has some drawbacks. The main one can be summarized as the lack of controllability over the nozzle parameters. The fabrication yields only $5-10\%$ usable nozzles, of which the diameter also differs from one another. Worse, the mentioned variability in tilting and/or curvature of the break plain influence the orifice and consequently the liquid filaments considerably. At least, these characteristics are assessable, yet the orifice can also be altered by sub-μm effects, like nano cracks (compare fig.16) or the shape and sharpness of the glass edge, which are technically not measurable and make nozzle behaviors kind of arbitrary. A minor remark from this is that the direction of the filament typically cannot be aligned to a defined axis and has to be accounted for by proper displacement mechanisms. In summary, each nozzle can be considered unique in its size and ability to produce stable liquid filaments and must be characterized individually, which makes the overall process of nozzle preparation quite time consuming.

3.3.2 Positioning and Thermal contact

To recap, item one and two on the requirements list (p.45), stable filaments measurable close to the nozzle exit, are achieved with the new glass pipette design. The third entry demands a high accuracy positioning system while at the same time maintaining good thermal conductivity.

Of course, all experiments with liquefied gas filaments have to be performed in a vacuum chamber to be able to reach low temperatures and, in this work, to make use of the evaporative cooling effect. In Madrid, the chamber is evacuated by a $2000\,l/s$ turbomolecular pump, backed by a $400\,m^3/h$ Roots blower and a $70\,m^3/h$ rotary pump. In order to cool the nozzle to the source temperature T_0, it has to be thermally connected to a cryostat, in this case a continuous helium flow cryostat, consisting at the vacuum side of a $415\,mm$ long and $20\,mm$ thick cylindrical rod with a M6 female thread at its copper tip. In most experiments of our group in Frankfurt the nozzle, which is connected into a copper adapter, is screwed directly into that female thread of the cryostat. The positioning of the nozzle is then provided by a manipulator outside the vacuum, onto which the complete cryostat is mounted via a CF63 flange. However, the accuracy of this external manipulator is limited to $\approx 10\,\mu m$ and the long, freely suspended rod of the cryostat leaves it prone to vibrations and mechanical hits, which make the repeatability of absolute positions unreliable.

To achieve an accurate positioning of $<1\,\mu m$ with high repeatability, the positioning system of the collaborating group in Madrid was adopted. For gas and cluster expansion, they already have successfully used a 3D transversal manipulator situated inside the vacuum chamber, consisting of 3 perpendicular linear stages each driven by a motorized actuator. The motors have a driving range of $25\,mm$ with a minimum step size of $0.1\,\mu m$ and are individually accessed by a single control unit, which offers
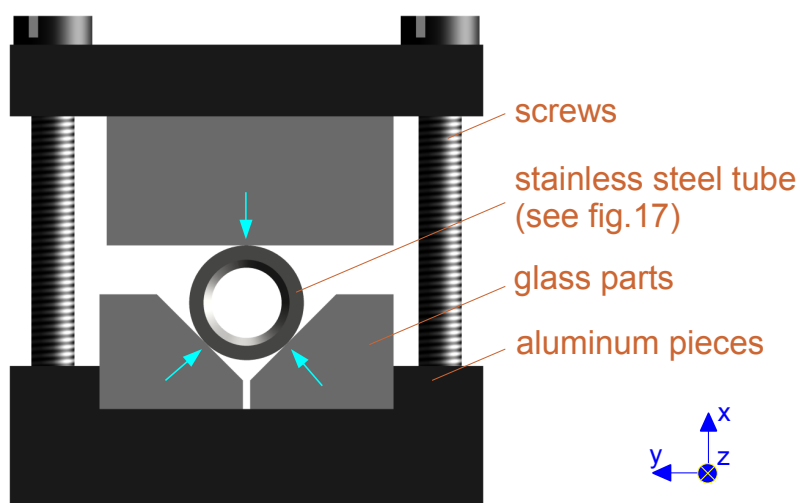
Figure 17: CAD front view of the glass pieces holding the stainless steel rod. The teal arrows indicate the three touching lines (in z-direction) for minimal thermal contact. The aluminum pieces are carefully tightened by four screws and are part of the manipulator stage.

absolute position readings relative to an assignable zero. In previous experiments, the (low temperature) nozzle has been connected to this manipulator with a self-invented system consisting of three glass pieces holding a 60 mm long hollow stainless steel tube with 8 mm outer, 6 mm inner diameter and a M6 female thread as the connector to the nozzle system (fig.17). The three narrow contact lines between the flat glass and the round stainless steel exactly define the alignment axis, and, in combination with the low thermal conductivity of these materials, keep thermal losses at a minimum at the same time. The shorter distance between hold point and nozzle tip additionally reduces the possibility of mechanical vibrations. Hence, the same type of connection was chosen to adapt our new glass pipette nozzle system to the preexisting manipulator and the relevant measures have been taken into account in the new nozzle system design.

This much more accurate movement demands that the nozzle has to be decoupled from the direct connection to the cryostat and a different method of thermal contact has to be found. In this regard, for previous experiments the Madrid group has used a copper strand connecting the nozzle to the non-moving cryostat, offering flexibility as well as sufficient thermal conductivity. A similar approach for the glass pipette design was therefore suggested and included into the design of the nozzle adapter.
The main differences compared to the system of the Madrid group are that the cryostat is a different model (continuous flow vs. closed cycle) with other dimensions and connections and the proposed flange for it to mount is from the side rather than from the top. The closed cycle cryostat of the Madrid group could not be used because it does not provide sufficient cooling power for our purposes. Regarding geometry and dimensions, possible candidates for the copper strand connection were tried out using CAD software. The final design of the nozzle adapter is displayed in fig.18 and its location inside the vacuum chamber in fig.21. Not shown for clarity are several layers of silver foil wrapped around nozzle system, copper strand and cryostat tip to reduce
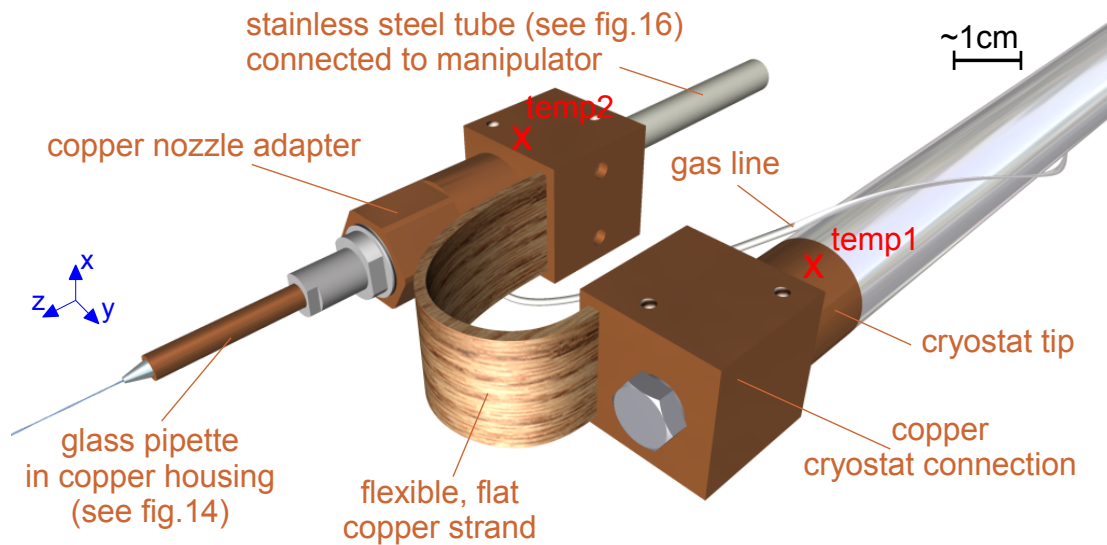
Figure 18: CAD rendered image of the nozzle system used for the experiments. The red crosses mark the position of the two temperature sensors temp1 and temp2. Not shown is the second copper strand on top of the first one, which was used since the second measurement campaign. For the experiment, all parts are wrapped into several layers of silver foil to reduce radiative heating.

losses through radiative heating. In order to have a backup system, the nozzle adapter piece has been manufactured twice.

Two silicon diodes determine the current temperature at the tip of the cryostat (temp1) and at the cryostat adapter (temp2). The latter can be considered roughly (+1 K) as the temperature of the liquid prior to expansion, as pretests in Frankfurt with an additional sensor at the very tip of the copper nozzle housing have proven. The nozzle system as shown in fig.18 without any connection to a manipulator (freely hanging) has been pretested by employing hydrogen filaments in Frankfurt to check for the thermal conductivity of the strand, demonstrating that temp1 and temp2 are equal under these controlled conditions. However, during the experimental phases in Madrid, a temperature gradient of up to 10 K appeared between the two sensors. Reasons for this are temperature losses over the stainless steel-glass connection (fig.17) from nozzle adapter to manipulator in combination with a limited thermal conductivity of the copper strand. Hence, further improvements to this design have been made in the second measurement campaign by adding a second copper strand on top of the first one, doubling the cross section of this critical part, while still maintaining sufficient flexibility. Additionally, in between all copper-copper connections (nozzle holder to nozzle adapter to copper strap to cryostat) a layer of ≈ 0.5 mm Indium foil was added, increasing the thermal contact [67], so that the temperature difference between temp1 and temp2 subsequently was < 5 K.

With this new design, where the nozzle system is decoupled from the cryostat via two flexible copper strands, a positioning of the nozzle of better than 1 µm is provided, while maintaining sufficient thermal contact to enable liquid hydrogen filaments. Item 3 of the requirements list therefore is fulfilled.
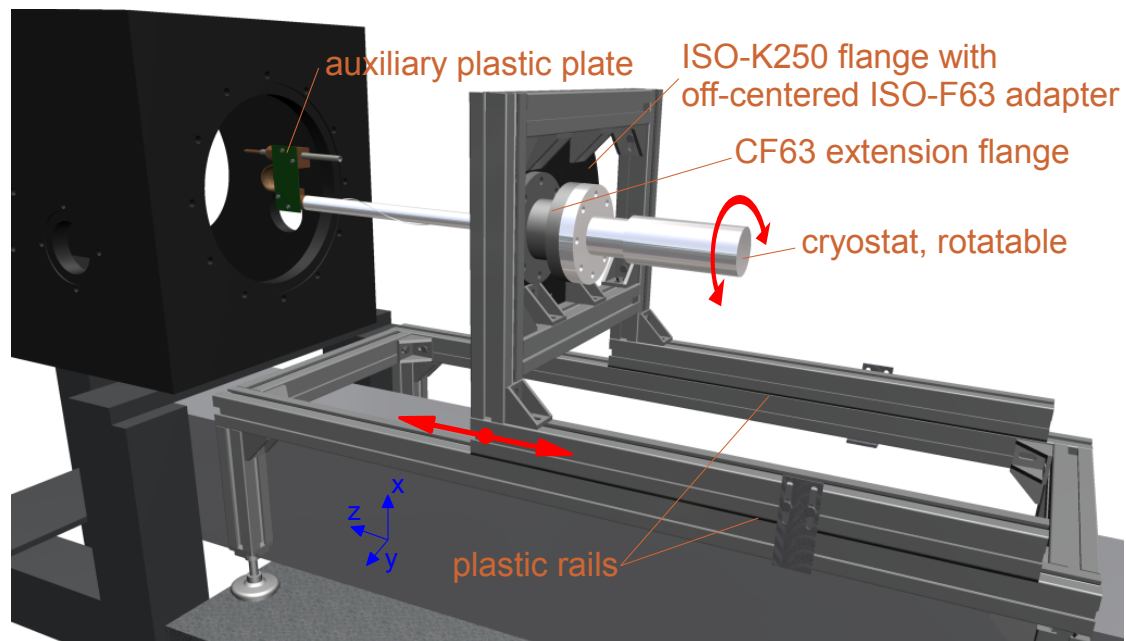
Figure 19: CAD view of the auxiliary mounting device made out of Flexlink. The red arrows indicate the degrees of freedom, i.e. a rotatable as well as linearly moving cryostat allowing for an easier mounting procedure of the nozzle inside the vacuum chamber. Not shown are several sheets of silver foil around the copper nozzle parts beneath the green auxiliary plastic plate.

3.3.3 Manual: Nozzle mounting procedure

Because room for handling through the front ISO-K250 flange opening of the vacuum chamber is limited and several delicate parts like the focusing lens, the objective and the glass pipette nozzle should not be touched or displaced, the mounting of the complete nozzle setup, as displayed in fig.18, was done outside the vacuum chamber. For this purpose an auxiliary mounting device out of Flexlink is aligned to the side flange of the vacuum chamber (illustrated in fig.19). The frame is used as an attachment for a non-standard ISO-K250 flange, with an off-centered female ISO-F63 flange. Onto the latter, the continuous flow cryostat is mounted with a CF63 extension piece in between, yet its screws are not tightened to keep it still rotatable (red circular arrows). Next, the complete nozzle system, comprising of copper strand, nozzle adapter and glass pipette nozzle, is tightened onto the tip of the cryostat, which is easier with the flange rotated, so that the copper strand is hanging downwards. To shield the nozzle from radiative heat during the experiments, all copper parts and the cryostat rod are wrapped into several layers of silver foil (not shown). To keep the copper strand and nozzle in place, an auxiliary, slightly flexible (green) plastic plate is mounted onto M3 female threads located at the cubical copper pieces by piercing small holes through the silver foil, which does not noticeably influence its shielding capacity. The cryostat can now be turned with the copper strand facing upwards as shown in fig.19 without the risk of applying torsion.

The auxiliary mounting device is built out of two independent Flexlink frames, which fit into each other via plastic rails and enable a linear movement (red straight arrows) of the cryostat towards the side opening of the vacuum chamber, onto which the ISO-K250 cryostat flange is screwed next. The cryostat is slowly rotated clockwise by 90°, until the stainless steel rod of the nozzle construction fits into the two bottom glass parts of the manipulator inside the vacuum chamber. The top glass part is put upon it and carefully tightened by four screws just enough to keep the nozzle in place (see fig.17). Now, the auxiliary plastic plate is removed and the nozzle is aligned into its final position, which is the pipette tip being roughly centered with respect to the laser focusing lens and objective. Lastly, the top glass part is screwed hand-tight, all remaining (rotatable) connections at the flanges are tightened and the auxiliary mounting device is disconnected from the ISO-K250 flange. All other flanges can now be closed and the chamber evacuated.

3.3.4 Manual: Cooling procedure and optimization

Before starting the cooling process, the chamber should already be evacuated for several hours to get rid of water vapor, which easily condenses and freezes onto the cold parts and can only be removed again by heating. The procedure for cooling basically is the same as in Frankfurt, yet the novel nozzle construction with the copper strand slightly changes the behaviour of the system. Hence, the descriptions and values given in this section are to be seen as guidelines for a proper use and low helium consumption, since liquid helium is expensive in Madrid ($\approx 10\,euro/l$).

The ARS continuous flow cryostat used in this experiment is special as it has an exceptionally long transfer line of 4 meters, entailing a long initial cooling time. Ironically, the one end of the transfer line, that is put into the Helium dewar is designed too short to reach its bottom. Hence, a $\approx 25\,cm$ long Teflon tube, which by chance fits perfectly, is used as an elongation to harness the full content of the dewar.

Prior to the start of cooling this transfer line is connected to a helium gas bottle and flushed with $\approx 0.5\,bar$ overpressure for 10 minutes to get rid of possible water contaminations inside of it, which may freeze and lower the He flow later on. Afterward, the (warm) transfer line is put into the liquid helium dewar, whose pressure should rise to $P_{liHe} \approx 0.5\,bar$, and checked for gas flow through the two He exits at its side and its other tip. The front end is plugged into the cryostat and screwed down to $\approx 18\,mm$ distance to the cryostat, which only slightly closes the needle valve at the tip of the transfer line. Both He exits are connected to (floating body) gas flow meters as indicators for the current consumption, which in the beginning are both completely opened and bounce between values $0 - 2$. To avoid possible deposition of water or oil vapor onto the nozzle tip, there should always be a small flow with $P_0 < 1\,bar$ through the nozzle.

The temperature of the nozzle is monitored by the two Si diodes described in section 3.3.2, which, in addition to the heater at the tip of the cryostat, are connected to a LakeShore temperature controller. The initial pressure $P_{liHe} = 0.4 - 0.5\,bar$ is maintained via a He gas bottle connected to the dewar with a pressure regulator. During the first $1.5 - 2\,h$, both sensors rise by $1 - 2\,K$, until the temperature starts to decrease slowly at first ($0.01\,K/s$), accelerating up to $0.5\,K/s$ at temp1 $\approx 150\,K$. Due to the worse thermal

conductivity of copper at room temperature (factor of 50 less with respect to 20 K [68]) and the small cross section of the copper strand, the temperature difference between temp1 and temp2 can rise up to 90 K, when temp1 is at ≈ 100 K. However, as temp1 approaches the 40 K mark, temp2 catches up increasingly and P_{liHe} can subsequently be slowly reduced to its final working pressure of ≈ 0.25 bar. Additionally, the gas flow meter connected to the side exit of the He transfer line can be reduced slightly.

At first, the temperature should be controlled with temp1 (= 20 K for pure p-H_2) to have a faster response to the temperature drop and oscillations. Suitable values to start with are P/I/D = 10/100/100 at heater mode *High* (max. 50 W), but may be adopted to the current conditions via the autotune option of the LakeShore controller. Care should be taken to not exceed the heating power to 100% as this may break the thin heater cables. For reference, hydrogen flow through the nozzle < 1 bar should have conditions close to temp1 = 20 K, temp2 = $22 - 24$ K, $P_{liHe} = 0.2 - 0.27$ bar, both flow meters at $15 - 22$ and heater *High* at $20 - 70\%$. When the temperatures have roughly stabilized, the controlling can be switched to sensor temp2, as at these temperatures the thermal conductivity of the copper stand is sufficient to have an immediate response to changes in temp1. When temp2 is stable within ± 1 K, the filling procedure described in sec.3.2.1 is used to establish liquid filaments. Due to the cooling/liquefying of the gas, the heater power drops and the temperature oscillations of temp2 usually decrease.

At stable filament conditions, the liquid helium consumption should be reduced to a minimum. The recommended way is to decrease P_{liHe} by setting the pressure regulator of the He gas bottle to lower values and carefully release pressure through a valve at the dewar. Another way is to slowly reduce the flow meter that is connected to the side exit of the transfer line, however this may induce temperature oscillations. Optimally, for hydrogen filaments the measurement conditions should be heater mode *High* $< 10\%$, $P_{liHe} < 0.25$ bar and a sum of both flow meters of $40 - 45$ at temp1 ≈ 12.5 K, temp2 = 16 K and $p_0 \approx 10$ bar. Usually, the heater increases slightly over time due to natural increase of P_{liHe} by evaporation and/or thermal equilibration of the cold parts. This can be compensated by releasing P_{liHe} carefully by a valve from time to time. On the other hand, if the cooling power decreases, indicated by sinking heater power, P_{liHe} can be raised via the pressure regulator of the connected He bottle, yet the response time may be several minutes.

At the end of the experiment, both flow meters are closed, the security valve of the liquid Helium dewar is completely opened and the transfer line is pulled up, but not completely out of the dewar. Hence, on the next experiment day, P_{liHe} can be build up in the dewar by lowering the transfer line into the liquid helium and by applying pressure using the pressure regulator of the He bottle.

3.3.5 Manual: Zero position of the nozzle

To determine the distance z that the filament has traveled, the zero position $z_0 = 0$ μm of the nozzle, i.e. the orifice overlapping with the laser focus, has to be found. Once aligned (previous to experiments, see section 3.4), the light path is never altered and only the nozzle is displaced via the linear manipulator it is mounted upon. As the nozzle system contracts due to changes in temperature, the zero position of the nozzle can only be defined at low temperatures, best, when the filament is already established.

For preparation, the nozzle is displaced in positive z direction, so that it is at least $300\,\mu m$ out of the focus, when the laser is let into the chamber[2]. To assure this, the position of its projected image onto a piece of paper situated at the entrance slit of the Raman spectrometer is checked by illuminating the nozzle from outside the chamber with white light directed into negative y direction. Additionally, with this method the nozzle is roughly centered in height (x direction). With the unblocked laser in the chamber, the nozzle system now is displaced in depth (y direction), until the laser and the filament overlap. This point is easily noticed, as the inside of the chamber glows in bright green light through the windows (too much for the naked eye), which originates from the huge amounts of stray light produced by the filament. The nozzle now is roughly aligned.

To define the actual zero position, the laser is blocked and the white light from the side is used again. With the nozzle still out of the laser focus position, the intensity of this light reaching the CCD of the Raman spectrometer through a $100\,\mu m$ entrance slit is registered by the PC software *Registra*. Next, the nozzle is moved in negative z direction, until it completely blocks the white light path to the spectrometer – due to the curvature and grinding of the pipette tip, it is almost opaque. The (background) count rate on the CCD again is noted and the mean value of both measurements is calculated. The nozzle is now moved in positive z direction with μm steps, until the current intensity detected by the PC equals this averaged value. The glass pipette tip is now at a position, where it blocks exactly half the white light on its way to the spectrometer, i.e. it is centered on the z axis with respect to the objective and the laser focus. The position is set as the zero position z_0 in the motor control for the following measurement series.

On subsequent days or when the expansion conditions P_0 and T_0 are changed significantly, the zero position should be redetermined, because backlash of the manipulator, thermal equilibration, pressure induced dilatation, etc. might alter it. However, in several checks of the z_0 position during the measurement campaigns, its position deviated by merely a few μm, which is not significant and highlights the great position stability of the whole system over several days with multiple cooling and warming cycles.

It might be the case that protruding edges or a tilted surface of the glass pipette make the position of the zero have an offset with respect to the real orifice. This offset also depends on the orientation of the nozzle around its channel axis, i.e. it may change if it is remounted onto the nozzle holder. To check for a possible difference, shadow imaging pictures are recorded at $z = 0$ as well as $100\,\mu m$ without and with the Raman laser at a reduced power of $100\,mW$ power. With the minimum zoom of the long-distance objective of the shadow imaging camera (see sec.3.5), the displacement of the nozzle is translated into a conversion $100\,\mu m \Leftrightarrow 6.295\,mm$ length scale of the picture (at zoom 100%). From a picture at $100\,\mu m$ with the laser hitting the filament (fig.20), one can determine both the position of the orifice (teal line) and the laser focus (red line) perpendicular to the filament axis (faint gray). If the $z = 0$ position deviates from the position of the real orifice, this will manifest in an offset of the distance teal-red with respect to the actual z position reading, at which the picture was taken. This is obviously not the case for the main nozzle XVII-06, yet the nozzle X4-3 used in the first measurement campaign yields an offset of $+30\,\mu m$, which has to be added to the z position readings.

---

2   If not in use, the laser is always blocked by an obstacle for safety reasons.

nozzle: XVII-06
sample gas: pH2
p_0 = 4 bar
T_0 = 16 K
P_{Laser} = 0.1 W
z = 100 µm

picture scale conversion:
6.295mm ↔ 100µm

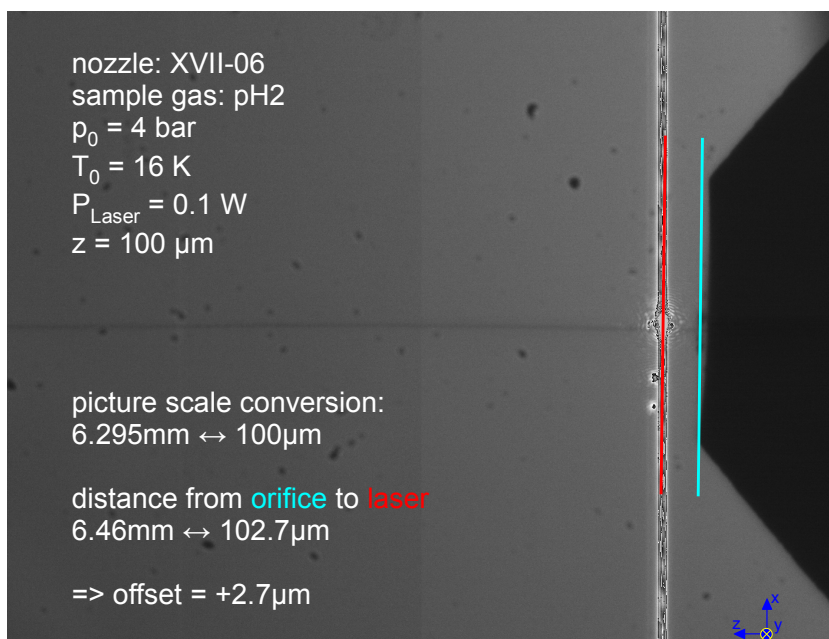distance from orifice to laser
6.46mm ↔ 102.7µm

=> offset = +2.7µm

Figure 20: Shadow imaging picture of nozzle XVII-06 at $z = 100\,\mu m$ to determine the offset of the zero position with respect to the pipette orifice. Teal and red lines mark the position of the orifice and laser focus, respectively, both perpendicular to the filament seen as a faint gray horizontal line in the center. The offset of $+2.7\mu m$ is within error bars and therefore neglectable.

3.4 Optical elements and light path

This section presents the equipment for Raman scattering, which was successfully used in previous experiments of the Madrid group [19, 69, 70], with subsection 3.4.1 dedicated to the functionality of the Raman spectrometer. Manuals 3.4.2 and 3.4.3 describe, how Raman spectra are taken for this experiment and how they are preprocessed for further analysis.

Following the light path in fig.14 on p.41, we start at the Raman laser, which is a continuous wave Ar^+ laser, with a wavelength of $514.5\,nm$ (green) and a maximum output power of $\approx 10\,W$. The laser features an internal mode-locking system, which stabilizes the wavenumber generated to $19429.769\,cm^{-1}$ in vacuum (no refractive index), which serves as the reference value for the Raman shifts later on. The light (green) exits the laser with a linear polarization in y-direction and propagates beneath the vacuum chamber to its center, where the light is reflected perpendicularly upwards by a 45° mirror (see fig.21). In case of recording rotational spectra, a $\lambda/2$-plate changes the linear polarization into z-direction to reduce the subsequent stray light of the filament in direction of the spectrometer by more than one order of magnitude. Inside the vacuum chamber the light is focused by a lens to a FWHM diameter of $14\,\mu m$ at the interaction point, which is greater than the filament diameter d_0, providing a homogeneous illumination.
The Raman scattered light (red) is collected at a 90° angle by a photographic objective, covering a solid angle of $0.23\,sr$, and exits the vacuum chamber parallelized. It passes
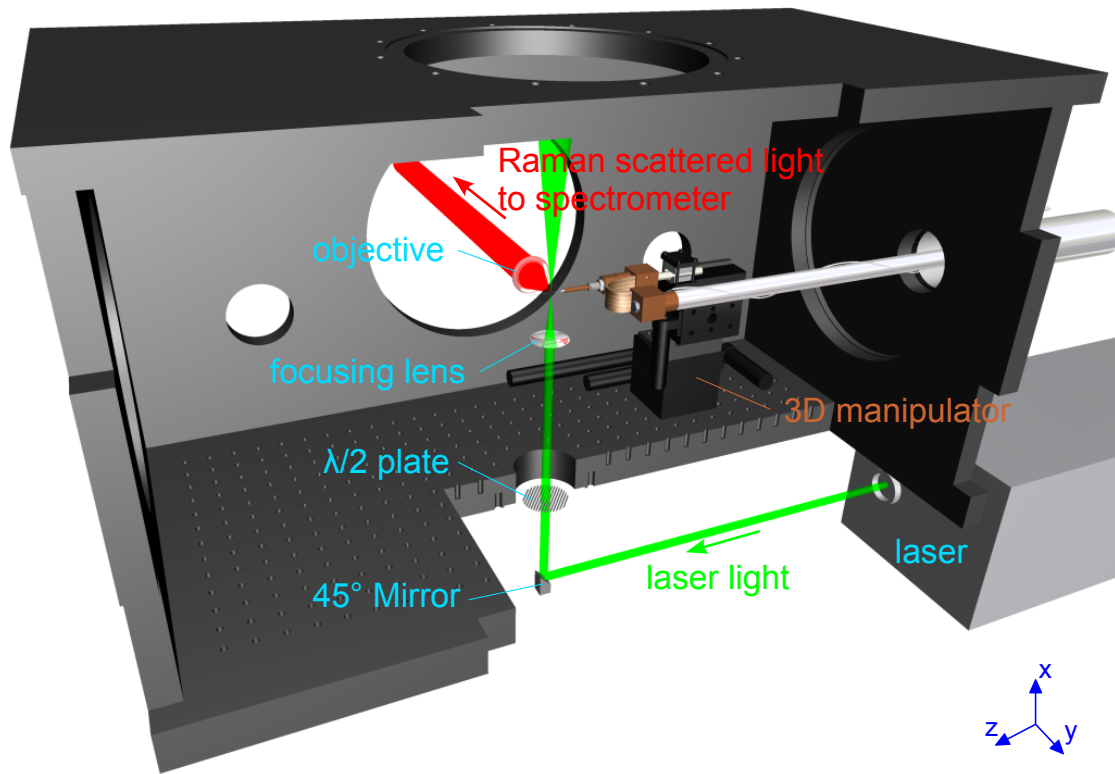
Figure 21: CAD view into the vacuum chamber, cut open to have an overview. Not shown are the positioning systems for the focusing lens and the objective.

through a Super-Notch filter, which is designed to reflect only the initial laser wavelength with a narrow bandwidth. The efficiency of the blocking is depending on the correct angle to the incoming light path, which is found by turning it while watching the amount of stray light from the filament seen on the Raman CCD. In addition to the reduction of green stray light by two orders of magnitude, its diameter of 15 mm skips a significant portion of the 40 mm parallel beam, which for us is beneficial as it reduces (spherical) aberration effects, hence yielding sharper images onto the Raman CCD.

Behind the Super-Notch filter, a doublet lens, accounting for chromatic aberration, focuses the light onto the entrance slit of the spectrometer. The width and height of the slit are changeable by micrometer screws. For these experiments the height was chosen to be at maximum of ≈ 20 mm to gain intensity and a width of 20 µm, which is close to the lower limit providing the highest spatial resolution. The objective plus lens combination magnify by a factor of 10, so that the projection from the chamber, i.e. the actual probed region, is a vertical slice of 2 mm height and, more important, just 2 µm width. This high spatial resolution in z direction is a key feature for this experiments. As the z axis can be translated into a time scale by $t = \frac{z}{v_0}$ with $v_0 \approx 100 - 200$ m/s, a temporal resolution of $10 - 20$ ns is obtained.

The laser focusing lens as well as the objective inside the chamber are mounted onto motorized stages, the doublet lens on a manual one. To be able to get this high spatial resolution, all optical elements have to be precisely aligned, which is also the reason why

it is preferred to rather displace the nozzle for the experiments. The main alignment is done apart from experiments. Yet, because the Super-Notch filter has to be adjusted during experimental time using the filament, small corrections to the light path have to be adopted by repositioning objective and doublet lens thereafter.

3.4.1 The Raman spectrometer

The original Raman spectrometer once was acquired as a commercial system, yet the majority of crucial components were exchanged and refined over the last decades [71] and even in between our measurement campaigns. Its interior is illustrated in fig.22. Behind the entrance slit (Slit1) of $20\,\mu m$ width, the Raman scattered light (red) is reflected by a mirror onto its core component, a holographic grating. Its line density of $2360\,grooves/mm$ determines the maximum spectral resolution, which is $\approx 0.11\,cm^{-1}$ at $4150cm^{-1}$ (p-H_2 vibrational) and $\approx 0.24\,cm^{-1}$ at $350\,cm^{-1}$ (p-H_2 rotational). The Raman scattered light actually consists of a variety of wavelengths. The rotational excitations of hydrogen produce green light, the vibrational ones are rather shifted towards red. Due to the grating, the mixed light is dispersed based on interference into unique directions associated with the wavelength. The spectral region to probe is selected by turning the grating around its vertical axis, until the first order refraction of that desired wavelength follows the path, illustrated in orange. That tilting is done with a micropositional translational stage capable of $0.1\,\mu m$ steps translated into an angular movement, the correspondence position $\leftrightarrow$ wavenumber being coped for by a fit function via software.

With Mirror3, the signal is directed to the lower horizontal level of the spectrometer, passing through Slit2 in between. Its purpose is to cut out the desired wavenumber interval and exclude all other light to reduce background. Hence, its width of $\approx 2mm$ is chosen to fit onto the CCD size and remains unchanged for all spectral regions. Two mirrors in the lower level of the spectrometer guide the light onto a spherical internal lens, which is movable in the direction of the light by a stepping motor. This is necessary to compensate the shifting of the focus based on chromatic aberration, when changing spectral regions far apart (e.g. vibrational to rotational). In the first measurement campaign, instead of the spherical lens, two cylindrical lenses were used for the focusing. Yet, as only one of them was movable, the image of the filament was blurred in one dimension (for vibrational regions), so they were replaced.

The CCD consists of a 512x512 pixel array with $19x19\,\mu m$ each and is refrigerated by liquid nitrogen to reduce the noise. The intensity of light collected by each pixel in a given time is read out by the self-written software *REGISTRA*, which is also capable of binning, i.e. summation of horizontal and vertical pixel rows (see section 3.4.2).

This setup projects a real image of the height of the entrance Slit1, which to recap is the image of the filament magnified 10x, onto the vertical axis of the CCD. In other words, the vertical position of pixels correspond to the x-axis of the filament with the relationship 1 pixel $\approx 0.9\,\mu m$.

The horizontal axis of the CCD, on the other hand, is not associated with a real projection of the z-axis, as the light is dispersed by the grating in this plain. Rather, it sees the spectral (=wavenumber) interval projected from Slit2, which, depending on the spectral region selected, covers $\approx 16cm^{-1}$ at $4150cm^{-1}$ and $\approx 24\,cm^{-1}$ at $350\,cm^{-1}$. Each
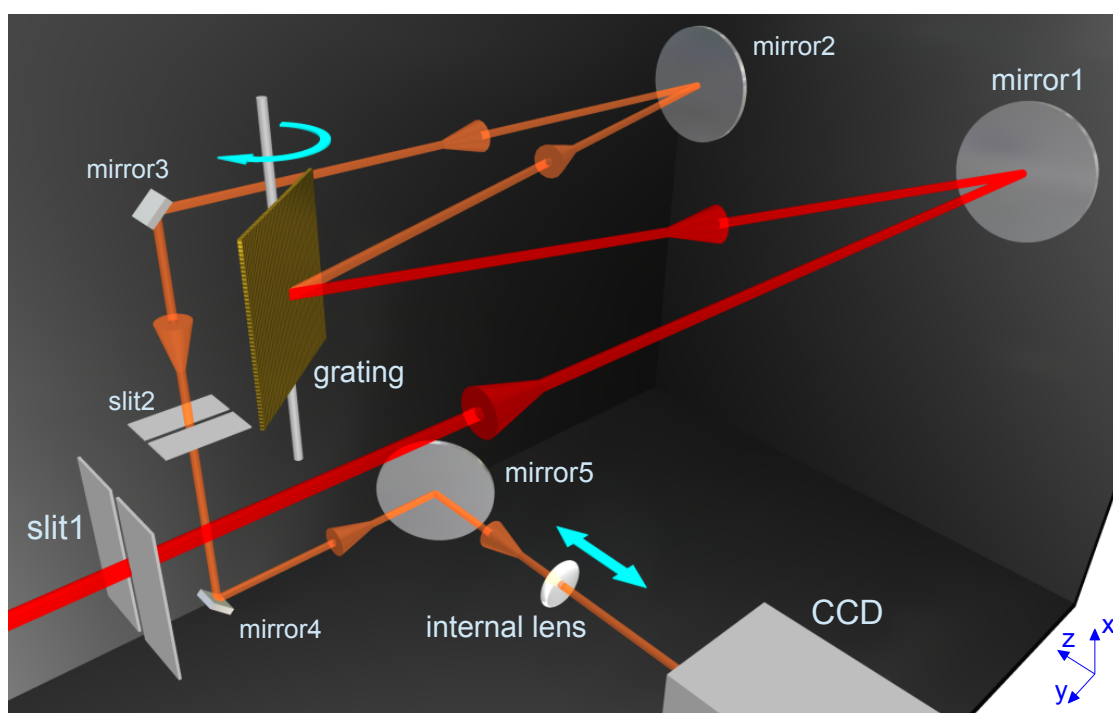
Figure 22: Schema of the interior of the spectrometer. The Raman scattered light (red) passes through the $20\,\mu m$ entrance slit (slit1) and is reflected onto the holographic grating, which disperses the light based on its wavelength. Selected by the angle of the grating, the desired wavenumber interval (orange) is cut out by slit2 and is focused onto the CCD.

horizontal pixel of the CCD therefore corresponds to a specific wavenumber, linearly increasing from pixel to pixel. This enables to record a spectrum of this wavenumber interval in a single readout, which is broad enough to cover all the bands of each particular excitation analyzed in this work. The software saves the spectra in text files with two columns, the first one is filled with the wavenumber interval spread on ≈ 300 rows (=pixels) and the second one with the intensity of each pixel channel in $counts/s$. An example plot of a spectrum is shown in fig.23 in section 3.4.3.

3.4.2 Manual: Taking Raman spectra

For each excitation of interest (vibrational and rotational region of each molecular species involved), a series of Raman spectra is recorded at increasing distances z from the nozzle orifice to reveal the time evolution of the filament by means of the correlation $t = z/v_0$. As stated before, only the nozzle is displaced, the laser focus and all optical equipment remain untouched throughout a series.

With the high spatial resolution of the Raman setup and a 20 μm wide entrance slit of the spectrometer, the volume of the filament probed is in shape of a horizontal cylinder[3] with a diameter of the actual filament $d_0 \approx 5\,\mu m$ and a height of 2 μm. The projection of this small region onto the Raman CCD is a horizontal stripe, the horizontal axis associated to an interval of the wavenumber as explained in section 3.4.1 and its small vertical extent corresponding to the actual diameter of the filament 10x magnified. The not illuminated horizontal bars of pixels above and below this do not contain any signal and only cause background noise.

Theoretically, a 5 μm filament should only illuminate a $\approx 5\,\text{Pixel}$ stripe due to the correspondence $1\,\text{Pixel} \Leftrightarrow 0.9\,\mu m$. But, mainly due to aberrations of different origin, this minimum value can technically not be achieved and the image is blurred onto adjacent pixels. Hence, a horizontal stripe of 20 Pixel centered around the maximum of intensity and covering $\approx 95\%$ of the total intensity, is chosen to be read out by the PC software. As each of these 20 single-pixel strips represents a different position in the height/x-axis of the filament, they can be used to analyze different parts (top, middle, bottom) of the filament. Therefore, not one but 10 Raman spectra of 2 Pixel width each are taken simultaneously by the PC software, which is discussed in the later chapter A.2. This 10-strip data can easily be converted into a single spectrum used for the main analysis by adding up their intensities. As mentioned previously, the horizontal axis of the CCD covers a wavenumber interval of $\approx 16 - 24\,cm^{-1}$, which is sufficient to collect all bands of one excitation of a substance in one take. This brings the advantage that the grating does not have to be turned in between spectra to record a broader wavenumber region, saving time and prohibiting backlash effects from moving.

We now focus on the procedure of correctly positioning the nozzle, which is also done via (live) Raman spectra. Because of a variety of uncertainties, like a tilted pipette surface discussed in chapter 3.3.1, it is not possible to align the filament axis perfectly with the z-axis defined by the movement of the motor. A typical tilting of the filament is $1 - 4\%$ in x as well as y direction, determined by the position readout of the motors after below procedure.

Therefore when the nozzle is moved into z direction to a new position, the x and y coordinates have to be adjusted to bring the filament inside the laser/objective focus again. The correct depth (y-position) is determined by looking for the highest total intensity of a live Raman spectrum (1 s update time), while moving the nozzle on this axis. For the height (x-position) of the filament, the PC software is set to display 5 live Raman spectra simultaneously in color code, each of them being a read out of a 20 Pixel horizontal strip on the CCD. The central strip is chosen to be the one, which shall be used for the data acquisition afterward (compare previous passage). Because this axis of the CCD corresponds to the actual height of the filament, $2 - 3$ adjacent stripes share the constant sum of intensity, yet the distribution shifts in between the stripes, when the nozzle is moved up or down inside the laser focus. The goal while displacing the nozzle in this x-direction is to accumulate most of the intensity (95%) into the central spectrum/stripe, so that its adjacent stripes then have a similarly small intensity. To increase the quality of the position adjustment, the x- and y-displacement procedures can be used iteratively.

---

3   To be precise, also the radial volume around this cylinder is recorded, yet as the particle density of the gas generated through evaporative cooling is orders of magnitude lower, there is almost no signal coming from these regions.

For acquiring measurement data $3-4$ Raman spectra are recorded consecutively at each z position of the nozzle after each above repositioning procedure. Starting in the vibrational region at $z = 0$ the nozzle is displaced in smaller steps of 50 or $100\,\mu m$ as in the beginning the bands change more rapidly due to the strong evaporative cooling, whereas later on, bigger steps can be taken. For the rotational bands, usually less positions of z are recorded, as less information can be extracted from the changes of the bands. With an initial laser power of $4\,W$, a Raman spectrum is recorded within $10-30\,s$, depending on the signal strength or number density of the excited molecular species, respectively. For taking $10-40$ displacement steps, the recording of a series takes $1-3\,h$, so that around 6 complete series can be acquired in a day of measurement. Each time the wavenumber region is changed to record a different excitation (rotation, vibration, different molecule), following adjustments to the Raman setup have to be made.

- The internal lens of the spectrometer has to be refocused due to chromatic aberration based on the change of the probed wavelength. To accommodate for this, at first the grating of the spectrometer is turned to the desired wavenumber position. White light is utilized to create a Gauss-shaped peak onto the live Raman spectrum, which corresponds to the focus on the CCD, and its FWHM is minimized by moving the internal lens.

- As the (movement of the) internal lens may not be perfectly aligned/centered, the center of this projection onto the CCD should be readjusted in the PC software.

- In case the excitation to probe is changed from vibrational to rotational the $\lambda/2$ waveplate should be rotated by $90°$ to reduce stray light or vice versa for the vibrational region to receive Raman signal at all.

- In the end, the width of the spectrometer entrance slit should be checked to be $20\,\mu m$ as it is set to greater values during the previous processes.

The time it takes to adopt these changes typically is used to check the stability of the filament by shadow imaging.

3.4.3 Manual: Calibrating and preprocessing Raman spectra

This section describes the procedures, which are done to the recorded Raman spectra after the measurements to prepare them for any further analysis. The steps are calibrating the wavenumber scale (x-axis) and normalizing the intensity (y-axis) for enabling comparisons between spectra. All preprocessing and analysis is done using the software *OriginPro 9G*.

Because we want to utilize the correlation between wavenumber and temperature (see chapter 2.3.2), we need to extract the absolute wavenumbers with a resolution better than the spectral resolution ($< 0.1\,cm^{-1}$). Two corrections to the wavenumber (x-axis) of the spectra have to be made in the following order:

1. Magnification: Multiply the wavenumber axis with a correction factor.

2. Calibration: Shift the whole spectrum to a band with known absolute position.

As it is easier to understand, the second item will be discussed first. The wavenumber scale of a spectrum is prone to shifts due to backlash of the motor moving the spectrometer grating, temperature effects etc.. For an absolute position of (unknown) Raman bands, a known excitation with a sharp wavelength independent on temperature or other variables usually is used for reference. For example, an iron-neon lamp provides well-known and undisturbed lines based on its electronic transitions.

However, in the first measurements with liquid filaments, apart from the expected lines for hydrogen, surprisingly additional lines showed up. These lines turned out not to be Raman bands, but to come from electron transitions of Ar, Ar^+ and Ar^{2+} atoms/ions present in the Ar-plasma of the Raman laser. These excitations have never been observed in gas or cluster jets before, yet due to the cylindrical surface of the liquid/solid filament, the plasma light is reflected in all directions and partially land on the CCD of the spectrometer. These plasma lines are quite beneficial for our purposes because they have a clearly defined wavelength, which can be looked up in databases. We tested their accuracy and possible dependencies, e.g. on the laser power, independently with an iron-neon lamp to verify their usability. Luckily, the number of plasma lines is high enough to have at least one intense plasma line in the vicinity ($10\,cm^{-1}$) of our Raman bands of interest. Even luckier, the plasma lines never happened to overlap in wavenumber with our Raman excitations, keeping the spectra clean of complicating features.

For the calibration of the wavelength, a (preferably intense) plasma line (see table 2) is fitted with a Gauss function. Its center is extracted, compared with the literature value (e.g. [72], mind refractive index of air!) and its offset is subtracted from the wavenumber axis, effectively shifting it to the correct value. Due to this fitting procedure and the intrinsic width of Raman bands, it is possible to extract the position of unknown lines with higher accuracy than the spectral resolution of the Raman setup.

The issue arising from the first item on the above list has been identified in the second measurement campaign. Due to the calibration to different plasma lines, it was discovered that the Raman bands and other plasma lines did not match, when the spectra were layed on top of each other. The mismatch increased linearly up to $0.1\,cm^{-1}$, the further the lines were apart from the calibration plasma lines. This indicated that the scaling of the wavenumber axis was incorrect. After intense consideration, the reason was identified to be the internal lens of the spectrometer. All initial calibration for the Raman spectrometer has been done near the wavelength of the Raman laser at $514.5\,nm$ in the green region. However, as the (non-achromatic) internal lens of the spectrometer has to be moved to focus to accommodate for the redshift of Raman excitations (see section section 3.4.2), its focal length and connected with it, its magnification is changed slightly depending on the wavenumber region.

For finding the correct magnification of each wavenumber region of interest (rotational/vibrational p-H_2/o-D_2) iron-neon lamp lines and plasma lines were recorded and the distance between these lines compared to the literature. By dividing the literature value by the measured one, a correction factor for the magnification is obtained, which is listed in table 2. To compensate this effect, the wavenumber axis of each Raman spectrum has to be multiplied with the factor according to its region before the calibration with the plasma line described in the previous paragraph is done. As the exact wavenumber calibration is most important for the vibrational p-H_2 region, its corrected value is already implemented into the Raman software and all other region remain to be multiplied by factors instead.
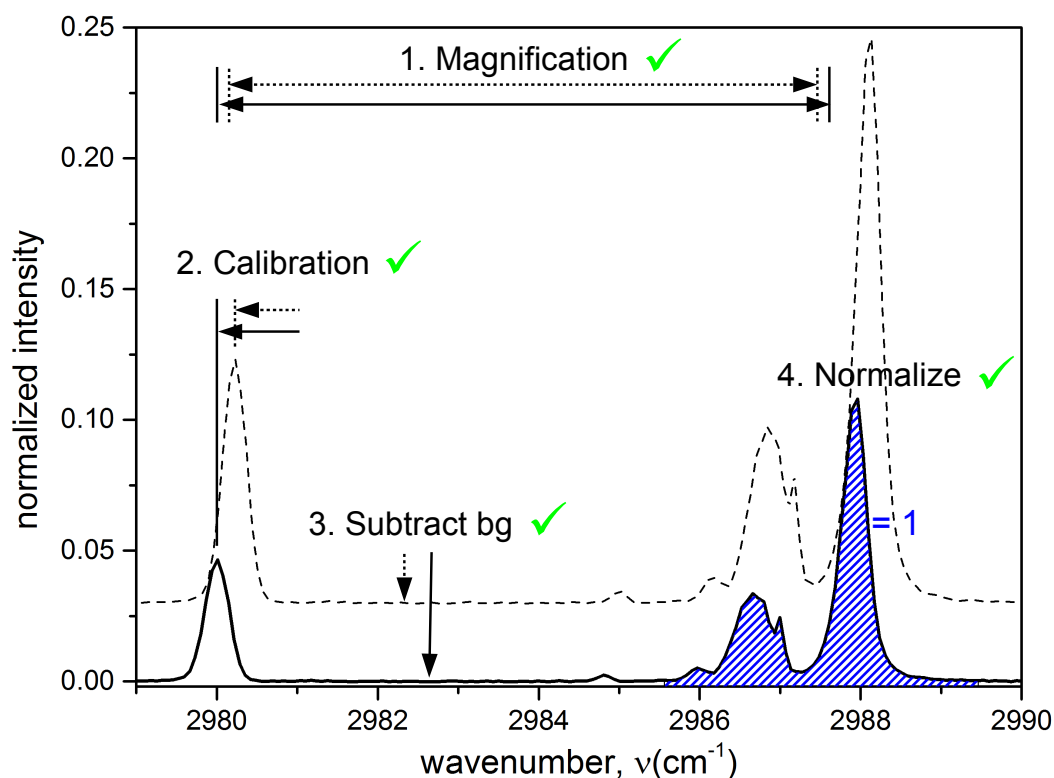
Figure 23: Illustration of the preprocessing steps of Raman spectra (inital: dashed, final: solid black line). 1. The wavenumber scale is stretched by the magnification factor. 2. The spectrum is calibrated to the known plasma line position. 3. The average of the background is subtracted. 4. The Raman signal is normalized to 1.

With the correct wavenumber x-scale after the previous two steps, the preparation of the intensity y-axis is the next step. Two procedures are applied:

3. Subtract background: Find an interval containing no signal, subtract the mean value of it from the spectrum.

4. Normalize: Set integral over Raman band to a constant value ($= 1$).

Both items are necessary to enable comparisons between similar spectra and fairly simple to explain. Depending on the distance z from the nozzle orifice, there may be different amounts of stray light, i.e. background on the spectrometer CCD. The intensity of the Raman signal can also vary drastically, if the filament is slightly moving. Also, in mixtures the Raman bands of the less abundant component are significantly lower in comparison to the pure substance. To get an equal signal and signal-to-background ratio, the two steps are done.

First, an interval for all Raman spectra in a series is identified, where there is no signal, i.e. neither a Raman band nor a plasma line. For each spectrum the average background is determined by calculating the mean of this interval and subsequently subtracted

region	magnification factor	plasma line (cm^{-1})
o-D_2 rotational	1.00696	185.632
p-H_2 rotational	1.00696	339.645
o-D_2 vibrational	1.00570	2980.002
p-H_2 vibrational	1	4138.901

Table 2: Raman excitations probed, the associated correction factors for the wavenumber scale and plasma line positions for calibration [72]. The magnification factors for o-D_2 and p-H_2 rotational are chosen identical, because the wavelengths of both excitations are close.

from the whole spectrum. Secondly, an interval covering the complete Raman signal (ortho/para liquid/solid) is determined, if possible excluding all other (plasma) lines. As the Raman PC software already delivers an integrated value for a single data point, the integral of this Raman interval is calculated simply by adding up all intensity values. Finally, the intensity of all data points is divided by this integral value, so that the sum over this interval containing the Raman signal now is equal to 1. All four procedures are illustrated in fig.23.

As a last remark, it is not entirely justifiable to normalize all spectra of one Raman series to the same constant 1. The reason is that the overall intensity declines, the further the spectrum is recorded from the nozzle exit, z, as the number of molecules decreases about 5% through evaporation. Yet, as the recorded intensity is fluctuating far greater up to a factor of 3 in between spectra, these small changes in the overall amount of molecules is not detectable. Furthermore, we are mainly interested in the relative rather than absolute intensities of the Raman bands.

3.5 Shadow imaging

Shadow imaging is the main method of our group in Frankfurt to optically analyze the expansion of liquid jets. It allows backlight-illuminated snapshots of µm-sized objects with ns exposure time. For this experiment the imaging setup was used in Frankfurt to pretest nozzles for their capability of producing stable liquid filaments of hydrogen. It was shipped to Madrid during the Raman beam campaigns to monitor the conditions of filaments probed.

The components are displayed in purple in fig.14 on p.41. The light for short-time exposure, i.e. the "photo flash" from the back, is produced by a computer controlled, pulsed infrared laser. A diffuser at its tip transforms the wavelength into the visible region and generates a homogeneously illuminated circular surface of 50 mm diameter. Usually, the recording CCD camera is pointed in a linear configuration towards this illuminated surface, but as due to the Raman equipment there is no free space for the laser, the latter is installed in a $\approx 30°$ angle and its light is reflected by a removable mirror onto the camera. The camera is equipped with a long-distance objective focused

onto the nozzle tip at $\approx 35\,mm$ distance. The computer synchronizes the laser with the camera, so that although the shortest readout of the CCD is in the order of µs, the ns-flash of the laser dictates the exposure and the shadow of the filament is seen as a silhouette against the bright background (compare fig.20).

The technique is able to live stream or record pictures of the filament with a rate of $3\,Hz$, with which changes of the filament in shape and position can easily be detected by eye at $\approx 5\,µm$ resolution. Therefore it is used to monitor the short-time stability of the filament within a few seconds, which is sufficient for taking Raman spectra with $10-30\,s$ recording time. The long-time stability can be checked by comparing pictures at different times of the day. However, with this configuration it is not possible to record shadow imaging pictures and Raman spectra simultaneously, because for the latter the mirror has to be removed. As the filaments were tested to be stable over short as well as long periods, this remark is of minor importance.

If the Raman laser is guided into the chamber and hits the filament, it is seen as a bright vertical stripe throughout the whole imaging picture, which comes from the crosstalk of saturated pixels, which is proven by tilting the camera to the side and the stripe still being perfectly vertical (see fig.20 on p.56). This effect occurs even at the lowest readout times and minimum laser power of $100\,mW$. Yet, it is useful for determining the offset of the zero position to the nozzle orifice (see section 3.3.5).

4 | PURE PARA-HYDROGEN

For the first measurements pure para-hydrogen was chosen, because we already had gathered experience in establishing filaments with it in Frankfurt and, additionally, its condensed phases as well as Raman excitations have been studied intensively in the literature. The main results of this chapter are now quite well understood and are published in a paper [73].

In the subsequent sections, almost all information is extracted from measurements of the main nozzle XVII-06 with diameter $d_0 = 5.3 \pm 0.5\,\mu m$, if not stated otherwise. However, series of pure p-H_2 were recorded in all three measurement campaigns and with different nozzles, which are listed in table 3. Therefore this chapter governs not only the information obtained about the behaviour of pure p-H_2, but also the characteristics of filaments which can be deduced from comparing data with different conditions.

To recap, a Raman series consists of spectra of one excitation (vibration or rotation), recorded at increasing distances z from the nozzle. With the correlation $t = \frac{z}{v_0}$, the dynamics are directly accessed with a temporal resolution of $10 - 20\,ns$. The velocities v_0 displayed in table 3 are mean values. Because the pressure P_0 in some measurements was not stable[1], the actual v_0 for each distance z was calculated individually with the current P_0 reading of the pressure gauge. All spectra shown are preprocessed according to the procedure explained in section 3.4.3 before the actual analysis.

4.1 Vibrational region

In fig.24 a series of cut Raman spectra of the vibrational region taken from data #4 (see table 3) is displayed. The full spectra extend further to lower wavenumbers, where a plasma line for calibration is situated, yet the skipped parts carry no Raman signal. The series shown consists of 19 spectra, consecutively shifted upwards by a constant value and distinguished by a color code from red to blue. The spectra are recorded at linearly increasing distances z from the nozzle orifice (except for $z = 5000\,\mu m$) marked at the right hand side. Each shown spectrum is averaged from $3 - 4$ subsequently recorded single spectra, the error bars are within the line width.

The right panel contains the excitation $Q_1(0)$, the first vibrational excitation of p-H_2, whereas the left panel is magnified by a factor of 100 too show the $Q_1(1)$ first vibrational excitation of the less abundant o-H_2. Note that the wavenumber axis is not interrupted. In each panel we can identify two bands, which, compared with the literature [35], correspond to signal from molecules in the liquid or in the solid phase, respectively.

---

1 The gas compressor described in section 3.2 did not work properly and caused variations of up to $\pm 2\,bar$

#	nozzle	d_0 (µm)	date	temp2 (K)	P_0 (bar)	v_0 (m/s)	% o-H_2
1	XVII-06	5.3	17/11/11	16.0	6.7	126*	1.2
2			18/11/11	16.0	13.3	178*	0.9
3			24/11/11	16.0	8.4	141	0.9
4			25/11/11	16.0	8.5	142	0.3
5			16/10/12	16.2+	14.0	182	0.2
6			16/10/12	16.9+	4.0	98	0.2
7	X4-3	4.0	19/05/10	15.4	7.0	129	0.9
8			02/06/10	15.8	13.7	180	0.7
9	XVII-01	1.9	15/12/11	16.5	23.5	236x	0.6

Table 3: All measurements of pure p-H_2. temp2 is the reading of the free length sensor (see fig.18 on p.51). The mean velocity v_0 is calculated by formula 2.3 on p.8. The ortho-hydrogen content is an estimation from the vibrational band explained in chapter 4.1.5.2.
+: estimated value, *: probably frozen orifice, x: droplet beam

Focusing on the liquid of p-H_2, one can see that the band is broad and changes its shape significantly with increasing distances z, which is discussed in the following section 4.1.1. At 700 µm, the solid band starts to appear and intensity is continuously reallocated from the liquid into the solid band, the further the filament has traveled, until the liquid has vanished completely. This process of solidification is topic of section 4.1.3. The solid peak is within spectrometer resolution, yet a small shift towards lower wavenumbers can be seen, discussed in section 4.1.5.1. o-H_2 in the left panel exhibits a very similar behaviour in all these aspects (section 4.1.5.2). As all data listed in table 3 show a very similar qualitative sequence of spectra, the measured vibrational spectra are only presented once as this example plot.

4.1.1 Temperature of the liquid

As described in section 2.1, the liquid filament cools through evaporation as soon as it exits the nozzle. For para-hydrogen, the temperature-wavenumber correlation has been measured at equilibrium conditions above the melting line for the liquid and below it for the solid [30]. It was also proposed to be valid for the supercooled liquid because of its explicit density dependence. Hence, we can use the Vilesov formula 2.10 on p.19 to extract temperatures from our data. To proceed as systematic as possible, the following analysis will be incremental, starting at the bare procedure and qualitative description, then adding piece by piece to interpret the puzzle. When the data set is discussed completely, comparisons to the other recorded data follows.
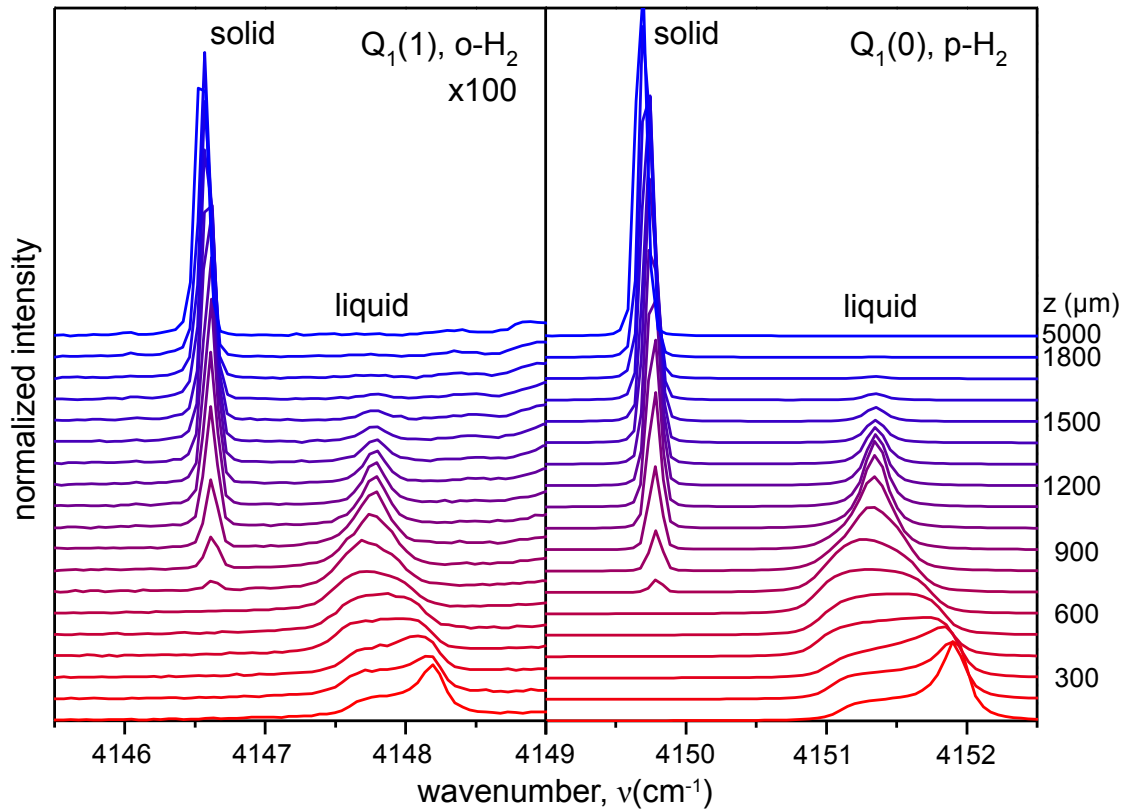
Figure 24: Series of Raman spectra in the vibrational region with conditions #4 in table 3. The vibrational excitation for p-H_2, $Q_1(0)$ is in the right panel, the left one is enhanced x100 to see the small band of o-H_2. Linearly increasing distances z from the nozzle orifice are displayed at the right side.

4.1.1.1 Temperature gradient

The straight forward way is to analyze the mean temperature of the liquid filament. Therefore in the interval $4150 - 4153 cm^{-1}$ where the liquid resides, the average wavenumber is calculated by the summation of wavenumber*intensity of each data point. Applying formula 2.10 yields the average temperature of the band, which is plotted as purple circles in fig.25 against the distance z. Error bars, coming from the deviations of the $3 - 4$ single spectra, are smaller than the symbols. One can see that the mean temperature decreases steadily, up to around $700\,\mu m$, where it slightly increases to a constant value, until the liquid band vanishes at $1700\,\mu m$. Notice that the drop of temperature stops at the same time as the solid peak in the spectra appears and starts to grow, which will be discussed later on.

The liquid band in fig.24 is much broader (FWHM $\approx 2 cm^{-1}$) than the spectral resolution of $0.11\,cm^{-1}$. To be precise, the Raman spectra are composed of the signal (continuous distribution of wavenumbers) in a convolution with the inherent peak shape function of the spectrometer. This function is close to a Gauss shape with the spectral resolution as the FWHM, yet its exact shape is unknown. Hence, a deconvolution of the liquid band was tried, but failed.
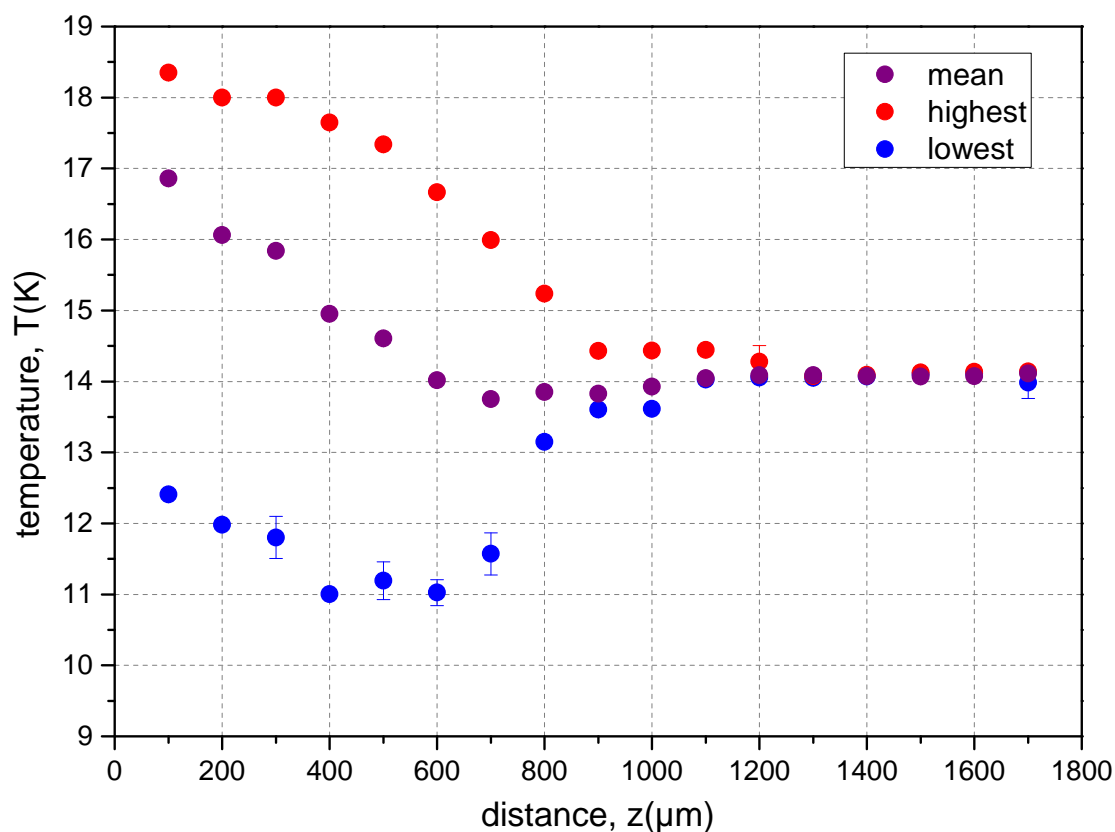
Figure 25: Temperatures of the liquid extracted from data #4 using formula 2.10 on p.19. Purple corresponds to the mean wavenumber of the band, whereas red and blue represent the highest and lowest signal, i.e. the inflection points accounting for the spectral resolution, respectively.

However, to get out more information than just the mean temperature of the filament, we can extract the lowest and highest temperature by determining the left and right flank of the liquid band, respectively. For a user-independent method, the steepest incline in the flanks, i.e. the inflection points, are chosen as this reference. The derivative of the interval of each liquid band is calculated and the waveunumber of its highest/lowest value extracted (see fig.26a). To account for the width of the intrinsic spectrometer convolution function, half of the spectral resolution value, $0.055\,\mathrm{cm}^{-1}$, is added/subtracted to/from the position of the left/right flank, respectively[2], which is indicated by the slight displacement of the dashed lines in fig.26a).

The final wavenumbers, translated into temperature with the Vilesov formula 2.10, are plotted in fig.25 as blue and red circles for the coldest and hottest spot, respectively. Again, the error bars correspond to the deviation of the $3-4$ single spectra recorded at each z position. Considering the warmest part in red, in the beginning it is almost constant and starts to decrease at $400\,\mathrm{\mu m}$ until it approaches the mean temperature asymptotically. The blue dots, corresponding to the coldest parts, already start at low

---

2   To justify this step, imagine a sharp transitions yielding just a single wavenumber. Yet, in the Raman spectrum it appears as an approximately Gauss shaped function with a FWHM of $0.11\,\mathrm{cm}^{-1}$. The inflection points, i.e. the steepest flanks, are roughly half this value off the center and hence do not correspond to the actual signal.
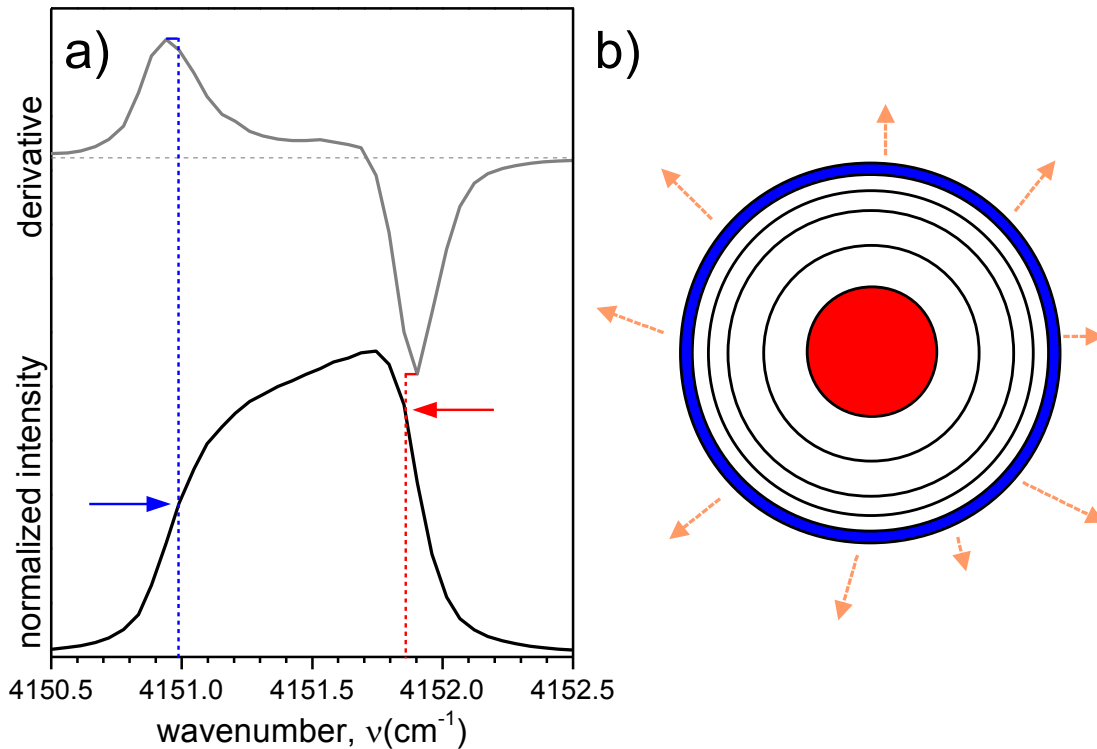
Figure 26: a) Raman spectrum (black line, bottom) recorded at $z = 300\,\mu m$ and its first derivative (gray line, top). The blue and red arrows indicate the lowest and highest temperature, respectively, accounting for the spectral resolution. b) Schematic cross section of the filament divided into concentric layers. Due to evaporation (orange arrows), the outer layer (blue) experiences the coldest temperatures, that gradually advance to the interior via heat conductivity.

temperature values, that further decrease until abruptly going up at $700\,\mu m$ to approach the mean value. The fact that all three curves end in the same value demonstrates nicely that accounting for half the spectrometer resolution when evaluating the inflection points is justified, as the last rest of the remaining liquid (peak) can only have one temperature.

The interpretation of this broad liquid band associated with a range of temperatures is a radial temperature gradient across the filament, which is schematically displayed in fig.26b. The cross section can be divided into several concentric layers with equal area/mass, so that their thickness decreases the further away from the center. Only the surface of the outermost layer is in contact with vacuum and experiences the cooling effect of the evaporating molecules, as described in chapter 2.1. This cooling is particularly efficient directly after the expansion, because of the high vapor pressure of the "warm" surface, so that the drop in temperature of the outer layer is faster than the transfer of heat to the interior takes place. Hence, a temperature gradient across the filament arises almost as soon as its surface is exposed to vacuum, which is evidenced by the first data points in fig.25. Yet, the now colder outermost layer results in less effective evaporation, lowering the subsequent cooling and allowing the inner layers to catch up in terms of temperature.

The occurrence of the first solid at $600\,\mu m$ is accompanied by an increase in temperature, mainly of the coldest spot, i.e. the outermost layer. This signals that the solid starts to form at the surface of the filament, which is in agreement with nucleation theory, which states exponentially growing nucleation rates at lower temperatures (compare chapter 2.5.1). The affiliated increase in temperature can be explained by two effects:

1. The heat of solidification released during the formation of the solid.

2. The rearrangement of signal from the liquid to the solid band.

Item 1 is a physical process. Because of the lower chemical potential of the solid phase in comparison to the liquid at temperatures below the melting point, the difference in energy is released in form of heat. This heat affects the solid that just has formed, as well as the adjacent liquid, increasing its temperature as noticeable in the plot, particularly in the coldest liquid region, where the solid first forms. The second effect is of statistical nature. The cold molecules that have solidified now have their vibrational energy shifted to lower wavenumbers into the solid band and do no longer contribute to the signal of the liquid. Hence, the coldest parts drop out, leaving behind the warmer parts to constitute the liquid band. Both explanations play a role, as also will be demonstrated for the $2\,\mu m$ filament in subsection 4.1.1.5, yet it is not possible to assign quantitative weights.

4.1.1.2 Corrected temperature values

Since all features of the plot 25 are qualitatively explained, we next focus on including corrections and clarifying details. As a main remark, the temperature scale is disputable because

- the final temperature of all three curves ends in the same value, which is above the melting point $T_M = 13.8\,K$, so that the liquid would not be able to solidify.

- the starting temperature at $z = 0$, extrapolated from the intersection of the red and purple curve, is above the estimated real $T(z = 0) = \texttt{temp2} + 1\,K = 17\,K$ (compare chapter 3.3.2).

- all three curves are above the ones of the simulated temperature gradient (following later in this section).

All three items indicate that the original formula 2.10 for the correlation wavenumber $\leftrightarrow$ temperature yields values that are $\approx 1\,K$ too high. This formula is obtained from a fit to experimental data and error bars are given, however it is not stated if these are of experimental and/or fitting origin. If these error bars are taken into account, the correlation almost loses its utility for us, because they translate into systematical error bars $\pm 3K$ to each data point. Additionally, the original fit for the liquid only applies to data at equilibrium conditions above the melting point. The proposed extrapolation to supercooled states below the melting point, where the error bars already intrinsically get bigger due to the diminishing increase of density (see [30]), is therefore even more unreliable.

We thus change the fit parameters within their error bars, $4157.1 \rightarrow 4157.2$ and $975 \rightarrow 970$, to shift the resulting values to lower temperatures:

$$T = \sqrt{\left(0.08277 - 3.01 \cdot 10^5 \cdot \sqrt{\frac{4157.2 - \nu}{970}}\right)} \tag{4.1}$$

This can be criticized to be arbitrary, but in terms of the three remarks of the list above, it supplies a physically more reasonable statement. The values obtained with this changed formula 4.1 are plotted in fig.27. Note that this time the correlation $t = z/\nu_0$ is used for the x-axis to show the temporal evolution of the filament. The lowest temperature reached is $T_{min} \approx 9.5\,\text{K}$, which results in an undercooling of $T_{min}/T_m = 0.69$, i.e. a remarkable 30% below the melting point. These low temperatures of the liquid are only accessible because of the combination of high cooling rate through evaporation in combination with the time resolution for probing the filament in the $20\,\text{ns}$ regime.
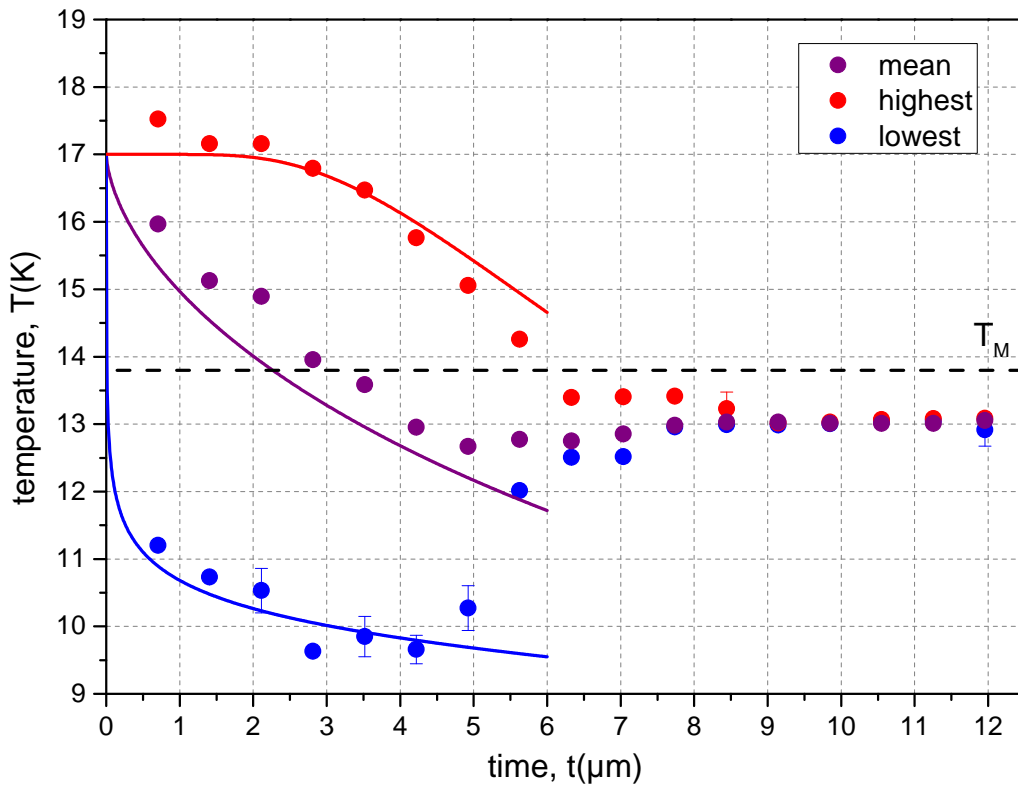

Figure 27: Circles: Corrected temperatures of the liquid extracted from data #4 using formula 4.1 vs. time. Lines: Numerical calculations for evaporative cooling with a layered model (see text) and conditions: $d_0 = 5.3\,\mu\text{m}$, $T_0 = 17\,\text{K}$ and $\nu_0 = 142\,\text{m/s}$. Purple is the mean of all layers, blue the outermost and red the innermost layer.

The formulas used for the simulation of the temperature gradient are described in app. B.1 and are plotted as lines in fig.27. The model already existed and has been published [23], yet based on the results in thesis it has been refined by introducing layers. To summarize, the cross section of the filament is divided into 100 concentric layers with equal area, accounting for an equal mass. Hence, the thickness of the rings decreases

from the inner core to the outer shell as illustrated in fig.26b. The calculation starts at $z = 0$ and delivers the current temperature of each of the 100 layers with $\Delta z = +1\,\mu m$ steps. Two physical concepts are involved to determine these temperatures: an energy balance determining the evaporation and secondly heat conductivity. The starting conditions for this plot are $d_0 = 4.0\,\mu m$, $T_0 = 17\,K$ and $v_0 = 142\,m/s$.

Only the outermost layer, whose outer surface is in contact with the vacuum experiences evaporative cooling corresponding to its current temperature. The higher the temperature, the higher the cooling due to the steep increase in the corresponding vapor pressure. Hence, the outermost layer, illustrated by the blue solid line in fig.27, almost immediately drops to temperatures below the melting point T_M. The interchange of heat in the model is solely governed by thermal conductivity of adjacent layers based on their current temperature difference. As the process of heat conductivity apparently happens slower than the cooling through evaporation, it takes about $1.5\,\mu s$ for the inner core to experience a change in temperature (red solid line). The mean temperature of all layers (purple solid line) decreases the fastest in the beginning, becoming more gradual as the efficiency of evaporation of the outermost layer diminishes.

This simple model delivers a fair agreement with the experimental data shown in fig.27, in case the latter is transformed with the corrected temperature formula 4.1. In detail, the calculation of the outermost layer is almost perfectly within error bars, the inner core in red decreases simultaneously to the data points and the mean is parallel to the corresponding experimental average, although $\approx 0.5\,K$ below. Note that the validity of the calculation ends as soon as the first solid appears, as the entailed heat of solidification and shift of intensity to the solid band described previously cannot be modeled. The effect of radiative heating of the (warm) vacuum chamber onto the filament has been implemented into the calculation. Yet, it was found to be orders of magnitude below evaporative cooling and therefore insignificant, mainly because of the short time scales we cope with. The model cannot take into account possible effects of heat convection, where molecules exchange between layers through currents, which may be formed by turbulances or the temperature gradient itself. However, there is neither a possibility to model it nor to see direct evidence in the data, because the effect would be a smaller and/or faster converging temperature gradient. As the present model is in good agreement with the data, we declare these effects to be negligible.

4.1.1.3   Comparison: Source conditions

The analysis of the temperature of the liquid from data #4 is now completed. Next, we turn to comparing measurements obtained under different source conditions as listed in table 3 on p.68.

At first, we choose data sets #5 and #6, that were recorded with the same nozzle directly one after another on the same day, yet with a very different pressure of 14 and 4 bar, respectively, to check for possible effects of the velocity v_0. Note that therefore the whole time evolution of data #5 is stretched to further distances z from the nozzle.

Unfortunately, the temperature sensor temp2 was mounted upside down on the nozzle copper block and did not yield correct values, so that the temperatures listed are estimates from the cryostat sensor temp1 with temp2 = temp1 + ΔT^+. The usual difference of these sensors at temp2 = 16 K with properly working temp2 is ΔT^+ = 3.3 K.
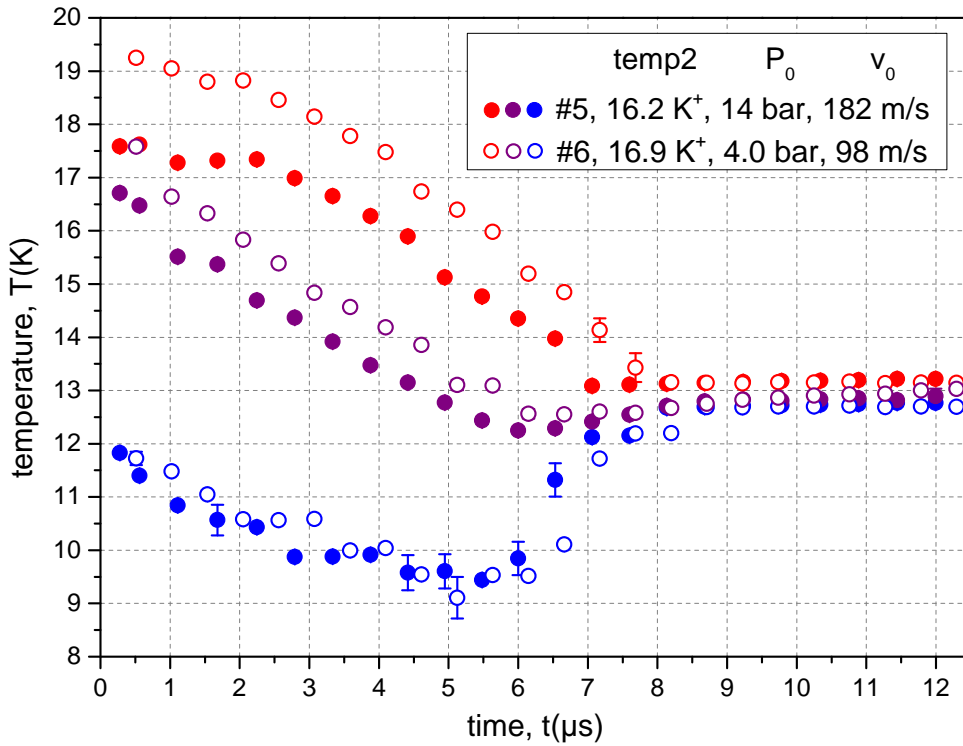
Figure 28: Temperature gradient plot from data #5 (filled) and #6 (hollow) from list on
p.68. Red, purple and blue data points correspond to the highest, mean and
lowest extracted temperature, respectively.

The mean/highest/lowest temperatures extracted from the spectra and transformed
using the corrected formula 4.1 are plotted against $t = z/v_0$ in fig.28 as filled (data #5)
and hollow (data #6) circles respectively. At first glance, both plots are similar in shape.
Beginning at the mean temperature in purple, one can see that the 4 bar data starts at a
≈ 1 K higher temperature with respect to the 14 bar data, which mainly comes from the
difference in (the estimated) temp2 reading. They descend almost parallel up to ≈ 5 μs,
where the first solid appears (identified by the blue circles rising in temperature). After
this point, both curves get closer and approach 13 K in the limit, indicating that neither
the starting temperature nor the pressure/velocity have an influence on the temperature
of the last liquid.
The coldest temperatures in blue, i.e. the outer layer of the filament, are almost on top of
each other from the start, even though the correlation ↔ wavenumber temperature via
formula 4.1 is more sensitive to changes in this region and would enhance differences.
This proves that the efficiency of evaporative cooling is similar for both conditions,
hence, independent of starting temperature and velocity. For both filaments, the outer
layer reaches ≈ 9.5 K before going up due to the formation of the solid. For the 4 bar
filament this is slightly delayed, which will be treated in the next chapter governing the
solid fraction.
The inner core of the filament, represented by the highest temperature in red, yields
significantly higher values of $+1.5$ K for the 4 bar data. This indicates that the difference
in starting temperature of the filament $T(z = 0)$ is more than 0.7 K as given by comparing
temp2. This can be reasoned as following: The mass flow of data #6 is only half the

value compared to #5, because its velocity v_0, with which the liquid exits the nozzle, is half. Hence, in the former case, the liquid remains double the time in the interior of the nozzle. As the very tip of it probably is warmer, based on thermal radiation from the warm vacuum chamber, the liquid has more time to heat up and exits the nozzle at a slightly higher temperature.

To conclude, the temperature gradient of hydrogen filaments is basically independent of the velocity v_0 or pressure P_0, respectively, and also proves the validity of our correlation $t = z/v_0$. Merely, lower pressures P_0 result in slightly higher starting temperatures and, connected, higher values for the inner core. Yet, evaporative cooling is efficient enough to keep the outer layer at similarly low temperatures. Also, the final temperature of the last liquid seems to be independent of the starting conditions.

If we compare #5, the data with high pressure $P_0 = 14\,\mathrm{bar}$ represented by full circles in fig.28, with the previous data set #4 at $P_0 = 8.5\,\mathrm{bar}$ in fig.27 on p.73 (not depicted in one plot), we find that all three temperature curves overlap very well, as for the latter the lower pressure is compensated by a little lower starting temperature. However, one significant difference can be detected at the point where the blue curve rises due to the appearance of the solid: For data #5 this happens after $\approx 6\,\mathrm{\mu s}$ whereas for data #4 the point is reached $1\,\mathrm{\mu s}$ earlier, which is almost 20%. Note that both filaments are produced with the same nozzle and the lowest temperature of the outer layer, where the nucleation starts, is comparable within error bars, maybe even a little lower for data #5, so that a higher nucleation rate based on lower temperature can be excluded.

This issue will be discussed in fig.32 as well as in the next chapter covering the solid, where it is much more evident. We solely conclude here that, although evaporative cooling and temperature gradient deduced from the spectra can be very similar, the appearance of the first solid accompanied by the temperature rise may be not.

4.1.1.4 Comparison: Nozzle diameter

In the next step, we analyze the influence of a smaller nozzle diameter. In fig.29 the temperature gradient for data #5 and #8 are plotted as well as the simulation for #8 with parameters $d_0 = 4.0\,\mathrm{\mu m}$, $T_0 = 16.8\,\mathrm{K}$ and $v_0 = 180\,\mathrm{m/s}$. The diameter of the second nozzle is significantly smaller with $d_0 = 4.0 \pm 0.3\,\mathrm{\mu m}$ as compared to $d_0 = 5.3 \pm 0.5\,\mathrm{\mu m}$, yet velocities of the filaments are chosen equal and the measured temperature temp2 is only 0.4 K lower.

Directly noticeable is that the mean temperature in purple and the highest temperature in red are both lower, whereas the coldest temperature in blue is on the same level compared to the hollow circles. The latter again is a nice proof that the process of evaporative cooling for the outer layer is independent from the starting parameters. Rather, the temperature of the outer layer is solely influenced by the vapor pressure which in the beginning is so high that, regardless of the source parameters, it always follows the same curve. This is only the case, because it happens much faster than the subsequent thermal conduction to the inner layers.

The starting temperature $T(z = 0)$, extrapolated from the red and purple curve, is only slightly below that of data #5 and both are in good agreement with $T(z = 0) =$ temp2 + 1 K. The mean temperature and especially the inner core show an increasing difference with time to the comparative data up to solidification, which means both cool faster. In other words, the temperature gradient of the smaller nozzle is less
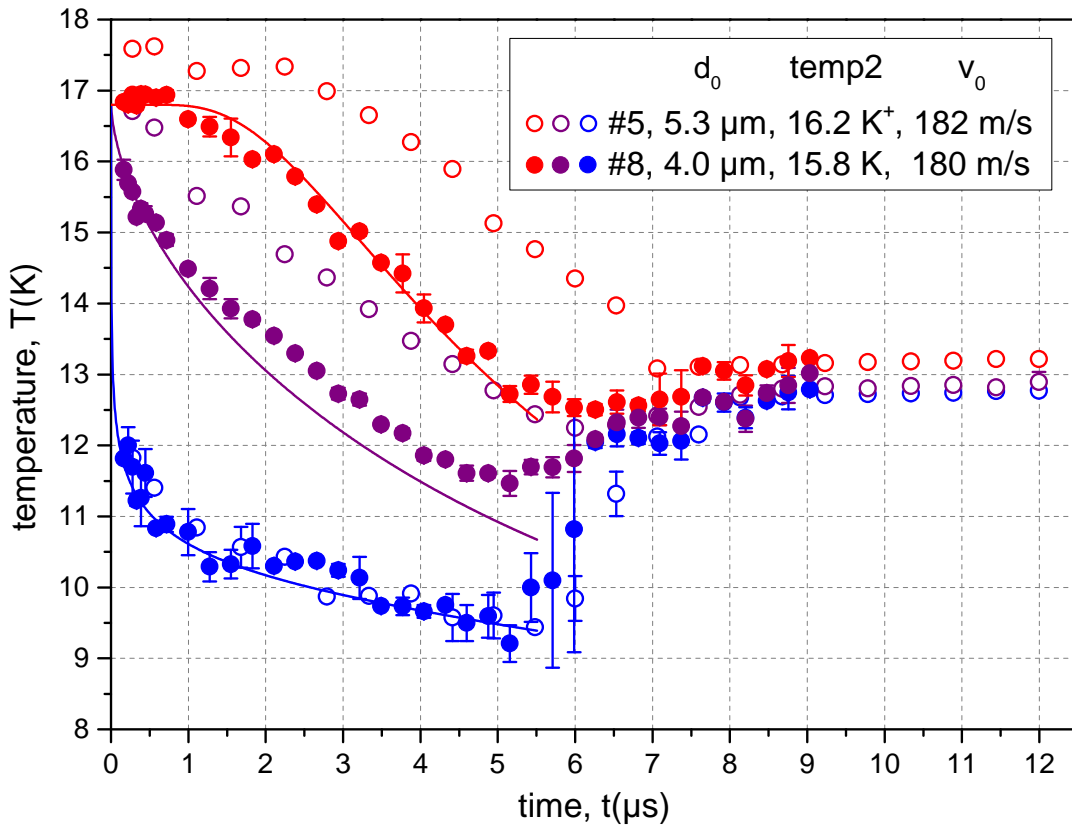
Figure 29: Influence of the nozzle diameter d_0. Temperature gradients are extracted from data sets #5 and #8 (hollow and filled circles, respectively). Solid lines represent simulation results for #8 with parameters $d_0 = 4.0\,\mu m$, $T_0 = 16.8\,K$ and $v_0 = 180\,m/s$.

pronounced. This is explained in terms of the smaller filament radius and, associated with it, molecule number. As the temperature of the outer layer is always similar, its (negative) heat is conducted to the inner core in less time in the narrower filament as there is less distance to bridge. Additionally, the cold parts make up a higher percentage of the total volume, resulting in a colder average temperature. This is in agreement with the inner core (red) starting earlier to decrease compared to the bigger filament as well as the average temperature reaching lower total values.

Another interesting finding is that the temperature increases stronger with the emergence of the solid for the mean and even the inner core rises. The main reason is that the absolute values at the start of the solidification are lower, which leads to higher growth velocities of the solid, which releases the heat in a shorter time. The details will be discussed in section 4.1.3.6.

Looking at the comparison between measurement #8 and its simulation (solid lines), we find a good overlap between the lowest as well as the highest temperatures. The experimental mean temperature is in agreement in the beginning, yet is increasingly higher with respect to the simulation the longer the filament travels. Considering the good correlation of the outer layer and inner core, it is surprising that the mean value deviates and no physical explanation is readily available. However, keep in mind that

the experimental temperature values are extracted with a somewhat arbitrary change in the parameters in formula 4.1, which may introduce discrepancies of the absolute values. Nevertheless, our simulation model seems to be valid also for different nozzle diameters d_0.

4.1.1.5 Droplet beam

To elucidate the influence of the filament size, another nozzle was probed in the second beam campaign. With a diameter of $d_0 = 1.9 \pm 0.2\,\mu m$, nozzle XVII-01 still holds our record of the smallest nozzle capable of producing stable liquid beams. However, the pretests in Frankfurt revealed that its liquid beams of hydrogen result in a Rayleigh breakup into a droplet beam pictured in fig.31a, rather than freezing into a solid filament. The reason for this is that despite the faster cooling of the overall filament, caused by the higher surface-to-volume ratio, the surface tension is strong enough to constrict and cut of the continuous liquid beam, before it solidifies. The breakup, determined by shadow imaging, occurs in the interval $300 - 600\,\mu m$ at $P_0 = 26\,bar$ and $temp2 = 16\,K$.

Corresponding Raman spectra of the $Q_1(0)$ band, measured in Madrid, are plotted in fig.30b. A main peculiarity is that the liquid band does not exhibit a broad distribution that shifts gradually towards lower wavenumbers with increasing distance z. Rather, at the first point measured at $50\,\mu m \Leftrightarrow 0.2\,\mu s$ it already is narrow, situated at low wavenumbers compared to fig.24 on p.69 and only moves slightly more downwards. The solid starts appearing much earlier (see later section 4.1.3.7) and is accompanied by the liquid band broadening towards higher wavenumbers, even higher than its initial position at $50\,\mu m$.

The temperature gradient is extracted as circles into fig.30a, although this denotation is not quite justified this time, as there is no real gradient between the highest and lowest temperature in the beginning, as the FWHM of the liquid band is close to the spectral resolution. All three temperature curves reach their lowest value already after $75\,\mu m$, which corresponds to a time of less than $0.5\,\mu s$ due to the high velocity v_0 of the beam. In all previously shown data, the highest temperature does not even start to decrease at this time. This means that evaporative cooling as well as the transfer of heat to the inside happen much faster than expected, which is clearly evidenced by the huge discrepancy to the simulated temperature gradient displayed as solid lines, for which a temperature gradient is clearly visible.

At first glance, another surprise is that as the solid peak grows, the highest temperature increases rather than the lowest, whereas all data previously discussed showed a behaviour vice versa. However, this is an effect based on the uniform temperature of the liquid. Due to the missing temperature gradient, this time we are not able to attribute the highest and lowest temperatures to the inner core and surface, respectively. We can be sure that the increase to higher wavenumbers/temperatures still comes from regions adjacent to the growing solid releasing the heat. We just cannot identify where the solid appears at first, although the outer surface of the liquid still is the most probable as it is the source of the temperature decrease. Nevertheless, the final temperature of the last remaining liquid is at $\approx 13\,K$ and in agreement with all previous data, which evidences that the temperature scaling is correct for this measurement.
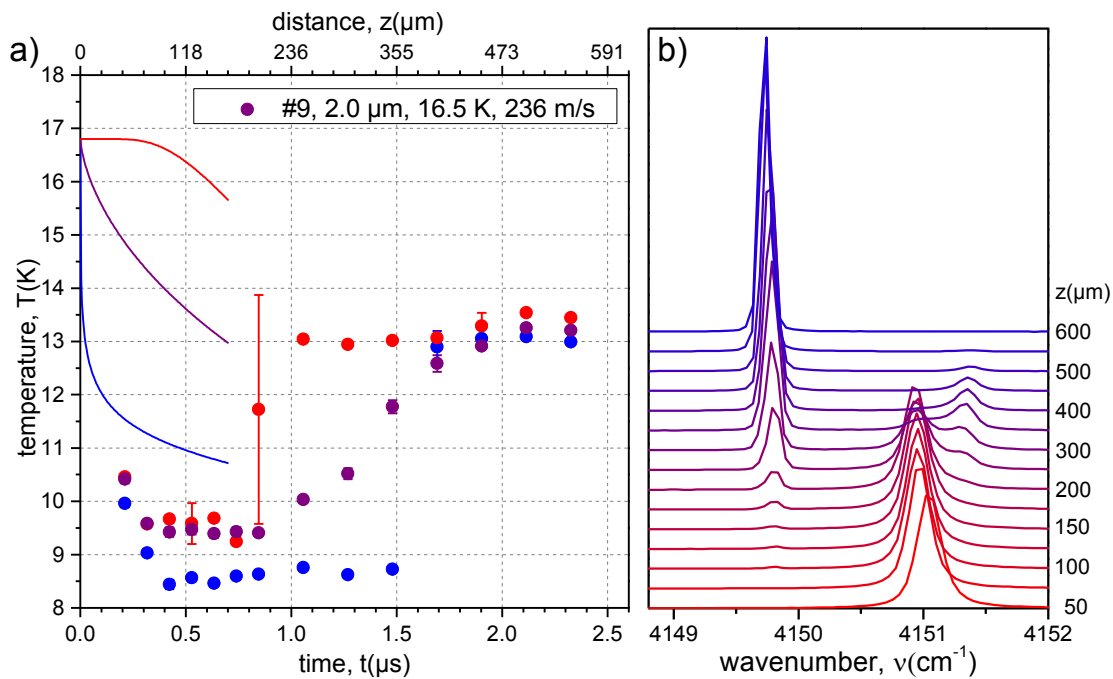
Figure 30: a) Temperature gradient as circles from data #9, with the filament breaking up into droplets. The simulated results are displayed as solid lines. b) Associated Raman spectra of the $Q_1(0)$ excitation at increasing distances z (right scale) from the orifice.

For the interpretation, the most important difference to all other data we have to obey is that we do not deal with a liquid filament which keeps its geometry during solidification. In the beginning of this paragraph it was stated that in pretests in Frankfurt the nozzle produced a liquid filament breaking up into droplets after $300 - 600\,\mu m$. Yet, the information extracted from the Raman spectra casts doubt on the assertion that the beam is comparable to these conditions. Two main arguments speak against it: For one, at least in the very beginning, the beam should emerge as a liquid filament, as the breakup starts at $300\,\mu m$ at the earliest. Hence, the temperature gradient simulation, which so far has been in good agreement with all experimental data, should at least qualitatively apply and not yield such vast discrepancies. Secondly, for the Rayleigh breakup, the beam still has to be liquid, at least in big parts. But as evidenced by the spectra and especially in the later section 4.1.3.7 covering the fraction of the solid, at $300\,\mu m$ the filament already is half solidified. A breakup of the filament into spherical droplets as seen in fig.31a at this stage is highly unlikely.

Unfortunately, the optical resolution of the long-distance objective used for shadow imaging pictures in Madrid does not provide sufficient resolution to observe the droplet beam. Yet, a rough comparison of the pictures from Frankfurt and Madrid can still be made and is illustrated in fig.31. In the picture in panel b, recorded in Madrid, the very faint hydrogen beam can just be detected by eye. But the line of the beam cannot be followed for long, because it fades quickly and blends with the background. It seems to not resemble the desired beam pictured in panel a, which shows a well defined line, even after the breakup into droplets.
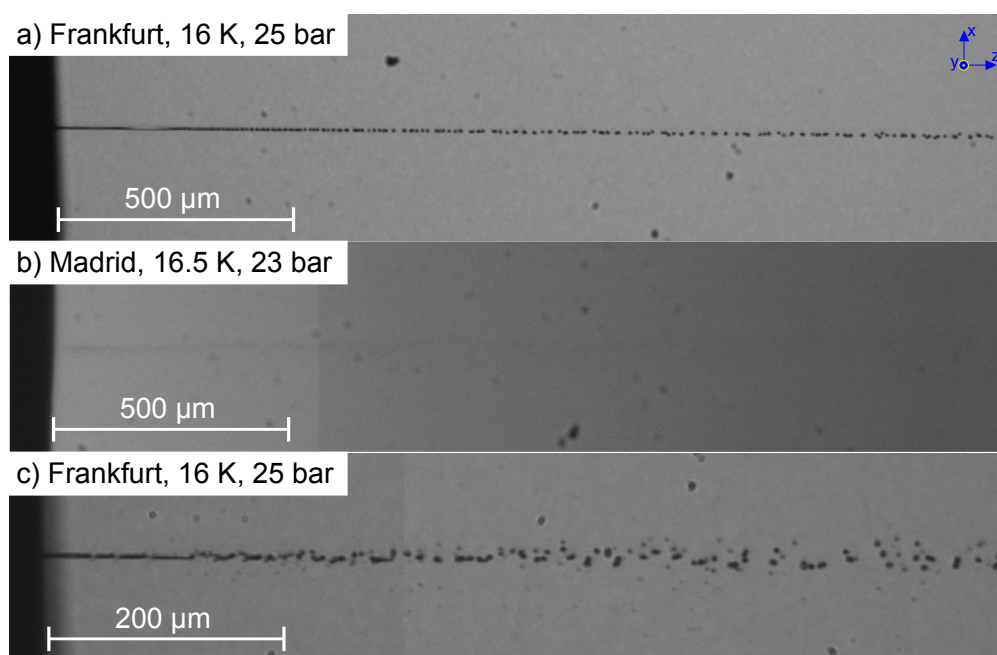
Figure 31: Shadow imaging pictures of beams produced with nozzle XVII-01, $d_0 = 1.9 \pm 0.2\,\mu m$. a) The desired beam could probably not be achieved. Instead the observed jet b) presumably looks more like c).

As the conditions for establishing such a neat beam with this particular nozzle are prone to changes, it is more likely that the beam probed by Raman spectroscopy in Madrid is closer to the one displayed in the close-up shot panel. Note that it was recorded at the very same conditions as in panel a, yet early on, this beam already exhibits structure and breaks up into droplets of very different size after $\approx 150\,\mu m$ which is probably due to cavitation effects. These droplets are not situated in a straight line, but rather resemble a spray spreading in a cone shape. In combination with the poor resolution in Madrid, this explains the fading beam in panel b because small, dispread droplets cannot be detected anymore. An early breakup of the liquid could also explain the abnormally fast cooling of the liquid seen in the analysis, because cavitation of the liquid would involve high surface to volume ratios enhancing the effect of evaporative cooling. If we take into account that the source temperature in Madrid was higher than in the pretests in Frankfurt, more cavitation events and an even earlier breakup of the liquid are likely.

Hence, the pure p-H_2 Raman data for this $2\mu m$ nozzle should be taken with care, because we do not know the details of the beam geometry and droplet sizes. Yet this data is still interesting, because we probably see the limit temperature for evaporative cooling. In the experiment, the whole liquid is at around $9\,K$, without further decrease and without substantial growth of the solid peak. This is roughly in agreement with the limit in the temperature gradient simulation at long distances, for which the vapor pressure at this temperature is too low to let a significant amount of molecules carry away heat through evaporation. We conclude that it is not possible to supercool para-hydrogen below $8.5\,K$ by evaporative cooling alone.

4.1.1.6 Repeatability

We now discuss effects regarding the quality and reproducibility of filaments. The panels a) and c) in the previous fig.31 serve as a good bridge to this section. Notice that both these jets of hydrogen are produced with the same nozzle and in addition the source parameters temp2 = 16 K and P_0 = 25 bar are equal, yet show a very different behaviour. As panel a) was taken shortly after panel c), a clogging of the nozzle channel with an obstacle can be excluded. The difference in the quality of the beams therefore has to have a different origin.
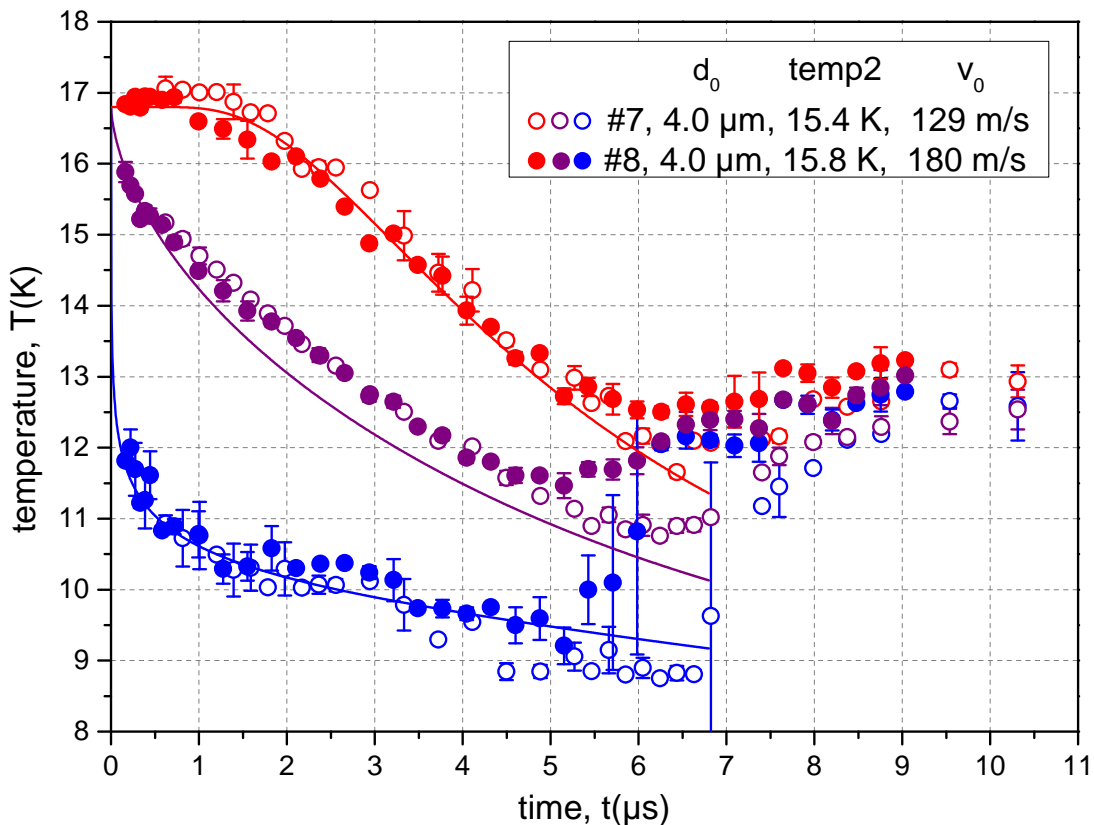

Figure 32: Possible effect on filaments of the same nozzle depending on source conditions #7 (hollow) and #8 (filled). Red, purple and blue data points correspond to the highest, mean and lowest extracted temperature, respectively. Solid lines are according to the temperature gradient simulation.

For further analysis, fig.32 shows data #7 and #8, which were recorded with the same nozzle X4-3, yet with slightly different source conditions and on another day. In their shadow imaging pictures, both liquid filaments freeze into the solid phase without any sign of breakup and look very stable in their direction. The smaller pressure P_0 or velocity v_0, respectively, of data #7 is compensated by the 0.4 K lower temperature temp2, so that both filaments basically exhibit the same temperature $T(z = 0)$ when exiting the nozzle as seen in fig.32. The temperature gradients of both filaments overlap almost perfectly in the beginning in all three curves.

However, there is a difference in the time after which the first solid appears, which is $\approx 5\,\mu s$ for data #8 and $\approx 6.5\,\mu s$ for data #7 (see later chapter 4.1.3.5 for details). The mean temperature (purple) rises, as soon as solidification sets in, yet because this happens later for data set #7, there is more time to cool and the lowest temperature is 0.7 K below the comparative data. In parallel, the lowest temperature also decreases 0.4 K below the corresponding values of #8. This is very surprising, since we have seen before that neither starting temperature $T(z = 0)$ nor pressure P_0 should have an influence on the lowest temperature achievable and both temperature gradients indeed look very similar except for that part.

A possible explanation for this is rather severe, as we have to discard some idealized assumptions. As shown in fig.16 on p.48, the nozzle orifice may have cracks or edges. These disturbances could alter the surface of the filament, so that its shape deviates from the assumed ideal cylinder. Small bumps on its surface (illustrated in fig33a) would have a higher surface to volume ratio and cool faster and to lower temperatures than the rest of the surface, because the negative heat cannot be transported away fast enough by heat conductivity. These cold spots would exhibit a too small volume ($< 0.1\%$ of total volume) to be detected in our Raman spectra and act as the origin of the first nucleation embryos initiating the solidification. However, it is questionable, how long such structure defects can survive, as the surface tension tends to smooth them out. Alternatively, cracks could produce tiny side beams of droplets, which freeze rapidly and reunite with the main filament introducing the solid.

These possible effects are probably connected to the partial freezing of the nozzle surface, discussed previously. Indications for a correlation were found in the first beam campaign, when data #7 was recorded. In this measurement, the beam sometimes slightly changed its angle, accompanied by a tiny change of $< 5\%$ in the vacuum gauge reading, whereas temp2 and P_0 remained unchanged, which is interpreted as partial freezing of the nozzle. These switches lasted between seconds and minutes and solely alternated between those two states, since their direction and Raman spectra repeated very well. The corresponding Raman spectra of these two alternating filaments revealed, similar to plot 32, good agreement between the overlap of the liquid bands, yet a different starting time of the first solid, which is why they were labeled as "good" and "bad" filament for the later and earlier solid, respectively. Interestingly, the good filament was the one with a slightly lower reading for the vacuum gauge, suggesting that this is the one with the smaller, because partially frozen, orifice.
The favored interpretation for this is that the cracks or edges producing the disturbances which lead to earlier freezing, are likely to accumulate hydrogen since they do not experience the force of the jet stream. Through evaporation the accumulated liquid hydrogen freezes and thereby these rough spot are evened or smoothed out. Hence, the sources of disturbances are gone, the filament freezes later yet the orifice is slightly smaller. From time to time, the hydrogen ice in these cracks evaporates or eventually is washed away by the liquid jet leading to the changes in the direction of the beam. Beware that this hypothesis is still highly speculative, but it is the most congruent explanation for the strange behaviour so far.

Direct evidence for freezing of the nozzle was obtained from high resolution shadow imaging pictures during pretests of nozzles in Frankfurt. If filaments with a particular nozzle (X8-12, 20.09.2012) were established by reducing the temperature at constant pressure, hydrogen ice formed at the orifice clearly seen in fig.33d. Pumping out the gas
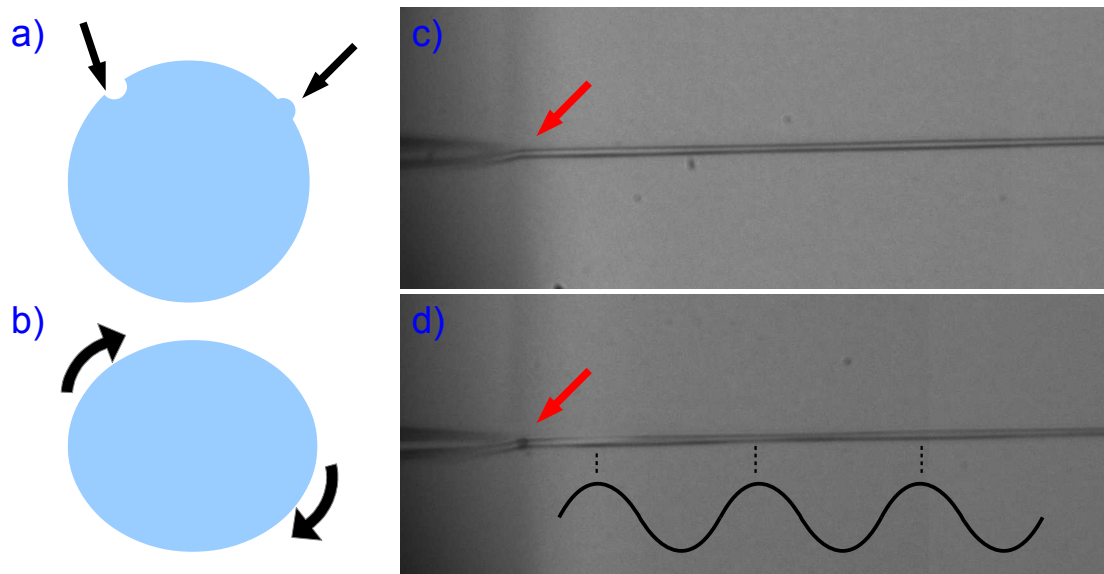
Figure 33: a) Illustration of bumps and holes within the filament surface, yielding local higher surface to volume ratios. b) Illustration of a twisting filament turning around the propagation axis. c) Shadow imaging picture of clean orifice (red arrow). d) The same nozzle, yet the orifice is frozen. The periodic shading of the filament may indicate a twisting.

line and refilling rapidly at 16 K however resulted in filaments without any structure at the exit of the nozzle, as seen in fig.33c. Hence, already the route to establish liquid filament may introduce different conditions that alter the freezing time and or direction of the filament. Unfortunately, these effects cannot be related to Raman spectra, because with the long-distance objective used in Madrid the optical resolution is not sufficient to observe a frozen orifice.

Additional evidence for deviations from perfectly cylindrical shaped filaments comes from these image observations. Some nozzles produce filaments that show structure, manifesting in recurring shades in the liquid directly after expansion (see fig.33d, black sinus line). This is interpreted as a periodical twisting of the filament around its propagation axis, as illustrated in fig.33b. Usually, this is associated with a (partial) clogging of the nozzle channel, however, even good nozzles/filaments may show tendencies towards such a behaviour. Of course any deviation from a perfect cylinder locally increases the surface to volume ratio which may alter the time for transition to the solid phase.

These effects challenge the repeatability and therefore universality of the results gathered in this work. Yet, so far we have seen that there is no noticeable influence on the temperature gradient across the filament of the filament, but only on the time interval, how long it lasts. In the next chapter we will find that the impact onto the growth of the solid also is accessible and can be set into limits. Hence, the unpredictable, arbitrary behaviour of nozzles or filaments, respectively, is unpleasant, however does not obliterate the value of the results in this work.

4.1.2 Summary: Temperature of the liquid

We propose a model in which the cross section of the filament is divided into concentric layers with equal mass. As soon as the surface of the filament is exposed to vacuum, only the outer layer cools rapidly by evaporation, establishing a radial temperature gradient. From the Raman spectra, the mean as well as the highest and lowest wavenumbers of the liquid band can be extracted from the very left and right inflection points, respectively (section 4.1.1.1). To receive absolute temperature values which are more physically reasonable with our data, the parameters in Vilesov's wavenumber-temperature correlation are changed within error bars. Mainly by thermal conductivity, the inner layers cool down more gradually in the order of µs, the further the filament travels. The data is in good agreement with numerical calculations of this described model (fig.27 on p.73). When the outer layer hits temperatures of $9 - 9.5\,\text{K}$, corresponding to a supercooling of 30%, the first solid is formed at this surface, which is evidenced by the accompanied rise in temperature of the adjacent liquid. With proceeding solidification, the gradient narrows and converges to a temperature of $\approx 13\,\text{K}$ in the final liquid (section 4.1.1.2). This overall behaviour is seen in all measurements of pure para-hydrogen with a freezing filament.
A lower starting pressure P_0, corresponding to smaller velocities v_0 of the filament, results in a higher initial temperature $T(z = 0)$, probably due to the longer exposure to radiative heat within the nozzle tip (section 4.1.1.3). A smaller nozzle diameter is accompanied by a more rapidly diminishing temperature gradient of the filament and an earlier appearing solid peak. However, the effectiveness of evaporative cooling, represented by the coldest temperatures, is independent of this starting temperature and only the mean and highest temperatures are quantitatively affected (section 4.1.1.4). The analysis of the droplet beam reveals the coldest temperature achievable through evaporative cooling with $T \approx 9\,\text{K}$ (section 4.1.1.5). Although filaments may have a very similar temperature gradient, the appearance of the first solid connected with the increase in temperature is unpredictable. This is related to the quality of the individual filament, which probably is influenced by the geometry of the nozzle orifice and linked to partial freezing, which may change the surface or shape of the filament (section 4.1.1.6).

4.1.3 Solid fraction

4.1.3.1 Definition and general interpretation

This section is dedicated to the solidification process that can be extracted from the vibrational region. When we take a look at the series of spectra in fig.24 on p.69, we can identify that there is a continuous redistribution from intensity of the liquid band into intensity of the solid band the further the distance z from the nozzle for both o-H_2 and p-H_2. As linear Raman spectroscopy is proportional to the number of molecules in a state and the cross sections for excitations in the liquid and the solid are similar (see chapter 2.3.2), we can extract the fraction of molecules that already have solidified and call this quantity the solid fraction.

The solid fraction at each position z is readily obtained by dividing the integral of the intensity of the solid band by the total intensity of solid plus liquid:

$$s_f^x(z) = \frac{I_{sol}^x}{I_{sol}^x + I_{liq}^x} \tag{4.2}$$

with $x = $ p-H_2. The solid fraction of the weak o-H_2 band is calculated by the maxvalue method, described later in chapter 5.1.2.1, because the intensity enhancement discussed later in chapter 4.1.5.2 introduces systematical errors. Due to above definition, the solid fraction ranges between 0 (only liquid) to 1 (completely solid).
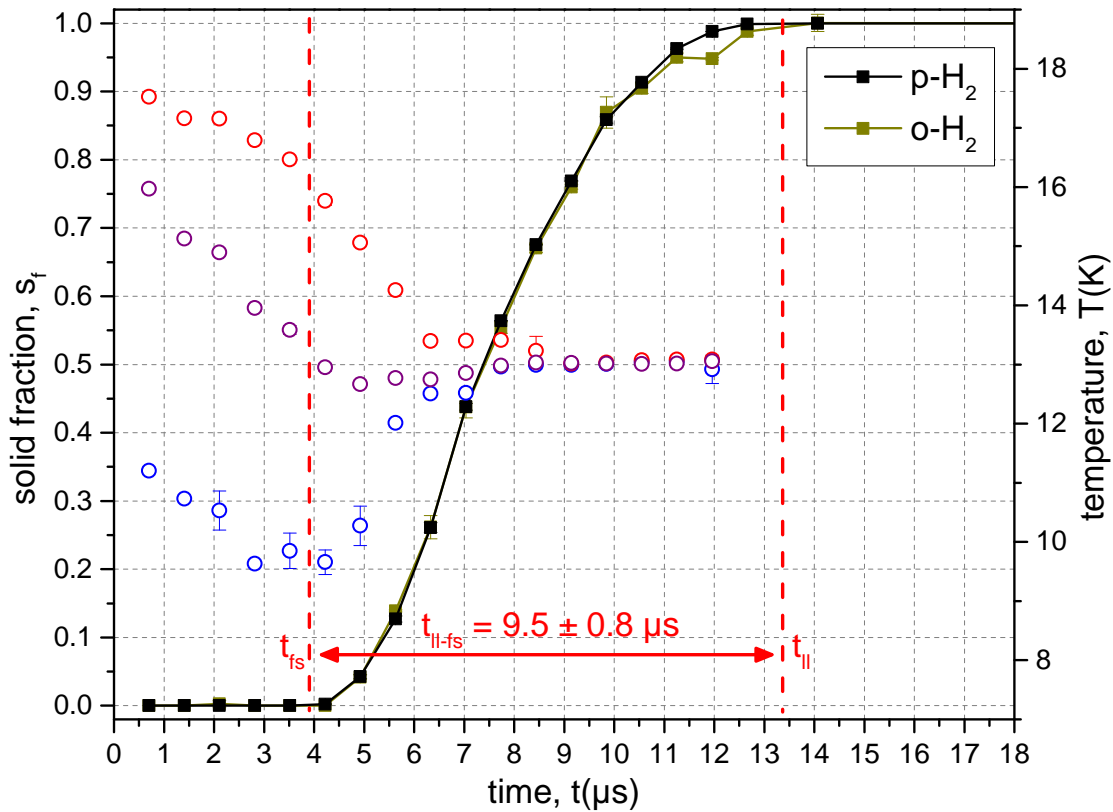

Figure 34: Solid fraction of o-H_2 and p-H_2 in olive and black, respectively, extracted from data #4. The lines are linear connections between the squares as guides to the eye. Red vertical lines mark the times in between those two spectra, where the first solid t_{fs} and last liquid t_{ll}, respectively, are detected and t_{ll-fs} is its difference. For comparison the temperature gradient is plotted as hollow circles with the scale on the right side.

For a systematical analysis, we again begin by plotting the solid fraction for data #4 into fig.34. Here, the solid fraction is plotted for p-H_2 and o-H_2 individually. We focus on p-H_2 in black first. One obvious feature is that the solid fraction for para-hydrogen is very smooth. As usual, the error bars are obtained from the standard derivative of the $3-4$ single spectra recorded at each z-position and for p-H_2 this error is much smaller than the size of the squares. In other words, spectra recorded at a particular distance z from the nozzle yield a constant value for the solid fraction. There are

two interpretations for this. For one, the filament may have very stable conditions for solidification. Imagine, we follow along its traveling path a slice of $\Delta z = 2\,\mu m$ exiting the nozzle with the velocity v_0, so that the molecules inside this volume are the same throughout this observation time. If we compare the evolution of several of these (randomly chosen) volumes, each of them would start to freeze after the exact same traveling distance or time t_{fs} (first solid), respectively, and the solidification would proceed equally for all of them. In this first scenario, each of these volumes would have the same, interchangeable history.

In the alternative interpretation, we take into account that spectra are recorded in a time interval of $10-30\,s$, which is large against the time resolution of $\approx 20\,ns$ associated with the stationary slice of $2\,\mu m$ width seen by the spectrometer. As the filament continuously passes through this probed slice, a single Raman spectrum collects signal from billions of volumes of this size. In this scenario, the volumes may very well have different histories, i.e. start to freeze at slightly different times and have different solid fractions afterwards. Yet, through the averaging of the huge amount of these (different) volumes united into a single spectrum, the solid fraction, recorded at a particular distance z, yields always the same value.

Unfortunately, there is no way to reduce the time interval for recording Raman spectra by orders of magnitude necessary to rule out one of these scenarios. Yet, we can argue that the second interpretation is the more realistic one. Evidence supporting it, comes from shadow imaging pictures in Frankfurt, which capture a snapshot within ns. Subsequent pictures taken indicate that the position at which structure appears and which is associated with the emergence of the solid, differs in the order of $100\,\mu m$ or $1\,\mu s$, respectively. This is in agreement with nucleation theory, which states that the formation of critical nucleation embryos is a statistical process and, hence, can happen at different times, even if thermodynamic properties are similar (compare chapter 2.5.1). We approve the second scenario and conclude that, although nucleation and the solid fraction, respectively, may differ in individual volumes, Raman spectra yield very stable values because of averaging over comparably long times.

Next, we make the comparison to the solid fraction from o-H_2 plotted in olive. Both curves overlap very well, indicating that the solidification process for both isomeric species is similar. The differences appearing towards the end ($s_f > 0.8$) are attributed to systematical errors during the analysis process, because the left tail of the growing solid p-H_2 band overlaps with the diminishing liquid band of o-H_2, progressively increasing its background as noticeable in fig.24 on p.69. Additionally, the error bars of o-H_2 are significantly bigger, as its intensity is roughly 100 times lower with respect to p-H_2, automatically entailing a higher percentaged variation in between spectra as the noise remains the same. The good agreement between the solid fractions of both isotopes indicates that neither a significant phase separation before solidification nor a phase segregation in the liquid-solid-interface during solidification is present. If one of the components had a higher tendency to join the solid phase, its solid fraction would consequently be higher for all points.

4.1.3.2 Growth rate of the solid

From the analysis of the solid fraction we can give a rough estimation of the growth rate u of the solid, which is the fundamental quantity for the crystallization kinetics [5]. We identify the two subsequent Raman spectra, in between which the first solid peak emerges, and those, where the last liquid peak disappears. The mean value of their associated propagation times yields the time for the first solid $t_{fs} = 3.9 \pm 0.4\,\mu s$ and the last liquid $t_{ll} = 13.4 \pm 0.7\,\mu s$, respectively, as well as error bars from their standard derivatives. The difference of these two values equals the time for complete solidification $t_{ll-fs} = 9.5 \pm 0.8\,\mu s$, which is the first part for the growth rate u.

For the second part, we take into account a result from the last chapter, where it was stated that the solid first emerges at the surface of the filament, where the coldest temperatures prevail. For this rough approximation we assume that the first solid layer is generated at the surface isotropically, which means the freezing is rotationally symmetric regarding the cross section of the filament. The distance for complete solidification then simply is given by the radius of the filament r, because starting from the frozen surface the liquid-solid-interface proceeds to the inner core (compare fig.35a). Our estimation for the growth rate u finally is:

$$u = \frac{r}{t_{ll-fs}} = \frac{(2.65 \pm 0.25)\,\mu m}{(9.5 \pm 0.8)\,\mu s} = (0.28 \pm 0.03)\,m/s \qquad (4.3)$$

Before we interpret this result, we first need to justify some of the simplifications made and see their limits. One main point of criticism regards isotropy. We assume correctly that the solid starts at the surface, which is supported by the previous chapter, but it is not clear that nucleation embryos are homogeneously distributed. On the contrary, previously in this section we concluded that the first nucleation embryos may appear rather randomly in time and likewise they do emerge randomly in space. Additionally, the nucleation rate strongly depends on temperature. If we take into account that the filament may have a shape deviating from a perfect cylinder, there very well may be regions where nucleation of the solid is preferred.

The real filament therefore probably does not freeze isotropically from a first solid outer shell to the inside, but rather exhibits randomly distributed spots on its surface, from which the solid starts growing radially as illustrated in fig.35b. However, we are not able to estimate, how many nucleation spots actually exist and they may indeed be distributed on the surface quite homogeneously as their probability of appearance strongly increases based on the ongoing evaporative cooling. Additionally, the position of these starting spots probably changes arbitrarily in the slice seen by the spectrometer, so that for the long recording time of a Raman spectrum and therefore averaging over billions of volumes, the whole surface seems to be isotropically covered. This statement is valid as long as there is no preferred, e.g. more undercooled, region due to nozzle orifice defects. Yet, even if we take the very extreme, unrealistic case that the filament starts to freeze at one side and the interface proceeds to the opposite side, the radius r in formula 4.3 is replaced by the diameter d and the value u is merely cut in half.

Another simplification is that we assume nucleation embryos only to appear at the very surface and not within the filament itself. This is readily justified by the extreme dependency of the formation of critical embryos on temperature pictured in fig.11 on p.31. As we found a strong temperature gradient from the surface to the core of the
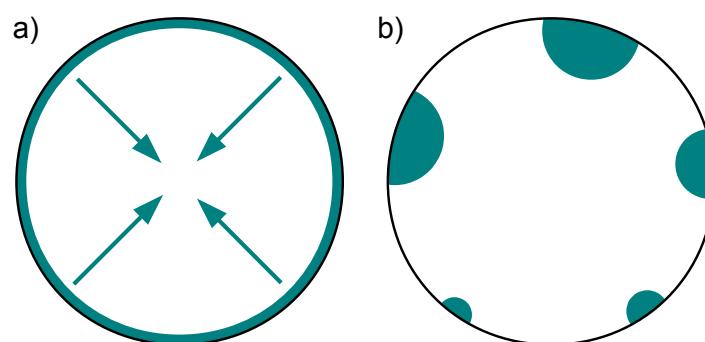
Figure 35: a) Simplified growth of the solid starting homogeneously from the outside layer advancing towards the center with constant velocity u. b) More realistic scenario, in which nucleation spots are randomly distributed in space as well as appearance time on the surface and grow radially.

filament in the previous section, we can exclude the scenario of nucleation embryos within the filament with confidence. We will see additional proof for this statement later in section 4.1.3.4.

The next remark is rooted in this temperature gradient. At first, solidification happens in the relatively cold regions close to the surface, but the temperature is increasingly higher the closer it approaches the core, what may directly influence the growth velocity u of the interface. This indeed needs to be analyzed in the next section, but for now we just presume that the current temperature is constant and given by its mean value extracted from the liquid band $T_{mean} \approx (12.5 \pm 0.5)\,\text{K}$ throughout the whole solidification process (compare purple data points in fig.27 on p.73).

Considering the above limitations, the error bars for the growth velocity in formula 4.3 probably are higher. Yet, for a first approximation the value still serves.

4.1.3.3 Growth mechanism

With the above legitimation for the estimation of u, we now focus on what we can actually learn from it. One important direct insight is that the velocity of the filament is much greater than the crystal growth rate, $v_0 >> u$, with a factor of more than 100. Hence, the nucleation and solid growth events of a certain volume do no influence subsequent parts of the filament. The advancing solid in (negative) z direction just gets carried out of the probed slice. In the isotropic approach described above, this allows us to view the solidification of the filament cross section as independent, two-dimensional slices static in time. This is only possible because Raman spectra are averaged over long periods. We will need this statement in section 4.1.3.4.

In the theory chapter 2.5.2, two different mechanisms for crystal growth were introduced, namely the diffusion limited model in eq.2.22 and the collision-limited model in eq.2.23 on the other hand. With the experimental value for u we are able to determine which of these models applies in the case of supercooled hydrogen.

To estimate the theoretical predictions from the two models, extrapolated values for the free energy or chemical potential, respectively, are necessary. The calculations and fits to obtain these quantities are presented in appendix B.2. Both models are embedded into
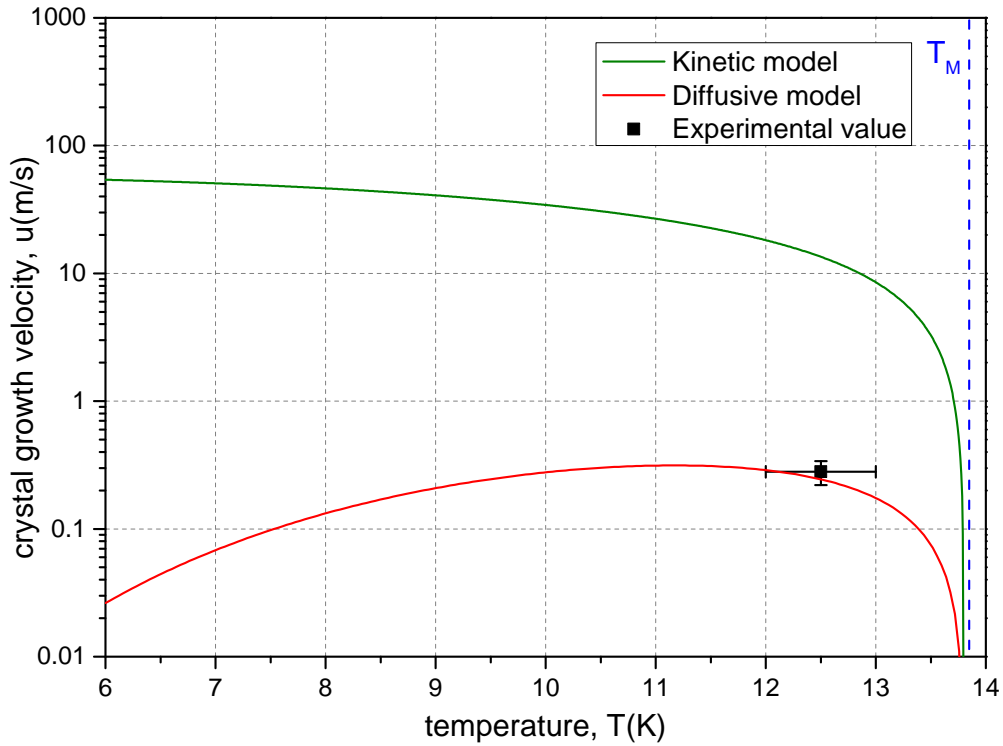
Figure 36: Semi-log plot of the numerical values with $f = 1$ for the crystal growth velocity u within the kinetic model (olive) and diffusive model (red), as well as the experimental data point (black square) for u from eq.4.3 at the mean temperature $T_{mean} = 12.5\,\mathrm{K}$ with error bars.

the formula for crystal growth eq.2.21 on p.34, which respects the free energy difference between the solid and liquid phase as well as the fraction of particles f between 0 and 1 contributing to the crystal growth. As mentioned, this factor f is the main critical part, as it covers all geometric and dynamic constellations and probabilities and therefore is entirely unknown. To still make a statement, we choose the unrealistic upper limit $f = 1$, which means all particles are added to the solid without any hindrance.

The plots for the two growth mechanisms under this condition together with the experimental estimation of u are shown in fig.36. We find that the diffusive model (red) yields values barely within the error bars of the experimental data point. As we have already chosen the maximum limit $f = 1$, more realistic smaller values $f < 1$ shift the curve even further downwards (linearly). Hence, we can exclude the validity of the diffusive model for the crystallization of para-hydrogen with confidence. On the other hand, the kinetic model with $f = 1$ delivers values above the experimental data point. However, reducing it to $f = 0.02$ lets the curve pass through the experimental point. This order of magnitude for f at least seems more realistic than the upper limit value and so we conclude that for para-hydrogen the kinetic model is more likely to apply. In a figurative image this can be interpreted as the molecules from the liquid phase colliding with and sticking to the solid interface with their thermal velocity, which is the actual speed of a particle, rather than diffusing, i.e. swapping places with neighbors, to get into the solid phase. One may argue that these two models merely represent idealized cases and also a hybrid of both mechanisms is possible. However, even in

this hypothetical mixed scenario, the kinetic model has to be the leading mechanism to come up for our experimental value.

Additionally we see that there indeed is a temperature dependence for u within the kinetic approach. In comparison to the experimental mean temperature of 12.5 K, the surface temperature of 9.5 K should exhibit a factor of ≈ 3 higher growth velocities according to this model. For our isotropic, layered model this means that in the beginning, the solid would proceed faster towards the inner core and slow down the further it reaches due to the increasing temperature. Therefore the estimation of u is a mean value of this process and in reality probably is not constant. Based on this, its error bars are probably greater and we use its value more as a measure of the order of magnitude.

4.1.3.4 Avrami equation

As we possess the time evolution of the complete solidification process through the experimentally obtained solid fraction, we are able to extract more information by fitting the Avrami equation 2.20 on p.34 to data #4.
In fig.37 two of these fits are plotted as green and red solid lines, respectively. The fit in green is done with the whole range of input data. It shows an astonishingly good agreement with the experimental data represented by black squares, which only slightly deviates in its shape at the end of the solidification process $s_f > 0.7$. This, at first, is surprising, because the Avrami formula as stated in the formula is not valid for the late stages because nucleation embryos are wrongfully allowed to be created in the solid phase [59]. From the fit parameters we extract the exponent of the time-dependency to be $n = 1.9 \pm 0.1$. In the original Avrami equation, which applies to a fixed volume with homogeneous temperature, this exponent is $n = 4$, comprising of the continuous creation of critical nucleation sites (1 part) and their growth in three dimensions (3 parts). The fitting result indicates that some of these components are not or only partially valid for our situation.

We stated before that we can view the solidification process as independent two-dimensional slices, because these slices do not influence each other based on $v_0 >> u$. Hence, in our case the growth only proceeds in this two-dimensional plain of the cross section and subsequently one growth direction is skipped, which reduces the time exponent n in the Avrami equation by 1. Additionally, we assume that nucleation embryos are solely formed at the surface of the filament, where the coldest parts reside. In this case, we do not have the Avrami condition, that nucleation sites are continuously produced throughout time and space, but rather only in the beginning. We deduce that the one component related to the nucleation rate also drops out of the exponent and we remain with $n = 2$, where the two components correspond to the growth of the solid in two dimensions.
This consideration, congruent with our model, agrees very well with our fitting value. Additionally, this explains the good fit even in the late crystallization stages, because in our case there are no more nucleation embryos created and the Avrami equation holds until the end. Though one has to be careful, because the fit can be prone to errors since changes in n can be compensated by the parameter k without exaggerating variation in the plot shape.
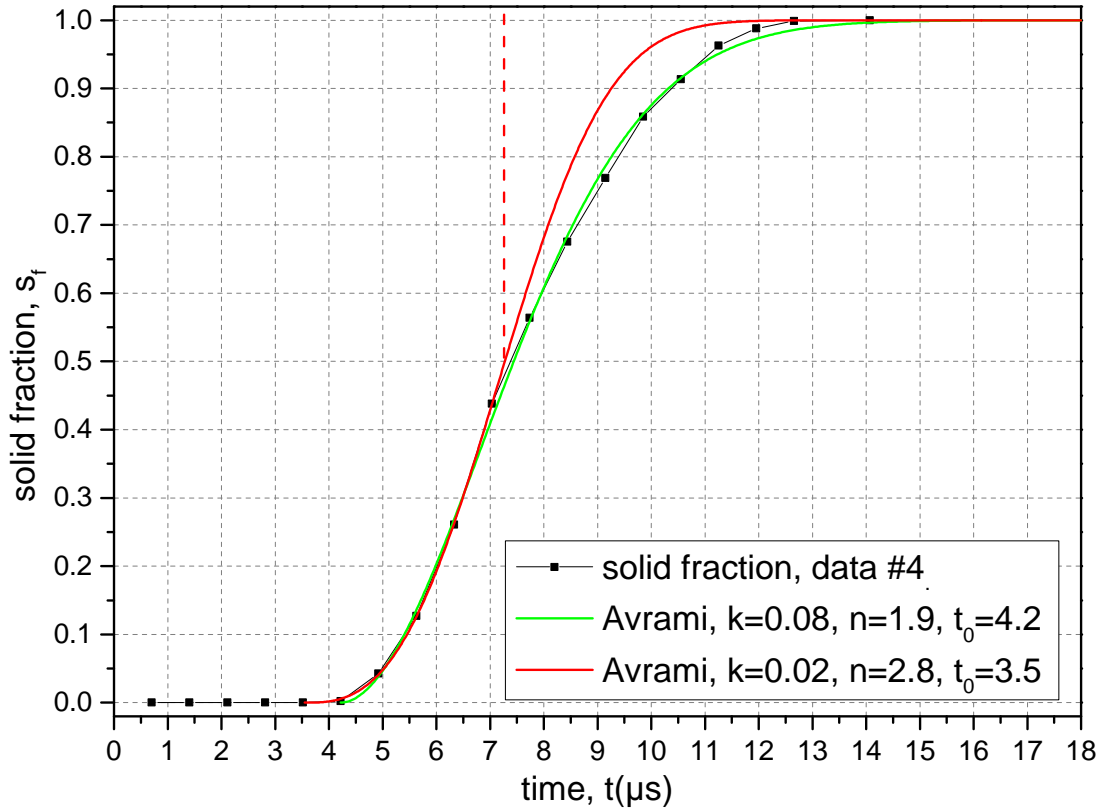
Figure 37: Experimental solid fraction from data #4 (black squares) and fits with the Avrami equation 2.20 on p.34 as solid lines. The green fit covers the whole data, whereas the input data for the red one is capped at $s_f = 0.5$, which corresponds to $t \approx 7.3\,\mu s$ (dashed red line).

To confirm this interpretation, a second fit (red) is done only for data points with $s_f < 0.5$ up to the red dashed line to consider particularly the beginning of solidification. We find that this fit yields higher values for the exponent with $n = 2.8 \pm 0.1$, which means the curvature of this plot is stronger. This can be explained, as in the beginning the nucleation rate in the outermost layer plays a role and contributes to the exponent with 1 in the idealized case. Together with the subsequent two-dimensional growth this comprises to an exponent of 3, which agrees well with the fitting value.

The better fit to the data with $s_f < 0.5$ to the initial phase of solidification is supported by the fit parameter t_0, which marks the point of the first critical nucleation embryos. Whereas the full plot in green yields $t_0 = 4.2 \pm 0.2$, which is above the first solid at $t_{fs} = 3.9\,\mu s$ extracted from the Raman spectra and therefore cannot be correct, the red fit results in $t_0 = 3.5 \pm 0.1$. This sounds reasonable because we are not sensitive to detect the first nucleation embryos which of course have to precede the first solid visible in the Raman spectra. Hence, both fitting curves agree surprisingly well with our proposed two-dimensional growth model, in which nucleation embryos are formed only at the surface.

At last, with the parameter $k = 0.02$, which we get from the red fit accounting for the initial nucleation, we can roughly estimate the nucleation rate I of our system (within

a few orders of magnitude). As we expect nucleation to happen on the surface, we assume the coldest temperature extracted from the data, $T_{low} = 9.5\,K$. Comparing equations 2.19 and 2.20 on p.33, we get the expression

$$I(T = 9.5\,K) = \frac{3k}{\pi u^2} = \frac{3 \cdot 0.02 \mu s^{-3}}{\pi \cdot (0.28 \mu m/\mu s)^2} \approx 10^{-1} \mu s^{-1} \mu m^{-3} = 10^{17} s^{-1} cm^{-3}\ . \quad (4.4)$$

However, keep in mind that the uncertainty grows significantly based on the cubical dependency on u, which already is a rough estimate. Additionally, according to the kinetic model its value is much higher, based on the lower temperature of the surface, $T_{low} = 9.5\,K$, compared to the mean temperature, $T_{mean} = 12.5\,K$, from which u is extracted here (compare green curve in fig.36). So, the nucleation rate stated here is likely to have error bars of a few orders of magnitude.

At least, the rough size of this value is reasonable as shown in the following consideration. If we approximate that the outermost 10% of the total cross section area of the filament are at $T_{low} \approx 9.5\,K$, this area, in shape of a ring, is $A_{9.5K} = 0.1 \cdot \pi d_0^2/4 = 2.2\,\mu m^2$. If we take into account that there are $\Delta z = 100\,\mu m$ steps, which corresponds to $0.8\,\mu s$, in between the recorded spectra of this series #4, we get the nucleation rate in this volume:

$$I_V(T = 9.5\,K) = A_{9.5K} \cdot \Delta z \cdot I(T = 9.5\,K) \approx 20 \mu s^{-1}\ , \quad (4.5)$$

which reads that there are 20 critical nucleation events happening in such a volume in shape of a hollow cylinder of $100\,\mu m$ length at this temperature. This value seems reasonable as its order of magnitude agrees with the experimental time scales of the solidification process.

Even if this estimation of the nucleation rate I could be off by several orders of magnitude, it demonstrates a particular strength of our experimental setup. Due to the time resolution of sub-μs and tiny nozzles of μm, we are able to access supercoolings corresponding to immense nucleation rates of $\approx 10^{17} s^{-1} cm^{-3}$, which would never be accessible in a bulk system.

4.1.3.5 Comparison: Source conditions

In this step of the analysis, we compare the solid fraction of data recorded under different conditions. In chapter 4.1.1, we found that the appearance of the first solid (associated with a rise in temperature) may deviate between measurements with similar source conditions, even though all three temperature plots for the considered regions are equal. These differences are particularly evident in the plots of the corresponding solid fractions displayed in the left panel of fig.38, which were all measured with the same nozzle XVII-06.

We first focus on data #4, 5, 6, which are plotted in black, red and green respectively. Comparing with the temperature gradient, we find indeed that a later increase of the coldest layer (order: #6, #5, #4) is correlated with the appearance of the first solid, i.e. values of the solid fraction $s_f > 0$. The formation of this first solid or critical nucleation embryos, respectively, inevitably initiates the solidification process so that the corresponding solid fraction curves of data #4, 5, 6 have different progresses at the same traveling time. The state of the solidification process between $0 < s_f < 1$ deviates
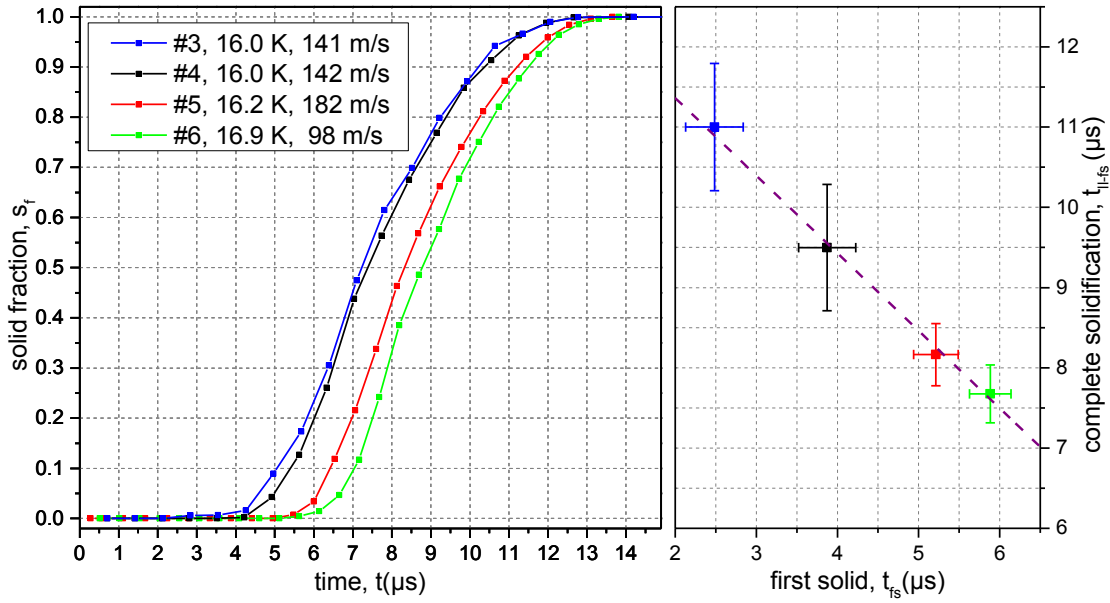
Figure 38: Left panel: Comparison of solid fractions with varying conditions. Right panel: Associated times for the duration of the solidification t_{ll-fs} vs. appearance of the first solid t_{fs}. The purple dashed line is a linear fit through the data points.

significantly, as e.g. after $7\,\mu s$ the green curve is at $s_f = 0.1$, whereas the black one already exceeds $s_f = 0.4$.

Considering the velocities v_0 of data #4, 5, 6 we find that there is no connection between it and the formation of the first solid, as the black curve with an intermediate value of v_0 solidifies much earlier than the red and green. The initial temperature, although correlated (higher `temp2` → later times), does not account for the later freezing times either. This is evidenced by the temperature gradients discussed in the previous chapter, in which the temperature plot of the outer layer does not depend on the starting value T_0 and all data overlap very well.

As already concluded, disturbances and deviations from a perfectly cylindrical filament, pictured in fig.33 on p.33, are the most likely candidate to initiate the formation of the solid and therefore determine the differences in the absolute time of the solid fractions. However, all solid fractions displayed in the left panel of fig.38 have a similar shape. This is evidenced by the the fitting parameter for the exponent in the Avrami equation yielding $n = 1.8 - 2.0$ for all four plots (see table 4), indicating the same, two-dimensional growth with formation of critical embryos only in the beginning. Therefore we conclude that disturbances and deviations from an ideal cylindrical shape can change the start of the solid fraction significantly, yet there is no severe impact on the overall growth process.

However, there is an interesting indirect influence of the time when the first solid starts t_{fs} onto the overall crystallization time t_{ll-fs}, which is plotted in the right panel of fig.38. The times for the first solid t_{fs} and last liquid t_{ll}, respectively, are extracted by looking directly for these events in subsequent spectra, taking their mean as well as standard derivative for error bars.

At first just looking at the horizontal axis, we again come across the big difference in

the starting time, which, this time with numbers, happens roughly 50% later for data #6 (green) with respect to #4 (black). Yet, if we now take into account the vertical axis, we find that for the earlier freezing time, on the other hand the time until the solidification process is finished is longer. For all data points shown, a shorter time for nucleation is connected with a longer solidification time, which can be fitted linearly, illustrated as the purple dashed line. Even more, this correlation is almost diagonal, which means, for each µs earlier freezing, the complete solidification process is one µs prolonged. In other words, regardless of the starting time t_{fs}, the time for the last liquid t_{ll} is almost equal in all cases, which can also be seen by all four solid fraction curves converging shortly before $s_f = 1$ in the left panel. A later solid does not simply shift the solid fraction curve, but shortens its overall duration.

data	n	k	t_0
#3	2.0 ± 0.1	0.05 ± 0.01	3.7 ± 0.2
#4	1.9 ± 0.1	0.08 ± 0.02	4.2 ± 0.2
#5	1.8 ± 0.1	0.09 ± 0.01	5.3 ± 0.1
#6	1.8 ± 0.1	0.10 ± 0.02	5.9 ± 0.1

Table 4: Results of the Avrami fits to the whole data range.

Since the overall growth behaviour of the solid fraction curves is similar (the same exponent n of the Avrami fit within error bars), the influence on the solidification time must lie within the fit parameter k, which contains the crystal growth velocity u and the nucleation rate I. Indeed, this parameter k increases from 0.05 to 0.10 the later the solid starts to appear (compare table 4).

The interpretation for this behaviour grounds in different temperatures of the liquid phase. We have noticed in the previous chapter that filaments which start to crystallize later reach lower temperatures in all three considered curves of the temperature gradient (compare fig.32 on p.81). We know from nucleation theory and the kinetic model that lower temperatures are connected with higher nucleation rates I as well as higher growth velocities u. Indeed, the growth rate roughly extracted from data #6 with $u = \frac{r}{t_{ll-fs}}$ (filament radius r is unchanged) is more than 20% greater than for the previously discussed data #4.

In a single sentence, the shorter total crystallization time for later freezing filaments is explained by a higher crystal growth velocity u based on the overall lower temperature of the filament, which previously has had more time to cool[3]. It is still surprising that all solidification curves end at the same time t_{ll}, the consequence of the diagonal purple fit in the right panel. Yet, this is probably a coincidence based on the later start of the solid t_{fs} being adequately compensated by the faster growth rates u.

Up to now data #3 has been neglected. The associated blue solid fraction curve in fig.38 looks similar to the black one and the source conditions T_0 and P_0 are identical, too (compare table 3 on p.68). However, the right panel of the figure reveals that the first solid is visible about 1.5 µs earlier.

---

3 The nucleation rate being higher at lower temperatures probably also plays a role, but because it is only relevant in the very beginning of the process, it has less influence.
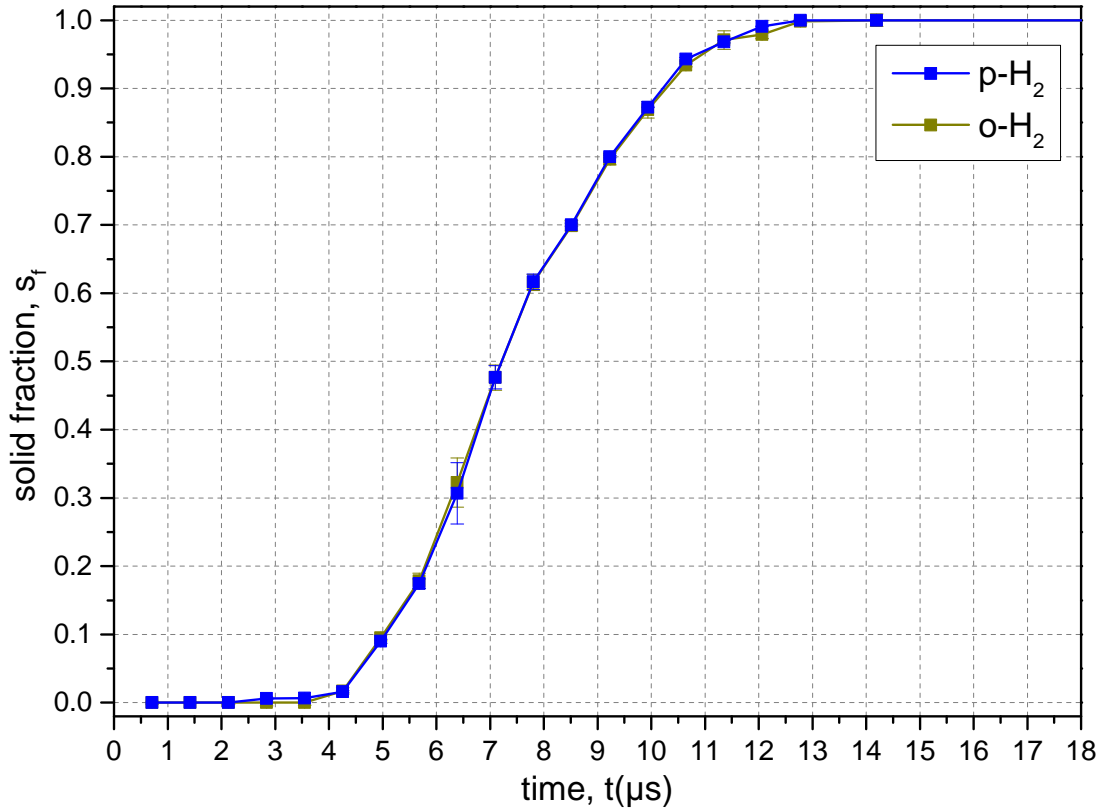
Figure 39: Solid fraction of p-H$_2$ and o-H$_2$ extracted from data #3 with ≈ 3 times increased ortho-hydrogen content with respect to all other data shown in fig.38.

The reason for this could be related to the fact that data #3 exhibits ≈ 3 times more ortho-hydrogen, which is estimated from the ratio of intensities of the corresponding total (liquid + solid) vibrational bands of the isotopes. This higher $J = 1$ content originates from a slightly different setup, in which P_0 was controlled with a pressure regulator instead of being regulated by the flow controllers (see chapter 3.2.1). The effect of lower o-H$_2$ ratios was actually detected on the following day with data #4 and all subsequent measurements have a similarly low o-H$_2$ mole fraction.

In fig.39 the solid fractions extracted from the p-H$_2$ and o-H$_2$ vibrational bands are presented, whereas the solid fraction for o-H$_2$ again is extracted by the maxvalue method described later in chapter 5.1.2.1. In the whole data range both curves are basically equal within error bars. Hence, there is no indication that the $J = 1$ component has a higher tendency to join the solid phase.

However, the increased amount of o-H$_2$ could indeed be responsible for the earlier nucleation of this data #3 compared to all other data. The physical origin is that the $J = 1$ isotopic species interacts stronger with both other $J = 1$ as well as $J = 0$ molecules due to its electric quadrupole moment [29] and by this could lower the energy barrier towards critical nucleation embryos. Unfortunately, our data is not sensitive enough to unambiguously prove the initiation of the solid through $J = 1$ impurities let alone its extent and details of the microscopic growth mechanism.

Nonetheless, the amount of $J = 1$ does not seem to have a paramount influence on the crystal growth, which is also evidenced in a later chapter A.1.

4.1.3.6 Comparison: Nozzle diameter

In this part, we compare different nozzles, particularly focusing in the changes related to the nozzle diameter d_0. For a systematical approach, we again start to compare data #5 and #8 with nozzle diameters $5.3\,\mu m$ and $4.0\,\mu m$, whose solid fractions in red and purple, respectively, are plotted in fig.40. The corresponding temperature gradients were discussed in fig.29 on p.77.

The solid fraction for the $4.0\,\mu m$ nozzle obviously starts to increase earlier. With ideal conditions (no disturbances/unknowns), we would predict this to happen, because there should be slightly smaller temperatures on the surface based on a lower surface to volume ratio resulting in a temperature gradient with overall lower values. In other words, the interior is cooled down faster and their needs to be less negative heat conducted to the interior.
Indeed, in section 4.1.1.4 we have seen that the curves of the mean and highest temperatures are below that of the bigger nozzle, whereas the lowest temperature curve is too similar to detect significant differences. However, as discussed previously the initiation of the solid is influenced by a number of unknown parameters depending on the particular nozzle and conditions, which could alter the start of nucleation. The data for the smaller nozzle was recorded in the first phase of measurement campaigns and has a factor of 2 higher ortho content, which might also have an impact on the formation of the first nucleation embryos.

Another feature of the plot is the more rapid total solidification process of the smaller nozzle, which lasts $t_{ll-fs}^{4.0\mu m} = 6.0\,\mu s$ in comparison to $t_{ll-fs}^{5.3\mu m} = 8.2\,\mu s$. This is expected, because the solidification front has less distance to travel in a smaller filament.
According to fig.29 on p.77 for the smaller nozzle the mean temperature of the liquid is lower prior to solidification. Hence, based on the kinetic model, the growth velocity should be higher as we have seen in the previous section. Estimating the growth rates with $u = \frac{r}{t_{ll-fs}}$ yields almost identical values with $u^{4.0\mu m} = 0.33 \pm 0.03\,m/s$ $u^{5.3\mu m} = 0.32 \pm 0.03\,m/s$, yet the error bars still allow for a higher growth rate of the smaller nozzle. Support for this statement is provided by the fit parameter k (fig.40), which is double the value for the smaller nozzle, indicating that the growth velocity and/or the nucleation rate is higher. As expected, the growth process seems to be similar indicated by a comparable fit exponent $n = 1.8 - 1.9$.
We conclude that solidification processes of filaments from different sized nozzles exhibit an overall congruent behaviour, even though the start of the solid fraction may vary.

4.1.3.7 Droplet beam

This section governs the solidification of the liquid beam produced by nozzle XVII-01 with $d_0 = 1.9\,\mu m$, for which the temperature gradient was discussed in chapter 4.1.1.5. As stated, the liquid beam probed probably resembles a more diffuse spray of droplets
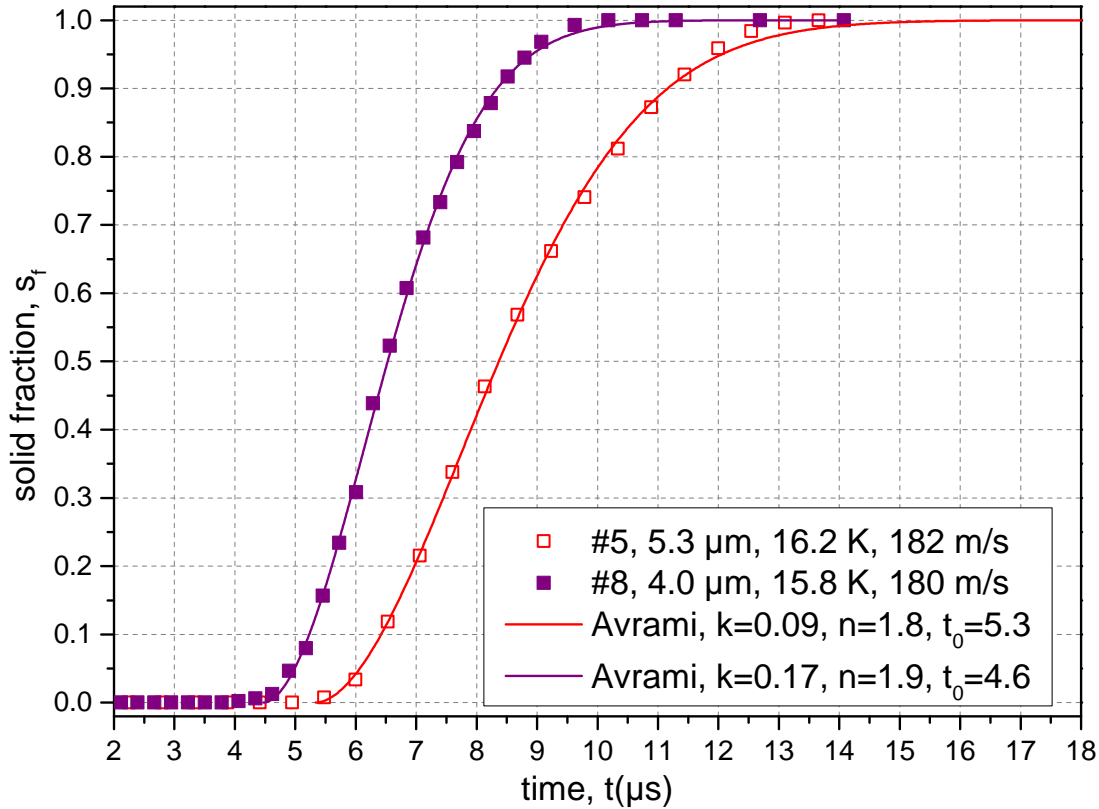
Figure 40: Solid fraction comparison of two different nozzle diameters extracted from data #5 and #8 and the corresponding Avrami fits over the whole data range.

rather than a neat Rayleigh droplet beam, based on the huge deviations to the simulated temperature gradient.

The solid fraction for the measurement is plotted in fig.41 together with the temperature gradient associated with the scale on the right hand side. A remarkable feature is that the first solid in the spectra already is detected after $t_{fs} = 0.26\,\mu s$, which is 1/15 of the previous values. However, in contrast to all previous data, the solid fraction does not increase sharply but rather gradually to $s_f = 0.02$ at $t = 0.65\,\mu s$, after which it finally resembles the well-known Avrami shape. This early first solid with a delayed start for the complete solidification can be interpreted as already independent droplets of different sizes. Small droplets cool faster due to their high surface to volume ratio and therefore start to freeze and completely solidify earlier than bigger ones. But they may exhibit only a small fraction of the total mass exiting the nozzle, hence their contribution to the total Raman signal remains small. On the other hand, bigger droplets start to freeze later and determine the curvature of the solid fraction plot based on their high fraction of the total mass. This solid fraction data therefore is an overlay of many individual solid fractions from droplets of different sizes.

This interpretation suggests that at least a partial breakup of the liquid beam into droplets happens early, $< 75\,\mu m$, because solidification would prevent it, which is further support for cavitation induced breakup. The time for complete solidification is extracted to $t_{ll-fs} = 2.16\,\mu s$, which is an upper limit, because it is constituted of
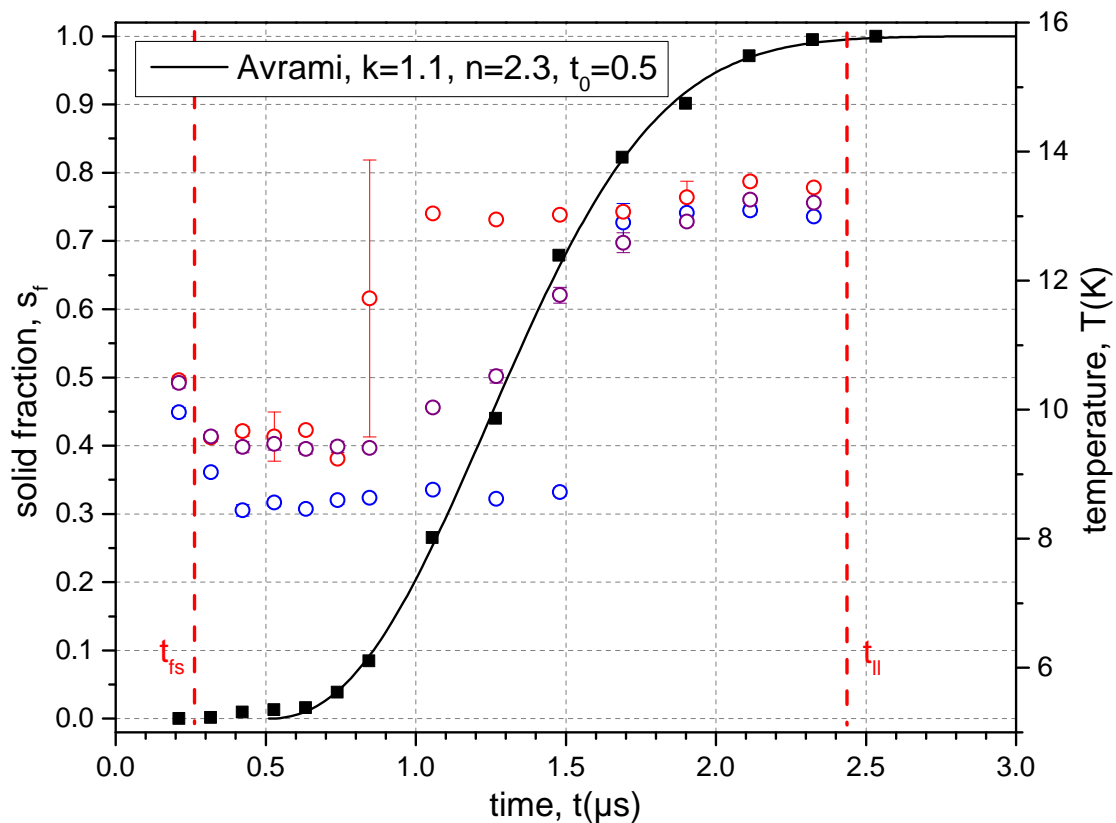
Figure 41: Solid fraction (left scale) and temperature gradient (right scale) of nozzle XVII-01 with $d_0 = 1.9\,\mu m$, producing a spray of droplets. The Avrami fit to the whole data range is shown as a solid black line, red dashed lines mark the time of the first solid t_{fs} and last liquid t_{ll}, respectively.

droplets of different sizes, whose initial solidification probably differs depending on their size as described above. Still it is a factor of 3.5 faster than any previous measurement. An estimation of the growth rate u does not make sense, since we do not know the size of droplets.

More information is revealed by the Avrami fit, shown as the solid black line. The fit parameter $n = 2.3 \pm 0.2$ indicates that the growth details are different. Indeed, for droplets in shape of a perfect sphere we expect a three-dimensional growth from the surface to the core, yielding $n = 3$. However, the droplets within our spray probably deviate from a perfect sphere due to the recent breakup and the resulting surface oscillations, which was also seen in droplet experiments of water in our group. Additionally, the overlay of solid fractions from droplets of different sizes makes the fit more prone to errors, because varying starting times for solidification t_{fs} stretch the solidification curve.

4.1.4 Summary: Solid fraction

The solid fraction represents, to which degree the filament is solidified at a particular distance z or time t, respectively, after exiting the nozzle. Although the appearance of the first solid and, connected with it, the solid fraction at a particular position probably vary on time scales of μs, Raman spectra average over many volumes due the long recording times in the order of seconds and therefore yield very small statistical errors for all measurements of pure p-H_2.

We propose an isotropic, two-dimensional crystal growth model, in which the filament is reduced to its cross section. We assume that nucleation events are distributed homogeneously and only on the surface, where the lowest temperatures prevail, so that the liquid-solid-interface proceeds towards the core isotropically. This model is supported by fitting the solid fraction curve with the Avrami equation, which yields an exponent $n \approx 2$, suggesting nucleation embryos to appear only in the beginning as well as 2 growth dimension.

Assuming a constant average temperature of $T = 12.5\,K$ across the filament, we extract a mean growth velocity of $u \approx 0.28\,m/s$ by dividing the radius of the filament by the time for complete solidification. This value is much smaller than the filament velocity $v_0 \approx 100\,m/s$ and supports the view that two-dimensional slices of the filament are independent from preceding ones in the view of crystal growth. The order of magnitude for u endorses the kinetic model as the main valid growth mechanism for supercooled para-hydrogen, because the diffusive model alone delivers values that are too small and can be excluded.

Comparing data recorded under different conditions with the same nozzle reveals that, though the appearance of the first solid may vary significantly, the shape of the solid fraction curve does not change. Filaments which start to freeze later exhibit a shorter total solidification time. This can be understood in terms of deeper coolings of the liquid resulting in higher growth velocities of the solid according to the kinetic model. Filaments with a smaller diameter d_0 start to solidify earlier based on their lower temperature and yield similar results for the growth velocity u. The individual solid fraction curves for o-H_2 and p-H_2 are equal for all measurements, signaling no different behaviour during crystal growth.

4.1.5 Miscellaneous

4.1.5.1 Temperature of the solid

The position of the solid band of both vibrational $Q_1(0)$ and $Q_1(1)$ transitions also depends on temperature or, more precisely, number density.

In contrast to the liquid band the FWHM is close to the spectral resolution rather than a broad distribution. Hence, no temperature gradient can be extracted. However, a small shift of both lines towards lower wavenumbers is noticeable in fig.24 on p.69, which is illustrated more clearly in fig.42 for p-H_2 in the upper and o-H_2 in the lower half for data #4. Both curves start at their highest value and strictly decrease, yet seem to approximate a limit value in the end towards the last point measured at

$z = 5000\,\mu m \Leftrightarrow 35\,\mu s$. Likewise to the liquid band lower wavenumbers are associated with lower temperatures based on the increase of density.

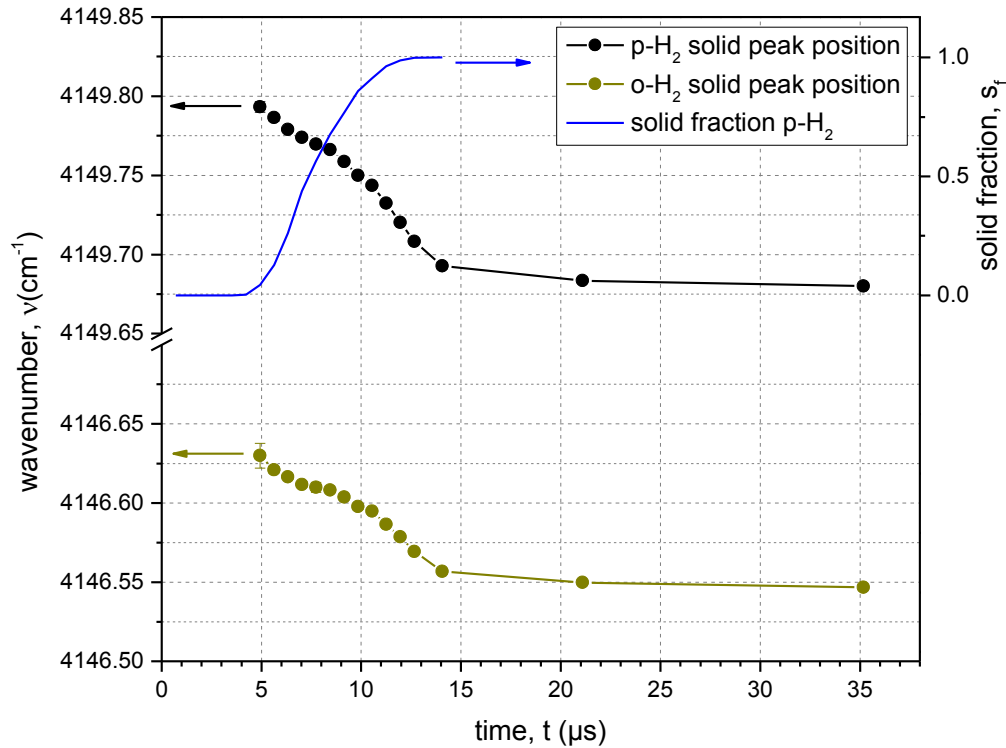**Figure 42:** Left scale: Mean wavenumber of the solid peak of p-H$_2$ (black) and o-H$_2$ (olive) of data #4 with y-axis break for detailed view. Upper right scale: Solid fraction of p-H$_2$ (blue).

Vilesov states in his paper [30] that the same correlation wavenumber $\leftrightarrow$ temperature applies to their p-H$_2$ data for both the liquid and the solid when the respective density is used. However, taking into account that their same error bars apply to the solid, the temperature values are even more questionable because the shift of the solid takes place in a much smaller wavenumber interval and is therefore even more prone to errors. If we use the original parameters from the paper, the position of the solid band corresponds to temperatures in the beginning of 13.5 K decreasing to 9.4 K at the last measured point. In view of the large error bars of the formula, these values are surprisingly physically reasonable, since they are below the melting line, which of course is necessary for the stability of the solid.

The fact that the highest temperatures appear in the beginning probably is grounded on the heat released during solidification. We have seen that this heat affects the adjacent liquid (section 4.1.1.1), yet the solid is likely to take part of the energy, too. Therefore the initial temperature of the first solid could very well be higher than the coldest temperature of the liquid (≈ 9.5 K) reached. The subsequent decrease in temperature of the solid is based on two effects, likewise to the increase in temperature of the liquid discussed previously. For one, the solid at the surface also exhibits a vapor pressure and therefore experiences cooling through evaporation, which is the main reason of the decrease in total wavenumber. On top of that, only the solid close to the solid-liquid-interface experiences the heat of solidification, yet its fraction decreases

because the total volume of the solid increases according to the solid fraction plotted in blue. This again is a statistical effect based on the increasing number of molecules considered.

After the solidification is complete, the temperature drop becomes more gradual and approaches a value that corresponds to the limit temperature of evaporative cooling for the solid. Interestingly, the Vilesov formula with the original parameters yields $\approx 9\,\mathrm{K}$, which is reasonable. On the other hand, with the changed parameters from chapter 4.1.1.2 for the liquid phase, the formula does not yield any values at all as the input is out of the definition interval.

All other data for pure p-H_2 present a very similar behaviour for the position of the solid peak and no further information can be drawn. The only noteworthy change can be seen in data with a significantly higher amount of o-H_2, like in data #3. Based on the interactions of vibrons originating from the same species, a higher mole fraction of an isomer decreases its excitation energy (see chapter 2.3.2). Hence, the complete o-H_2 band is shifted slightly towards higher wavenumbers, whereas p-H_2 is moved in the opposite direction. This effect is tiny with $< 0.05\,\mathrm{cm}^{-1}$, yet visible in this analysis due to the small absolute shift of the solid cooling.

4.1.5.2 o–H_2 – p–H_2 intensity ratio

In this section we analyze the ratio of Raman intensities of the two isomeric species. Additionally, the ortho-hydrogen content presented in table 3 on p.68 is determined.

In the theory chapter 2.3.2 regarding Raman-effects in condensed hydrogen, it was stated that the intensity of the vibrational o-H_2 bands is enhanced with respect to p-H_2 due to resonance effects based on the slightly lower excitation energy of the former. The enhancement factor ξ, defined in eq.2.11 on p.19, depends on several parameters like energy difference of the excitations [34], density and mole fraction of the constituents [31]. Therefore changes of the intensity ratio in our data yield information about the state of the condensed phases.

In fig.43 the ratio of total intensities of the o-H_2 to p-H_2 bands, i.e. the integral over o-H_2 divided by the integral over p-H_2, is plotted for data #3 as red diamonds. As an orientation of the current state of the filament, the solid fraction is plotted as a black solid line with its scale to the right hand side. Note that this is the data with a higher ortho-hydrogen content with respect to later data. We find that the ratio of intensities increases almost linearly in the pure liquid phase as well as in the growing solid up to about $8\,\mu s$. The rise then becomes more gradual and changes only slightly as soon as the solidification process is finished. At the last point, the intensity of the $Q_1(1)$ band associated with o-H_2 is $\approx 50\%$ stronger than in the beginning, so that the intensity gain is quite significant.

This strong increase in the relative intensity of o-H_2 is the reason, why the standard solid fraction defined in eq.4.2 on p.85 is not valid for the weak component, since the denominator in said formula is not constant. However, the influence on the strong p-H_2 solid fraction is negligible, because its total intensity during the transition from liquid to solid changes by less than 2%.

Our plot represents the enumerator in formula 2.11. The denominator stands for the actual ratio of o-H_2 to p-H_2 molecules, which at first we declare as unknown. In our
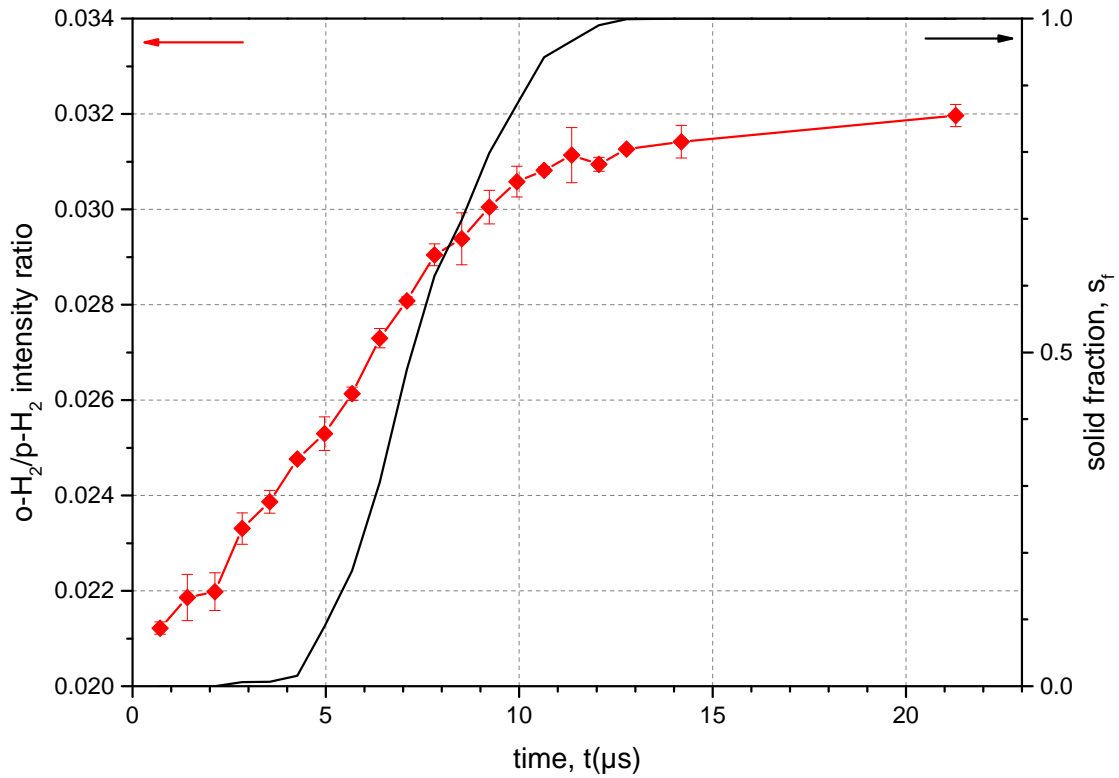
Figure 43: Ratio of the intensities of solid + liquid o-H_2 to solid + liquid p-H_2 of data #3 as red diamonds. The solid black line with the scale on the right side represents the p-H_2 solid fraction from chapter 4.1.3.5.

experiments the conversion from ortho- to para-hydrogen in the converter takes place in continuous flow and all conditions like pressures and temperatures are held constant throughout the measurements. Spectra taken for comparison before and after one series at the same distance z do no show vast discrepancies in the intensity ratio. Therefore we assume that the mole fraction of ortho-hydrogen and with it the denominator in eq.2.11 remains constant. Our plot then yields the changes in the enhancement factor ξ. Under this assumption, the initial increase of the curve is grounded in the cooling of the liquid. Previously we have discussed that lower temperatures in the condensed phases of hydrogen are associated with higher densities. On microscopic scales, this shorter distance between the molecules enables easier hopping of vibrons (see chapter 2.3.2) which emphasizes the intensity enhancement. Additionally, the energy difference in wavenumbers between the $Q_1(1)$ and $Q_1(0)$ liquid excitations becomes slightly smaller, which further increases the enhancement factor.

Yet, the cooling and increase in density of the liquid diminishes as soon as the first solid starts to appear and another effect is responsible for the ongoing increase in the plot. The solid both is denser and the energy difference of its excitations is smaller than in the liquid so that the enhancement factor is naturally higher as evidenced by measurements and calculations [34]. The further increase of the ratio for $t > 4\,\mu s$ is therefore based on the redistribution of molecules from the liquid into the solid state indicated by the solid fraction plot. It is rather a coincidence that the slope of the red curve does not change when fading from the first effect (cooling of the liquid) to the

second one (solidification)[4].

In the last stages of crystallization $t > 10\,\mu s$ the rise of the intensity ratio plot diminishes, because the increase in solid fraction and therefore in overall density becomes more gradual. The final ascent after complete solidification $t > 13\,\mu s$ is grounded in the temperature decrease of the solid discussed in the previous section, which is associated with only a minor increase in density.

The behaviour of the intensity plot presented in fig.43 is qualitatively similar in all other data for para-hydrogen listed in table 3, regardless of the actual ortho-hydrogen content. However, the lower the $o\text{-}H_2$ mol fraction is, the higher are the statistical error bars due to worse signal-to-noise ratio. Furthermore systematical errors begin to emerge because tails of the $p\text{-}H_2$ band distort the background of the small ortho-hydrogen excitations.

To determine the actual mole fraction of ortho-molecules listed in table 3, we solve eq.2.11 for the denominator. For the enhancement factor we choose the value $\xi = 3.4$ extracted from theory [34] and in agreement with measurements [35] at $T = 2\,K$. We use our measured value of the intensity ratio at the last data point, which corresponds to the pure solid at $\approx 8\,K$. Although our temperature is higher, the enhancement factor ξ remains roughly the same, since the temperature dependency of the density in the solid phase is not sensitive. Inserting both values finally delivers the approximate $o\text{-}H_2$ mole fraction for the series.

There is also the possibility to check the conversion rate apart from experiments by filling the vacuum chamber with a few $mbar$ of converted hydrogen gas. However, the method above has the benefit of yielding in-situ values and therefore accounts for possible back-conversion rates, which evidently were detected.

---

4 It has been tried to distinguish between these two effects by plotting the isomer intensity ratio of the liquid and solid bands separately. However, the initial solid and the diminishing liquid of ortho-hydrogen yield only small intensities, what significantly enhances errors.

4.2 Rotational region

This chapter governs the rotational excitation of para-hydrogen $S_0(0)$ and is divided into two main parts. The first is a qualitative analysis in section 4.2.1, which focuses on the overall behaviour of the solidification process (subsection 4.2.1.1), the structure of the solid and its interpretation (subsection 4.2.1.1) as well as comparisons between different source conditions (subsection 4.2.1.2). In the second part, details of these features are approached quantitatively with measures of intensities or peak areas, respectively (subsection 4.2.2.1).

A representative Raman series from data #3 is presented in fig.44 with its evolution along the filament axis z in color code from red to blue. Again, each spectrum consists of $3-4$ single spectra that are averaged, the error bars being within line width.
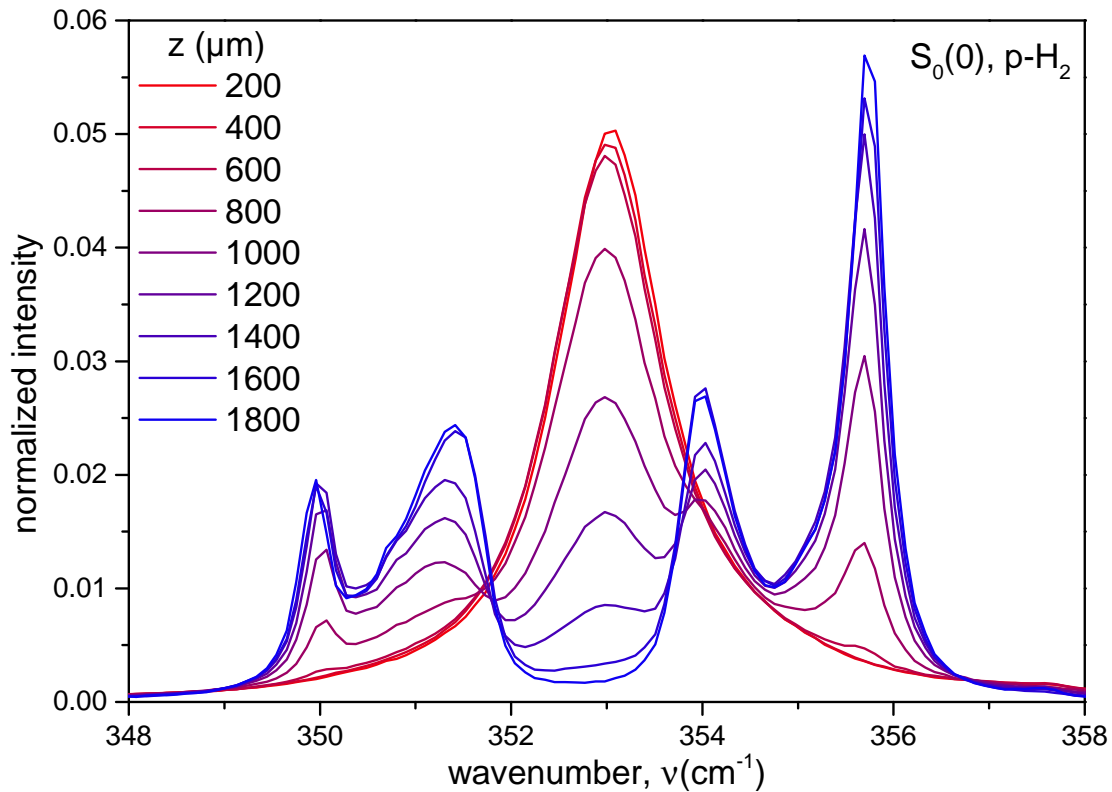
Figure 44: Evolution of the rotational excitation $S_0(0)$ of p-H_2 along the filament axis z in color code from red to blue with steps $\Delta z = 200\,\mu m$.

In the beginning, the $S_0(0)$ band exhibits a broad distribution centered around $353\,cm^{-1}$, which roughly resembles a symmetric Lorentz shape with tails extending to both sides. This shape is typical for the liquid phase and has been observed for para-hydrogen before [36]. It is based on the arbitrary environment of excited molecules in the liquid, due to which the roton energy varies.

With increasing distance z from the nozzle, this liquid band slightly shifts towards lower wavenumbers and becomes broader, visible by the shrinking of the maximal intensity, since the integral over the signal is normalized to 1. This is connected to the increasing

density of the liquid based on cooling. A smaller distance between molecules enhances the intermolecular interaction so that the rotons can hop to adjacent molecules more easily, effectively lowering the mean excitation energy.

After $z = 600\,\mu m$ features start to appear, detectable at first in the tails of the Lorentz band at $350\,cm^{-1}$ and $355.8\,cm^{-1}$ and in later spectra also at $351\,cm^{-1}$ and $354\,cm^{-1}$. The further the distance to the nozzle z, the more intensity is redistributed into these 4 main peaks. This, of course, represents the transition to the solid phase. The position of the first solid as well as the development of the intensity of bands correlates very well with the solid fraction extracted from the vibrational excitation in chapter 4.1.3.5. In comparison to the initial broad liquid band of the $S_0(0)$ transition, these four bands associated with the solid phase exhibit more the shape of a Gauss distribution based on their less extending tails. Additionally, all peaks except the very left one are rather asymmetric, indicating that there is more structure lying beneath.

Note that the alternative excitation of ortho-hydrogen, $S_0(1)$, is far off at $\approx 590\,cm^{-1}$ and too small to be detected, because there is no enhancement of this band involved (see chapter 2.3.2).

4.2.1 Qualitative analysis

The qualitative analysis focuses on the more general, obvious features retrieved from our data. The interpretation is based on the visual evaluation of spectra, so that we obtain information about the static properties.

4.2.1.1 Structure of the solid

In this section we discuss the origin of the band structure of the solid phase. The spectrum at $z = 1800\,\mu m$ associated with complete solidification is plotted separately in the left part of fig.45 with the main peaks enumerated from left to right for easier reference.

To recap, in the literature bulk liquid para-hydrogen is always found to freeze into an hcp crystal structure when cooled below the melting point at equilibrium conditions (see theory chapter 2.3.2). This hcp structure appears in Raman spectra as 3 lines separated by $\approx 2cm^{-1}$ as pictured in fig.6 on p.20. The experimental positions of these hcp lines are marked by black dotted lines in fig.45. Disregarding the discrepancies at first, our main peaks (2), (3) and (4) can be identified to belong to an hcp lattice. However, peak (1) on the very left remains unassigned and so our band structure is not explicable by an hcp crystal lattice alone.

Besides hcp, the closest alternative structure for dense packing is the fcc lattice, each illustrated in the right part of fig.45. Both consist of stacked planar layers, the only difference being the stacking order. Whereas for hcp the orientation of layers a and b alternates, in the fcc lattice the third layer c is shifted with respect to layer a.

It is possible to calculate the rotational Raman excitation bands for an fcc lattice for para-hydrogen [25], which yields two bands marked as red dotted lines in the spectrum of fig.45. Peak (1) corresponds very well to the up to now unassigned lower energy band, while the high energy fcc excitation is close to the hcp $m = 0$ line and probably

constitutes to peak (4). Hence, the rotational spectrum reveals that our supercooled liquid freezes into a crystal structure constituted of both hcp and fcc contributions.
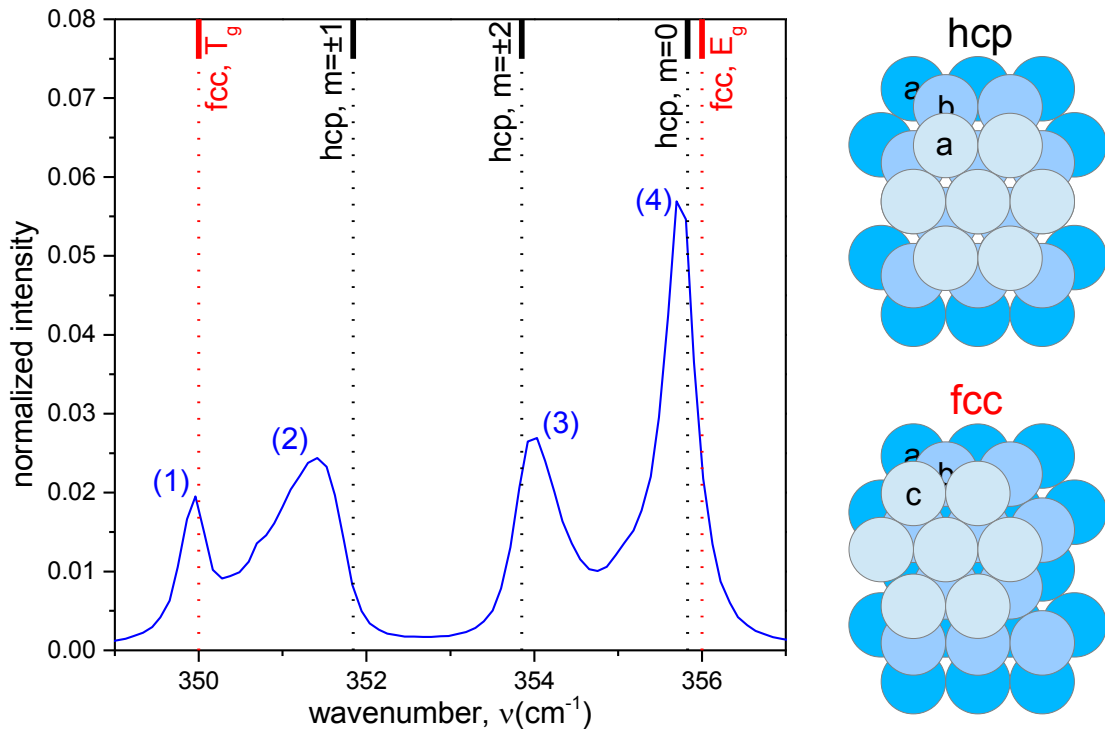

Figure 45: Left: $S_0(0)$ spectrum of data #3 at $z = 1800\,\mu m$ after complete solidification with enumerated main peaks. Black and red dotted lines mark the position of the experimental hcp [36] and theoretical fcc [25] line positions and notations, respectively. Right: Illustration of the hcp and fcc stacking.

In the literature, solid hydrogen has also been produced by the condensation of gas onto a cold surface below liquid helium temperatures $T < 4\,K$ [74, 75], in contrast to the transition from liquid to solid that we utilize here. In those experiments a similar band structure to our data has been observed, consisting of coexisting hcp and fcc lines. Furthermore, expansion of gaseous mixtures of helium and para-hydrogen also lead to rapidly cooled condensed mixed crystals of fcc and hcp [76].

Silvera points out that the static energies for the theoretical hcp and fcc lattices for para-hydrogen are quite similar and may change with temperature [27, p.428]. Based on the appearance of fcc in the gas condensing measurements, he suggests that at temperatures far below the melting temperature $T_m = 13.8\,K$ the fcc structure may be the more stable one, in contrast to hcp being energetically favorable close to the melting point.

With regard to the gas condensing experiments and the melting point, in our experiments we observe intermediate temperatures around $8 - 10\,K$ of the liquid prior to solidification. Hence, following Silvera's proposal, the energy of the two lattice structures may be more similar under these conditions, in which case molecules would be able to stack in either hcp or fcc lattice structures, since both would be approximately (meta)stable configurations. The probability for stacking of local hcp of fcc lattices then is governed by the particular kinetic details of the involved molecules and appears arbitrary from a macroscopic view point. The resulting crystal is a random hcp (rhcp)

polymorph consisting of arbitrarily arranged sub-lattices of hcp and fcc [77].
Support for this idea of rhcp structures can be found within our spectra. Whereas in a pure hcp crystal of p-H_2 the three lines each are symmetric, we find strong asymmetries in the shape of our peaks. The shoulders, i.e. the flanks with increased intensities, are found only in between the hcp-fcc peaks and not e.g. in between the hcp peaks (2) and (3). Since rotons spread to several adjacent layers around the excitation center, these shoulders in the spectrum indicate that the surrounding of these probed regions deviates from a perfect hcp or fcc structure. Hence, the signal in between the main peaks probably comes from the borders of fcc-hcp facets or regions with lack of symmetry due to defects and alternating stacking order, i.e. rhcp.
Additionally, the deviations from the literature peak positions support the statement that this polycrystal probably consists of rather small crystallizes. The maxima of peaks (2)-(4) are all shifted towards the intermediate rhcp regions, so that the hcp peaks are not equidistant, which requires a large enough pure lattice for the rotons to travel. Similar asymmetric peaks including the intermediate shoulders are also observed in all condensed gas experiments featuring fcc.

However, we point out that there is a significant difference between experimental methods here. Whereas all previous measurements in the literature study a static crystalline phase that has stabilized, with our approach we directly observe the crystallization process, i.e. the dynamic transition that occurs on time scales orders of magnitude shorter. Due to this, not only static properties play a role, but also dynamic aspects related to kinetics and geometry at the point of the transition.
To be more specific, besides the total energy also e.g. the energy barrier towards those two crystal lattices may be relevant. The empirical Ostwald's rule of stages states that during crystallization metastable states may necessarily have to be achieved on the way to the final lattice structure [58]. Hence, our observed mixed lattices could be a temporary, metastable configuration that changes on longer time scales towards a final, stable form with a different arrangement. Metastability may even be more relevant in our case, because the thermodynamic conditions are far off equilibrium values due to the strong supercooling. Evidence for the validity of Ostwald's rule and a more detailed discussion will follow in the quantitative analysis in section 4.2.2.1.

4.2.1.2 Comparison: different source conditions

Likewise to the vibrational band, in this section we will compare data measured under different source conditions to reveal further insights. It is subdivided into three parts. The first one discusses effects of the ortho-hydrogen content, the second focuses onto the influence of the nozzle (diameter) and the third governs the difference between filaments and sprays.

Comparison: Ortho–hydrogen content

The rotational spectra that we have discussed so far are from measurement #3 with increased o-H_2 content (compare table 3 on p.68). In fig.46 we plot its rotational structure of the solid (blue) in comparison to data #4 (red) exhibiting $\approx$ 3 times less of the isomeric impurity. Both filaments are produced by the same nozzle at similar

source conditions and the presented spectra are recorded at an almost equal traveling distance or time, respectively.

Obviously, all main peaks are higher in the spectrum that contains less ortho-hydrogen. Since all spectra are normalized, the higher peaks are compensated by less intensity in their extending tails. Although the main peaks are sharper, the asymmetry and structure in between them is still maintained.
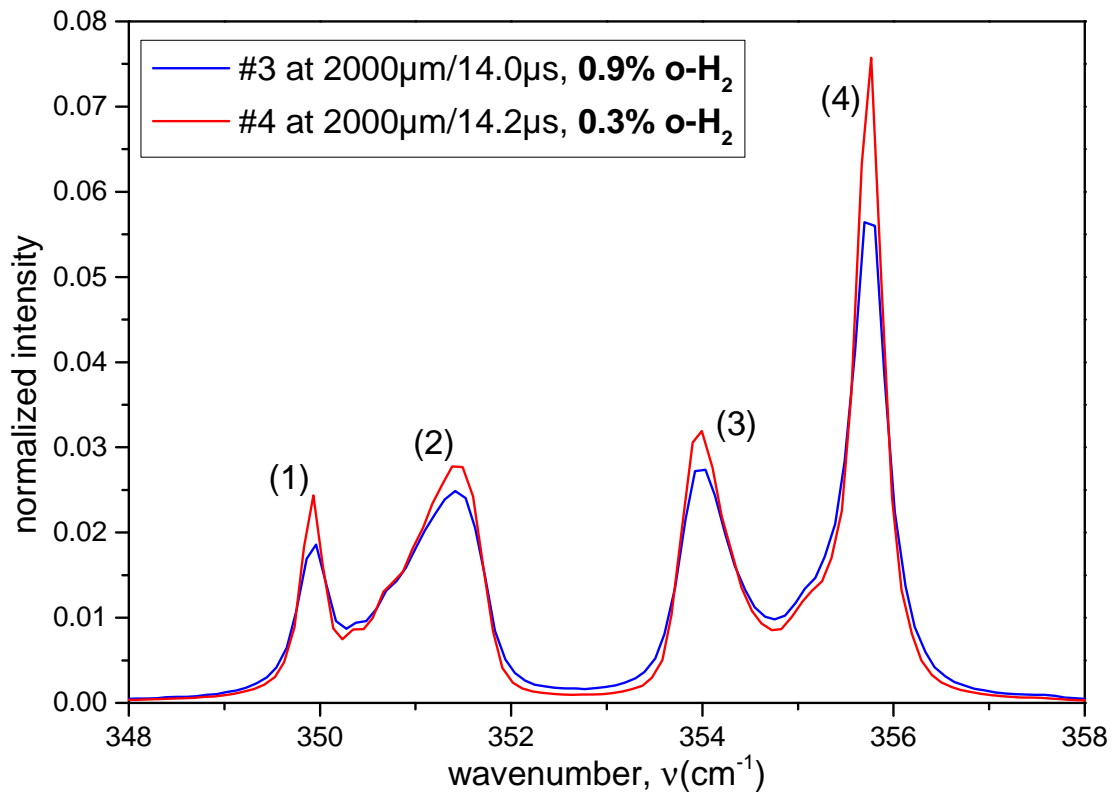

Figure 46: Comparison: o-H_2 content. Same nozzle, similar source conditions and evolution time, but high (blue) and low (red) mole fraction of ortho-hydrogen.

The effect of ortho-hydrogen as an impurity to para-hydrogen has been studied before in Raman scattering [78] and infrared spectroscopy [79]. Basically, o-H_2 molecules destroy the symmetry of the p-H_2 lattice and act as scattering centers for the traveling excitations of the latter. Rotons originating from p-H_2 are unable to hop onto their isomeric counterparts, because their excitation energy is far away at $\approx 590 \text{cm}^{-1}$. Increasing the amount of impurities leads to more varied environments of excited molecule, which effectively changes the energy of the rotons and in their summation makes the $S_0(0)$ bands diffuse. This effect has been observed in a pure hcp lattice, yet the same qualitative explanation holds for our mixed crystal. Most importantly, the asymmetric structure in between the main peak remains regardless of the amount of impurities. This supports the view from the previous section that its cause lies within the coexistence of fcc and hcp lattices rather than in the o-H_2 mol fraction.

Comparison: Nozzle diameter

Next, we analyze the effect of a smaller nozzle diameter. In fig.47 we compare our familiar data #3 produced by a 5.3 μm nozzle in blue with data #7 from the 4.0 μm one in green. Both spectra are chosen right after complete solidification and offer a similar o-H_2 impurity amount. Note that the data sets were recorded in different measurement campaigns so that the internal focusing lens and the positioning of the S-Notchfilter are different. This manifests in a worse signal-to-noise ratio for the earlier data #7 noticeable as the more rugged background.

Considering the main features, we find that peak (2) including its shoulder towards lower values contains more intensity than the comparative data #3. This is compensated by peaks (3) and (4) being lower, while (1) is more or less unchanged. Considering the maximum heights, for the small nozzle peak (2) surpasses (3), whereas the situation for the data of the bigger nozzle is vice versa.
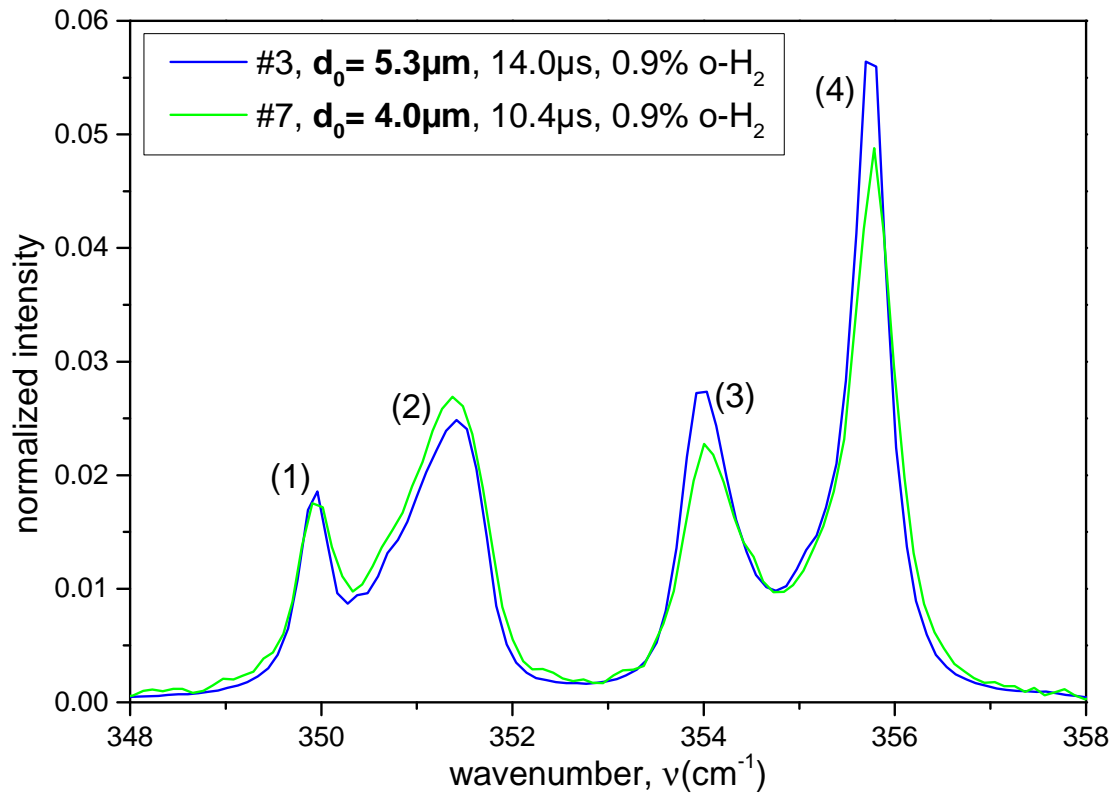
Figure 47: Comparison: Filament diameter. Big (blue) and small (green) nozzle with similar ortho-hydrogen content after complete solidification.

At first, this redistribution of intensities, especially between (2) and (3), is surprising, because both bands belong to the hcp lattice. However, from the literature we know that the intensities of the three hcp peaks depend on the orientation of the crystal [25, p.121]. In a randomly oriented polycrystal of pure hcp, the ratio of intensities from left to right is 2 : 2 : 1. This ratio changes, if the crystal exhibits a favored orientation, and depends on the angle of illumination and observation. We are unable to extract total values for this ratio from our spectra, since the overlap with fcc and the induced asymmetry make an explicit assignment of integral areas impossible. Yet, already this

change of intensities that we observe in the comparison in fig.47 casts doubt upon the assertion that our (poly-)crystals are completely randomly orientated.

Support for a preferential direction of the crystalline phase in our measurements is given by our growth model which we proposed in the vibrational section 4.1.3.2. We argued that the growth of the solid starts at the surface of the filament and, in the most simplified model, advances radially inwards in an isotropic way. With this assumption, we describe a preferred growth direction, which is likely to determine a favored orientation of the crystals based on the common alignment towards the center of the filament. Yet, since we probe the whole filament cross section at once, the projection of this rotationally symmetric geometry onto the spectrometer yields an averaged value. In the perfect, completely isotropic scenario, the summation over all solid growth vectors in the cross section view cancels out to zero, i.e. in the mean there would be no preferred direction.

However, if we take into account that due to e.g. cracks at the nozzle exit (compare section 4.1.1.6) there are regions on the filament surface that tend to initiate the crystal growth, it is likely that anisotropies occur. In this case, growth in a particular direction would be slightly more common. These anisotropies are specific to a nozzle or even a measurement and may determine preferred orientations for the crystal lattice. The different intensity ratio of the hcp lines that we see in the figure, therefore probably is based on the particular geometry of the crystal growth. Even with the long recording time of Raman spectra and the connected averaging, these preferential orientations seem to at least partially prevail.

Comparison: Droplet beam

At last, we take a look at the $2\,\mu m$ nozzle, which produces a spray rather than a filament. Fig.48 shows a $S_0(0)$ spectrum of this data #9 (orange) after complete solidification at $4.2\,\mu s$ compared to our standard spectrum.

Obviously, the distribution of intensities is moved out of the main peaks (2)-(4) mostly into the intermediate regions between (1) and (2) as well as (3) and (4), so that the asymmetric peak shapes are more pronounced. Additionally to their shrinking, the positions (in wavenumbers) of the maxima of peaks (2) and (3) are shifted apart from one another. Peak (1) is the only one that has slightly grown. Notice that the overall background is increased due to much less signal based on a) a smaller number of total molecules and b) the divergence of the spray.

Since a significant fraction of intensity has diminished from the main peaks (2)-(4), it is evident that fewer molecules are situated in an hcp lattice. Furthermore, these hcp-like lattices deviate more from an ideal, extended hcp lattice, visible by peaks (2) and (3) being shifted apart further towards the fcc peaks. We cannot distinguish between contributions of fcc and hcp within peak (4), yet the slightly growing stand-alone fcc peak (1) indicates that the amount of molecules in an fcc configuration is higher than in the comparative data #3. The increase in the intermediate regions signals that the amount of randomly stacked rhcp structures is significantly higher in the solidified spray data.

The most probable reason for both more fcc and rhcp is grounded in the lower temperature of the liquid prior to crystallization for data #8, which we have evidenced in fig.30 on p.79. In one of the previously mentioned gas condensing experiments [74]
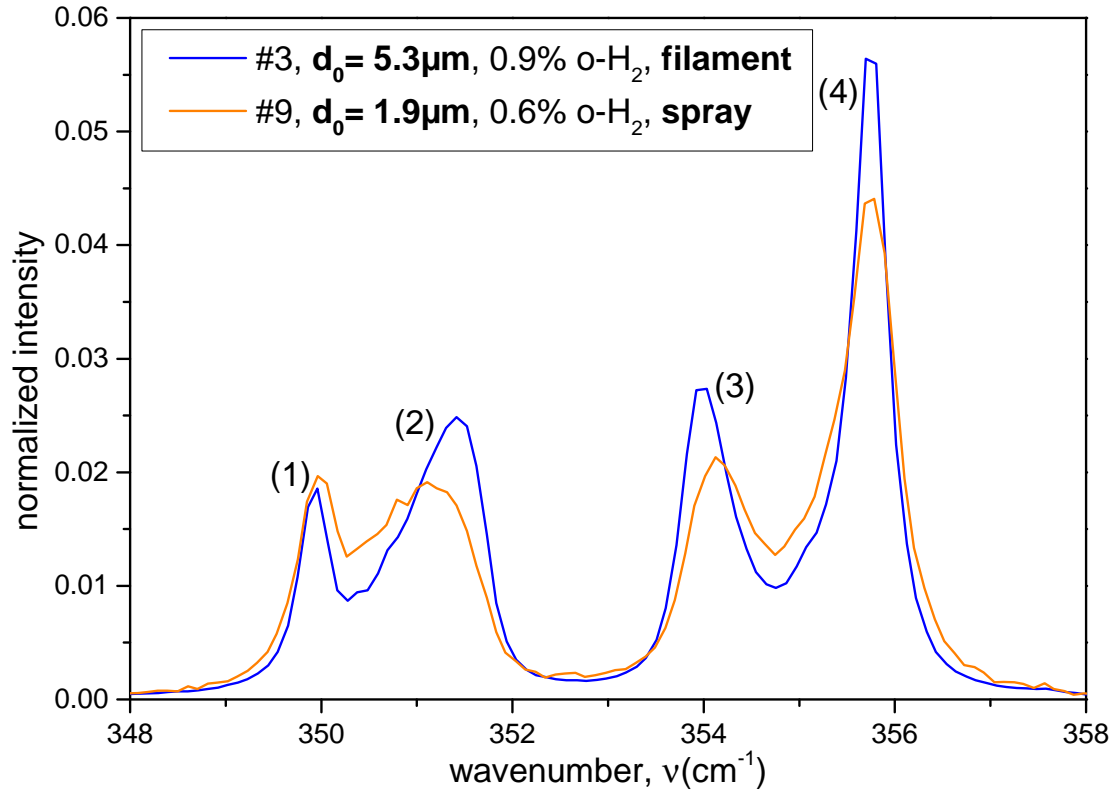
Figure 48: Comparison: Solidified spray (orange) vs frozen filament (blue).

it was found that by gradually heating up a sample containing a mixed fcc-hcp-rhcp structure similar to ours, the fcc peak (1) shrinks with increasing temperature. Hence on the other hand, lower temperatures seem to favor the existence of the fcc lattice, which is in agreement with Silvera's proposal that fcc should be more stable at lower temperatures.

Additionally, in that paper it was reported that para-hydrogen gas condensed onto colder surfaces leads to smaller crystallites. If this statement also applied in our case, a higher number of molecules would be situated in intermediate rhcp regions, which is congruent with what we observe for our measurement #8 featuring the lower temperature of the liquid. However, note that our crystal growth mechanism is different, originating from the liquid rather than the gas phase. Also the geometry of this spray with an unknown distribution of droplet sizes deviates significantly from the neat filament of the comparison data #3, which could further have an influence onto the preferences of the lattice structures that we observe.

4.2.2 Quantitative analysis

To extract additional information to the visual comparison of static spectra in the previous chapter, a quantitative analysis regarding the dynamics, i.e. the evolution of parameters, is done in this part. The core of this approach is reconstructing the rotational band structure for the complete transformation from liquid to solid pictured

in fig.44 on p.104 with a set of peak fit functions, which is done with routines in *Origin Pro* due to the number of single spectra involved.

For the fitting of a complete rotational spectrum, a set of 7 peak functions is used, 1 for the liquid band and 6 for the solid structure. An example fit is plotted in fig. 49, in which the liquid fit function is marked in orange as l1 and the solid peaks in green as s1 to s6. The blue solid line is the experimental data set, whereas the red solid line is computed as the sum of all 7 fitting peaks. The overlap between this reconstructed spectrum and the original one is similarly decent for all fitted spectra regardless of the progress of solidification.
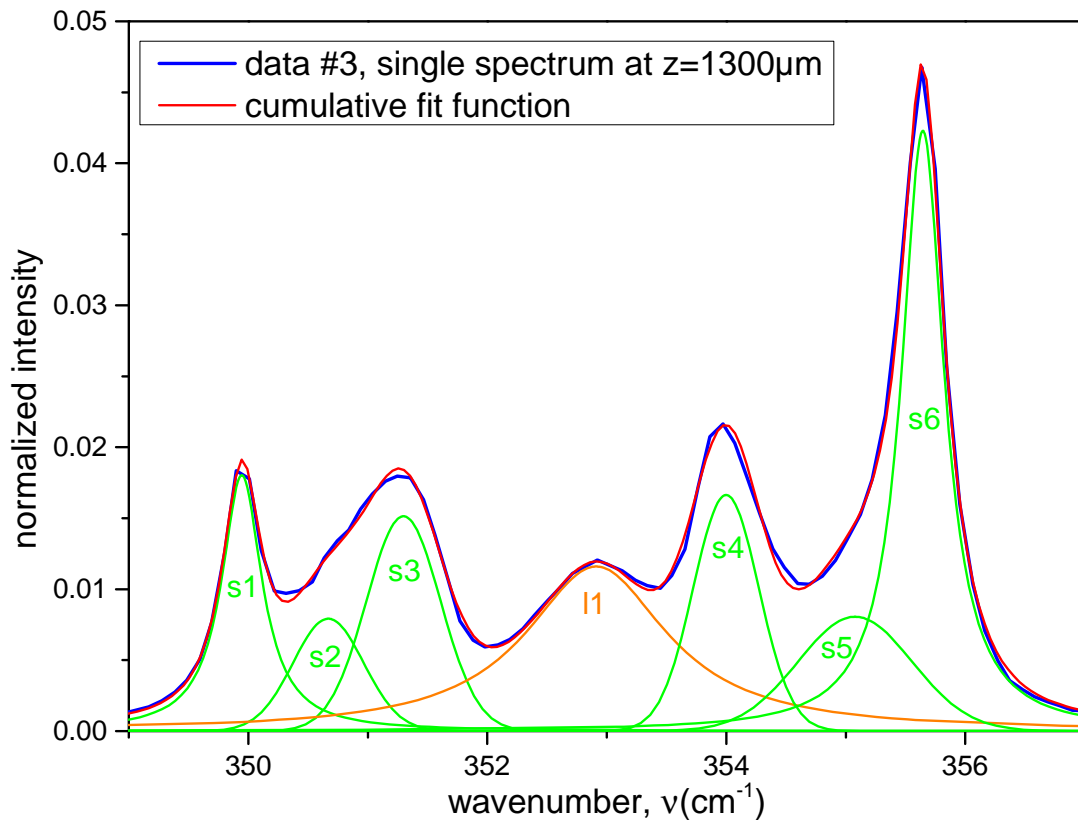
Figure 49: Exemplary fit to a single spectra of data #3 at $z = 1300\,\mu m$ as a blue solid line. The 6 fit peak functions for the solid are labeled as s1 to s6 in green and l1 represents the corresponding fit for the liquid in orange. The cumulative fit function is represented by the red solid line.

However, there are some important remarks on the fitting procedure. Up to now, there is no theoretical description available for the Raman band structure of the rhcp mixed crystal in between the fcc and hcp peaks. Therefore the fit peaks s2 and s5 do not represent real physical quantities but are merely introduced to allow for the good resemblance of the original spectra.

After trying different functions and conditions, both those auxiliary fit peaks are chosen to have a Gauss shape with their parameters having following restrictions. For one, their width is not allowed to exceed a certain value, which is necessary for all solid peaks, because their low intensities in the beginning of the solidification process would

broaden them to unrealistic values otherwise. Furthermore, the maximum area of *s2* is limited to a fraction (50%) of the adjacent peak *s3*, the same being valid for *s5* with respect to *s6* (30%). This constraint keeps the auxiliary peaks from growing beyond their neighboring main peaks.

The liquid fit *l1* is in shape of a Lorentz curve, which is in accordance with theory. Peaks *s2-s5* are chosen as Gauss functions, in agreement with the known hcp line shape. However peaks *s1* and *s6* are fitted with Lorentz peaks to account for their extending tails to lower and higher wavenumbers, respectively, which probably are rooted in the increased o-H_2 content of 0.9%. This attribution of peak shapes for the solid is rather inconsequent, but resembles the spectrum in the cumulative form best.

All above restrictions can be criticized to be arbitrary and introduce systematical errors just for the sake of resembling the measured spectra well. Therefore special care has to be taken, when the changes in the extracted parameters are discussed and interpreted. This is particularly valid in the first stages of solidification, when the peaks *s1-s6* are small, in part severely overlapping with the liquid peak *l1* (compare fig.44) and often at their limiting parameter values, which may yield significant systematical errors.

4.2.2.1 Evolution of the fcc–hcp ratio

An interesting question which can be approached within this quantitative analysis is the evolution of the hcp and fcc phases. Referring to the previous fig.49, for this we use the ratio of areas of fitting peaks associated with hcp and fcc, respectively. We are not able to state absolute contents for the phases, because we do not know how a) the individual contributions of the two lattices to fitting peak *s6* are and b) the auxiliary peaks *s2* and *s5* are to be assigned. Yet, we are able to observe the change in the area ratios of the peaks associated with the lattices, which yields information about their dynamics.

We construct two variants, VAR1 and VAR2, to observe the fcc-hcp ratio. For both these ratios, the enumerator is occupied solely by the area A_{s1} of fitting peak *s1*, which corresponds to a clean fcc peak (compare fig.49), while the difference between them is set into their denominator:

$$\text{VAR1} = \frac{A_{s1}}{A_{s1} + A_{s2} + A_{s3}}; \text{VAR2} = \frac{A_{s1}}{A_{s1} + A_{s2} + A_{s3} + A_{s4} + A_{s5} + A_{s6}} \quad (4.6)$$

VAR1 is divided by the sum of the fit peak areas *s1-s3*. This ratio is chosen because all these peaks do not experience severe overlap with the liquid peak, so that the values are less prone to fitting errors in the beginning. On the other hand, VAR2 compares to the sum of areas of all solid peaks combined. This variant uses a similar definition as in the paper [74], which deals with condensed crystals and will be used in our interpretation later on. Additionally, this definition ensures to exclude effects based on intensity exchanges between hcp peaks as observed in the previous fig.47. Since only A_{s1} is in the enumerator, VAR1 and VAR2 increase, when higher amounts of fcc are present in subsequent spectra.

VAR1 and VAR2 extracted from data #3 are plotted in fig.50 as green and blue circles, respectively, whereas VAR2 is scaled by a factor of 3 for comparison since absolute values have no meaning. As usual, the error bars just present the standard derivatives

of the single spectra fits taken at the same measurement point z, rather than real uncertainties. For orientation, the solid fraction as a black solid line with the scale on the right as well as the time for the last liquid as a vertical red dashed line are illustrated.

For the very first data points up to $7\,\mu s$, an inconsistency between the two plots is detected, since VAR2 increases whereas VAR1 shows the opposite behaviour. As mentioned, systematical fitting errors are largest in the beginning due to the overlap with the large liquid peak $l1$, so that we choose to skip data points, which are associated with solid fractions $s_f < 30\%$. Thereafter, both ratios exhibit a similar trend, which is a continuous decrease by $\approx 20\%$ up to the point of complete solidification t_{ll} marked by the red dashed line. Beyond this point, both ratios show a slight tendency towards even lower values.
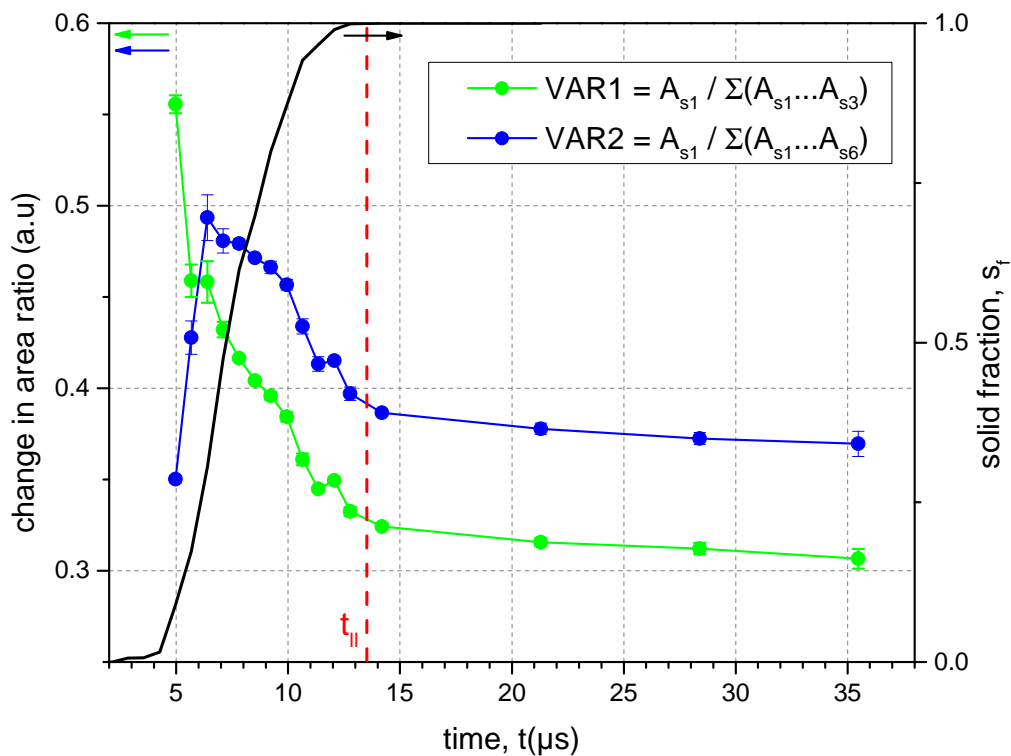
Figure 50: VAR1 and VAR2 (see text) as measures of change in the fcc-hcp ratio. The black solid line corresponds to the solid fraction with its scale to the right. The vertical red dashed line marks the time for the end of solidification t_{ll}.

The main reason for the noticeable drop in the fcc amount during solidification can be related to temperature effects. For the liquid filament we have found a continuous temperature gradient from the cold parts at the surface to the warmer inner core (see chapter 4.1.1.1). The solid-liquid-interface follows this gradient so that the current temperature of the liquid at this interface increases, the further the crystallization has proceeded. We have stated previously that fcc probably is more stable at lower temperatures. Combining these two statements, we expect the probability of molecules to arrange in an fcc lattice to be highest in the beginning where the coldest liquid resides. On later stages of solidification, the liquid is increasingly warmer and the probability of newly formed fcc structures decreases. Keep in mind that our observables VAR1

and VAR2 correspond to the accumulated solidified phase rather than just the interface. Therefore the fcc-hcp ratio in the recently transformed solid in later stages is even lower than our ratios indicate, because the fraction added becomes continuously smaller based on these cumulative statistics.

Additionally to the temperature of the currently transforming liquid phase, another contribution probably assists in the decrease of the fcc-hcp ratio. As stated, similar mixed crystals were produced by gas condensation on cold surfaces $< 4\,$K. In one experiment [74], these mixed crystal were afterwards heated step by step up to $11\,$K, retaining each temperature steady for several minutes in between to equilibrate and take Raman spectra. It was found that, the higher the temperature was, the more the fcc peak s1 shrank in favor of the hcp peaks, evidenced by a ratio similarly defined to VAR2. At constant temperature, this change happened in the order of minutes until an equilibrium was approximated. It is important to point out that in those experiments there is no liquid involved, hence the transformation is entirely within the solid phase. The interpretation for this is that fcc is increasingly unstable compared to hcp at higher temperatures, yet the two phases are separated by a spectrum of energy barriers [74, p.105]. Upon heating, this energy barrier becomes increasingly easier to cross and the fcc lattice experiences a martensitic transformation, i.e. the molecules rearrange, probably shift layerwise, into the more stable hcp configuration. Because of the energy barrier, this process happens slowly within minutes and depending on the environmental structure, some fcc regions seem to be more stable than others. Otherwise the transformation would happen completely at one critical temperature. For solid hydrogen, a martensitic transformation has been observed at high pressures by ultrasonic propagation [80].

In our case, the decrease of the fcc ratios may also be partially based on this martensitic transformation. In the above hydrogen gas condensing experiments, the fcc peak completely disappeared through heating at around $T = 0.5T_M \approx 7\,$K. According to our analysis in section 4.1.5.1, this is approximately the limit of evaporative cooling of the solid, so that at least during the formation of our solid the temperature of it is definitely above this value. Hence, a fully equilibrated solid filament would not exhibit any fcc lattices.

However, since we probe the solidification itself, the crystal structure that initially forms does not necessarily have to be the energetically most stable form, but may just have a lower energy barrier according to Ostwald's rule of stages. The fact that we obviously observe fcc peaks, although our solid is above the limiting temperature according to [74], is a strong indication that in our experiment a metastable crystal is grown through Ostwald's rule. Through martensitic transformations, this initially formed crystal is likely to change its structure towards a more stable form with lower or maybe even no fcc content.

During the crystal growth up to t_{ll}, there is no way to clearly identify a martensitic transformation because the total amount of fcc and hcp both grow. Yet, its contribution to the decrease in the fcc ratios should be significantly smaller compared to the main effect, i.e. the increasing temperature of the liquid towards the core. Evidence for this statement is provided by the plots in fig.50, which show the main decrease of the fcc ratio during the growth of the solid. If martensitic transformations were the major aspect, the change in ratio should remain strong even after complete solidification, which obviously is not the case.

However, the idea that martensitic transformations are likely to happen is supported by data points which are recorded after complete solidification. Beyond $t_{ll} \approx 13.5\,\mu s$ in fig.50 both ratios VAR1 and VAR2 still show a slight but continuous decrease in their values. To check if this is not an artifact due to fitting, the associated spectra are displayed separately in fig.51. In none of these spectra a liquid peak can be detected, which usually is situated between the main peaks (2) and (3) slightly below $353\,cm^{-1}$. The increased background in this region is attributed to tails of the peaks and the o-H_2 content (see previous section 4.2.1.2). Hence, all changes within the peak intensities have to happen within the pure solid phase.
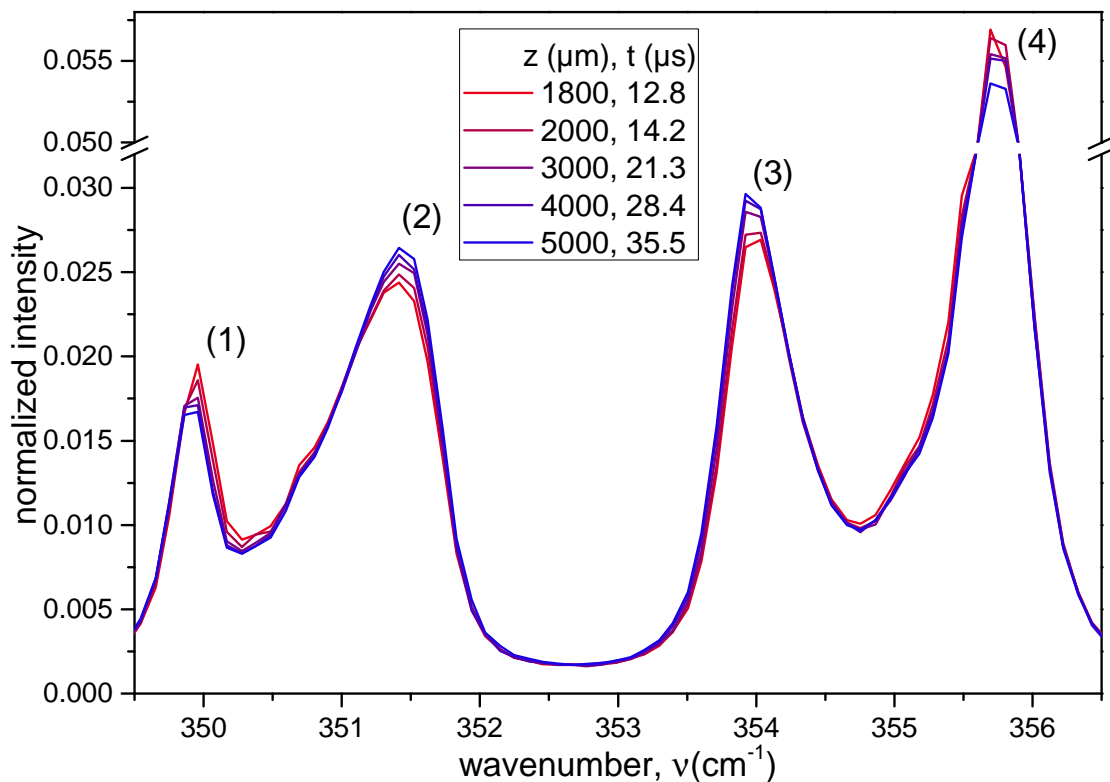

Figure 51: Rotational Raman spectra of data #3 after complete solidification $t \geqslant 12.8\,\mu s$. For clearer details of changes in the peaks, the y-axis is interrupted.

With increasing time/distance from the nozzle, one can see that the fcc peak (1) and the fcc+hcp peak (4) continuously decrease. Additionally, the regions associated with mixed crystal phases in between peaks (1) and (2) as well as (3) and (4) seem to diminish slightly. This decrease is compensated by peaks (2) and (3) clearly increasing. Since these two are associated with pure hcp, this behaviour is interpreted as a transition from fcc and rhcp regions into a pure hcp lattice. As obviously there is no liquid phase involved, the transition is expected to be martensitic.

This is a clear indication for the metastability of the initially formed crystal and the validity for Ostwald's rule for in our filaments. We stated that the limit temperature of evaporative cooling for the solid is $T \approx 7\,K$. Because according to the gas condensed crystals in [74] the fcc phase vanishes completely upon heating to this temperature, the crystal we observe has to be off-equilibrium. Probably enhanced by the strong supercooling of the liquid, the crystal initially grows into an easily accessible structure,

which is a mixed polycrystal of fcc and hcp crystallites. Due to the instability of the fcc phase at these temperatures, it experiences a martensitic transformation to the stable hcp structure. Yet, because there is an energy barrier separating the two lattices, this transformation happens slowly. Since we probe on time scales 10^7 times shorter compared to the transformation observed in [74], the decrease is barely noticeable and it remains open, if the fcc peak diminishes completely on long time scales.

4.2.3 Summary: Rotational region

In the rotational region of para-hydrogen $S_0(0)$ we observe that the peak associated with the liquid phase transforms into an asymmetric band structure with 4 main peaks, which we identify as a mixed crystal of fcc and hcp lattices (see fig.45 on p.106). The asymmetric shoulders in between adjacent fcc and hcp peaks are likely coming from border regions of the two lattices and rhcp structures, i.e. regions with unclear symmetry based on arbitrary layer stacking.

In the literature the bulk liquid has exclusively been found to freeze into a pure hcp lattice and crystals with mixed lattices similar to our case have only been observed in experiments, in which para-hydrogen gas was condensed onto a cold surface. Since in those experiments, the crystal structure does not persist upon heating to temperatures $\approx 8\,\mathrm{K}$ that prevail in our experiment, it is likely that our filament initially freezes into a metastable structure. This probably roots in the strong supercooling and is in agreement with Ostwald's rule, that the initial crystal that grows does not have to be the most stable form, but one that is easily accessible.

Reducing the amount of ortho-hydrogen leads to sharper overall structures, yet the observed asymmetries associated with intermediate fcc-hcp regions remain.

Using a different nozzle, we find that the intensities of the main peaks are distributed slightly different, which indicates that the orientation of the lattices may not be completely arbitrary. We attribute this effect to unique properties of nozzles like defects at the orifice, which likely introduce disturbances that initiate the crystal growth and induce preferred growth directions of the nozzle.

In the measurements of the smallest nozzle producing a spray of droplets the fcc related peaks as well as the mixed crystal regions in between peaks carry more intensity. This is explained by the overall lower temperatures of the liquid evidenced in the previous chapters, for which the fcc configuration becomes more stable and therefore likely. Additionally, smaller crystallites are probably formed yielding more molecules in intermediate rhcp environments.

In the quantitative analysis support for a metastable crystal is provided by observing the change in ratio of fcc throughout the crystallization process and beyond. In the beginning, where the coldest liquid parts of the liquid freeze, the fcc amount is highest and diminishes continuously, the further the solidification has proceeded. After complete solidification a tiny, but continuing decrease of fcc is detected, which probably is based on martensitic transformations from hcp to fcc and again highlights the metastability of the crystal and validity of Ostwald's rule.

5 | PURE ORTHO-DEUTERIUM

In the second campaign in 2011, measurements with pure ortho-deuterium were conducted. To recap, o-D_2 is the isotopic pendant to p-H_2 with $J = 0$ in the ground state. Their differences are discussed in the background section 2.4.

For the procedure of our measurements, two main aspects have to be obeyed: 1) The melting point of o-D_2 is higher and therefore the cryostat has to work at higher temperatures temp2, 2) The mass density ρ is more than twice that of p-H_2, so that according to formula 2.3 on p.8 higher nozzle pressures P_0 are needed to receive similar filament velocities v_0.

Since less information can be extracted in comparison to para-hydrogen, only two measurements with different nozzles were performed that are listed in table 5.

#	nozzle	d_0 (µm)	date	temp2 (K)	P_0 (bar)	v_0 (m/s)	% p-D_2
A	XVII-06	5.3	30/11/11	19.6	13.0	115	2.5
B	XVII-01	1.9	16/12/11	20.0	25.0	160	2.5

Table 5: All measurements of pure o-D_2. The mean velocity v_0 is calculated by formula 2.3 on p.8. The p-D_2 content is estimated from measurements in the gas phase.

5.1 Vibrational region

A series of vibrational spectra from measurement #A is presented in fig.52. The first important difference to para-hydrogen is that the vibrational excitation $Q_1(0)$ of $J = 0$ o-D_2 is now overlapping with $Q_1(1)$ from $J = 1$ p-D_2. Whereas for p-H_2 the excitations $Q_1(0)$ and $Q_1(1)$ could well be separated into two panels (compare fig.24 on p.69), for deuterium the two isomeric liquid as well as solid bands are now closer to one another ($\approx 0.7\,\mathrm{cm}^{-1}$) than to their associated partner band according the transition from liquid to solid ($\approx 1.5\,\mathrm{cm}^{-1}$).

This proximity of the isomeric excitations leads to another peculiarity. Based on prior measurements of pure, i.e. fully converted at 20 K, ortho-deuterium in the gas phase, the para-deuterium, $J = 1$, content was determined to be 2.5%, which is the physical minimum value at that temperature (see chapter 2.4.1). However, due to the intensity enhancement, which was discussed in the background chapter 2.3, the $J = 1$ lines appear to be much stronger in intensity, up to a factor of 50 above their real mol fraction [34]. For comparison, for para-hydrogen measurements in section 4.1.5.2 we stated an intensity enhancement factor of 3.5. The reason for the stronger effect is grounded in
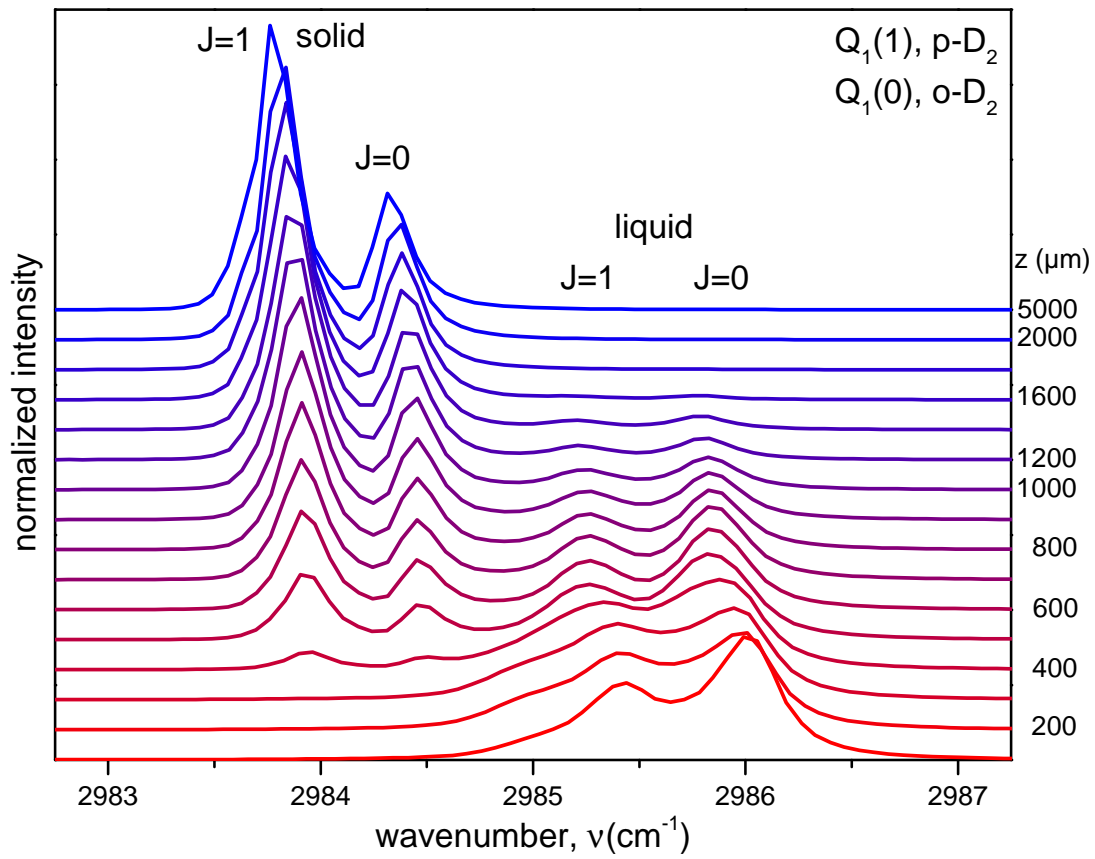
Figure 52: Series of vibrational excitations $Q_1(0)$ for o-D_2 and $Q_1(1)$ for p-D_2 from data #A. The distance z at which each spectrum is recorded is displayed on the right side, whereas omitted values are intermediate.

the vicinity of the isomeric peaks, because the closer the gap between the excitation energies of the isomers is, the more the resonance responsible for the intensity anomaly is enhanced. Furthermore the closer intermolecular distance in deuterium compared to hydrogen benefits the intensity enhancement, since vibrons can easier hop onto adjacent molecules.

The intensity anomaly causes an interesting illusion. Whereas in the liquid phase the absolute height of the $J = 1$ peak is at about 60% of the $J = 0$ peak, in the solid the $J = 1$ is stronger with double the intensity (compare fig.52). This is explained in terms of a closer intermolecular distance in the solid, which additionally enhances the resonance effect [34]. Since there is no known mechanism for causing excessive probabilities of spin-flips in pure deuterium within the short time scales of our observations, we expect the amount of para-deuterium and ortho-deuterium, respectively, to be constant.

5.1.1 Temperature of the filament

By closely examining the liquid bands of deuterium in fig.52, one can see that both p-D_2 and o-D_2 main peaks shift and develop growing asymmetric tails towards lower

wavenumbers. Similar to the case of pure para-hydrogen, this corresponds to the cooling of the liquid, since it is accompanied by an increase in density resulting in easier hopping of the vibrons. However, the strong overlap of the isomeric $J = 1$ excitation particularly in the liquid band makes it impossible to extract a temperature gradient for ortho-deuterium as we did for para-hydrogen in section 4.1.1. Furthermore, no correlation wavenumber $\leftrightarrow$ temperature has been stated for ortho-deuterium. Therefore we start with the adoption of the temperature gradient simulation in section 5.1.1.1, before analyzing the data in a qualitative way in section 5.1.1.2.

5.1.1.1 Temperature gradient simulation

To still estimate temperature values for the liquid, we can use our temperature gradient simulation that we have developed for para-hydrogen in 4.1.1.2 and which has been proven to be in good agreement with that data. For the ortho-deuterium calculation, the same formulas with 100 concentric layers are used and and only some parameters have to be changed, which are the equilibrium vapor pressure curve for o-D_2, the heat capacity and heat conductivity for exchange between layers as well as thermodynamic constants (compare appendix B.1). The source conditions d_0, P_0 and T_0 are taken from the experimental values, whereas likewise to the case of p-H_2, T_0 is chosen higher than the sensor reading temp2 with $T_0 = temp2 + 1\,K$ to account for radiative heating from the surrounding chamber at room temperature onto the nozzle tip.

In fig.53 the temperature simulation for pure o-D_2 with conditions #A is plotted in comparison to the simulation of p-H_2 for data #4, which was already discussed in chapter 4.1.1.2. Note that although the source pressure P_0 for the ortho-deuterium simulation is significantly higher, the velocity v_0 is below that of para-hydrogen based on the higher mass density coming into play in the denominator of formula 3.4 on p.42. Yet, because we have chosen time on the x-axis, effects of velocity should not play a role as we have seen in the previous chapter 4.1.1.3 for para-hydrogen compared at different pressures P_0.

The overall behaviour of the simulated temperature gradient looks similar. Pay attention to the starting temperature T_0, which is absolutely and relatively closer to the respective melting point for o-D_2 than for p-H_2. Regardless of this, the surface layer, i.e. the lowest temperature curve, drops below the respective melting point T_M almost instantaneously for p-H_2 as well as o-D_2. If we consider the relative undercooling of this layer, the progress is nearly equal and reaches $T/T_M = 0.75$ after $3\,\mu s$. This is a result of a similar vapor pressure curve relative to their respective melting points of both isotopes.
Since the deuterium simulation starts at a T_0 closer to the melting point T_M, the mean temperature crosses T_M earlier than the corresponding para-hydrogen curve. However, the thermal conductivity, which is responsible for the transfer of heat to the inner layers, is lower for ortho-deuterium. This can be detected in the difference of inner core (highest respective curve) to the surface (lowest curve). This difference, which represents the temperature gradient across the filament, narrows faster for the hydrogen simulation. Hence, it takes more time for inner layers to cool in the o-D_2 case.

An important remark is that the presented temperature simulation of the liquid is only valid for the pure liquid case and therefore only holds up to the emergence of the
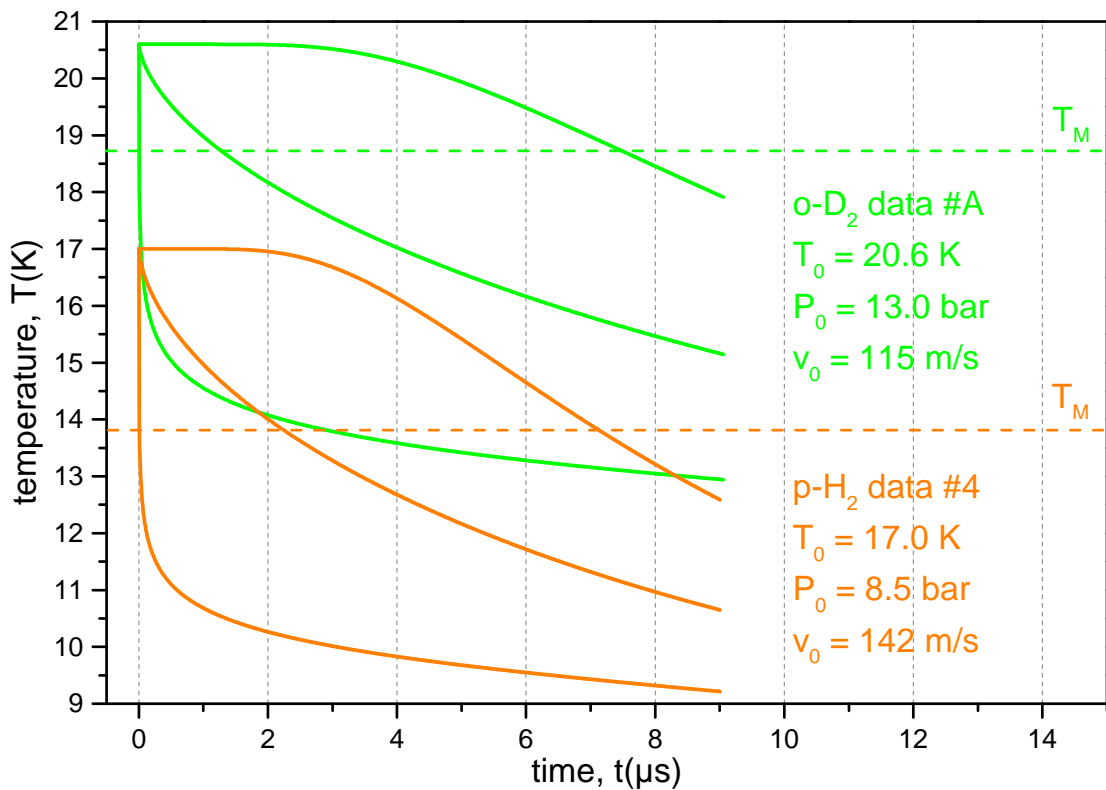
Figure 53: Simulation of the temperature gradient for pure p-H$_2$ data #4 (p.68) in orange and o-D$_2$ data #A (p.119) in green. The three lines correspond to highest, mean and lowest temperature of the simulation from top to bottom. Dashed horizontal lines represent the associated melting points T$_M$.

first solid. For the p-H$_2$ measurement this time is $t_{fs} = 3.9\,\mu s$, whereas for o-D$_2$ it is $t_{fs} = 3.0\,\mu s$. After this point, the heat released during the subsequent solidification makes an estimate of the temperature of the liquid for o-D$_2$ difficult, because we cannot evaluate shifts of the distribution in the liquid band due to the overlap of bands. However, the process is expected to be similar to para-hydrogen, which evidenced a strong increase of the lowest temperature and a slight increase of the mean temperature (compare plot 27 on p.73).

5.1.1.2 Comparison: Nozzle diameter

As stated in the previous section, we are neither able to extract temperatures nor a wavenumber distribution for our ortho-deuterium data. However, by utilizing the temperature simulation and comparing data with different source conditions, we get a qualitative picture of the progression of the liquid.

Similar to what we have done for para-hydrogen, we can extract a mean value for the wavenumber of the liquid band. Yet in contrast, this liquid band now is constituted of the overlapping $J = 1$ and $J = 0$ components, which both shift to lower wavenumbers (compare the two bands marked with "liquid" in fig.52). Note that the extraction of the mean position of the liquid band is not straightforward due to the increasing overlap

with the adjacent solid bands at lower wavenumbers. The procedure is described in the later section 5.1.2.1 governing the solid fraction.

We have two data sets for pure ortho-deuterium to compare, which are listed in table 5 on p.119. Data #A is done with our main nozzle having an orifice diameter of $d_0 = 5.3\,\mu m$. Data #B was recorded using the smallest nozzle with $d_0 = 1.9\,\mu m$, which in the case of pure para-hydrogen produced a spray of droplets (compare section 4.1.1.5). Interestingly, in contrast to those measurements, the ortho-deuterium filament with the small nozzle does not experience a breakup into droplets and rather freezes into a solid filament similar to nozzles with a bigger d_0. This probably is due to the fact that the initial starting temperature T_0 is closer to the melting point T_M than for the p-H_2 case. Hence, no excessive formation of convection bubbles occurs inside the liquid exposed to the low pressure vacuum conditions. We therefore assume that our simulation of the temperature gradient is valid for both measurements, which makes the comparison particularly appealing.
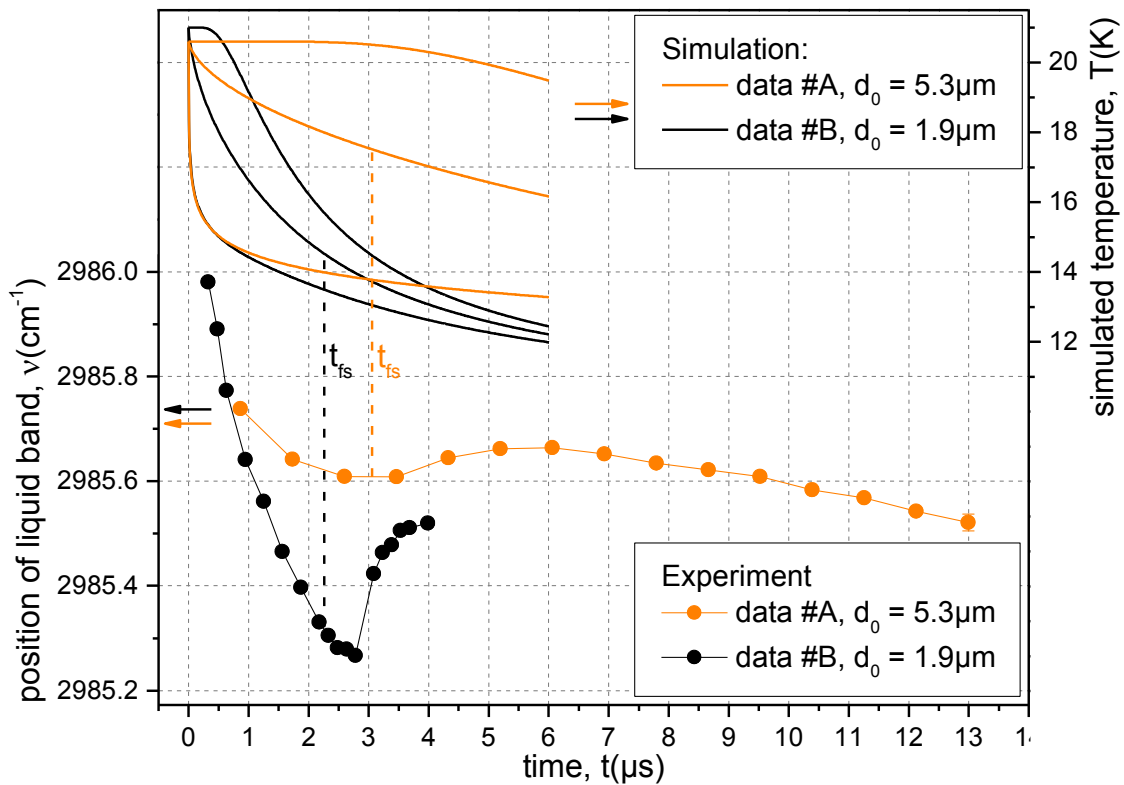
Figure 54: Upper half: Simulated temperature gradient of pure ortho-deuterium data #A in orange and #B in black with scale on the right. Lower half: Experimental mean wavenumber of the combined $J = 1$ and $J = 0$ liquid bands of above data in the same color code with scale on the left. The vertical dashed lines mark the time for appearance of the first solid t_{fs}.

The extracted mean wavenumbers of the liquid band of both measurements are plotted together with the corresponding temperature simulations in fig.54. We first focus on the simulation of the big (orange) an small (black) nozzle in the upper part. The lowest temperature curve, which is associated with the surface of the filament, in both cases exhibits similar values up to $\approx 1\,\mu s$. This is based on the very efficient and fast evapo-

rative cooling at high temperature compared to the relatively slow heat conductivity to inner layers. After this point, the surface of the bigger nozzle experiences a more shallow decrease, because the efficiency of evaporation diminishes drastically at lower temperatures and heat exchange with the inner layers of the filament plays an increasing role.

The difference in the temperature gradient, i.e. the difference from the lower to upper curve, is immense. Whereas after $2\,\mu s$ the small nozzle has a gradient of just $2\,K$, the inner core of the big nozzle after the same time has not even experienced any cooling at all. Since the first solid indicated by the dashed lines emerges afterwards, we consider the temperature of the small filament as approximately homogeneous.

We now turn our focus to the experimental mean wavenumber of the liquid in the lower part of fig.54. For both measurements we observe the expected decrease of the mean wavenumber, which we already experienced for pure para-hydrogen. This decrease correlates well with the above mean temperature of the simulation (middle lines). Note however that there probably is not a linear dependency between wavenumber and temperature, but rather a more complicated formula as in the case of para-hydrogen on p.73. The mean wavenumber of the smaller filament drops significantly below that of the big filament, i.e the liquid in the former is at a lower mean temperature, when the solid starts to appear and grow.

As soon as the first solid is detected (marked as t_{fs}), for the big filament the mean temperature starts to increase due to the heat released on solidification. After this initial increase, the wavenumber again tends to decrease, based on ongoing evaporative cooling of the solid, being more effective than the heat released. The small nozzle does not seem to increase with the first solid at once, what likely can be blamed on systematical errors of the extraction method rather than a physical meaning[1]. Interestingly, the final wavenumuber or temperature, respectively, is equal for the big and the small nozzle, like it was the case in all para-hydrogen data.

We conclude that, although the analysis does not yield absolute values for the temperature of the liquid band, the qualitative behaviour of ortho-deuterium is consistent with the simulation as well as compared with the para-hydrogen data. Hence, o-D_2 filaments are undercooled to a similar extent.

5.1.2 Solid fraction

5.1.2.1 Definitions and methods for extraction

Likewise to the analysis of para-hydrogen, from the ortho-deuterium measurements we can extract a solid fraction s_f, which represents the fraction of molecules that have solidified at each time/distance step from the nozzle. However, the extraction of this quantity proves to be more challenging, because

a) the excitations of the two isomers are not separated anymore,

---

1 Since the liquid bands in this case are at lower wavenumbers, the overlap with the solid band is more severe and one cannot clearly separate the excitations, which wrongfully attributes intensity of the solid to the liquid band leading to the observed inconsistency.

b) the intensities of the $J = 1$ component are no longer negligible compared to $J = 0$,

c) the relative intensities of the two isomers to one another are different in the liquid and the solid and

d) the liquid and solid bands overlap in their tails.

Total solid fraction

To overcome these issues, a reliable approach is to not extract separate solid fractions for o-D_2 and p-D_2, but a combined one with the total liquid and solid intensities which we call the total solid fraction:

$$s_f^x(z) = \frac{I_{sol}^x}{I_{sol}^x + I_{liq}^x} \, , \tag{5.1}$$

with $x = oD_2 + pD_2$. Since we do not have to take care about discriminating between the isomers, this definition solves problems a)-c) at the cost of losing information about the individual behaviour of the two species. However, in the analysis of para-hydrogen we found that the individual solid fractions exhibit an almost identical shape, so that we do not expect a significant different behaviour for ortho- and para-deuterium anyways.

However, issue d) still needs to be addressed. Usually, the total intensity of a band is calculated by simply adding up the single intensities of each wavenumber data point associated with this band (see section 3.4.3). However, when bands are overlapping, data points in between carry intensities from both excitations and can not be clearly attributed to one band anymore. This becomes even more severe in our case, in which intensity is redistributed from the liquid into the solid, so that the contribution of the tails to one data point changes during the progress of crystallization.
To account for this, we choose an adaptive border value for the attribution of a wavenumber data point to liquid or solid, respectively. This border is chosen as the local minimum between the $J = 0$ solid peak and the adjacent $J = 1$ liquid peak as illustrated in fig.55 and is determined by automated routines in *Origin Pro*. All data points on the left of this spectrum-specific value are added to the solid and everything on the right side to the liquid intensity in the above formula 5.1. During the progress of solidification this local minimum shifts towards higher wavenumbers, since the $J = 1$ solid band and its tail grow in intensity, whereas the liquid $J = 0$ band diminishes.

This method produces flaws, because this strict border cuts off the tails of the bands and assigns them to the opposing aggregate phase. If the liquid and solid intensities are roughly the same size like in the purple spectrum, the tails of the liquid and solid bands that reach beyond the cut off region can be assumed similar and the errors made in the assignment cancel each other out. Yet, in the case in which one phase carries much more intensity than the other, this defined border leads to an overestimation of the excitation with small signal, because significant parts of the tail of the adjacent big peak reach into its region (compare blue and red spectra in fig. 55).
The false area added is estimated to be up to 60% of the true area in the case for the beginning of solidification (red spectrum). The overestimation of the area of the solid happens even before solidification, because the noise of the background fakes a local
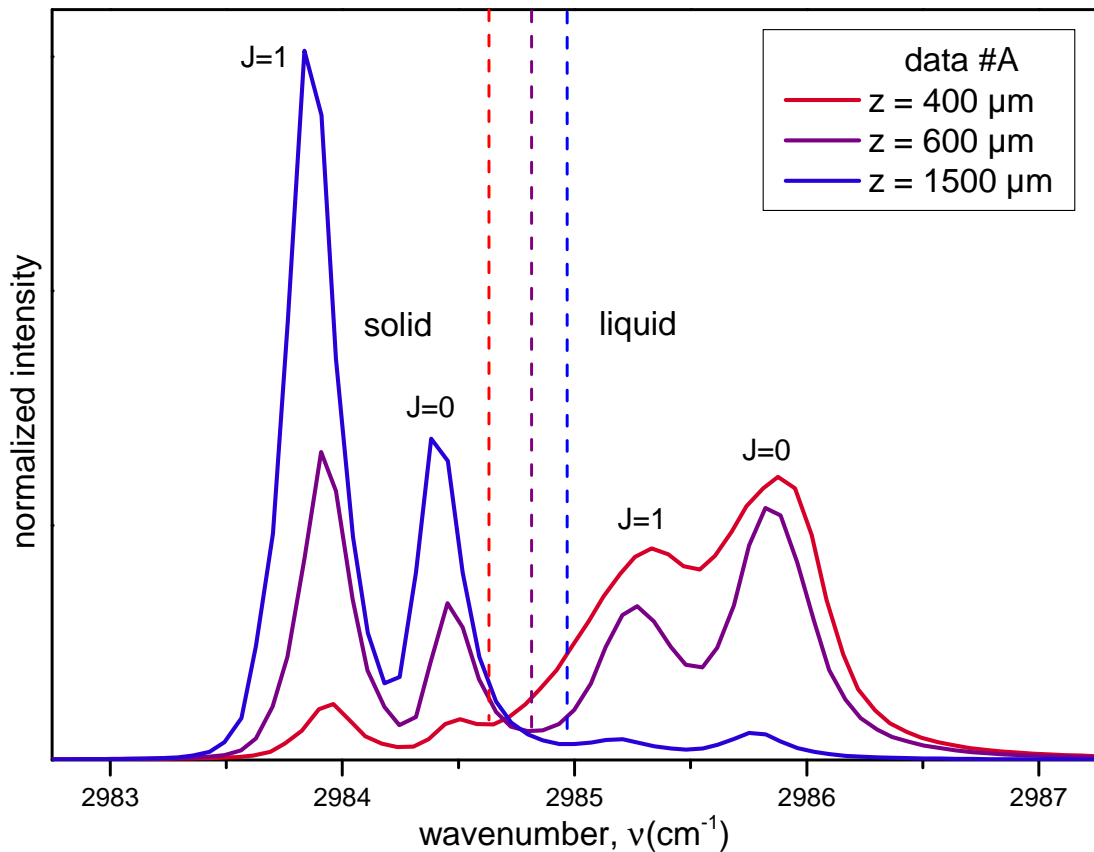
Figure 55: Three spectra in the vibrational band depicting the transition from liquid to solid for the pure ortho-deuterium data #A. The dashed vertical line in corresponding color marks the minimum between the solid $J = 0$ and liquid $J = 1$ peaks, which is defined as the border between liquid and solid for extracting the solid fraction s_f.

minimum that the routine searches for. This manifests in values $s_f > 0$ even without any real solid present in the spectrum (compare s_f for $t < 3\,\mu s$ for the black plot in fig.56). However, since the absolute area of that region is small, the systematic error in the solid fraction s_f defined in formula 5.1 is limited to a maximum of 5 percentage points.

Maxvalue solid fraction

Another definition of the solid fraction shall be introduced here, which which was already used in extracting the o-H_2 solid fraction in the pure p-H_2 measurements (sections 4.1.3.1 and 4.1.3.5) and will be essential later in chapter 6.1.5 covering mixtures of p-H_2 and o-D_2. This approach relies on the assumption that there is no big difference between the individual solid fractions of the $J = 0$ and $J = 1$ components. As there is no evidence in the literature and in our previous measurements for significant partitioning of the isomers, we treat this statement as fulfilled. Additionally, it is mandatory to have the total intensity of all spectra normalized as described in section 3.4.3.
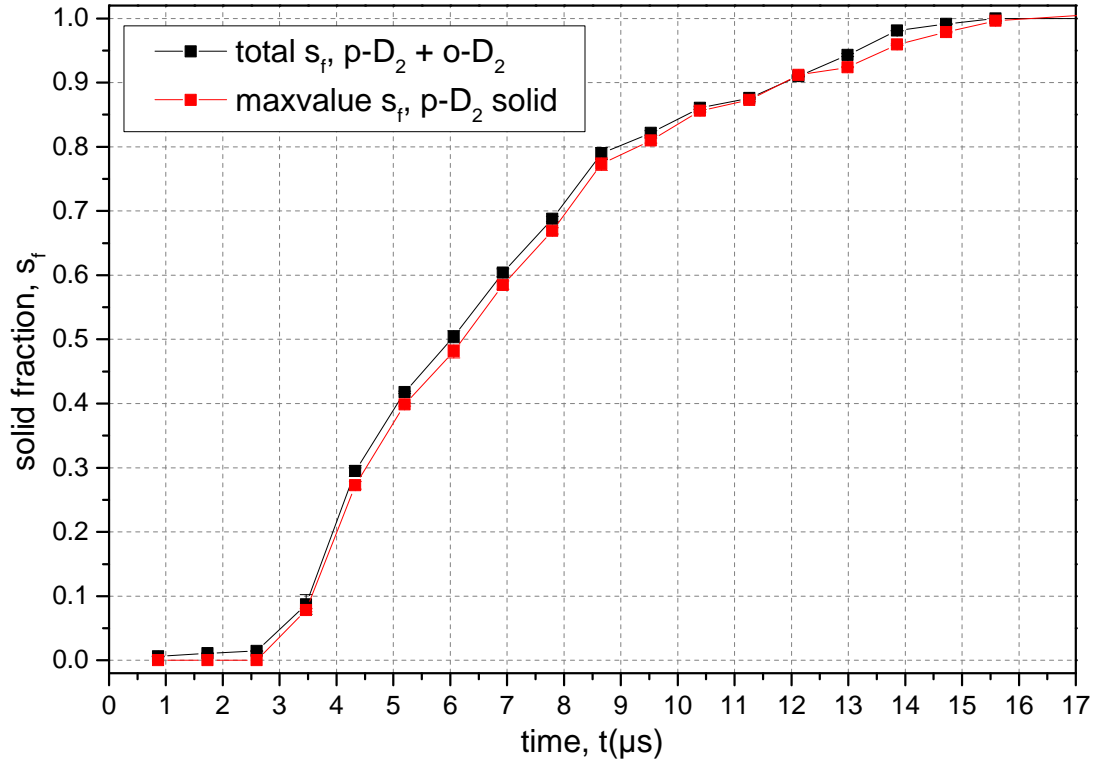
Figure 56: Different methods for the solid fraction s_f for data #A. Black data points use the total solid fraction with formula 5.1, whereas the red ones are extracted solely from the p-D_2 solid band via the maxvalue formula 5.2.

The idea is to focus just on one excitation line, which is mostly separated from overlaps and tails of adjacent bands and therefore unaffected. With above assumption, it does not matter, if this line belongs to $J = 0$ or $J = 1$ nor if it represents the liquid or the solid. In our pure ortho-deuterium measurement, the best candidate is the $J = 1$ solid component on the very left in the previous fig.52, which only overlaps with small contributions of its liquid counterpart and the adjacent $J = 0$ solid peak. For each individual spectrum, we define the current area, i.e. intensity, of this peak $I_{sol}^{pD_2}$ as all data points up to the minimum between the $J = 1$ and $J = 0$ solids. When the solidification is completed (no liquid peaks left), the intensity of this peak does not change anymore and we define this as the maximum value $I_{maxsol}^{pD_2}$, i.e. a constant. The current solid fraction of each spectrum at distance z now simply is given by the current value divided by the maximum value:

$$s_f^{pD_2}(z) = \frac{I_{sol}^{pD_2}(z)}{I_{maxsol}^{pD_2}} \tag{5.2}$$

This method, which we call the maxvalue solid fraction, mostly eliminates the systematic errors due to overlapping bands in the beginning and end of solidification. Drawbacks are that it is sensitive to variations of the isomeric constitution throughout the measurement as well as changes in the intensity enhancement. For example, if the distance between the solid $J = 1$ and $J = 0$ bands gets smaller, more intensity is shifted into the solid p-D_2 band and the maxvalue solid fraction would yield deviating values.

The total and maxvalue solid fraction are plotted for data #A in fig.56. The vicinity of all data points with a maximum deviation of 3 percentage points evidences the validity for both methods. Since the maxvalue solid fraction in red yields correct values $s_f = 0$ when there is no solid visible in the spectra($t < 3\,\mu s$), we will use this curve in the subsequent analysis.

5.1.2.2   Analysis and comparison with para–hydrogen

We now turn to interpreting the solid fraction of ortho-deuterium. In fig.57 the maxvalue solid fraction from data #A is plotted in comparison to the para-hydrogen data #4, both produced with the same nozzle.

Obviously, the ortho-deuterium filament starts to freeze earlier, yet the whole solidification process takes longer to complete. Furthermore, the overall progression of the curve seems less smooth. Whereas the para-hydrogen data exhibits a neat curvature at the start and end of solidification, o-D_2 shows more odd, unpredictable behaviour, especially above $s_f > 0.75$.

In terms of the shape of the curve, we keep in mind that the solid fraction for ortho-deuterium is way more cumbersome to extract from the spectra, leading to increased systematical errors which are not included in the purely statistical error bars within the square shaped data points. However, reexamining the previous fig.56, we find that both methods, although extracted with different processes, show a similarly rough structured solid fraction. This indicates that this structure arises from the solidification itself. Reasons for this could be deviations from the isotropic growth model from the surface to the inner core of the filament or temperature related effects that lead to increased and reduced growth periods. A key feature herein could play the more pronounced temperature gradient across the filament. Yet, because we do not know the shape of the solid fraction with certainty nor the temperature gradient of the liquid during solidification, the details are not assessable for us. Furthermore, a reasonable fit with the Avrami equation is not possible, mainly because the biggest systematical errors occur in the beginning of solidification, which is the key part for fitting.

Regarding the emergence time of the first solid t_{fs}, we have seen in chapter 4.1.3.5 for para-hydrogen that it may vary greatly due to disturbances inducing the first critical solid embryos. However, with $t_{fs}^{oD2} = (3.0 \pm 0.4)\,\mu s$ the value for ortho-deuterium is earlier than any of the para-hydrogen measurements with this nozzle, so that we can safely assume that ortho-deuterium filaments tend to start freezing earlier.

In the comparison of the temperature simulations in fig.53 on p.122 we found that the outer surface layer for both isotopes exhibits similar relative undercoolings T/T_M. This means that deuterium seems to have an overall higher probability of forming critical nucleation embryos. There could be several reasons for this. For one, twice the mass leads to lower thermal velocities or higher momenta of the molecules, respectively, which could favor critical clustering. Support for a mainly mass related explanation is given by the ratio of the times for the first solid

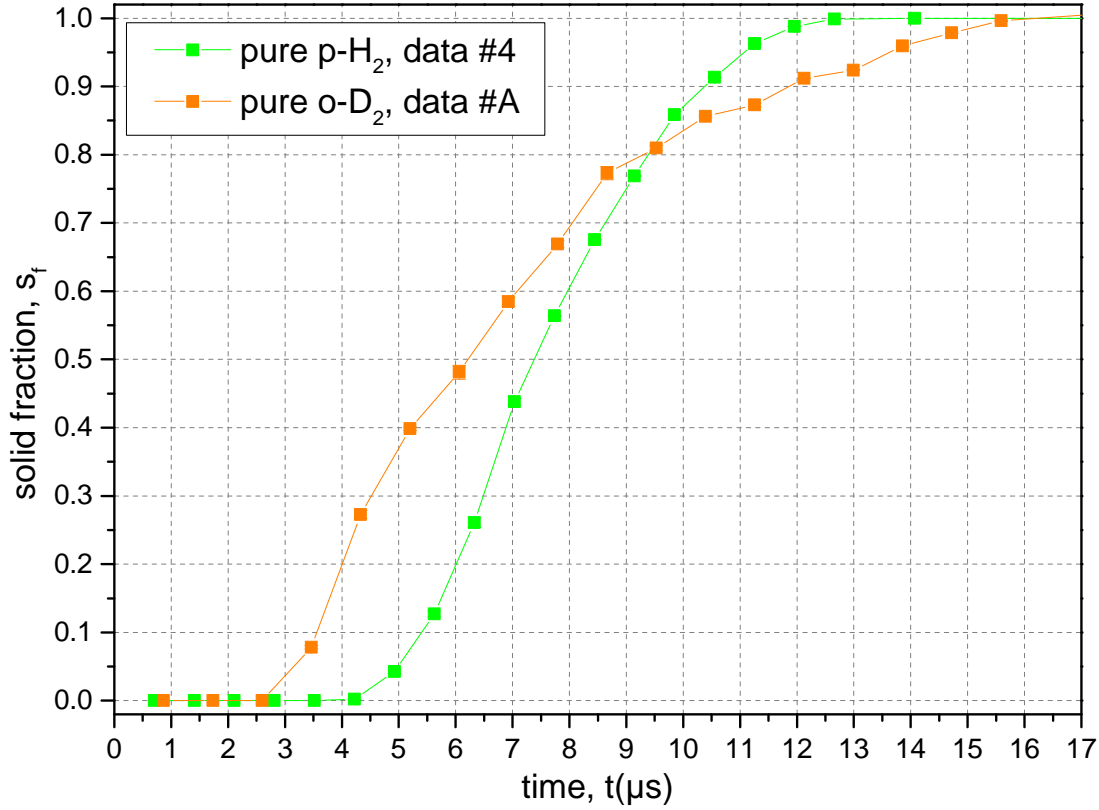$$\frac{t_{fs}^{pH2}}{t_{fs}^{oD2}} = 1.3 \pm 0.2 \,, \tag{5.3}$$

Figure 57: Comparison of solid fractions with a $d_0 = 5.3\,\mu m$ nozzle for pure p-H$_2$ (green) with conditions #4 on p.68 and o-D$_2$ (orange) #A on p.119.

which is close to the square root of the mass ratio ≈ 1.4 that we often encounter in the comparison of the isotopes (compare chapter 2.4.1). Note that the error bars may be higher, because we have seen that the time for the first solid possibly depends on disturbances within the filament.

Another possibility for the different starting time t_{fs} is the smaller intermolecular distance in ortho-deuterium based on the smaller zero point vibrations, which could decrease the nucleation energy barrier. Furthermore, the higher amount of J = 1 molecules may initiate embryo formation. However, since nucleation itself is still poorly understood and we only observe the macroscopic results, we are only able to speculate about the microscopic details.

Compared to para-hydrogen, we find that the process of solidification lasts longer for ortho-deuterium. We again extract the duration of crystallization as the time from the first solid up to the last liquid in the spectra as $t_{ll-fs}^{oD2} = 13.4 \pm 1.0\,\mu s$. The corresponding time for hydrogen is $t_{ll-fs}^{pH2} = 9.5 \pm 0.8\,\mu s$. The (inverse) ratio of these two values is

$$\frac{t_{ll-fs}^{oD2}}{t_{ll-fs}^{pH2}} = 1.4 \pm 0.2 \tag{5.4}$$

and again in good agreement with the square-rooted ratio of the molecular masses. This time we have good support that this is not a coincidence. In chapter 4.1.3.3 we found evidence that for para-hydrogen the kinetic model is the valid growth mechanism for

the crystal. It suggests itself that this also applies for the ortho-deuterium, because the intermolecular potential is the same. In the theory chapter 2.5.2 the basic growth velocity u_0 for the kinetic model is defined in formula 2.23. Constructing the ratio for the two isotopes yields:

$$\frac{u_0^{oD2}}{u_0^{pH2}} = \frac{\sqrt{\frac{3k_BT}{m^{oD2}}}}{\sqrt{\frac{3k_BT}{m^{pH2}}}} = \sqrt{\frac{m^{pH2}}{m^{oD2}}} = \frac{1}{\sqrt{2}} \ , \tag{5.5}$$

if we disregard different temperatures at solidification. Since t_{ll-fs} changes inversely to u_0, this simple calculation reveals that the longer crystallization time or slower growth velocity, respectively, is explainable by a lower thermal velocity of ortho-deuterium molecules. However keep in mind that the absolute temperature as well as the chemical potential differences and the number of active sites are not considered here and may also play a role according to formula 2.21 on p.34. If for example the higher temperature at solidification for o-D$_2$ is included, the above estimation gets closer to 1, but is still within the error bars of the experimental ratio 5.4.

5.1.2.3 Comparison: Nozzle diameter

Comparison: Small and big ortho–deuterium filaments

Here, we analyze the solid fraction of the pure ortho-deuterium measurement #B using the small nozzle with $d_0 = 1.9\,\mu m$ (orange curve in fig.58). The time for complete solidification yields $t_{ll-fs}^{1.9\,\mu m} = 2.9 \pm 0.2\,\mu s$ and, assuming an isotropic growth from surface to core, a growth velocity of $u^{1.9\,\mu m} = 0.33 \pm 0.04\,m/s$. Compared to the growth velocity of o-D$_2$ data #A with the big nozzle (orange curve in fig.57), $u^{5.3\,\mu m} = 0.20 \pm 0.02\,m/s$, this is more than 50% faster. Additionally, the first solid for the small filament appears earlier at $t_{fs}^{1.9\,\mu m} = 2.0 \pm 0.2\,\mu s$ with respect to $t_{fs}^{5.3\,\mu m} = 3.0 \pm 0.4\,\mu s$.

In the analysis of the average position of the liquid band in fig.54 we found that the smaller nozzle cools much faster and hence in the mean to lower temperatures. Also note that the big filament exhibits a considerable temperature gradient, whereas the small filament is almost homogeneous. The kinetic model predicts increased growth velocities for lower temperatures, mainly based on the higher difference in the chemical potential of the liquid and solid phase. Hence, the kinetic theory is in qualitative agreement with our experimental values for the growth velocity above. This is an important result, which we will utilize later in the interpretation of p-H$_2$ and o-D$_2$ mixtures.

The earlier starting time t_{fs} of the small filament can also be explained in terms of temperature. Focusing on the surface temperature, i.e. the respective lowest simulated curve in fig.54 on p.123, we find that the small filament reaches lower absolute temperatures earlier, what significantly increases the probability of critical nucleation embryos according to classical nucleation theory.
Yet, the lowest temperature achieved at the start of solidification (marked by dashed t_{fs} line) by the outer layer is slightly below that of the bigger filament. A physical reason for this is the smaller total volume of the 1.9 μm filament, which reduces the probability with which critical embryos are generated.
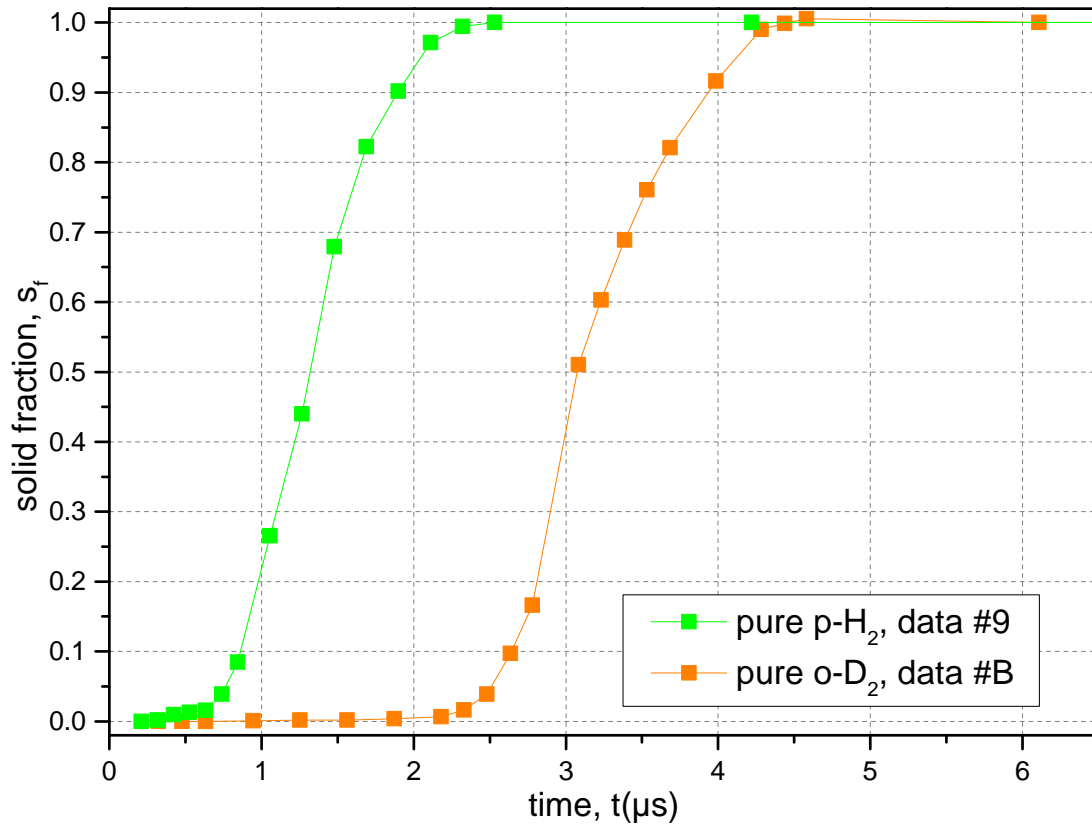
Comparison: Para-hydrogen and ortho-deuterium

Figure 58: Comparison of solid fractions with a $d_0 = 1.9 \, \mu m$ nozzle for a pure para-hydrogen spray (green) with conditions #9 on p.68 and an ortho-deuterium filament (orange) #B on p.119.

In the next step, we compare the measurements of para-hydrogen and ortho-deuterium for the $d_0 = 1.9 \, \mu m$ nozzle. We need to be careful with the interpretation of the data, because the para-hydrogen beam is not a freezing filament but rather a spray, as we discussed in chapter 4.1.3.7.

The solid fractions are plotted in fig.58, whereas the solid fraction for ortho-deuterium is extracted with the maxvalue method (see section 5.1.2.1). The most obvious feature is that para-hydrogen freezes considerably before the ortho-deuterium filament and is almost finished, before the latter even begins. This is likely due to the early breakup of the liquid para-hydrogen resulting in high surface-to-volume ratios and the low temperatures almost from the start.

Despite the difference in t_{fs}, both curves show a similar solidification time with $t_{ll-fs}^{pH2} = (2.2 \pm 0.2) \, \mu s$ and $t_{ll-fs}^{oD2} = (2.9 \pm 0.2) \, \mu s$. This indicates that the biggest droplets in the para-hydrogen spray, which probably make up for the highest fraction of molecules, have a similar diameter to the $1.9 \, \mu m$ ortho-deuterium filament. Note however that the $p-H_2$ solid fraction is constituted of a variety of individual solid fractions from differently sized droplets.

5.1.3 Summary: Vibrational region

Based on the good agreement between experiment and temperature simulation for para-hydrogen, we adapt the simulation to estimate the temperature of the liquid ortho-deuterium filaments. The simulated temperature curve for the $d_0 = 5.3\,\mu m$ nozzle reveals a similar behaviour, with the outer layer being basically equal to para-hydrogen considering the supercooling relative to the their respective melting points (fig53 on p.122). The main difference for ortho-deuterium is the lower thermal conductivity, which lets the temperature gradient across the filament have a longer equilibration time.
The experimental mean positions of the liquid band are in qualitative agreement with the simulation of the average temperature. In the measurement with the small nozzle $d_0 = 1.9\,\mu m$ the ortho-deuterium filament freezes similar to other liquid filaments, rather than breaking up into droplets like para-hydrogen did. In experiment as well as simulation, the small ortho-deuterium filament exhibits significantly faster and deeper coolings than the bigger nozzle.

For the extraction of the solid fraction, two methods are presented, one employing both $J = 0$ and $J = 1$ solid and liquid bands (total solid fraction), the other one utilizing the stand-alone $J = 1$ solid band only (maxvalue solid fraction). Compared to para-hydrogen, ortho-deuterium freezes earlier and the solidification lasts longer (fig.57 on p.129), which probably is due to the higher mass or lower thermal velocity of o-D_2 molecules, respectively, indicated by the time ratios ≈ 1.4 of the isotopes.
Compared to the bigger filament, the small filament starts to freeze earlier and the crystal growth velocity is higher, which is in qualitative agreement with the kinetic model. The small nozzle exhibits similarly freezing times for the p-H_2 spray and o-D_2 filament, although the former freezes much earlier, suggesting maximal droplet sizes similar to d_0 in the former case.

5.2 Rotational region

As for the pure p-H_2 measurements, we next discuss the rotational region $S_0(0)$ of o-D_2. However, this chapter does not include a quantitative analysis, because the spectra are broader, which makes fits more prone to systematical errors.
We first discuss the structure in section 5.2.1, then compare the two measurements with different nozzle diameter in section 5.2.1.1 and at the end discuss the similarities and differences to the p-H_2 data in section 5.2.1.2.
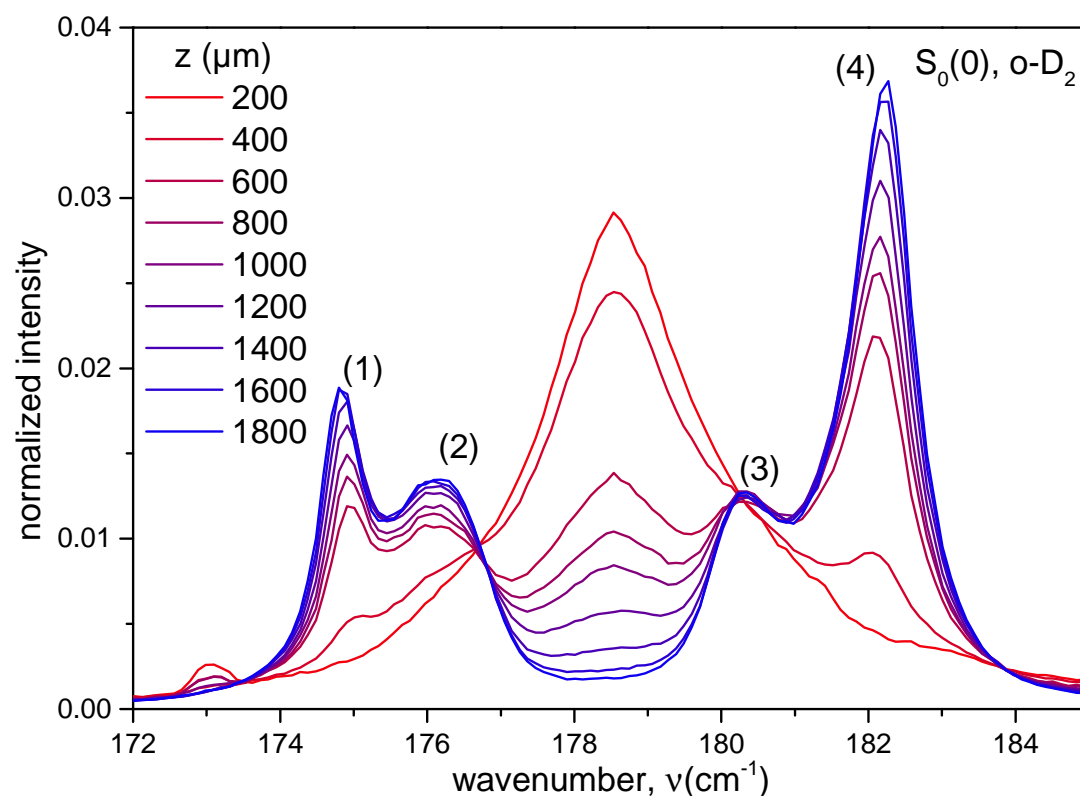
Figure 59: Evolution of the rotational excitation $S_0(0)$ of o-D_2 of data #A along the filament axis z in color code from red to blue with steps $\Delta z = 200\,\mu m$. The peaks of the solid (blueish spectra) are enumerated from (1) to (4).

In fig.59 the evolution of the $S_0(0)$ band of data #A along the filament is illustrated. In the liquid phase, this excitation exhibits a Lorentz-like shape at $178.5\,cm^{-1}$, which is in agreement with the literature value [36]. The small peak at $173\,cm^{-1}$ is a plasma line from the Ar^+ laser (see chapter 3.4.3) and not relevant. With increasing distance z from the nozzle, the intensity of the liquid peak is redistributed into 4 sharper peaks, enumerated from (1) to (4). This behaviour follows the transition from liquid to solid, which we evidenced in the analysis of the solid fraction.

5.2.1 Structure of the solid

The overall transition as well as the 4 peak structure of the spectra in the solid closely reminds of the para-hydrogen rotational analysis in chapter 4.2. When grown at equilibrium conditions, ortho-deuterium is known to freeze into a pure hcp crystal [36]. Indeed, we can identify peaks (2) to (4) to belong to an hcp crystal by comparing with literature values [31], which are marked as black dotted vertical lines in fig.60. Peak (1) and peak (4) are in agreement with experimental values for an fcc lattice. Hence, similar to the pure para-hydrogen case, our supercooled liquid freezes into a polycrystal consisting of both hcp and fcc crystallites. A similar line structure consisting of these 4 peaks has been observed in ortho-deuterium gas condensation onto cold surfaces at liquid helium temperatures [74].

In contrast to the p-H_2 $S_0(0)$ line of the solid, at first sight it is not obvious that the 4 peaks in fig.60 are asymmetric towards the regions in between (1)-(2) and (3)-(4). However, upon closer inspection of fig.60, the asymmetry in between peaks (3) and (4) can still be detected, which is expected to happen, following our previous explanation that the intensity from this region comes from border regions of fcc and hcp and rhcp lattices with varying stacking order. Further evidence for rhcp is provided by the deviations of the hcp peaks from the literature positions, which signals that there are no largely extended hcp lattices, but rather smaller crystallites.
The reason for the overall more blurry spectra is rooted in the significantly higher amount of J = 1 molecules. As explained in chapter 4.2.1.2 for p-H_2, these molecules break the symmetry of the lattice resulting in smoothed spectra in which details are washed out. In the previous fig.46 this effect was already noticeable with 0.9% J = 1 molecules, however in our o-D_2 measurements with 2.5% there are even a factor 3 more of these impurity sites present. These also are responsible for the extending tails of the peaks, which is especially noticeable in the high underground in between peaks (2) and (3) upon complete solidification (fig.60). The blurred structure of the spectra is also the reason, why a quantitative analysis with peak fittings would yield arbitrary results with large systematical errors particularly in the width of the fit functions and the auxiliary intermediate rhcp peaks.

In the gas condensation experiments [74], likewise to their p-H_2 measurements, a reduction of peak (1) in favor of the hcp peaks upon heating of the sample has been observed. Therefore we expect a similar behaviour to our para-hydrogen measurements, i.e. a decrease of the fcc peak in later stages, where warmer liquids reside. Following Ostwald's rule, the initial crystal structure probably is metastable and should martensitically transform, detectable in a change in peak intensities after complete solidification. The evolution of the fcc to hcp ratio for o-D_2 is not easy to evaluate without the quantitative analysis. We estimate the change of this ratio by comparing the heights and areas of peaks (1) and (2). During the growth of the crystal that was pictured in fig.59 no explicit trend can be deduced because the amount of background beneath these two peaks varies due to the diminishing liquid peak. A better inspection can be done for the completely solidified spectra illustrated in fig.60. Recall that for p-H_2 we found a redistribution of intensities of peaks (1) and (4) into (2) and (3) after the transition to the solid, which we explained as a martensitic transformation or reorganization of molecules into the more stable hcp lattice (compare fig.51 on p.116).
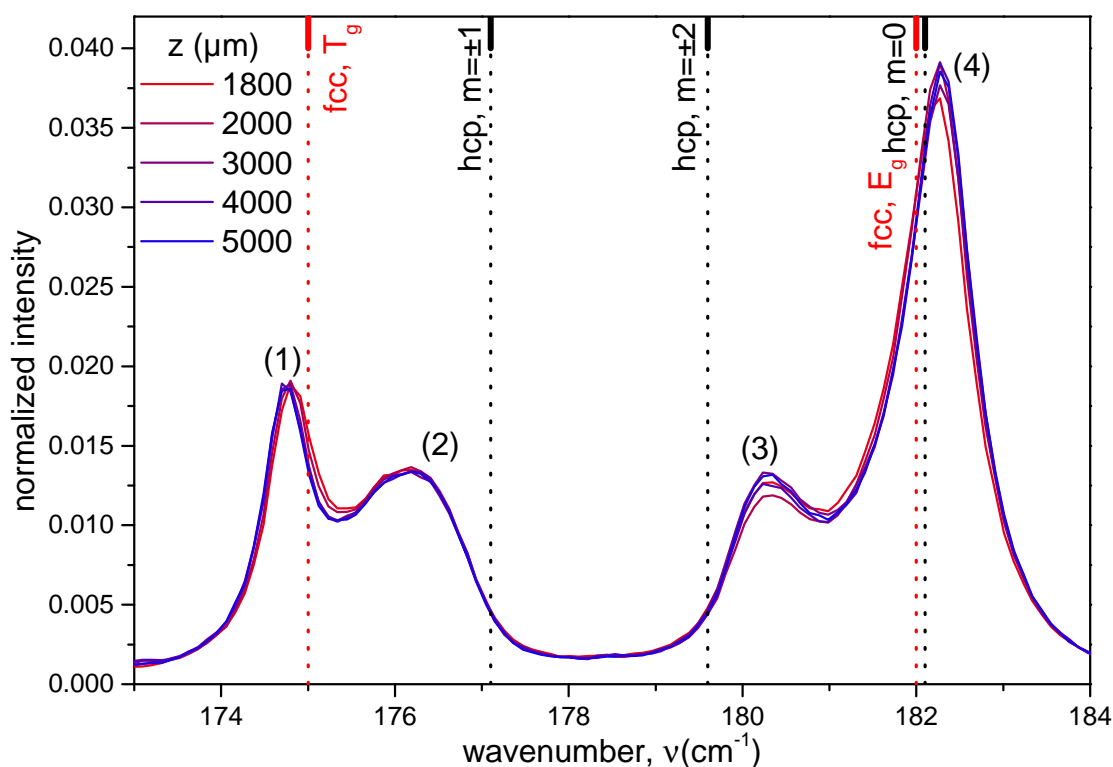
Figure 60: Evolution of the rotational excitation $S_0(0)$ of o-D_2 after complete solidification. Dotted black and red vertical lines represent the experimental positions of a pure hcp [31] and fcc lattice [74], respectively.

For o-D_2 this trend is not detected in fig.60. Peak (2) appears almost unchanged, whereas peak (1) merely experiences a shift to lower wavenumbers, rather than the expected reduction in intensity, which is related to lower temperatures or higher densities, respectively [81]. The presumed fcc-hcp border region in between those two peaks may show a slight decrease, which however may also be related to the shift of peak (1). Peaks (3) and (4) as well as the region in between do not show an unambiguous behaviour and seem to arbitrarily change in height, although the $3-4$ single spectra taken at each position z are almost identical.

This behaviour indicates that for o-D_2 there is no extensive transformation of the fcc to hcp lattice after complete solidification. Hence, no proof for an initial metastable structure and Ostwald's rule is provided. However, note that a transformation could happen on longer time scales. Based on the gas condensing experiments [74], ortho-deuterium also should consist of almost pure hcp at our observed temperatures. So, although we see no clear evidence, it is likely that our initial crystal formed is metastable and the product of Ostwald's rule. More information on this topic is gathered in the following section and the final discussion will follow in section 5.2.1.2.

5.2.1.1   Comparison: Nozzle diameter

In this section we compare the two pure o-D_2 measurements with different filament sizes. In section 5.1.1.2 we found that due to this size difference, the mean temperature of the liquid for the smaller nozzle is considerably lower. In chapter 4.2.1.2 the pure p-H_2 revealed that lower temperatures of the liquid are connected to higher fractions of the fcc lattice, since this configuration is proposed to become more stable under these conditions. Therefore for o-D_2 we expect a similar behaviour with more fcc for the smaller nozzle.
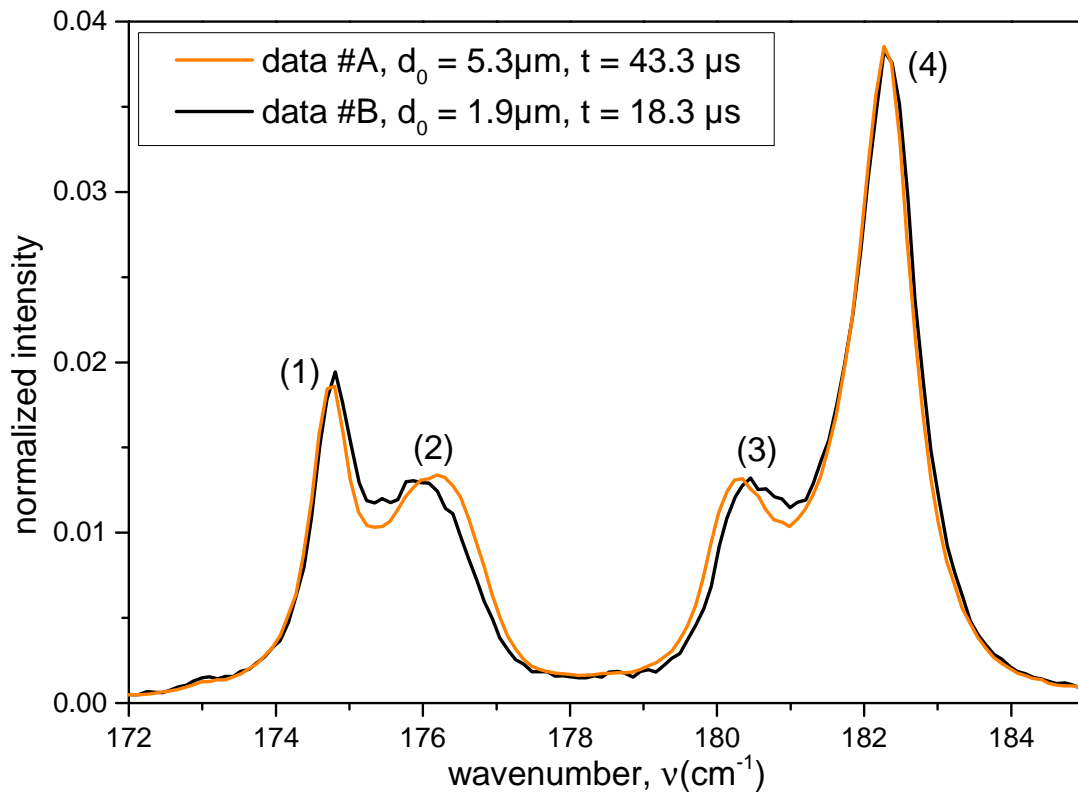
Figure 61: Comparison of the $S_0(0)$ line of the small and big pure o-D_2 filament after complete solidification.

In fig.61 rotational spectra of the completely solidified filament of data #A and #B are plotted in orange and black, respectively. The line structure of the small filament data is less smooth due to the worse signal-to-noise ratio. There is almost no variation in the area fraction of peaks (1) as well as (4). The main difference between the spectra is that the intensity in between peaks (1)-(2) and (3)-(4) is higher for the small nozzle, while peaks (2) and (3) are shifted apart from one another and additionally have less intensity.

More intensity carried by the areas in between indicates that a higher fraction of the signal comes from molecules which are situated in mixed fcc-hcp lattice regions at the expense of pure hcp. The deuterium gas condensation experiments [74] also evidenced that polycrystals produced at smaller temperatures exhibit smaller crystallites, what in reverse means that more molecules are situated in mixed rhcp lattice configurations.

Although we use the transition liquid-solid rather than gas-solid, we can utilize the same argument to explain our increased signal from intermediate rhcp regions. Smaller crystallites also explain the further shift apart of peaks (2) and (3), indicating that the pure hcp lattices are smaller. In the previous section 5.1.2.3 we discovered that the crystal growth velocity is twice the value for the smaller filament. This faster growth of the crystal seems to make a neat lattice stacking less likely and increases the amount of random stacking.

The almost identical area of the fcc peaks surprises based on the fact that in the smaller filament lower temperatures prevail and is in contrast to the pure p-H_2 data. However, this behaviour agrees with the findings of the previous section, in which we did not encounter a transition from fcc to hcp in the evolution of the filament. Combining both statements, it seems that the fcc amount in the polycrystals of o-D_2 is not excessively influenced by the temperature of the liquid. As for the 5.3 μm nozzle, no change in the peak intensities and therefore no evidence for a transformation is found after complete solidification for the 1.9 μm filament.

5.2.1.2 Comparison: Structure of o-D_2 and p-H_2

In the previous sections we already discussed the evolution of the o-D_2 rotational measurements compared to p-H_2. In this section we take a look at the static features. Fig.62 shows the spectra of the entirely solidified p-H_2 and o-D_2 filaments from the same nozzle wit $d_0 = 5.3$ μm. The x-axis are shifted and scaled to obtain an overlap of the main peaks (1) and (4) for direct comparison. Since the line structure is much sharper for para-hydrogen and the ortho-deuterium spectrum would be quite low, the area of the spectra is not normalized to 1 as usual, but instead the maximum height, i.e. peak (4), is assigned the value 1.

An obvious feature is that for o-D_2 the fcc-peak (1) is considerably higher than in the p-H_2 case, not only in its absolute height or area, respectively, but also relative to the hcp peaks (2) and (3). In both spectra, the latter two peaks are similar in their relative height, but their maxima are shifted further apart from one another. One has to keep in mind that the $J = 1$ impurity amount is about a factor of 3 higher for the ortho-deuterium data. This leads to the broadening of all bands and makes a comparison of the intermediate regions difficult.
Despite the broader bands and the unknown contribution of fcc and hcp to peak (4), we are confident to say that the fraction of molecules in an fcc lattice is higher for the ortho-deuterium filament. Support for this is given by the similar height of hcp peaks (2) and (3) in the two spectra, which makes it unlikely that the orientations of the polycrystals are much different, what would change the hcp contribution to the shared peak (4). A higher number of molecules in fcc and rhcp configurations is consistent with the hcp peaks (2) and (3) being shifted further apart, indicating that the pure hcp lattices are less extended.

The simulation of the temperature gradient in section 5.1.1.1 revealed that the relative supercooling of the isotopes is similar. In the analysis of the previous o-D_2 rotational data we found that the amount of fcc does not significantly change with stronger supercooling and no direct evidence for a martensitic transformation or Ostwald's rule, respectively, was obtained. Therefore it seems that for ortho-deuterium the fcc and hcp
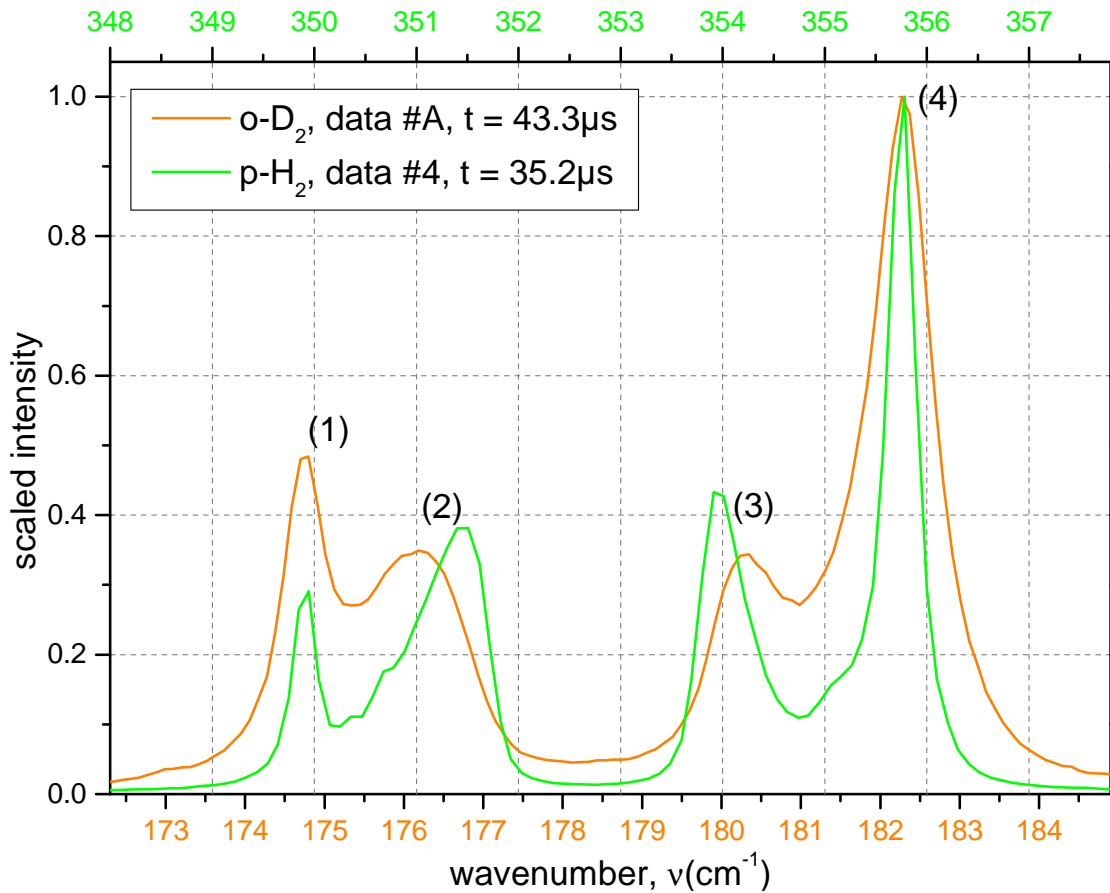
Figure 62: Comparison of $S_0(0)$ line after complete solidification of o-D_2 (bottom scale) and p-H_2 (top scale) shifted and scaled to match the positions of the outermost peaks. The intensity is scaled to be 1 at the point of highest intensity.

lattices exhibit a closer energy than for para-hydrogen at these relative supercoolings. A similar energy of the lattices over a broader temperature interval leads to more equal contributions and a stable structure that does not martensitically transform that easily. Indeed, in the gas condensing experiments it was found that the fcc phase of ortho-deuterium persists to higher temperatures relative to the melting point upon heating [74]. Based on their results, they claim that the fcc phase is more stable in ortho-deuterium.

The origin for this hypothesis may be rooted in the smaller zero point vibrations and closer intermolecular distance of the o-D_2 molecules, which could promote a more similar energy of the two lattice options. Support for increased stability of fcc at higher densities is provided by experiments with pressurized para-hydrogen [82]. Therein, a (partial) transition of the pure hcp crystal towards fcc was observed by applying a few kbar pressure. Ortho-deuterium exhibits a naturally higher number density and may therefore exploit the same mechanism in favor of fcc being energetically more stable already at ambient pressures.

The lack of proof for a diminishing fcc phase in our ortho-deuterium data may be explained by lower martensitic transformation rates based on this higher stability. A

smaller probability to rearrange could have its origin in less mobility of the heavier molecules or a reduced rate for tunneling [83]. However, the unavoidable higher $J = 1$ content can also have an influence on the stability as well as the structure of the crystal, because at high $J = 1$ contents fcc becomes more favorable [27, p.428].

5.2.2 Summary: Rotational region

The temporal evolution for the rotational band $S_0(0)$ of ortho-deuterium filaments is similar to the para-hydrogen case. During solidification, the intensity of the liquid peak is redistributed into 4 peaks, that can be identified as a mixture of hcp and fcc peaks, yet due to the higher $J = 1$ amount all peaks are broader in comparison to p-H_2. According to the literature, this structure probably is metastable and the result of Ostwald's rule of stages. However in the experimental data no sign of a martensitic transformation i.e. a diminishing of this fcc peak after complete solidification is detected within the time scales in neither of the measurements.
The smaller filament shows almost the same fcc content (fig.58 on p.131). However, more signal if situated in the intermediate rhcp regions , which probably is due to smaller crystallites based on the lower temperatures of liquid and, connected with it, higher crystal growth rates.

Since o-D_2 reveals a higher amount of the fcc phase in comparison to the p-H_2 spectra, all above results are interpreted as fcc being more stable for the heavier isotope, which is consistent with the literature. Reasons for this may be the smaller intermolecular distance and/or a reduced tunneling rate, decreasing the probability of passing the energy barrier necessary for the transformation to the energetically stable hcp lattice.

6 | MIXTURES OF PARA-HYDROGEN AND ORTHO-DEUTERIUM

After the successful measurements of para-hydrogen in the first and ortho-deuterium in the second beam campaign, we were eager to study, how mixtures of these two isotopes would behave. For this purpose, the gas samples for producing mixed filaments can be easily and continuously prepared with two mass flow controllers described in the setup section 3.2. Despite the different thermodynamic properties, especially the melting point T_M, it was possible to produce stable filaments in the whole range of p-H_2−o-D_2 compositions in the second and third beam time.

name, #	date	temp2 (K)	P_0 (bar)	v_0 (m/s)	% o-D_2
100-0 or #4	25/11/11	16	8.5	142	0.0
99-1	17/10/12	16	11.5	164	1.0 ± 0.1
97-3	02/12/11	16	8.9	143	3.2 ± 0.4
95-5	18/10/12	16	9.3	144	4.6 ± 0.6
91-9	19/10/12	16	10.0	144	9.1 ± 1.2
83-17	01/12/11	17	12.9	159	16.7 ± 0.8
48-52	02/12/11	17	14.2	143	51.6 ± 1.4
48-52-warm	13/12/11	17.7	14.0	141	51.6 ± 1.4
16-84	13/12/11	19	14.7	129	84.0 ± 0.7
4-96	24/10/12	20	15.3	127	95.7 ± 1.1
2-98	23/10/12	20	16.3	130	97.6 ± 0.6
0-100 or #A	30/11/11	19.6	13.0	115	100.0

Table 6: Measurements of p-H_2−o-D_2 mixtures using nozzle XVII-06 with $d_0 = 5.3\,\mu m$.

The recorded Raman data is summarized in table 6. The first and last entry in the list represent the measurements of pure para-hydrogen and ortho-deuterium, respectively, which were extensively discussed in the previous chapters. The double lines divide the table into three parts. In the first part, the conditions can be considered as p-H_2 with a small, $< 10\%$ impurity (o-D_2), whereas the last part marks the opposite case.

The relative mol fraction of the composition of each measurement (% o-D_2) is calculated as the mean value and standard derivative of three independent quantities:

1. The ratio of the two flow controller readings for p-H_2 and o-D_2 during the experiment

2. The intensity ratio of the respective vibrational $(Q_1(1) + Q_1(0))$ excitations from p-H_2 and o-D_2 in the condensed phases of the measurement

3. If available, the intensity ratio of the $Q_1(1) + Q_1(0)$ lines in the gas phase measured apart from experiments with the vacuum chamber filled with $\approx 10\,\mathrm{mbar}$ of the gas mixture.

For easier reference, the short names for the measurements are rounded values of this ratio in the form {%pH2}-{%oD2}, e.g. 83-17 with $16.7 \pm 0.8\%$ o-D_2 content.

The velocity of each filament is calculated with the standard Bernoulli formula 2.3 on p.8. The necessary liquid mass density of the mixtures is estimated to be a linear combination of the proportions of the isotopes:

$$\rho_{mix} = \frac{\%pH2}{100} \cdot \rho_{pH2} + \frac{\%oD2}{100} \cdot \rho_{oD2} \tag{6.1}$$

This linear relationship is justified by theoretical calculations [84] and experiment [45]. All mixtures have been produced with the same setup, i.e. the steady pressure P_0 is a result of the flow through the two mass flow controllers and therefore the compressor works at P_0 as the highest value. Based on this, we expect no excessive back conversion of the $J = 1$ isomeric components and the initial contents are determined to be 0.2% for p-H_2 and 2.5% for o-D_2.

Almost all measurements consist of 4 Raman series: the vibrational and rotational excitations of each p-H_2 and o-D_2, which all are in a different wavenumber regime. This chapter is again divided into the main sections vibrational 6.1 and rotational region 6.2 and most of the time the excitations from the two isotopes will be discussed in a combined way rather than separately.

6.1 Vibrational region

The amount of data for evaluation is not easy to handle and has to be reasonably reduced for plots and analysis. Not only does each mixture offer two vibrational bands (p-H_2 and o-D_2) with ≈ 50 single spectra each covering the transition from liquid to solid, but since we particularly want to look for the behaviour of the mixtures to one another based upon their composition, we have to compare the 11 measurements in table 6. For easier recognition, a color code is introduced with p-H_2 in green, o-D_2 in orange and mixtures in between according to the color gradient.

In fig.63 Raman spectra of the 11 series are presented, each shifted upwards for visibility with the o-D_2 content indicated on the left side. The figure is divided into two panels with an interruption in the wavenumber axis, the left showing the combined $Q_1(1) + Q_1(0)$ vibrational excitation of o-D_2 (and p-D_2) and the right $Q_1(0)$ of p-H_2. The $Q_1(1)$ excitation of o-H_2 is not illustrated, because it is too small and not of main interest. For the sake of clarity, each row does not contain the whole transition from liquid to solid, but rather just the very first, totally liquid spectrum (dotted line) and the last, totally solid one (solid line). The qualitative redistribution of intensity from the

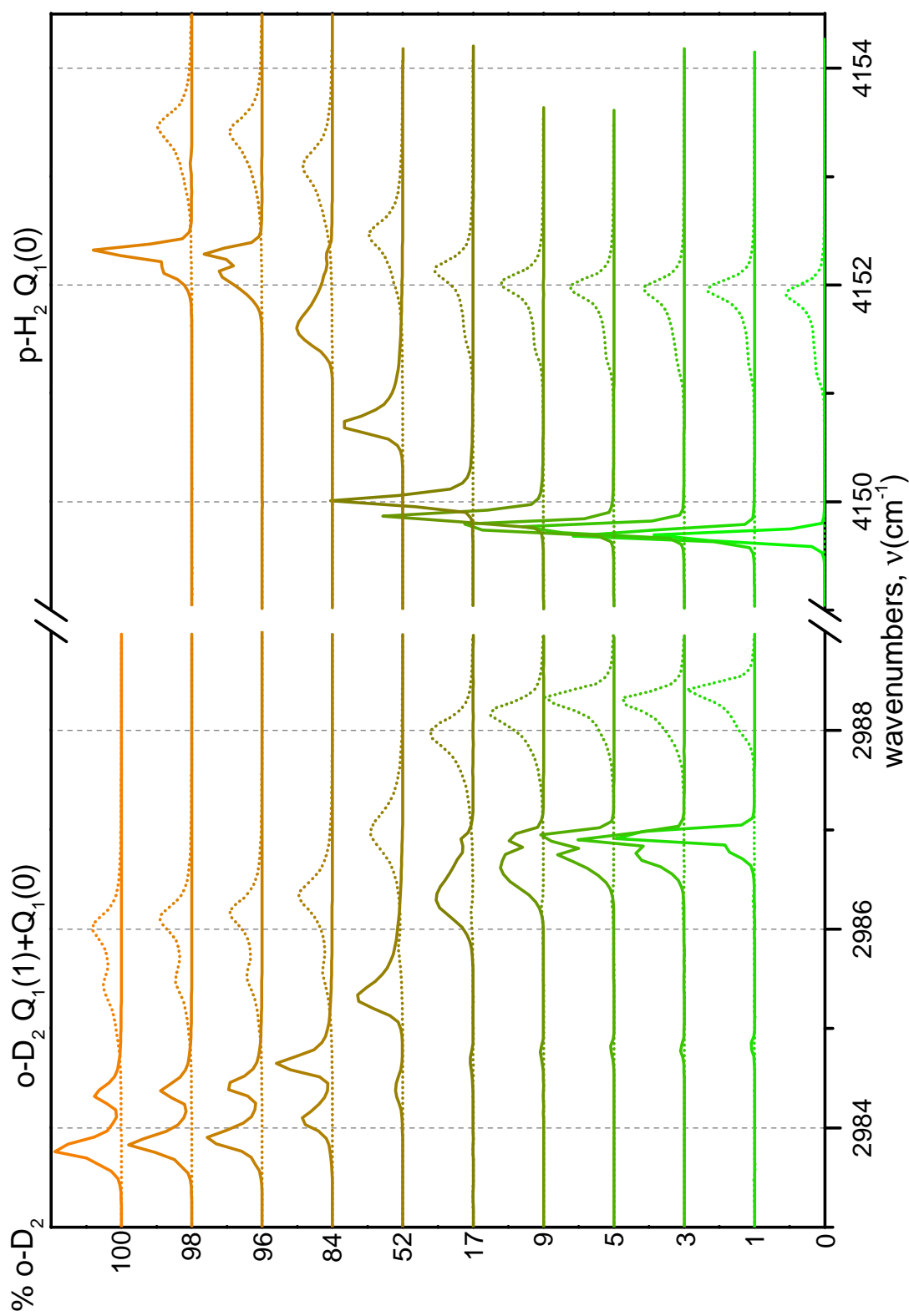**Figure 63:** Spectra of the o-D$_2$ (left panel) and p-H$_2$ (right panel) vibrational region of all Raman series in table 6. The graphs are stapled with increasing o-D$_2$ content (green towards orange) on the left side. Each row contains two spectra, representing the first, completely liquid (dotted) and last, completely solid (solid) measured spectrum of a series.

liquid to the solid proceeds similar to the pure para-hydrogen and ortho-deuterium cases and the quantitative details will be discussed later on.

Several features can be noticed in this figure. We start at the bottom pair of spectra in green in the right panel, which represents the well-known pure para-hydrogen measurement #4 or 100-0, respectively. Upon introducing increasing amounts of p-D_2 as an impurity, i.e. the subsequent spectra above this one in darker green, we observe a gradual shift of the solid as well as liquid band towards higher wavenumbers, whereas the shift for the solid is stronger. Additionally, the bands become broader, particularly evidenced by the solid band in the 48-52 mixture in olive. When para-hydrogen is the minority in the top spectra in orange, the solid band develops a multi peak structure, with the intensities strongly depending on the total amount of p-H_2.
For pure ortho-deuterium, we start at the top pair of orange spectra in the left panel. Here, we see the familiar double peak structure in the liquid as well as in the solid, which comes from the strong intensity enhancement of the $J = 1$ component (compare chapter 5.1). Upon inserting p-H_2 as an impurity (spectra below towards green) these bands shift to higher wavenumbers, likewise to the dilution of pure para-hydrogen. Yet, the $J = 1$ component, which always is the left one in the liquid as well as in the solid, experiences a less pronounced shift. Furthermore, this $J = 1$ band loses intensity in favor of the $J = 0$ peak in the liquid as well as the solid, the more impurities are added. Finally in the lower spectra in green, in which deuterium is the less abundant species, a multi peak structure in the solid appears, similar to what para-hydrogen exhibits.

The following sections will start with the analysis of the just described positions and shape of bands as well as their intensities in the liquid/solid p-H_2 and o-D_2 vibrational 6.1.1. After this, the temperature of the liquid will be covered 6.1.3, as a prerequisite for the most important part, the discussion of the solid fraction in section 6.1.5.

6.1.1 Band positions, intensities and structure

6.1.1.1 Shift of bands

The observed shifts of the bands towards higher wavenumbers upon dilution have been measured for mixtures of p-H_2 and o-D_2 before [31]. The responsible effect is similar to isomeric mixtures of e.g. o-H_2 and p-H_2 [78].
The energy of the vibron, i.e. the position of the bands, depends on the environment of an excited molecule. If the vicinity consists only of molecules of the same species, in an illustrative picture the excitation can hop onto adjacent partners, what effectively lowers the energy of the vibron (compare chapter 2.3.2). This resonance effect is disturbed, if foreign molecules with a different excitation energy are inserted, as hopping onto these is not possible. The higher the amount of impurities is, the less likely it is that adjacent molecules are identical. The excitation is not able to travel as freely and the corresponding energy is increased compared to the pure substance, manifesting as a shift towards higher wavenumbers (to the right) in Raman spectra. This explanation is valid, regardless if o-D_2 is mixed into p-H_2 (fig.63 right panel, bottom to top) or the other way round (left panel, top to bottom), since their excitation energies are far apart (compare wavenumber scale).
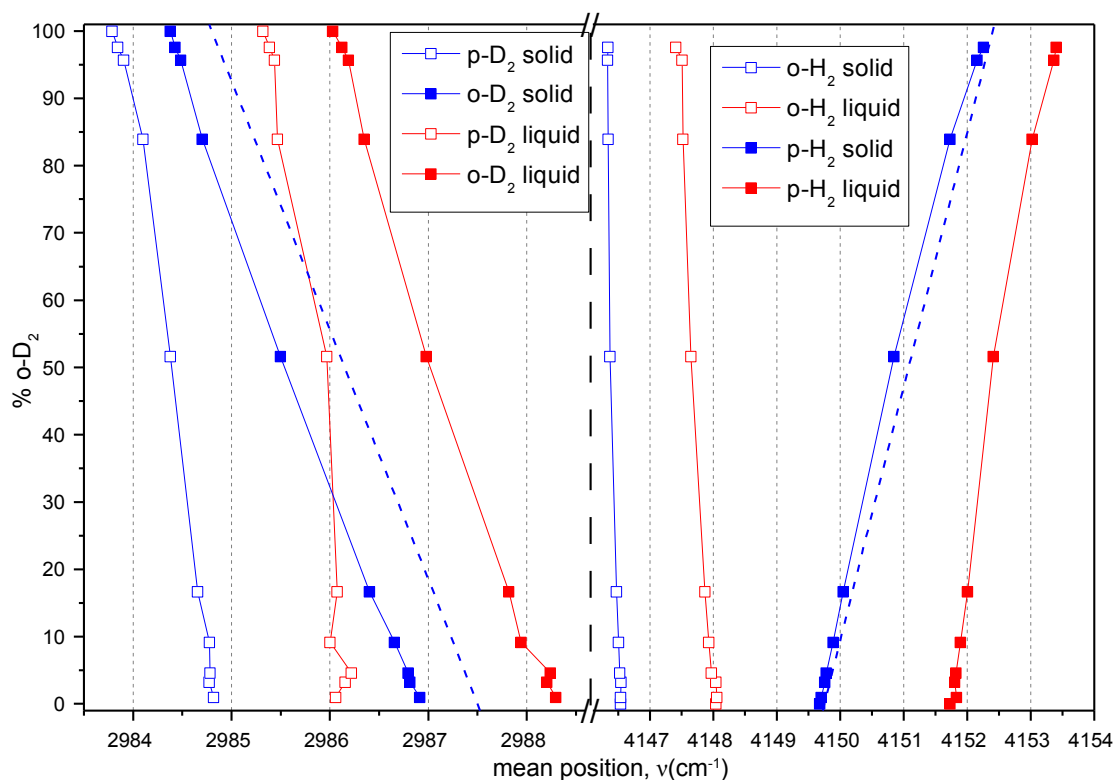
Figure 64: o-D$_2$ (left panel) and p-H$_2$ (right panel) mean positions of the J $= 1$ (hollow squares) and J $= 0$ (filled squares) excitations of the solid (blue) and liquid (red) bands extracted from fig.63. The blue dashed lines mark fitted experimental positions for the o-D$_2$ [31] and p-H$_2$ solid band [78] (see text).

For a quantitative analysis, we look at the wavenumber position of the liquid and solid bands of the spectra in fig.63 depending on the o-D$_2$ amount as a parameter. For each shown spectrum, we extract the mean positions for the J $= 0$ and J $= 1$ components separately, but we do not distinguish the multi peak structure of the solid band in the diluted mixtures. Note that for clarity again only the first (only liquid) and last (only solid) spectra are chosen.

The resulting 4 data sets each for o-D$_2$ and p-H$_2$ are plotted in the right and left panel, respectively, in fig.64. With the y-axis chosen as the o-D$_2$ content increasing linearly from bottom to top, the plot can be easily compared to fig.63 for orientation.

All 8 data sets exhibit a roughly linear dependency on the o-D$_2$ amount. However, since we just plot the average of a band, extending and overlapping tails, especially for liquid deuterium, as well as the multi peak structure of bands may induce higher systematical errors for medium and low mol fractions for a substance. Higher errors are also expected for all liquid bands, because the time the filament has traveled varies for the first spectra between all measurements, what changes the temperature and hence position of the liquid (more to this in the later section 6.1.3).

For a detailed analysis, we start at pure ortho-deuterium at the top in the left panel. As explained in chapter 5.1, the J $= 1$ and J $= 0$ excitations in the liquid (red) as well as solid (blue) are closer to one another than to their associated isomeric partner

band (same symbol) of the solid and liquid. Upon inserting p-H_2 as an impurity (data points beneath), all bands shift to higher wavenumbers due to the diminishing traveling options of vibrons explained in the beginning of this section.

However, this shift is stronger for o-D_2 (filled squares) than for p-D_2 (open squares). This is, because o-D_2 is the most abundant species with 97.5%, so that in the 0-100 pure o-D_2 measurement almost all nearest neighbors are $J = 0$ molecules. Hence, when impurities are inserted, the relative amount of same species partners is more drastically reduced than for the $J = 1$ component, which with 2.5% already has a low probability of having an adjacent same species molecule. Due to the resulting different magnitude in these shifts, the band position of the two isomeric species drift apart from one another with higher dilutions. The position of the p-D_2 liquid (red open squares) and o-D_2 solid (blue filled squares) even cross each other at $\approx$ 30% o-D_2 content until at the bottom points with 2% o-D_2 the two isomers are separated from one another, similar to the pure p-H_2 case.

In [31] mixtures of H_2-D_2-HD were measured. Their position of the o-D_2 solid band depending on the D_2 mol fraction is plotted as a blue dashed line in the left panel of fig.64. There is a good agreement between the slope to our o-D_2 solid band (blue filled squares), however their absolute position is always $\approx 0.5\,\mathrm{cm}^{-1}$ higher. Reasons for this are probably the presence of HD as well as a higher $J = 1$ content $(4 - 6\%)$ for both isotopes in their mixtures, shifting their positions to higher wavenumbers. Nevertheless, the parallel behaviour to our measurements proves that the same mechanism, i.e. vibron energy depends on the amount of same-species partners, is at work.

We next focus on the right panel of fig.64 and start at the pure p-H_2 measurements at the bottom. As expected, the main $J = 0$ component (filled squares) shifts towards higher wavenumbers upon dilution (data points above) based on the same-partner vibron argument which we utilized for deuterium. Yet, here we detect that the shift is slightly stronger for the solid (blue filled squares) than for the liquid (red filled squares). This is due to the fact that the higher density in the solid makes hopping of vibrons easier, so that the effect of dilution and connected reduction of same-species partners has more impact on the energy of this excitation. This argument also applies to all other liquid-solid band pairs of both isotopes/isomers, but due to the undisturbed band structure of p-H_2, it is most distinct and visible here.

The position of the solid p-H_2 band has been measured in mixtures of p-H_2 with o-H_2 in [78] and is marked as the blue dashed line in the right panel. Although the situation in those experiments is different, since we mix the isomeric species with similar excitation energy, the agreement with our measurements is good and proves that the explanation with reduced traveling vibrons is valid.

However, whereas the position agreement to this dashed line at high and low o-D_2 mol fractions is almost equal, slight differences with a clear trend towards lower wavenumbers are detectable for intermediate o-D_2 contents. If we assume a physical explanation for this observed deviation from a linear behaviour, this effect can most likely be attributed to a tendency to clustering of o-D_2 and p-H_2 molecules, respectively. In this case, the probability of finding same-species partners is increased, what reduces the energy of the vibrons, shifting the band to lower wavenumbers. Support for p-H_2 and o-D_2 cluster formation for mol fractions $> 10\%$ is provided by calculations of the excess energy of clusters in the solid phase [44].

As the last step, we take a look at the behaviour of o-H_2 (right panel, hollow squares). Surprisingly, this component exhibits a tiny, but evident trend for both the liquid and solid towards lower wavenumbers with increasing dilution (bottom to top), which is in contrast to the three other isomeric/isotopic excitations. We recall that the amount of $J = 1$ is only about 0.2%, so that in pure p-H_2 for a random distribution statistically 97.6% molecules are singled out (estimations in appendix B.3). Hence, our previous main argument that same-species partners are substituted through dilution, which increases the vibron energy, has no impact here.

It has been evidenced in theory [85] and experiment [86] for isotopically pure substances in both condensed phases that the $J = 1$ state is able to hop onto adjacent $J = 0$ molecules through EQQ interactions, so that adjacent molecules can exchange their state. Since hydrogen and deuterium have the same interaction potential, it is likely that this transfer of states is also possible in between isotopic species. If we insert fully converted deuterium with a $J = 1$ content of 2.5% into fully converted hydrogen carrying only 0.2% $J = 1$ molecules, the total amount of $J = 1$ increases. Based on the above transfer of states and a statistical equilibration, the number of o-H_2 rises, the more deuterium is added. Our mixtures are prepared in the gas phase, are afterwards condensed and finally expanded into vacuum, so there is time in the order of minutes for the transfer of states to happen.

Since due to their increased number the vibrons of o-H_2 now have a higher probability of traveling to an adjacent same-species partner, the excitation is shifted to lower wavenumbers, which is in agreement with what we observe.

In the opposite case, p-D_2 has a reduced chance of having another p-D_2 as a direct partner. Hence, this effect assists the shift towards higher wavenumbers for the p-D_2 excitations.

6.1.1.2 Intensity ratio of the isomers

Besides the mean position of the bands, we can analyze the intensity ratio of the isomers $I_{J=1}/I_{J=0}$ of both isotopes as a function of the o-D_2 content. The spectra in the left panel of fig.63 already evidence that this ratio diminishes significantly for deuterium upon dilution. Again, we first approach this effect from a qualitative perspective and make predictions, before looking at the actual data quantitatively.

In the pure ortho-deuterium measurement the $J = 1$ isomers make up only 2.5% of the total molecules. The reason why its bands are clearly visible at all is due to the enormous intensity enhancement up to a factor of 50 (see chapter 2.3.2). We recall that its mechanism is grounded in the slightly lower energy of the $J = 1$ component, which, upon excitation, in a classical picture is able to drive adjacent $J = 0$ molecules, whereas the other way around the movement is inhibited. If we insert increasing amounts of impurities with a very different excitation energy, e.g. H_2 into D_2, the initial intensity enhancement is reduced based on two consequences:

1. The adjacent partners of a $J = 1$ molecule are consequently substituted with impurity molecules that do not perform this resonance, since the excitation energy is far off.

2. Due to the effect of the prior section 6.1.1.1, the energy gap between the $J = 0$ and $J = 1$ excitation grows in the liquid as well as in the solid, which additionally reduces the strength of the resonance effect.

In the case of a very diluted sample, in which the probability of finding $J = 1$ and $J = 0$ molecules of the same isotope as nearest neighbors is low, the intensity enhancement should almost completely vanish. Hence, the intensity ratio of the isomeric bands of this diluted isotope should approach its natural value according to the actual content of the two isomer species. We note that, this is expected to happen regardless of the impurity substance, as long as there is no vibrational excitation energy close to the respective bands.
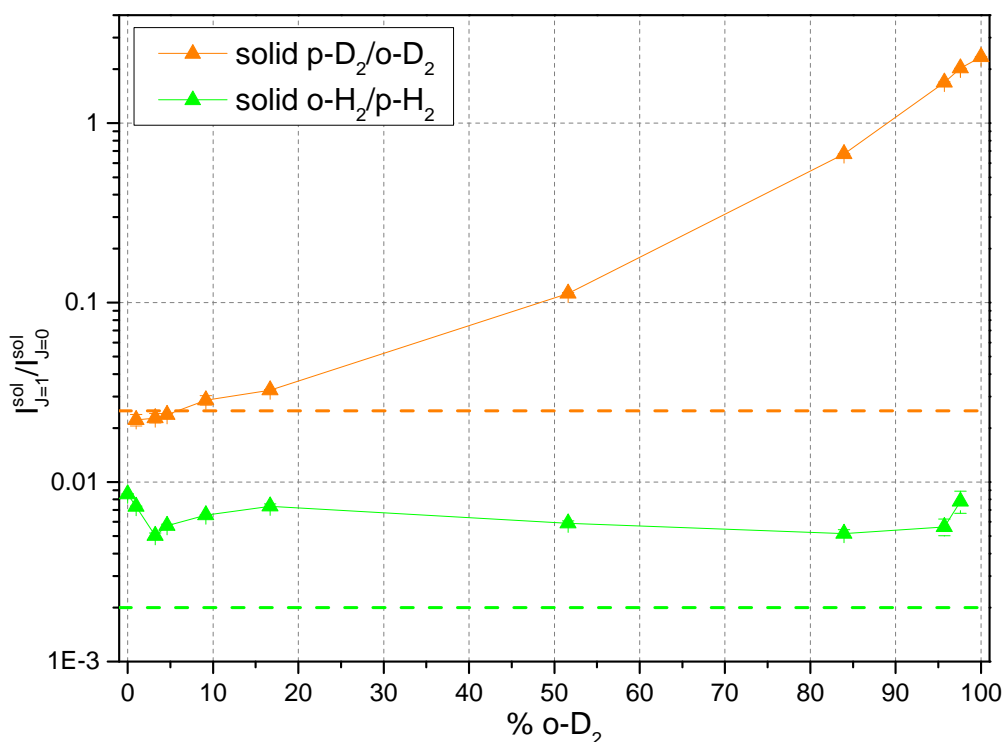

Figure 65: Intensity ratios in logarithmic scale of the solid bands $I_{J=1}/I_{J=0}$ for deuterium (orange) and hydrogen (green). The horizontal dashed lines in the same color represent the expected actual number ratio after conversion with $N_{J=1}^{oD2} \approx 2.5\%$ and $N_{J=1}^{pH2} \approx 0.2\%$.

The intensity ratio for the solid bands $I_{J=1}^{sol}/I_{J=0}^{sol}$ of the completely solidified filaments, i.e. the solid line spectra in fig.63, is plotted for deuterium (orange) and hydrogen (green) as a function of the o-D_2 content in fig.65. An extraction of the intensity ratio of the liquid bands is not possible, because in deuterium the overlap of these bands prohibits any reasonable separation and in hydrogen the $J = 1$ band is too weak and broad to distinguish it confidently from the noise of the background.

Looking at the deuterium plot in orange, we clearly see the decrease of the intensity ratio from the pure substance (right) to increasing impurities (further left), as predicted in the above explanation. At high dilutions (very left), the ratio approaches the actual amount of p-D_2 relative to o-D_2 in the sample (dashed orange line) and seems to reach

even values below.

The hydrogen ratio in green, however, exhibits a different, unpredictable behaviour. Upon diluting pure hydrogen (left to right), the data points do not signal a trend towards the real ratio at lower values (dashed line), but yield a rather arbitrary progression with a factor of 2 between the maximum and minimum values. The point with the highest dilution on the very right even carries a similar value as the pure substance.

The most likely explanation for the behaviour of the hydrogen plot is the increase of the total amount of $J = 1$ states through the introduction of fully converted deuterium, which we already utilized to explain the shift of o-H_2 towards lower wavenumbers in the previous section 6.1.1.1. Based on EQQ interaction, the $J = 1$ state is able to transfer onto adjacent molecules and through statistical equilibration the amount of $J = 1$ on hydrogen molecules increases.

This effect is able to counter the decreasing intensity enhancement for o-H_2 stated in the beginning. As a consequence, if we assume that in the highest diluted mixture 2-98 (right data point) almost no intensity enhancement occurs for H_2, the actual amount of $J = 1$ molecules in hydrogen would be the value of this data point, i.e. $\approx 0.8\%$ instead of the fully converted 0.2%.

Further indications for a statistical transfer of $J = 1$ onto hydrogen is provided by the deuterium intensity ratio (orange) at low mol fractions (left hand side), which is at values below its physical conversion limit of 2.5% (dashed line).

6.1.1.3 Peak structure of the solid

We now turn to the multi peak structure of the solid band, which emerges for each p-H_2 and o-D_2 upon high dilutions (compare fig.63).

For a detailed view, the ortho-deuterium solid band is plotted in fig.66 for various low concentrations. With increased dilution of deuterium (orange to green), the broad band on the left shifts to the right. Additionally, a growing second peak on the very right appears. In contrast to the rest of the solid band, this peak does not experience a significant shift with further dilution.

In section 6.1.1.1 we stated that a vibrational band structure shifts towards higher wavenumbers with increasing dilution, because statistically less partners of the identical species are adjacent to the excited molecule and the free traveling of the vibrons is progressively hindered. At low mol fractions the probability increases that molecules of this substance have only 1 partner of the same species or are even completely singled out. The peak structure that we observe in fig.66 can be related to this circumstance.

Evidence for this is provided by measurements of isomeric mixtures o-H_2−p-H_2 in [78]. In those experiments, a similar structure for the diluted isomer was observed. Our peak with steady position on the very right probably comes from molecules without any nearest neighbors of the same species ($nn = 0$ or monomers). It is obvious that the lower the content of a substance is, the higher is the chance of finding those molecules singled out. It can be calculated for a random distribution (see later section B.3) that in the most extreme mixture 99-1 the majority, i.e. almost 90% of o-D_2 molecules is situated in this type of isolated environment. In the corresponding spectrum almost the entire intensity of the band is accumulated in this peak, confirming this estimation. Since for every molecule in this situation the nn environment is completely equal, i.e.
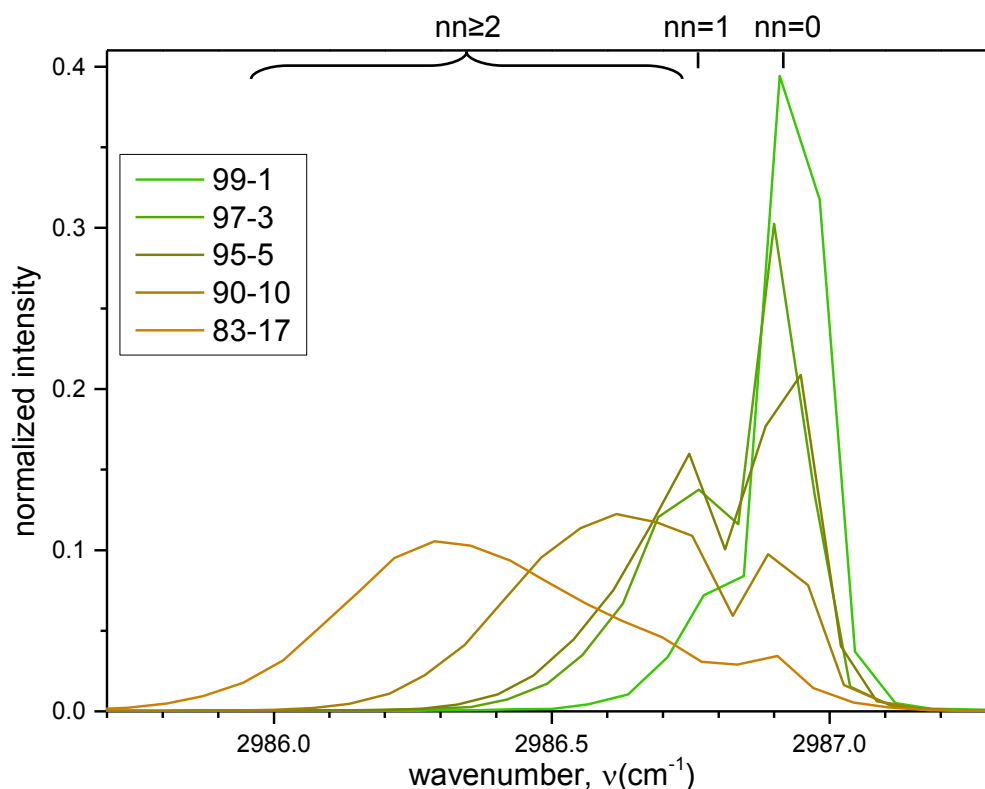
Figure 66: Close view of the structure of the solid o-D_2 band at high dilutions ranging from 1 to 17% o-D_2. The ticks and region at the top indicate the number of o-D_2 nearest neighbor (nn) molecules (see text).

they are surrounded only by molecules with a very different excitation energy, the vibrons generated by this configuration yield always the same energy[1]. As seen in the figure, this excitation does not move, is sharp and within spectrometer resolution, visible at the edged shape coming from single wavenumber data points.

The next higher configuration is an o-D_2 molecule with 1 adjacent same species partner. Since the vibron is able to induce a resonance on this partner, its energy is slightly lower, indicated by $nn = 1$ in fig.66. However, the absolute vibron energy of such a pair, or call it a (isomeric+isotopic) dimer, is not as sharp as in the above case of a monomer, because

- the intermolecular distance between the two molecules may vary and

- there may be additional same-species molecules adjacent to the second partner.

Regarding the first point, it is likely that the mean intermolecular distance changes between the mixtures, based on the different number density of (pure) hydrogen and (pure) deuterium. This is surely true for the mean distance in the liquid, but probably also applies to the lattice constants in the crystals (more to this later in chapter 6.2). Yet, even in the same measurement the distance between pairs of molecules may change

---

1 The energy may only be influenced slightly by variations in the intermolecular distance to the neighbors due to number density/temperature. Yet, since the vibration does not interact with the neighbors, the effect should be minor.

based on the actual environment. Since the vibron depends on this distance, the energy is not as clearly defined as in the previous monomer case.

The second item on the list takes into account that the adjacent same species partner of the excited molecule may have additional partners of the same type that are not nearest neighbors of the main excited molecule. These constructs are actually roughly linear trimers or chains of even higher order, yet are excited not in the middle but at one end. In that case the vibron can travel further opposed to just a dimer and its energy is lower, yet with a diminishing effect due to the intrinsic limited range of vibrons.

Combining both points we conclude that vibrons originating from dimers and higher order constructs do not have a definite energy like the monomer, but a spectrum of energies and therefore produce a broad Raman band, which we see in the spectra 66 marked with $nn \geqslant 2$. The higher the amount of the impurity is, the greater is the probability for higher order agglomerations and the more the band shifts to lower wavenumbers. In the limit this reaches the perfect symmetry of a pure substance, in which the vibrons can freely travel in all directions.
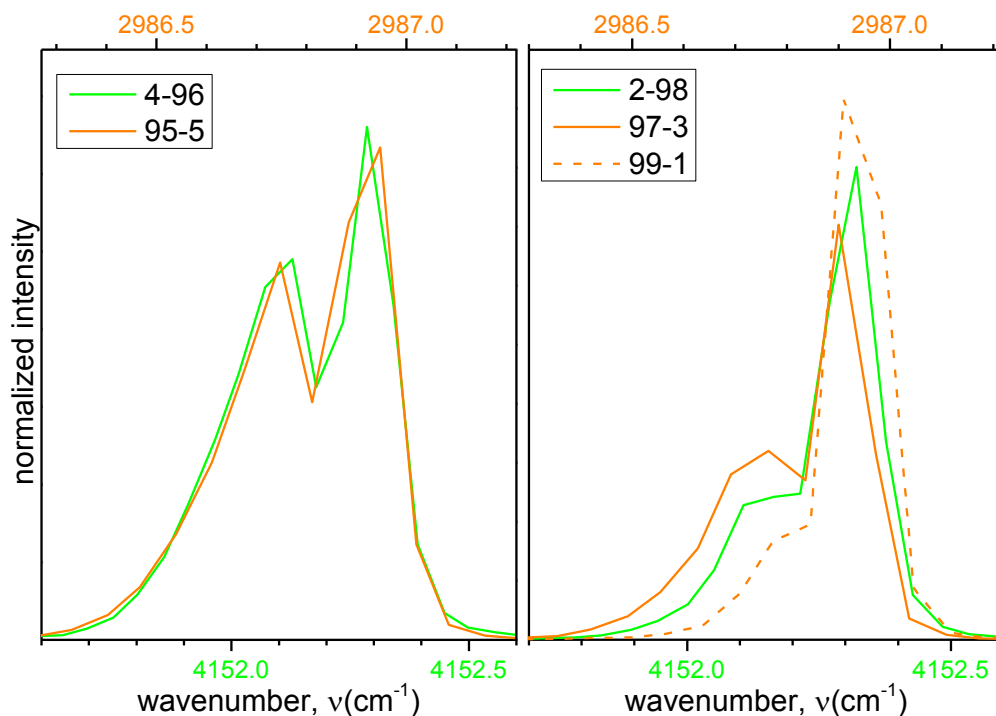

Figure 67: Comparison of the structure of the solid p-H$_2$ (green) and o-D$_2$ (orange) bands at similar dilutions, $\approx 5\%$ (left panel) and $\approx 2\%$ (right panel).

As we now know the origin of the multi peak structure of highly diluted substances, we go on with comparing this structure of o-D$_2$ and p-H$_2$ at similar mol fractions, shifted on top of each other in fig.67. In the left panel the p-H$_2$ (green) and o-D$_2$ (orange) contents are $4.3 \pm 1.1\%$ and $4.6 \pm 0.6\%$, respectively. The corresponding solid band and especially the ratios between the $nn = 0$ and $nn \geqslant 1$ peaks are almost entirely equal. In the right panel there is p-H$_2$ at $2.4 \pm 0.6\%$ (green) and o-D$_2$ with $3.2 \pm 0.4\%$ (solid orange) as well as $1.0 \pm 0.1\%$ (dashed orange). This impurity content of the para-hydrogen spectrum is in between the ortho-deuterium ones and this is consistent with what we see in the figure. Whereas the solid orange line shows more molecules situated

in $nn \geqslant 1$ and less in $nn = 0$ with respect to the green solid spectrum, the dashed orange one is just the other way around.

Both panels indicate that o-D_2 and p-H_2 behave similarly when inserted as an impurity in their isotopic counterpart in terms of their same-species nearest neighbor distribution. Unfortunately, we are unable to fit these spectra, to extract absolute values for the amount of single molecules, pairs, etc., because the peaks are overlapping and are constituted of too few wavenumber data points to be reconstructed reasonably. For example, test fits for the spectra on the left yield relative areas of the $nn = 0$ peak of $30 - 60\%$, depending on the shape, allowed width and position of the $nn \geqslant 1$ peak. Hence, we are unable to state, if the impurities tend to form clusters or are randomly distributed within the main substance. However, we will come back to this, when discussing the rotational region in chapter 6.2.2.

6.1.2 Summary: Band positions, intensities and structure

Compared to the pure substances, in the mixtures we experience a shift of the mean vibrational positions of the liquid and solid bands for both deuterium isomers and para-hydrogen towards higher wavenumbers upon dilution (fig.63 on p.143). This is based on the reduced capability of vibrons to travel freely, because adjacent same-species partners are consequently replaced by molecules with a different excitation energy, onto which the vibrons are not able to hop.
Contrary to the other species, the ortho-hydrogen bands exhibit a slight shift to lower wavenumbers, probably because the increased amount of $J = 1$ states introduced by deuterium is transferred and leads to a higher ortho-hydrogen content in the mixtures than in the pure substance.

For deuterium, the intensity ratio of the solid $J = 1$ to $J = 0$ bands decreases upon dilution (fig.65 on p.148), which grounds in the resonance effect, that is responsible for the strong intensity anomaly in the first place, being reduced. Reasons are the the growing energy gap between those isomeric excitations and the decreasing probability or amount of deuterium molecules being placed as nearest neighbors. At high dilutions the intensity ratio approaches its natural value according to the actual $J = 1$ content. Hydrogen does not show a clear trend towards the equilibrium $J = 1$ content with more impurities, but rather remains above it. This is related to the increasing $J = 1$ content introduced by deuterium and being statistically transferred onto hydrogen.

When highly diluted, the solid structure for both o-D_2 and p-H_2 develops an additional peak at higher wavenumbers, which is at a constant position independent of the mixture (fig.66 on p.150). Likely, $J = 0$ molecules which are completely surrounded by foreign molecules produce always this same excitation energy, because the vibrons are not able to travel.
o-D_2 and p-H_2 reveal the same solid structure at similar dilutions, indicating that the isotopes behave equally with regards to their local distribution in the main substance.

6.1.3 Temperature of the liquid

6.1.3.1 Temperature gradient of p–H$_2$ at low o–D$_2$ contents

For the pure para-hydrogen filaments we evidenced a temperature gradient of the liquid from low temperatures at the surface to higher temperatures in the core due to the interplay of evaporative cooling and heat conductivity (see chapter 4.1.1). This section governs, how this gradient evolves, when increasing ortho-deuterium impurities are inserted.
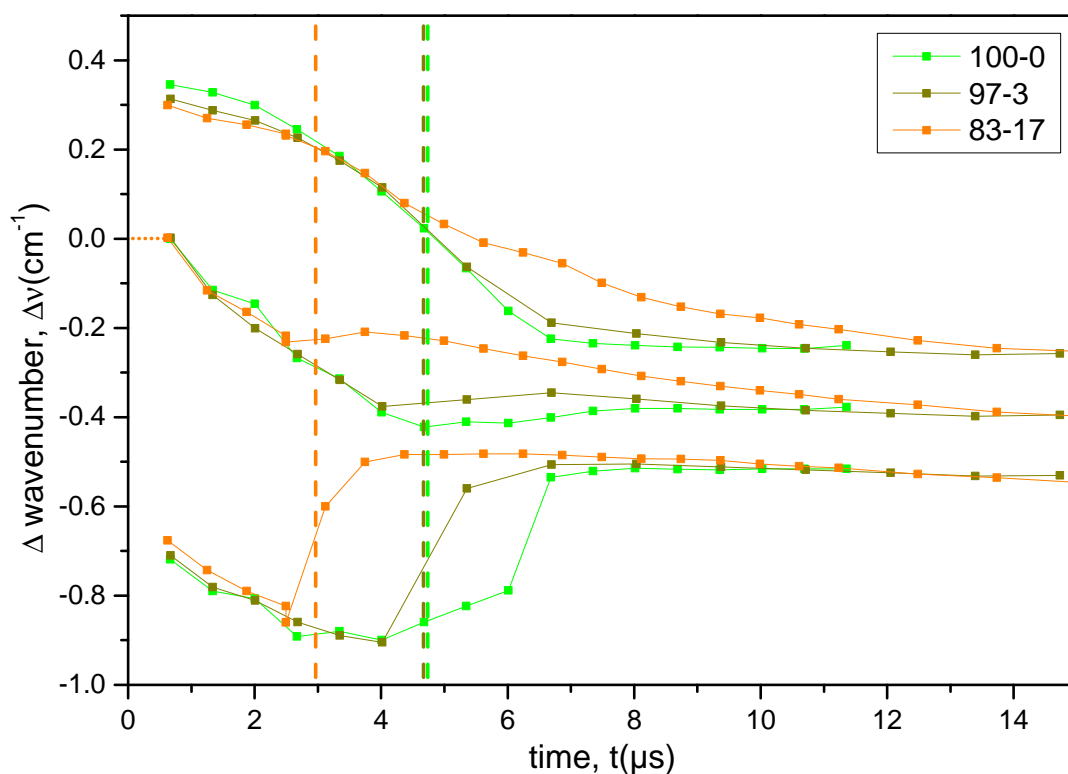

Figure 68: Comparison of the wavenumber gradient of the liquid p-H$_2$ band for several mixtures, shifted to be $\Delta v = 0$ for the first data point of the mean wavenumber. The corresponding dashed lines mark the onset of crystallization.

In fig.63 on p.143 we observe for dilutions $< 20\%$ o-D$_2$ a broad liquid p-H$_2$ band structure similar to the pure p-H$_2$ case. As stated in section 6.1.1.1 this band shifts towards higher wavenumbers upon dilution so that the Vilesov formula used for extracting actual temperature values cannot be utilized. However, we are able to apply the preceding step, which is extracting the mean wavenumber position of this band as well as the highest and lowest wavenumber based on the inflection point method introduced in chapter 4.1.1.1.

In fig.68 the temporal evolution of the relative shifts of these three values are plotted for the mixtures 100-0, 97-3 and 83-17 from green to orange. The positions are shifted to match the first mean wavenumber to be zero to compensate for the impurity induced shift towards higher wavenumbers.

Comparing the very first spectra taken at $\approx 0.7\,\mu s$ we find that the width of the liquid band, indicated by the difference from the high to the low wavenumber data point, is slightly diminishing for increased impurity. Since all measurements have the same starting temperature $temp2 = 16\,K$, this probably is an effect based on the reduced traveling options of the vibrons rather than a smaller temperature gradient[2].

In the next time steps up to the horizontal blue dashed line, all three curves for each measurement shift towards lower wavenumbers due to evaporative cooling and heat conductivity and we want to inspect each layer separately. The slopes of the lowest curves, which represent the outer layer, are equal for all three measurements, indicating that the effectiveness of evaporative cooling is similar. It seems that introducing 17% ortho-deuterium molecules does not have a significant influence on the vapor pressure curve of this mixture. Due to the fact that we do not know the equilibrium vapor pressure curve of these mixtures, we are unable to simulate the temperature gradient as we did for the pure substances.

The mean wavenumber (middle) evidences a similarly good agreement between all measurements. Merely the upper curve, standing for the warm inner core of the filament, shows a decreasing slope for higher dilutions. This can be reasoned by the worse thermal conductivity of ortho-deuterium stated in chapter 5.1.1.1, reducing the overall conductivity of the mixtures towards the core of the filament.

At the orange dashed line at $\approx 3\,\mu s$, the first solid starts to appear for the 83-17 mixture and its lowest and mean wavenumber/temperature increase, so that the comparison ends. The 97-3 measurement reaches lower temperatures in the lowest and mean curve, until it meets the same fate at $\approx 4.5\,\mu s$. We conclude that up to the appearance of the crystal the temperature gradient evolution of the liquid p-H_2 band and particularly the evaporative cooling curve is similar for o-D_2 impurities up to 17%.

The occurrence of the first solid will be discussed in a later chapter 6.1.5.5. However, for all three measurements in fig.68 we notice that an increase due to the heat of solidification occurs and that this is strongest for the lowest wavenumber curves. This indicates that, similarly to the pure p-H_2 case, the solid starts to form at the coldest spots situated at the surface of the filament.

It would be interesting to also analyze the temperature gradient at the opposing mixtures with high o-D_2 amount. Unfortunately, a comparison even of the mean temperature of the liquid deuterium band is not possible, because the $J = 1$ and $J = 0$ bands overlap and as evidenced in chapter 6.1.1.1 the intensity ratio decreases, what results in uncorrectable systematical errors in the mean position of the combined band. It is expected that evaporative cooling becomes more effective upon introducing p-H_2 into o-D_2, which bases on the significantly higher vapor pressure of the lighter isotope at these higher starting temperatures of $\approx 20\,K$. Additionally, the temperature gradient compared to pure o-D_2 should get slightly less pronounced due to the higher thermal conductivity of hydrogen.

---

2 The shrinking of the width is also visible at even higher dilutions in fig.63 additionally to the increasingly blurred structure. Therefore no wavenumber gradient is extracted for those mixtures.

6.1.3.2 Mean temperature of the liquid during solidification

An important information is given by the temperature during solidification, since we have seen for pure para-hydrogen in chapter 4.1.3.5 that this temperature of the liquid influences the growth velocity of the crystal u. We are unable to extract absolute temperature values for the mixtures, because the Vilesov formula does not apply. Hence, in a first approximation we estimate the temperature in comparison to the pure substances.

For the pure para-hydrogen measurement 100-0 the mean temperature at the liquid at the start of solidification is determined to be 13 K with the Vilesov formula, in agreement with the temperature simulation. During solidification, this temperature increases slightly at first, but then goes down to 13 K again (compare fig.34 on p.85), so that we treat this value as constant during solidification.
For pure ortho-deuterium (0-100) the simulation yields 17.5 K at the occurrence of the first solid. Although we cannot extract temperature values, the mean position of the liquid band then basically reproduces the behaviour of pure p-H_2 and finishes slightly below the starting value (compare fig.54 on p.123), so that 17.5 K are the assumed mean temperature during the growth of the crystal.
In the previous section it was shown that at least up to 17% o-D_2 content the temperature gradient of mixtures, including evaporative cooling and thermal conductivity, behaves similarly to the pure para-hydrogen case. Combining all above statements, we assume a linear relationship for the mean temperature of the liquid during solidification for the mixtures depending on the fraction x of o-D_2:

$$T_x^{mean} = 13(1-x) + 17.5x \,[\text{K}] \tag{6.2}$$

To evaluate the validity of the above temperature estimation, we take a look at the behaviour of the wavenumber position of the liquid p-H_2 band from the mixtures at different time stages as a representation of the mean temperature.

In the previous section 6.1.1.1, we found that the p-H_2 bands shift towards higher wavenumbers as a function of the o-D_2 mol fraction, mainly due to the reduced traveling options of vibrons. In particular, the solid and liquid exhibit an almost linear shift with only a slight curvature to lower wavenumbers for intermediate mixtures (compare blue dashed line in the right panel of fig.64 on p.145). The positions of the liquid band in that figure are deduced from the first spectra, i.e. shortly after exiting the nozzle, and therefore correspond to the warmest temperature of each series, which probably still is above the solidification temperature. These wavenumber positions of the very first spectra represent the warm liquid and are our first reference points.
As additional reference points, we use the position of the liquid band of the mixtures at another specific incident. In the measurements of the pure substances we observed that regardless of the source conditions (P_0, d_0 and T_0), the peak position of the last liquid shortly before complete solidification ($s_f = 90\%$) always is at the same position (e.g. see fig.28 on p.75). Since this remaining liquid transforms into the solid shortly after, its temperature has to be below the melting point. Hence, we extract this wavenumber position of the last liquid band of p-H_2 from all mixtures as a temperature reference for a cold liquid that is about to solidify.
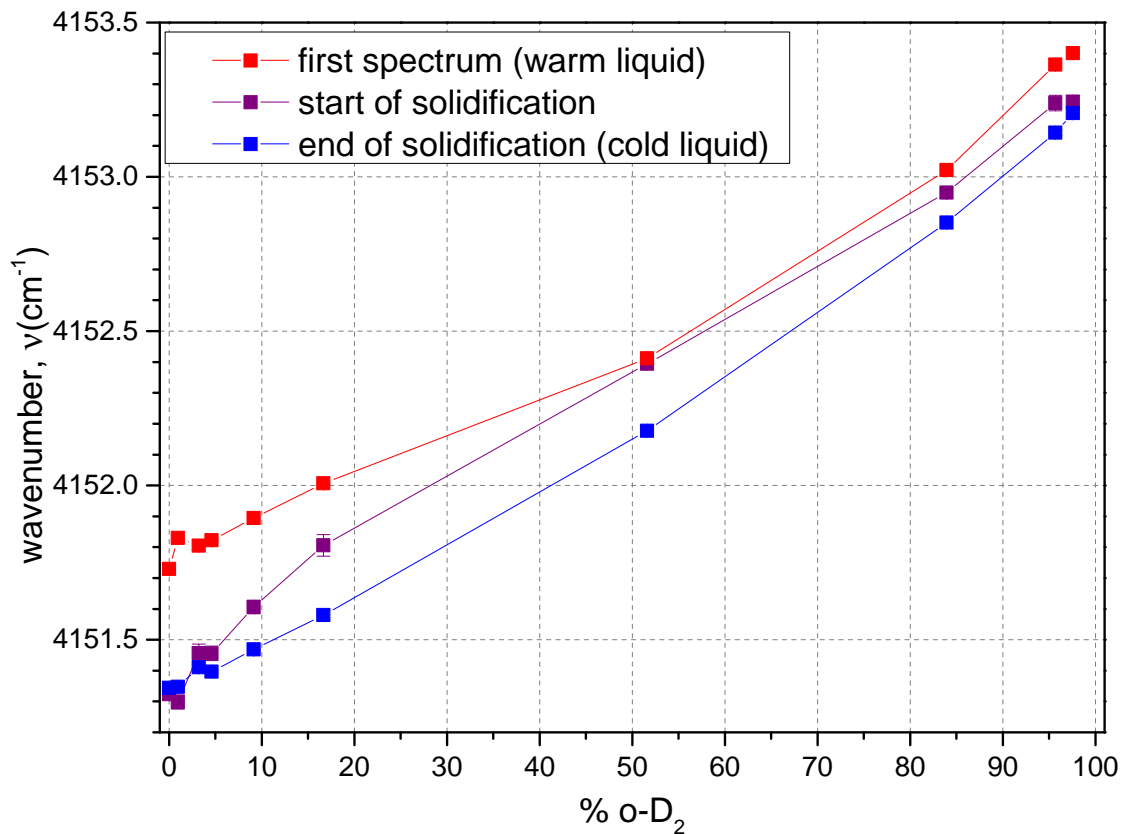
Figure 69: Mean position of the p-H$_2$ liquid band in the first spectrum (red), at the start of solidification (purple) and at almost complete solidification (blue).

These mean position of the p-H$_2$ liquid band for the first spectra (warm liquid) as well as shortly before complete solidification (cold liquid) are plotted in fig.69 as red and blue squares, respectively. The red data points are roughly in a straight line, the variation mainly coming from the the not linearly increasing starting temperatures of the filaments (see `temp2` in table 6 on p.141).

The blue plot reveals an almost linear behaviour, very similar to that of the solid band in fig.64 even with the slight trend towards lower wavenumbers for intermediate mixtures[3]. Since that solid is estimated to be at the limit temperature of evaporative cooling, the similarity indicates that the temperature of the last liquid also depends linearly on the composition. This finding confirms that at least for the late stages of solidification our linear approximation for the mean temperature of the filament in eq.6.2 estimates correct values.

To see, if the temperature estimation of eq.6.2 is justified for the whole crystallization process, we additionally extract the mean wavenumber of the liquid band at the start of solidification (plotted in purple), which in the time evolution of course lies in between the former red and blue points. As mentioned in the beginning of this section, for the pure substances the temperature at this event is roughly the same as for the last liquid,

---

3 The convergence of the red and blue curve towards higher dilutions stems from the intrinsic narrowing of the p-H$_2$ liquid band due to limited traveling options of vibrons, making the temperatures correspond to a smaller wavenumber interval.

evidenced in fig.69 by the overlap of the purple and blue data points at the very left and right. However for the intermediate p-H$_2$—o-D$_2$ mixtures, its position and therefore temperature is increasingly above that of the last liquid, approaching even the warm liquid for the equimolar mixture. The reason for this warmer liquid is that in these intermediate mixtures the first solid appears much earlier, resulting in a shorter cooling time. This will be extensively covered in the later chapter 6.1.5.5.

What we can actually conclude from this analysis is that the mean temperature of the liquid during solidification is not constant for mixtures. For the start of of solidification, this mean temperature is higher than suggested by formula 6.2, especially for intermediate mixtures. However, it is important to note that in this consideration we only talk about the average temperature. Of course, there is a temperature gradient across the filaments, so that the liquid that currently transforms at the liquid-solid-interface probably is colder than this average.

Towards the end of solidification, when the mean wavenumber of the band actually represents the presently transforming (last) liquid, the temperature approaches the predictions of eq.6.2 for all isotopic compositions. Hence, we stick to said formula and estimate a linear relationship between temperature and o-D$_2$ concentration, but keep in mind that the actual temperature during solidification may be higher for intermediate impurity amounts.

6.1.3.3   Comparison to the binary phase diagram

The statement of the previous section that the mean temperature of the liquid for near equimolar mixtures may be higher than estimated by eq.6.2 leads to interesting consequences. We recall that the mixtures of p-H$_2$ and o-D$_2$ construct a binary phase diagram (compare fig.8 on p.25) that consists not of a single melting line, but of a liquidus and solidus line instead. Equilibrium conditions situated in between these two lines lead to stable coexisting liquid and solid phases with different contents of the isotopes.

The binary phase diagram is plotted again in fig.70 as well as the experimental temperature readings `temp2` (red) of all mixtures. Although we do not know the actual correspondence wavenumber↔temperature of the liquid, this graph is comparable to the previous fig69. In the latter, the wavenumber positions of the liquid band right after exiting the nozzle (red) correspond to slightly lower values than the starting temperatures `temp2`, because the filament already has cooled traveling 50-100 µm. As mentioned, the wavenumber positions of the last liquid in blue probably agree with eq.6.2, which is plotted as a blue dashed line in fig70.

When we now look at the position of the liquid at the start of solidification in purple in fig.69, these points may very well lie within the coexistence region between the liquidus and solidus in fig.70, especially for the equimolar mixture. This indicates that conditions during crystallization may favor a (partial) phase separation of the isotopes. However, note that there is a substantial difference of the phase diagram to our data here. The phase diagram only predicts the behaviour of the equilibrium phase and for changes in thermodynamic conditions, e.g. lowering the temperature, it takes in the order of minutes for the mixtures to reach the new equilibrium conditions. We on the other hand observe the actual phase transition at far off-equilibrium conditions at time
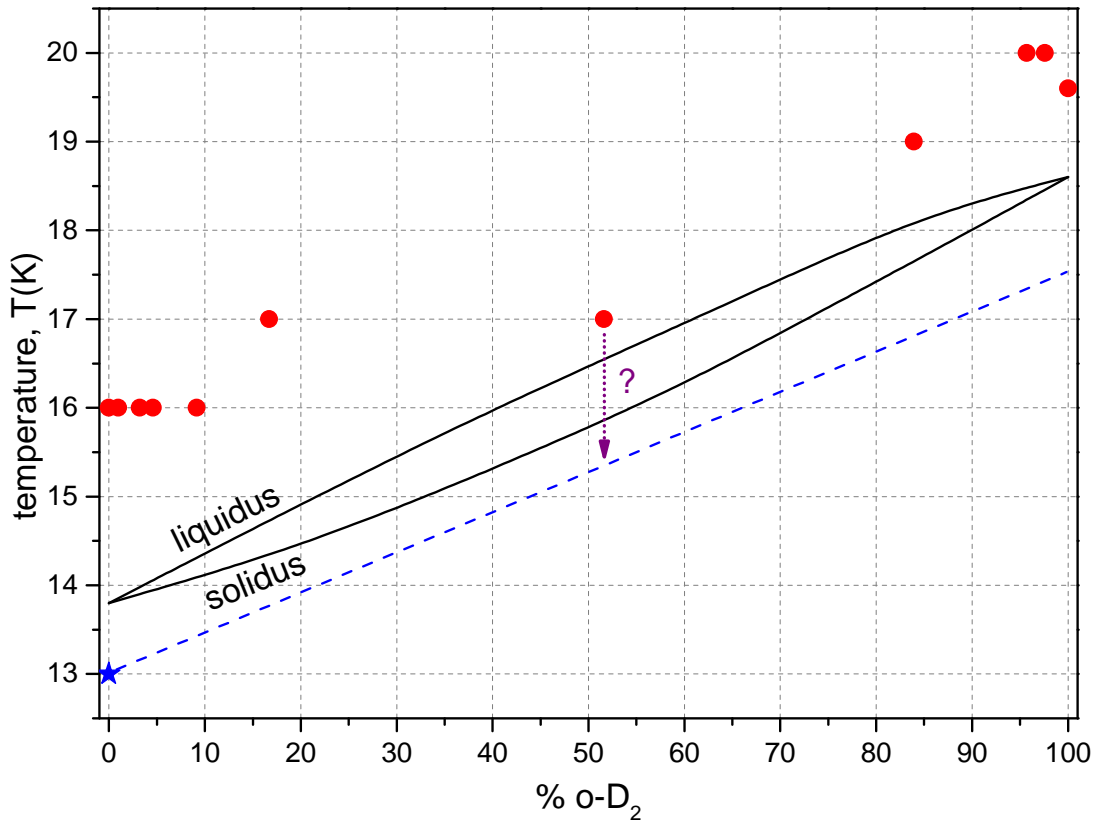
Figure 70: Temperature of the sensor `temp2` for the various mixtures as red circles. The black lines represent the solidus and liquidus lines of the corresponding binary phase diagram. The blue star marks the measured mean temperature of pure p-H_2 during solidification and the blue dashed line the estimate for mixtures according to eq.6.2.

scales of microseconds. Therefore the slow equilibration process does not necessarily have to apply to our experiment.

Yet, the macroscopic partial phase separation, with higher contents of o-D_2 in the solid phase, at equilibrium conditions is the result of microscopic events. This signals that at a constant temperature within the liquidus-solidus region o-D_2 probably has a higher tendency to join the crystalline phase than p-H_2 has. This is understandable, because o-D_2 is supercooled with regard to its pure melting point, whereas p-H_2 is not. It may very well be that this different tendency also plays a role in the dynamic crystallization phase. This will be an important sign to look for in the discussion of crystallization following later on.

6.1.4 Summary: Temperature of the liquid

Comparing the wavenumber gradient of the liquid band of pure p-H_2 with respect to mixtures containing small amounts of o-D_2 reveals a similar behaviour of the temperature gradient evolution of the corresponding filaments (fig.68 on p.153). In

detail, the evaporative cooling seems to be not influenced significantly by introducing small amounts of o-D$_2$ and only the heat conductivity towards the core may be slightly worse. We are not able to determine the influence of p-H$_2$ impurities inserted into o-D$_2$, which may be more drastic in terms of cooling based on the higher vapor pressure of the lighter isotope at the higher starting temperatures.

For estimating the mean temperature at solidification for the mixtures we propose a linear relationship interpolated between the temperatures of the mean substances, that are confirmed by simulation and experiment in the previous chapters. The measured wavenumber position, i.e. the temperature, of the last liquid towards the end of solidification is in agreement with this proposed linear relationship (fig.69 on p.156). Yet, the mean temperature at the start of crystallization is above these values in intermediate mixtures due to their earlier freezing times (discussed later). As we are unable to extract temperature gradients, the actual temperature at the interface may however be lower than the discussed mean temperatures.

Based on the binary phase diagram and especially the partial phase separation in the region between the liquidus and solidus lines (fig.70 on p.158), there may be a different behaviour of o-D$_2$ and p-H$_2$ molecules during solidification. In particular, the tendency to join the crystal may be lower for the heavier isotope, due to the (stronger) supercooling with regards to their melting points in the pure substances.

6.1.5 Solid fraction

This section contains the most interesting findings regarding mixtures of p-H$_2$ and o-D$_2$, however also the most complicated to interpret and the results are not fully understood.

In each mixture the solid fraction is extracted separately for the two isotopes. For pure ortho-deuterium we have seen that the solid fraction cannot be extracted by our standard method used for para-hydrogen and alternative techniques were presented in section 5.1.2.1. Depending on the overlaps of the $J = 0$ and $J = 1$ bands, different procedures are used to deduce the solid fraction from the deuterium vibrational region, which are listed in table 7.

For a systematic approach the information of the data will be provided step by step and at first merely in a descriptive way, starting with the comparison of the solid fraction of the main component with small dilutions (section 6.1.5.1), analyzing the shape of the curves using Avrami fits (6.1.5.2) and evaluating the influence of (starting) temperature (6.1.5.3). We then combine the data from both the solid fractions of each measurement (6.1.5.5), reduce the amount of information by extracting starting and crystallization times (6.1.5.5) and finally compare with data from the small filament (6.1.5.6).
A following extra chapter (6.1.6) is dedicated to the evaluation and interpretation of all above results.

name, #	deuterium	hydrogen
100-0	-	standard, p-H_2
99-1	standard, o-D_2	standard, p-H_2
97-3	standard, o-D_2	standard, p-H_2
95-5	standard, o-D_2	standard, p-H_2
91-9	standard, o-D_2	standard, p-H_2
83-17	maxvalue, o-D_2 liquid	standard, p-H_2
48-52	maxvalue, o-D_2 liquid	standard, p-H_2
16-84	total, o-D_2 + p-D_2	standard, p-H_2
4-96	total, o-D_2 + p-D_2	standard, p-H_2
2-98	total, o-D_2 + p-D_2	standard, p-H_2
0-100	total, o-D_2 + p-D_2	-

Table 7: Methods used of extracting the solid fraction. Standard refers to eq.4.2 on p.85, maxvalue to eq.5.2 on p.127 and total to eq.5.1 on p.125.

6.1.5.1 p–H_2 and o–D_2 solid fraction with small dilutions

For the start, we examine how the solid fraction of p-H_2 is influenced, when increasing amounts of o-D_2 as an impurity are inserted. In fig.71 the corresponding plots for the solid fractions are presented in color code from pure p-H_2 (green) to 83% p-H_2 (orange). The error bars originate from the standard derivative of the 3 to 4 single spectra recorded at each time step and do not exceed $s_f \pm 0.01$.

Although the figure seems a bit crowded, two evident trends are easily recognized. Taking a look at the start of solidification with $s_f < 0.1$, we identify that inserting o-D_2 results in an earlier start of the solidification process. From the pure para-hydrogen measurements we know that this starting time may vary due to disturbances within the filament. Yet, the time for the first solid of the mixture 83-17 is less than half of that of the pure p-H_2 filament and therefore beyond the error bars associated with disturbances, making the correlation starting time $\leftrightarrow$ o-D_2 content unambiguous.
The second peculiarity is that the time it takes for the filament to completely solidify is significantly extended if o-D_2 is inserted. This becomes particularly visible, when we look at the time interval it takes to reach $s_f = 0.9$. The effect is even more severe, when we take into account the above finding that the solidification starts earlier for increased dilution. Combined, this results in twice the duration of the crystallization process for even a small amount of just 3% o-D_2. For the 83-17 mixture this time is tripled.
Additionally, a minor feature is that all presented solid fraction curves exhibit a smooth progress and only small variation in the slope are visible. Hence, the neat behaviour of p-H_2 seems to be uninfluenced by this impurity.

For the opposite case, the solid fractions for pure ortho-deuterium and for dilutions with para-hydrogen are plotted in fig.72. The error bars and therefore the variation in between spectra subsequently recorded at each position are slightly larger than in
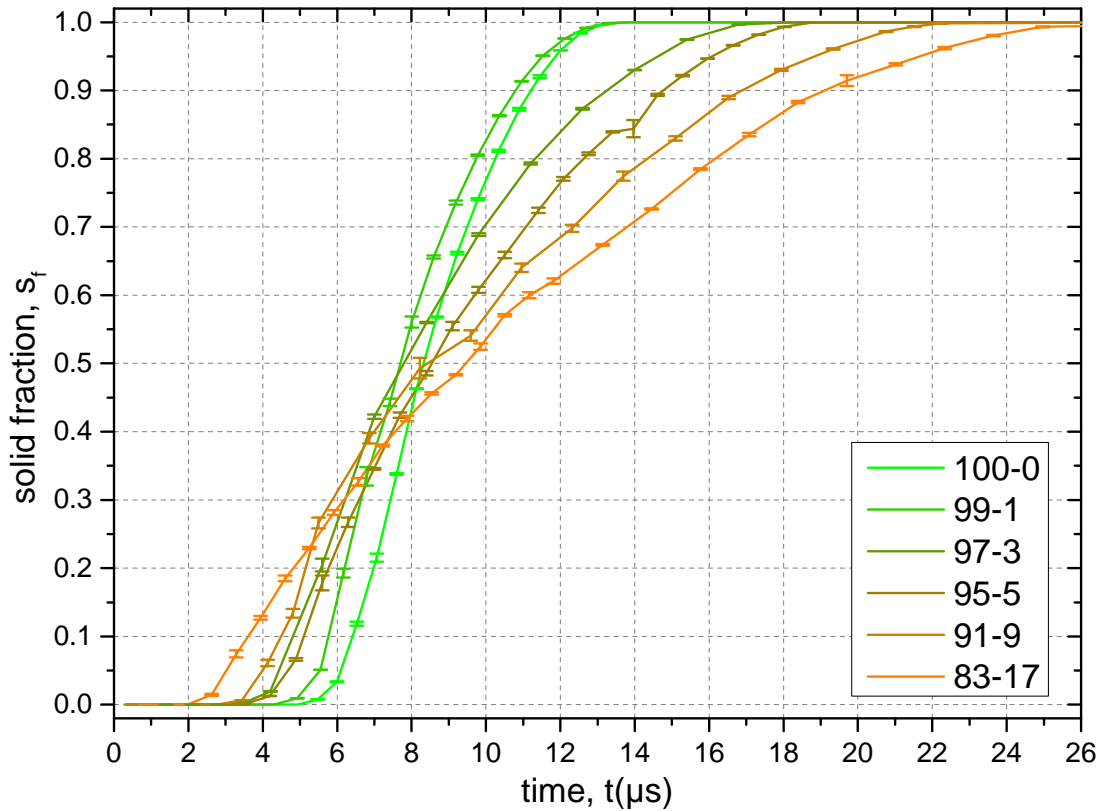
Figure 71: Hydrogen solid fraction of pure p-H_2 (green) and mixtures with low o-D_2 content (towards orange) with error bars from single spectra.

the previously discussed para-hydrogen case. All curves are less smooth, i.e. have a varying increase of the solid fraction, which has already been seen in the pure ortho-deuterium measurements. Yet according to the error bars, this structure is stable for all measurements so that apparently the bumpy progress seems to be inherent and unconcerned by the presence of p-H_2.

Comparing the pure ortho-deuterium measurement (orange) with the one having 2% hydrogen inserted (brown), no clear trend is visible, neither in the start nor in the duration, and the curves even cross each other two times at $s_f > 0.85$. Inserting higher amounts of p-H_2 like 4% (dark green) leads to an earlier appearance of the solid and a slightly longer crystallization process. The final 16% impurity content explicitly endorse an earlier freezing as well as a prolonged solidification, similar to what we have seen for the previous p-H_2 case. However, the progress of solidification seems to have phases with considerably different growth rates, indicated by the variation in the slope of the solid fraction.

All in all, for both p-H_2 and o-D_2 the crystallization starts earlier and lasts longer upon inserting the opposite isotope, yet the effect is significantly stronger for the p-H_2 case. The smoothness of the curves is determined by the main substance.
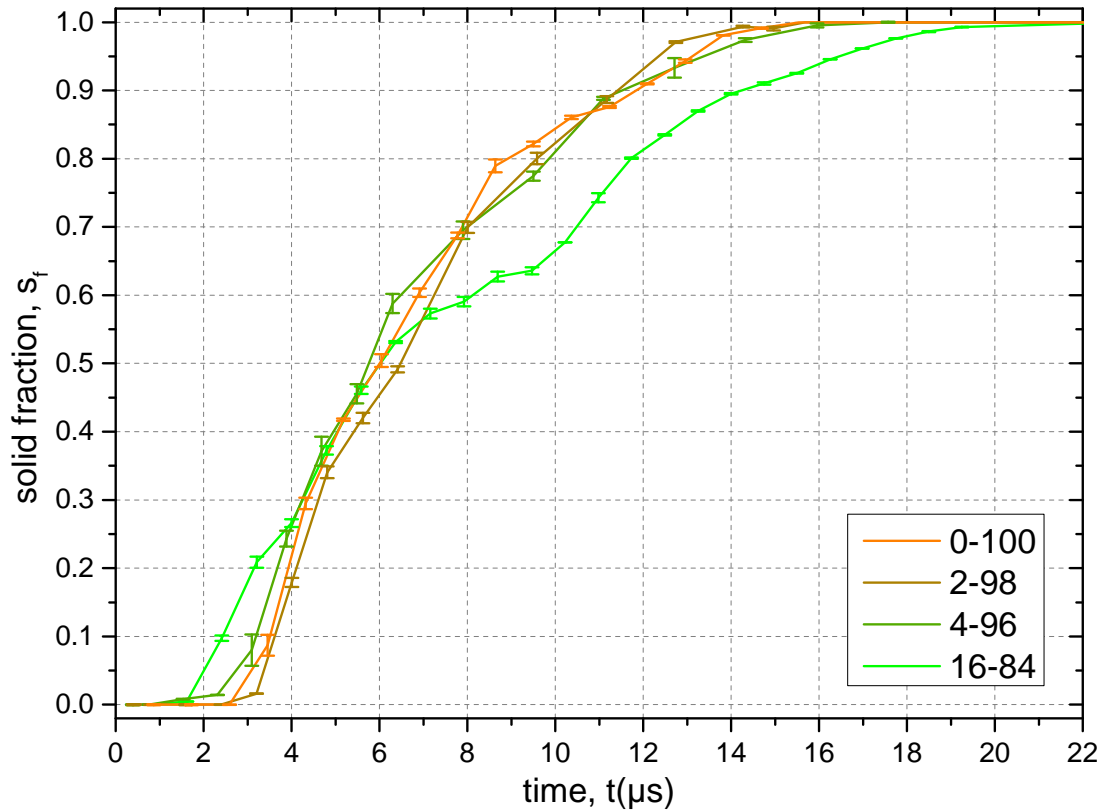
Figure 72: Deuterium solid fraction of pure o-D_2 (orange) and mixtures with low o-D_2 content (towards green) with error bars from single spectra.

6.1.5.2 Avrami fits

To gather more information about the shape of the solid fraction, we can fit the curves with the Avrami equation, as we did in chapter 4.1.3.4 for pure para-hydrogen. Due to the structure within data with ortho-deuterium as the main component, this analysis is only possible for the smooth p-H_2 data with low ortho-deuterium amounts, which is plotted in fig.71. The input data always is the entire p-H_2 solid fraction data set.

The fitting results for the parameters n and k (see formula 2.20 on p.34) are presented as a function of the o-D_2 content in fig.73. Although the accuracy of fitting has to be taken with care and the error bars may be larger, the parameter n clearly yields lower values, when p-H_2 is diluted with o-D_2. This is particularly evident, if we recall that this parameter was almost constant for all pure p-H_2 data with $n = 1.9 \pm 0.1$.
The different values for n are even visible in the shape of the curves in the previous fig.71. Whereas pure p-H_2 in green for $s_f < 0.2$ as well as $s_f > 0.8$ shows a gradual curvature, i.e. increase/decrease in the slope, the 91-9 and 83-17 mixtures rise abruptly but approach $s_f = 1$ very slowly (also compare with the example Avrami plots in fig.13 on p.35). The parameter k in the lower half of fig.73 exhibits less obvious behaviour, yet also possesses a slight trend towards lower values with increasing o-D_2 concentration.

For pure para-hydrogen the fitting value $n \approx 2$ was interpreted as two-dimensional growth towards the center of the filament with nucleation embryos only being formed
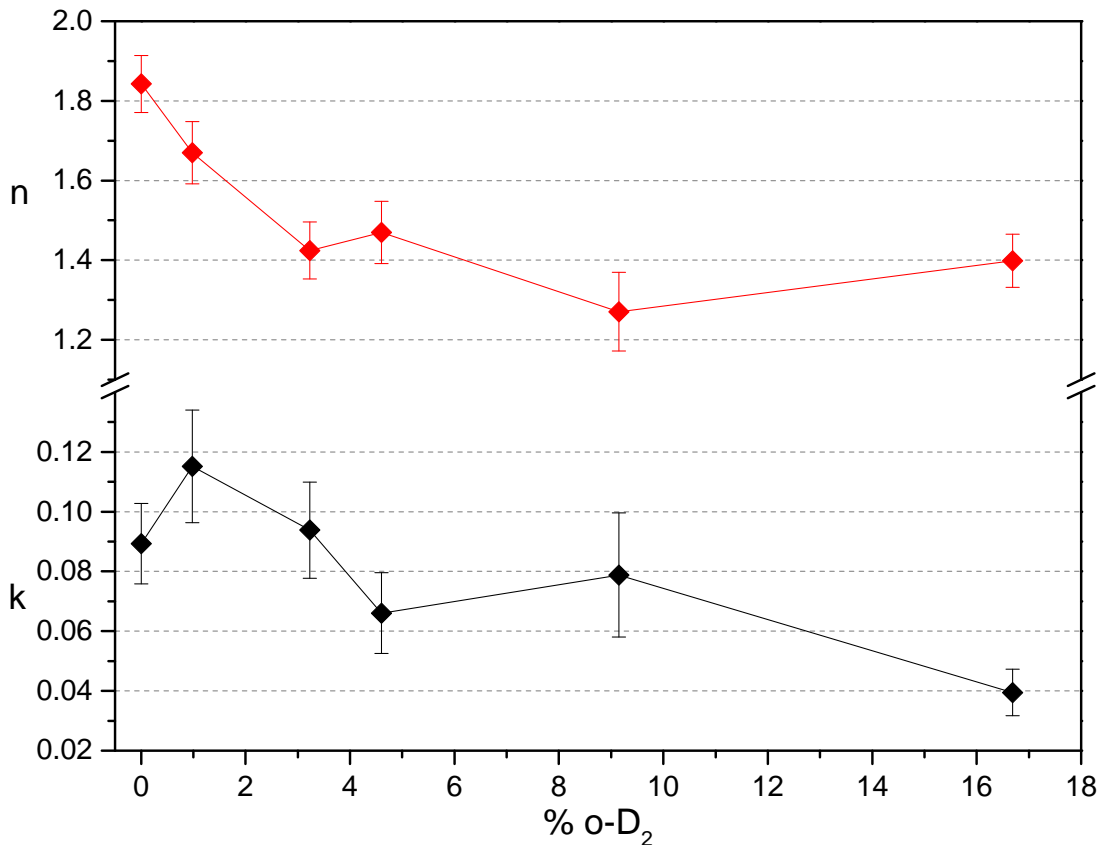
Figure 73: Parameters n (red, upper half) and k (black, lower half) with error bars from the Avrami fits of the p-H$_2$ solid fractions of mixtures with up to 17% o-D$_2$ impurities (fig.71 on p.161).

in the beginning on the surface. Taking into account the evidenced strongest increase in the wavenumber of the outer layer in the liquid in 6.1.3.1 and the fact that all filaments inevitably freeze, it is unlikely that this overall freezing process from outside to inside is different for the mixtures. The value n < 2 for the mixtures thus indicates that the dynamics during the growth itself, i.e. the progression of the liquid-solid-interface, are changed and probably do not conform simply with a roughly constant growth velocity as in the case of pure p-H$_2$ and postulated by the Avrami equation.

It is questionable, if the Avrami fit in its current form is applicable to such conditions and probably the resulting parameters contain increased systematical errors. Nevertheless, this analysis is important as it signals that in mixtures different mechanics participate in the growth dynamics.

6.1.5.3 Comparison: Different starting temperature

To analyze the effect of temperature, measurement 48-52 at `temp2` $= 17$ K has been repeated, yet with a higher initial temperature of sensor `temp2` $= 17.7$ K, labeled 48-52-warm, while the source pressure P$_0$ is the same. The solid fraction as well as the mean wavenumber of the liquid band are plotted in fig.74 as blue and red data points, respectively.
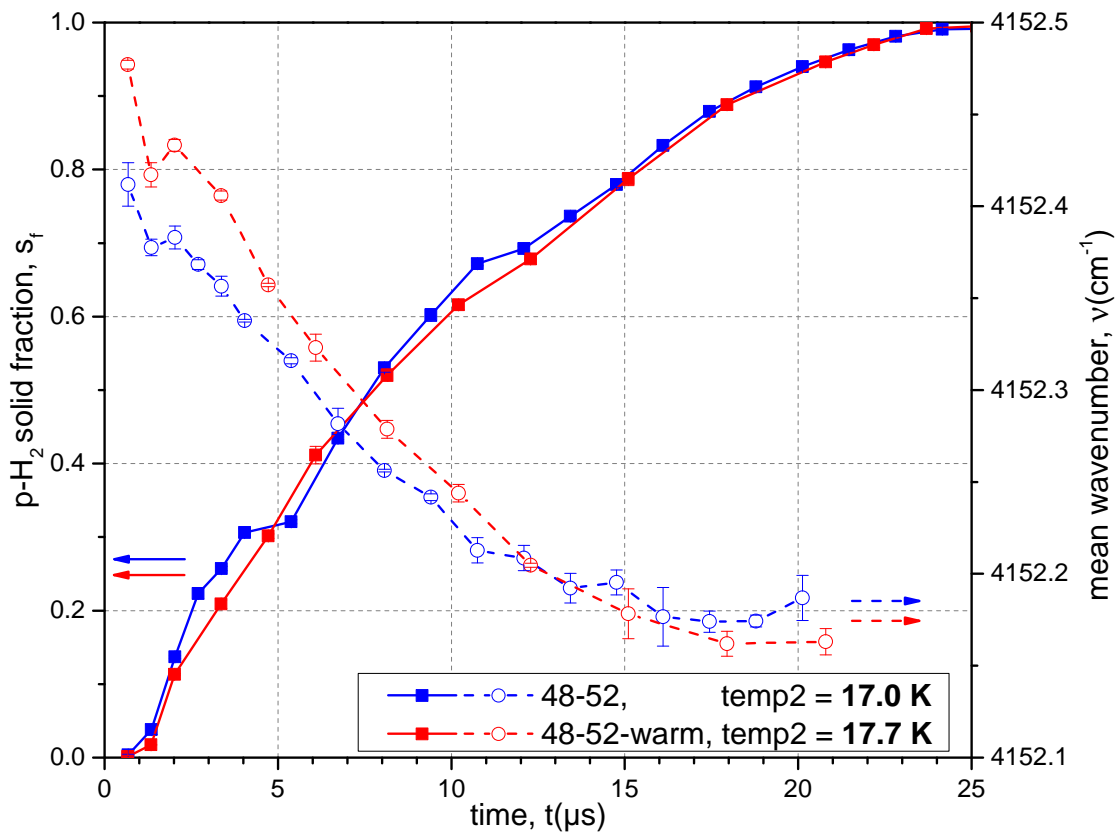
Figure 74: Solid fraction (squares and solid lines, left scale) and mean temperature of the liquid band (hollow circles and dashed lines, right scale) for the equimolar mixtures with starting temperatures $\texttt{temp2} = 17\,\text{K}$ (blue) and $\texttt{temp2} = 17.7\,\text{K}$ (red).

Starting with the mean wavenumber as hollow circles and dashed lines, we clearly detect that in the beginning the values for the measurement with the warmer starting temperature (red) are higher and approach the blue data points at $\approx 12\,\mu\text{s}$, after which they are approximately equal. Hence, during a significant period at the start of crystallization, the liquid of the second data set is warmer by up to $0.7\,\text{K}$.

Comparing the solid fraction (squares and solid lines), we find that the overall process is similar, yet the blue curve shows more structure and is less smooth than the warm one. At $s_f > 0.75$, when the temperature of the liquid is alike, the plots overlap decently. For both plots the first solid is formed almost immediately and independently of the starting temperature. This is expected due to the strong effectiveness of evaporative cooling of the outer layer in the beginning, which with a higher starting temperature only becomes more influential. Most interestingly, the total crystallization time t_{ll-fs} for both measurements is indistinguishable.

Combining the two data sets, we conclude that a higher starting temperature leads to higher mean temperatures of the liquid in the beginning of crystallization, however the solid fraction curve is not altered significantly. Hence, temperature seems to not have a paramount impact on the crystallization time for mixtures. Merely the structure, that indicates time periods with increased growth, may be related to temperature effects.

6.1.5.4 Comparison: p–H$_2$ and o–D$_2$ solid fraction

As stated in table 7, we are able to extract the solid fraction for o-D$_2$ and p-H$_2$ separately for each mixture. This is interesting, because it allows a comparison of the behaviour of the isotopes. Both solid fractions for all mixtures are illustrated in fig.75.

Before we look at the plots in detail, we clarify the validity of these measurements. The vibrational D$_2$ and H$_2$ series are not measured simultaneously, but one after another. By remeasuring spectra at the same z distance at the start and end of each series, it was assured that there is no significant backlash from the manipulator, positioning the nozzle. If occurring, variations in the source pressure P$_0$, which changes the velocity v_0 and therefore the translation distance $\leftrightarrow$ time, have been corrected by calculating the time for each z position individually by the current P$_0$. Remeasured data points after the recording of a whole series at a slightly altered P$_0 \pm 3\,\mathrm{bar}$ and translated into time match the solid fraction curve well. According to above justifications the error bars of the time axis of the two isotopic solid fractions at least relative to one another are negligible.
Systematical errors in the absolute value of the solid fraction are only significant for deuterium due to the less exact extraction method and mainly have impact for the start ($s_f < 0.05$) and end of solidification ($s_f > 0.95$). As discussed in the previous sections, the statistical errors do not exceed $s_f \pm 0.02$, which is roughly the line width of the plots in fig.75. We conclude that all differences in the solid fractions of the two isotopes are expected to be of physical origin.

For the discussion we start at the 5 mixtures with low o-D$_2$ content at the bottom part of fig.75 ranging from 1% to 17%. Except for the 99-1 measurement, for the next 4 data sets on top the o-D$_2$ solid fraction (orange) is above that of p-H$_2$ (green) for the entire crystallization process. Even more, this difference between the two curves is increasing for higher o-D$_2$ contents.
For a detailed view, the mixture 83-17 is pictured in the left panel of fig.76. When around half of the filament has solidified at $t \approx 10\,\mu s$, the difference in the two solid fraction curves is at $\Delta s_f \approx 0.1$. In other words, compared to p-H$_2$ a significantly higher percentage of the o-D$_2$ molecules has already solidified. This is a strong signal for a phase segregation (or fractionation or partitioning [87]) of the isotopic species at the liquid-solid-interface. It seems that for mixtures with p-H$_2$ as the main component o-D$_2$ molecules have a higher tendency to join the solid.
Regarding the initial nucleation process, we are not able to state, to which mol fraction p-H$_2$ and o-D$_2$ contribute to the nucleation embryos, because the higher relative statistical and systematic errors at $s_f < 0.05$ make estimations vague. Furthermore, the first real nucleation sites take up a way too small volume fraction to be detected by this experimental method.

Next, we take a look at the mixtures 48-52 to 2-98 at the top in fig.75. In these measurements, no clear lead of one of the isotopic solid fractions is detected. However, there are still significant differences between the curves. For example, mixture 16-84 exhibits a higher o-D$_2$ solid fraction at the beginning of solidification, whereas later on p-H$_2$ advances with $\Delta s_f \approx 0.1$ two times. In between there are several cross overs and periods of overlap. For the measurement 4-96 the behaviour is different with a huge lead of p-H$_2$ at the start and less variations later on. Hence, fractionation also is
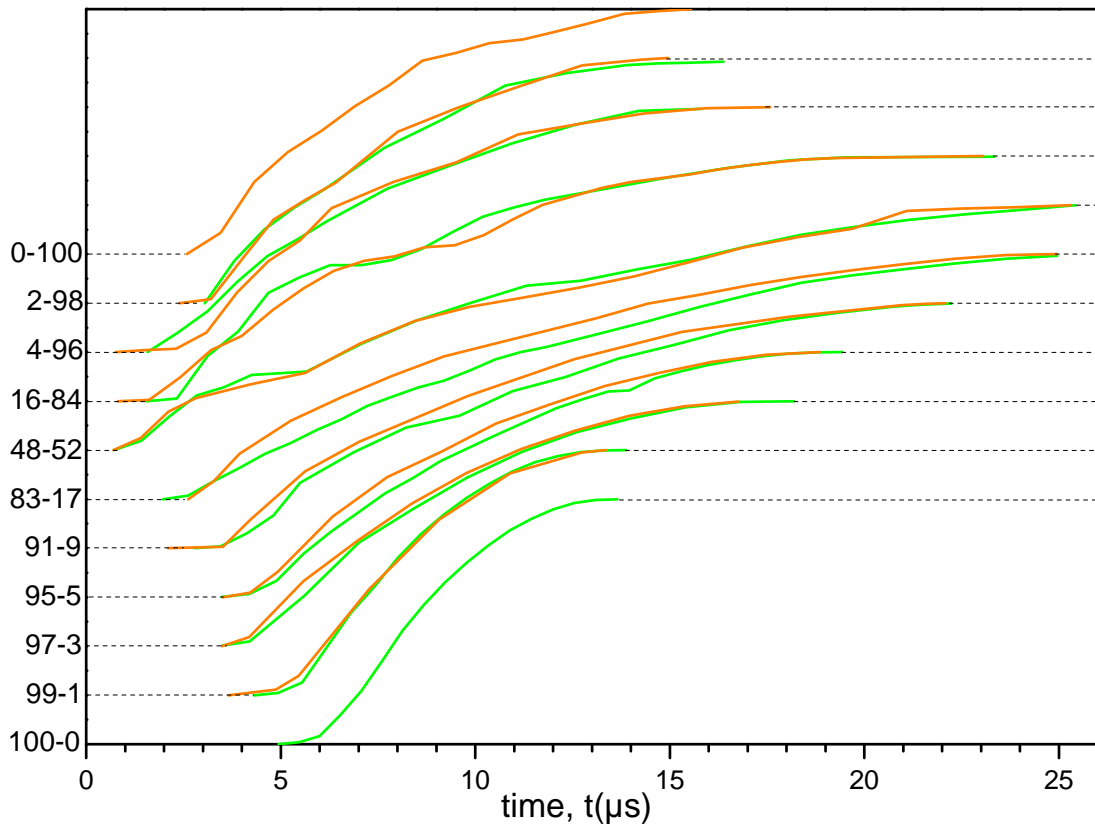
Figure 75: Solid fractions for p-H_2 (green) and o-D_2 (orange) for all mixtures listed in table 7, shifted with increasing o-D_2 content from bottom to top.

obviously happening at high to equimolar o-D_2 content, yet the individual behaviour seems rather arbitrary.

A reason for this might be the rough, not smooth solid fraction already intrinsic to pure o-D_2. Alternatively, the temperature of the liquid may play a crucial rule. In the low o-D_2 mixtures both isotopes, yet especially deuterium, are deeply supercooled below their respective pure substance melting points. In contrast, at high o-D_2 contents, the temperature of the mixed liquid probably is even above the pure p-H_2 melting point of $T_M^{pH2} = 13.8$ K. A detailed discussion will follow in chapter 6.1.6.3.

Further strong evidence for isotopic partitioning combined with a temperature above T_M^{pH2} comes from the mixtures 16-84, 4-96 and 2-98. In these three measurements, the liquid does not entirely transform to the solid phase, but a small amount of the liquid p-H_2 peak remains, which makes up 0.2%, 0.9% and 1.8% of the total para-hydrogen molecules, respectively. The associated deuterium spectra do not exhibit any liquid peak and completely solidify in all measurements. The intensity of this liquid p-H_2 band persists constant to the furthest point measured, which corresponds to almost twice the time for complete solidification of the o-D_2 component. This makes itself present in the p-H_2 solid fraction not reaching the value 1 as illustrated for the closer view of mixture 2-98 in the right panel of fig.76.

The most reasonable explanation for this effect is as following. The temperature of the filament, regardless if liquid or solid, is mainly determined by the major component,
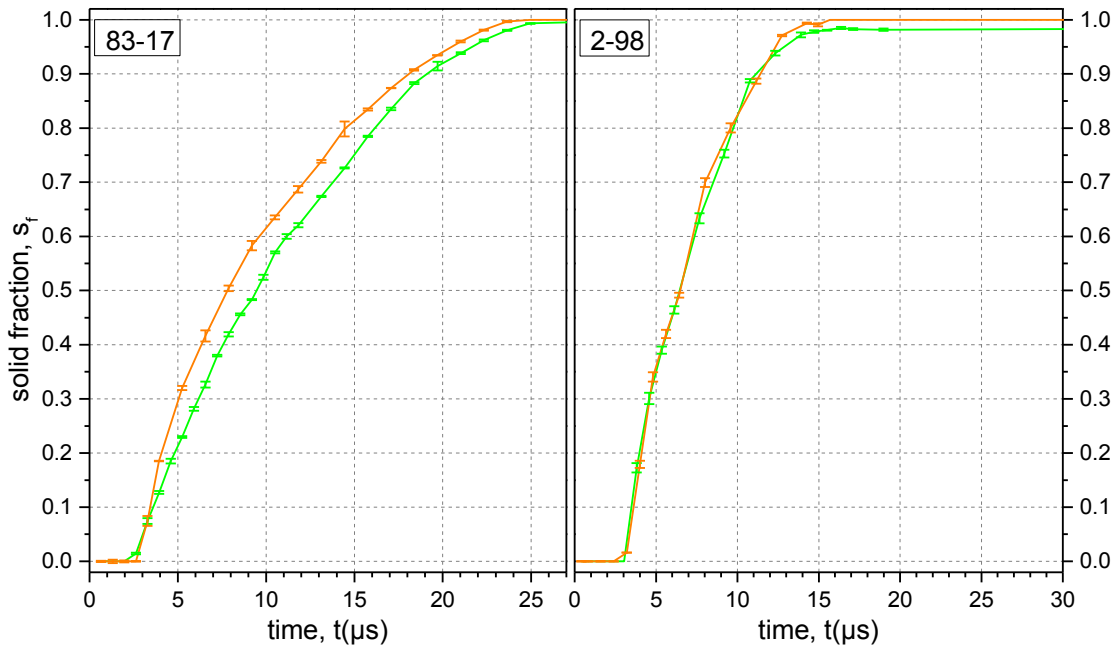
Figure 76: Detailed view of the p-H$_2$ (green) and o-D$_2$ (orange) solid fraction of mixtures 83-17 (left panel) and 2-98 (right panel).

o-D$_2$, based on the higher starting temperature and especially its vapor pressure responsible for the effectiveness of evaporative cooling. This is particularly true, when the surface has solidified because then the more volatile para-hydrogen molecules are hindered to move to the surface to evaporate. On longer time scales the temperature of the filament approaches its limit according to its vapor pressure, which again is mainly determined by deuterium in this case. In the phase diagram on p.158 this scenario is situated in the upper right corner probably around or slightly below the blue dashed line, which is below the solidus.

Secondly, our data suggests that during the crystallization process isotopic partitioning happens at the liquid-solid interface, most likely with o-D$_2$ molecules having a higher tendency to join the solid. Hence, towards the end of solidification the remaining liquid is enriched in p-H$_2$. As the temperature in the entire filament is assumed to be roughly uniform at long traveling times, these conditions correspond to points in the phase diagram that are shifted horizontally towards the left (lower o-D$_2$ concentrations) in the phase diagram on p.158. Now, these thermodynamic conditions may very well be situated in between the liquidus and solidus or even above the liquidus line, so that the liquid, consisting mainly of p-H$_2$, does not solidify at this temperature. As this is the limit temperature of evaporative cooling, the remaining liquid is stable at these circumstances. From this argumentation and the expected crystal growth from outside to inside it follows that this remaining liquid which we see in mixtures with low p-H$_2$ content is probably situated in the core of the filament.

This finding will be of paramount importance in the later discussion of the growth mechanics.

6.1.5.5 First solid and solidification time

Since a plot of all solid fractions from both isotopes is too crowded, we compress the data by extracting the times for the first solid t_{fs}, the last liquid t_{ll} and total crystallization t_{ll-fs}. As before, this is done by looking for the (dis)appearance of the associated peaks within spectra measured at subsequent distances z, yet separately for the vibrational deuterium and hydrogen regions. In case of the remaining liquid p-H$_2$ peak in the three mixtures with high o-D$_2$ content, the time t_{ll} is defined as the subsequent spectra, in which the intensity of this band does not diminish anymore. The corresponding data points for the first solid t_{fs} and crystallization time t_{ll-fs} are condensed into fig.77.
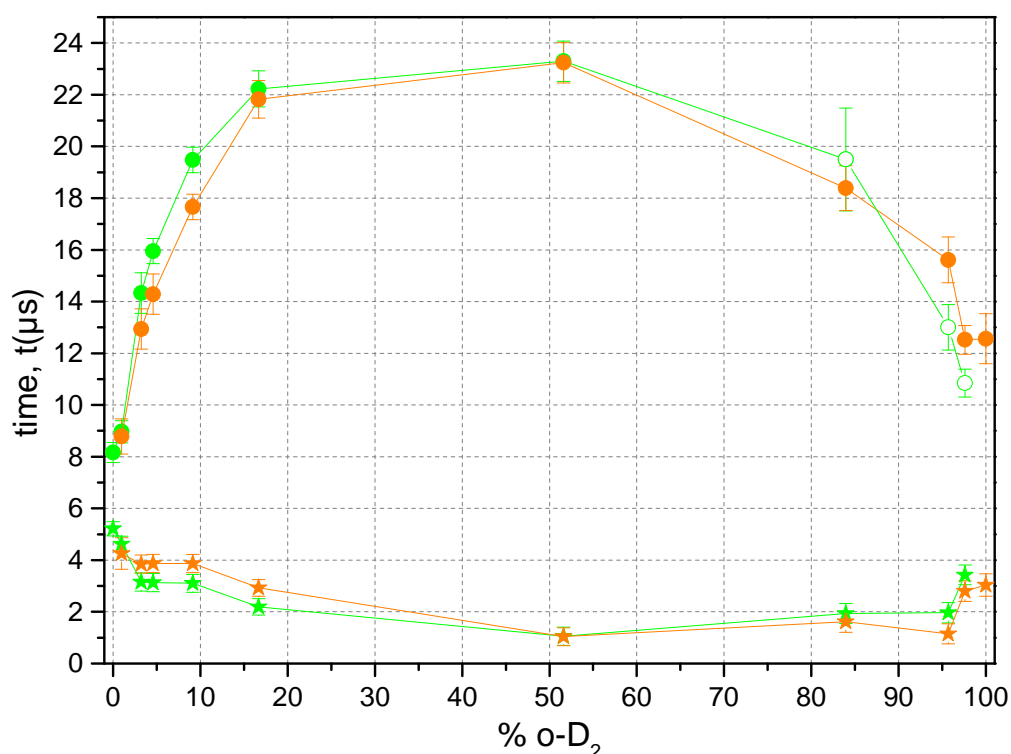

Figure 77: Appearance of the first solid t_{fs} (stars) and duration of solidification t_{ll-fs} (circles) for the p-H$_2$ (green) and o-D$_2$ (orange) components of the mixtures. Open green circles for high o-D$_2$ contents mark the times, at which the intensity of the persisting liquid p-H$_2$ peak remains unchanged.

One interesting information retrieved from the t_{fs} curves (bottom) is that the first solid appears earlier relative to the pure substances upon dilution, regardless if p-H$_2$ or o-D$_2$ is the main component. The earliest solid starting times are detected in the 48-52 mixture, resulting in the roughly u-shaped plot.

For some mixtures the start of crystallization differs slightly for the two isotopic species. It is not clear if this is of physical origin, because the sensitivity for the less abundant species is reduced due to the lower signal-to-noise ratio, leading to a delayed detection of the small initial/final peaks. The fact that the solid for the main component seems to always appear first and the two curves cross at the equimolar mixture support a rather systematical error origin. Also keep in mind that even if this effect is rooted in physical

meaning, this first solid does not represent the composition of the nucleation embryos, which are formed earlier than the displayed times, yet are not visible in the spectra due to their small volume fraction.

The total crystallization time t_{ll-fs} (top curves) also exhibits differences between the p-H_2 and o-D_2 data points, which probably base on the same sensitivity argument, since the values are calculated from the first solid to the last liquid. Nevertheless, the most important feature is the strongly enhanced time for solidification for the mixtures, which has already been described in section 6.1.5.1. Yet in this plot, we have a quantitative measure and detect that the maximum of the crystallization time probably is situated between the 83-17 and 48-52 mixtures.
Additionally, the asymmetry of the curve is visible. For p-H_2 on the left side of fig.77 even small dilutions lead to a rapid ascend in the crystallization time which already doubles at $\approx$ 5% o-D_2. For pure o-D_2 on the right the solidification time already starts higher by a factor of $\approx$ 1.4 (compare chapter 5.1.2.2) and the rise upon dilution is unambiguously less pronounced. This asymmetric, reverse-u shape of the total crystallization time will be the main feature to clarify in the later interpretation 6.1.6, so that this figure will be referenced frequently.

More information is retrieved from the times it takes for the solid fractions to reach certain percentages. In detail, the solid fraction curves are linearly interpolated[4] and the times at which the solid fraction is at the values 0.02, 0.18, 0.34, 0.50, 0.66, 0.82, 0.98 (steps of 0.16) are extracted independently for the two isotopes.
The smallest value 0.02 is an alternative to the previous method of determining the time for the first solid t_{fs}. The maximum value is chosen to be 0.98 on purpose to respect that the solid fraction does not reach 1 in all cases (remaining p-H_2 liquid) and corresponds to the last liquid t_{ll}.
In fig.78 the above time stages are plotted relative to the starting time for 0.02, which is chosen to be $t(s_f = 0.02) \equiv 0$ for each data set. For example, for the equimolar mixture (data points situated at 52% o-D_2) 34% of both p-H_2 (green) and o-D_2 (orange) have solidified roughly 4.8 μs after the start of solidification (defined as 2% solid).

This plot serves several purposes. For one, the top data points (98%) represent an alternative way of extracting the total solidification time t_{ll-fs} for both isotopes, complementary to the previous fig.77. Though the absolute times may vary, the main asymmetric inverted-u shape of the plot with the maximum located between 20 and 50% o-D_2 remains.
Secondly, this plot captures the differences in the solid fraction between the two isotopes. For example for the mixtures with p-H_2 as the main component (towards the left), it is clearly visible that the o-D_2 solid fraction (orange) attains the different crystallization stages at earlier times, as was discussed in the previous section. However, one has to be careful, because the extraction method bears systematical errors. As the starting time $t(s_f = 0.02)$ is extracted and set to be zero for the solid fractions of each isotope separately, this may induce an offset between the two data sets. E.g. this is noticeable in the mixture 16-84, in which p-H_2 reaches all crystallization stages earlier than o-D_2 due to an offset of $\Delta t(fs = 0.02) = -0.6\,\mu s$ between the hydrogen and deuterium solid fractions.

---

4 All plots of solid fractions are already presented this way, i.e. the data points are interconnected with straight lines.
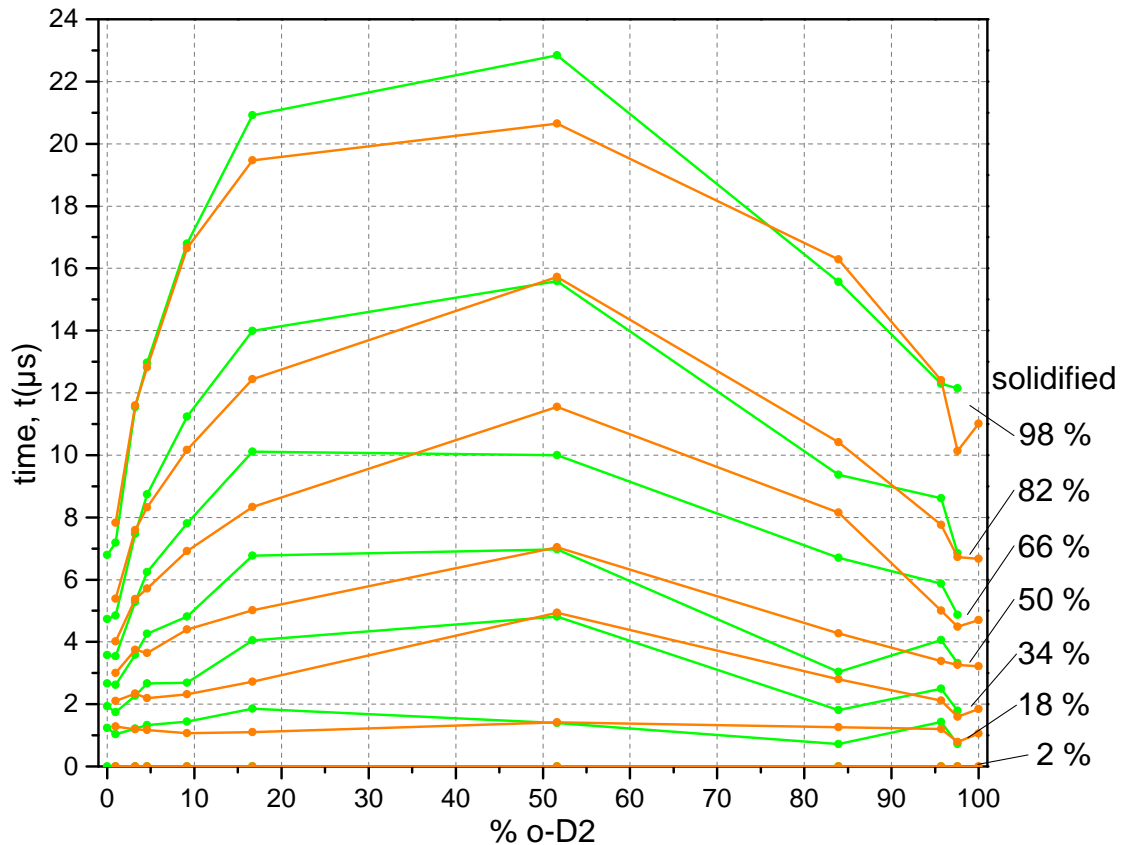
Figure 78: Time until x% (right scale) for p-H$_2$ (green) and o-D$_2$ (orange) have solidified relative to when 2% are solid (see text).

The plot reveals a third information resource, which is connected with the change in shape of the solid fractions covered in the Avrami fit section 6.1.5.2. As stated, the crystallization stages marked on the right side all have the same interval of $\Delta = 16\%$. Yet the time to complete these steps varies, visible at the increasing distances between the data points of one measurement towards higher values. This is grounded in the steep inclination of the solid fraction in the beginning, which becomes more gradual towards the end of solidification (compare fig.71 on p.161).

An interesting revelation is that in the early stages of crystallization all mixtures as well as the pure substances approximately have the same crystallization rate, indicated by the the almost horizontal progression of the 18% data points. The familiar inverted-u shape of the total crystallization time (98%) is developed gradually at later stages. This may signal that the delay/hindrance in the crystallization rate is not uniform during the whole process, but rather stronger towards the end.

6.1.5.6   Comparison: Nozzle diameter

As complementary data some of the mixtures were also recorded with the $d_0 = 1.9\,\mu m$ nozzle, which are listed in table 8. Note that the pure para-hydrogen measurement is not a filament, but rather a droplet spray as analyzed in chapter 4.1.3.7. The corresponding

solid fractions are plotted in the left panel of fig.79, whereas all except the pure ortho-deuterium one are extracted from the hydrogen vibrational region.

name, #	date	temp2 (K)	P_0 (bar)	v_0 (m/s)	% o-D_2
100-0$_s$ or #9	15/12/11	16.5	23.5	236^x	0.0
83-17$_s$	16/12/11	16	15	170	16.7 ± 0.8
48-52$_s$	16/12/11	19	24.5	187	51.6 ± 1.4
0-100$_s$ or #B	16/12/11	25	13.0	161	100.0

Table 8: Measurements with mixtures of p-H_2 and o-D_2 using the small nozzle XVII-01 with $d_0 = 1.9 \, \mu m$. ^{x}: droplet beam

Due to the smaller diameter of the nozzle the crystallization process happens on a much smaller time scale. The pure substances (green and orange) roughly have a parallel curvature and in comparison the mixtures (dark green and brown) exhibit prolonged solidification times. Particularly interesting are the pure ortho-deuterium (orange) and 83-17$_s$ mixture (dark green), which progress almost equally for $s_f < 0.4$, yet afterwards the latter displays a more shallow increase, indicating that the later stages of solidification exhibit a delayed crystallization.

For a deeper analysis we extract the time of the first solid t_{fs} and total solidification t_{ll-fs} to compare with the previous data featuring the $d_0 = 5.3 \, \mu m$ nozzle. The results are plotted in the right panel of fig.79.
Comparing the starting time of solidification (stars, bottom), we find a very similar behaviour of the small nozzle (red), reproducing the same shape of the curve as the big nozzle (black) and evidencing that mixtures tend to freeze earlier. The stark deviation of the pure para-hydrogen data on the very left (red hollow data points) is due to the droplet spray of that measurement and shall be neglected.
Even more interesting is the duration of solidification (circles, top). For an easier comparison, the scale of the small nozzle data (red) on the right hand side is stretched by a factor of 5. We find that the curves are in good agreement within error bars with the big nozzle data and resemble the same reverse-u shape with the maximum between 20 and 50% o-D_2, evidencing that this behaviour is reproducible and independent of the nozzle.

Furthermore, due to the higher surface-to-volume ratio of the $1.9 \, \mu m$ nozzle the evaporative cooling is more effective and all filaments exhibit lower mean temperatures of the liquid with respect to the corresponding $5.3 \, \mu m$ data. The right plot in fig.79 proves that the observed longer crystallization times in the mixtures persist largely independently of this absolute temperature.
Assuming that the crystal growth is isotropic, i.e. freezes symmetrically from the surface to the core, we again can estimate the mean crystallization rate with $u = r/t_{ll-fs}$. Disregarding the pure p-H_2 droplet beam, the three other measurements each yield a ratio of $u^{1.9 \mu m}/u^{5.3 \mu m} = 1.7 \pm 0.15$, which means the crystallization velocity in the small nozzle is roughly 70% higher, regardless of the composition. Since we did not see any significant increase in the crystallization time for the two 48-52 mixtures with a
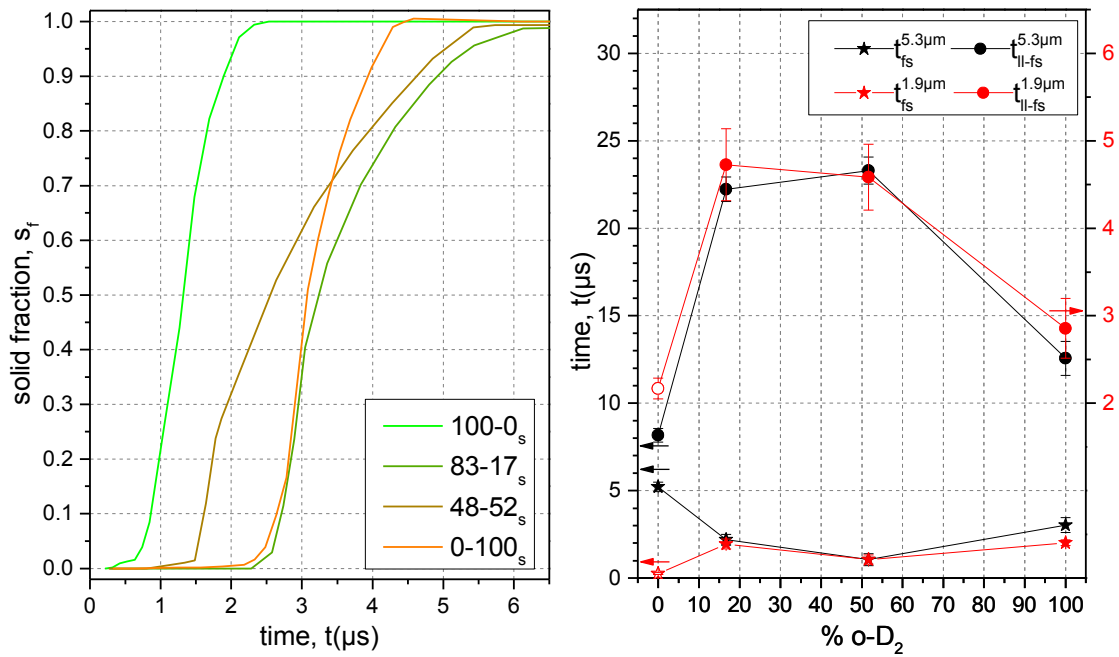
Figure 79: Left panel: Solid fractions from measurements in table 8. $100\text{-}0_s$, $83\text{-}17_s$ and $48\text{-}52_s$ are extracted from the p-H_2 vibrational spectra, whereas $0\text{-}100_s$ (orange) comes from the o+p-D_2 vibrational.
Right panel: First solid t_{fs} (stars, bottom) and crystallization time t_{ll-fs} (circles, top) for measurements with the big (black) and small (red) nozzle. For comparison $t_{ll-fs}^{1.9\,\mu m}$ is stretched by a factor of 5 with scale on the right.

difference in the starting temp of $0.7\,\text{K}$ in section 6.1.5.3, this factor is surprisingly high and indicates that either the temperatures are significantly lower in the $2\,\mu m$ nozzle or the diameters of the filaments contain systematical errors.

Nevertheless, since this factor is almost constant for the three measurement, we conclude that lower temperatures increase the crystallization velocity for the pure substances similarly as for the mixtures, again signaling an independence of temperature.

6.1.6 Interpretation: solid fraction

All experimental data around the solid fractions has been presented and we now focus on the interpretation of the observed effects on microscopic scales. Basically there are two main aspects that need to be explained:

1. the earlier appearance of the solid in mixtures with respect to the pure substances

2. the longer crystallization times of the mixtures.

Up to now, there exist several approaches to access these features, yet none of these hypothesis is able to prove its validity unambiguously. The main reason is that all explanations rely on microscopic effects, but our experiment only yield information about the macroscopic behaviour.

In the following section the different theories are discussed in the light of our experimental findings to reveal congruences as well as inconsistencies. This will be done mostly in a qualitative way, because the current theoretical frameworks do not possess quantitative evaluations or critical parameters are unknown.

6.1.6.1 Temperature related effects

A more trivial, macroscopic approach to explain the earlier and longer freezing of our mixtures is related to temperature effects. For example, it is known that the melting point of liquids can be depressed by the insertion of certain substances[5].
The qualitative and quantitative effects of mixing two substances are governed by the corresponding binary phase diagram. Fortunately, the binary phase for our mixtures of p-H_2 and o-D_2 has been investigated and is available. Even though it is disputable if those mixtures can be considered ideal (compare chapter 2.4.1), the deviations from ideality can be considered small, which means that the total Gibbs energy for any composition may be treated as a linear combination of the energies of the pure systems according to their mol fractions and only a small term, i.e. the mixing enthalpy, is added. This fact expresses itself as the cigar like shape of our binary phase diagram, which does not deviate severely from the line connecting the pure melting points.
For a depression of the melting point or other temperature related effects, the binary phase diagram should exhibit an eutectic point, i.e. a local minimum of the solidus/liquidus lines in between the pure melting points like in certain metallic alloys, which here obviously is not the case. Additionally no temperature dependent coexisting liquid and/or solid phases as in the Ne—n-D_2 phase diagram displayed in fig.9 on p.27 exist. Hence, no straightforward explanation for our early and longer crystallization can be deduced from the binary phase diagram itself.

Next, we think think about how the absolute temperature could affect the appearance of the first solid by considering the pure liquids with small impurities of the other isotope. Based on our discussion in section 6.1.3.2, for pure para-hydrogen the mean temperature at the start of solidification is roughly 13 K. Ortho-deuterium inserted into these conditions is extremely supercooled with respect to its normal melting point and could very well be imagined to serve as seeds for nucleation embryos. In other – by the way very beautiful – experiments [88, p.6807], an increase in the nucleation rate by a factor of 100 has been determined based on the addition of 1% o-D_2, confirming this statement.
This argumentation becomes stronger, if we take into account statistical, in this case compositional, fluctuations, in which simply by diffusion agglomerations of o-D_2 molecules are formed. With increased amounts of o-D_2 the chance to find such statistical cluster rises significantly, while the relative supercooling of o-D_2 still is very strong. E.g. in the mixture with 17% o-D_2 content the mean temperature of the liquid still is estimated by eq.6.2 to be 13.8 K, which is 28% below the normal melting point of deuterium and the majority of o-D_2 molecules ($\approx$ 90%, see app.B.3) will have at least 1 same species partners. Statistical fluctuations in such an environment are likely to create a supercooled, large enough critical cluster, that could explain the earlier onset of freezing for mixtures with low o-D_2 content. Note additionally that based on the

---

5 Imagine putting salt into water/ice to keep people from slipping on your sidewalk.

temperature gradient the surface of the filament is even more supercooled, decreasing the critical size necessary.

On the other hand, if we insert para-hydrogen into pure ortho-deuterium, we experimentally also find an earlier appearance of the solid. This time the impurity p-H_2 molecules situated at a mean liquid temperature of $T \approx 17.5$ K do not experience a supercooling relative to their normal melting point at all and the previous argument does not apply. Yet here we may argue that the evaporation of the p-H_2 molecules due to this high temperature is significantly higher and therefore the local temperature at the surface decreases faster than in the pure ortho-deuterium case without impurities. The remaining ortho-deuterium molecules at this surface experience lower temperatures and therefore have increased probabilities to form nucleation embryos leading to an earlier start of the solid.

In conclusion, the observed earlier start of solidification upon diluting the two pure isotopic liquids may be explainable by strongly supercooled o-D_2 in the high p-H_2 content case and a faster cooling of the surface due to evaporation of p-H_2 in the opposite composition. However, note that this is just a speculation, which is in qualitative agreement, and other hypothesis in later sections may also play a role.

One could argue that the earlier freezing of the mixtures is the reason why these mixtures also take longer to freeze, as in the previous fig.77 there seems to be a correlation between the two effects. Due to the earlier start of the crystallization, there is less time for evaporative cooling and the mean temperature of the liquid is warmer. According to the crystal growth theory in the previous fig.36 on p.89 higher temperatures are connected to lower crystallization rates, which is in qualitative agreement with what we observe in our experiment. Yet, in the following we will provide evidence that this argument is quantitatively not sufficient to explain the strong increase in crystallization time in the mixtures.

In fig.68 on p.153 we find that in pure para-hydrogen $100-0$ and in the 97-3 mixture the mean wavenumber of the liquid, which corresponds to its mean temperature, exhibits quite similar values and deviate only due to the earlier start of solidification in the mixture. This minor difference in temperature is estimated to be well below < 0.5 K and is unlikely to account for twice the crystallization time in figure 77.

This becomes particularly evident, if we combine this finding with fig.74 on p.164 comparing the two measurements of the 48-52 mixture. There, the analysis showed that despite the different starting temperature of $\Delta T = 0.7$ K and the detected offset in the mean wavenumber of the liquid band as a consequence, both data sets reveal an almost equal solid fraction and total crystallization time. Following the message from that figure, the even stronger temperature difference in the comparison of two measurements almost has no influence onto the crystallization time, strongly opposing the argument that temperature is the main reason for its increase in mixtures.

Further evidence that a different mechanism rather than just the temperature is responsible for the long crystallization times is provided by the Avrami analysis in section 6.1.5.2 as well as the crystallization stages in graph 78 on p.170. In both we find that the shape of the curve increasingly deviates from that of pure para-hydrogen upon dilution with ortho-deuterium. If just the temperature were to be the reason, the curves should simply be stretched in time with similar fitting values for n, as was the case in the pure para-hydrogen chapter 4.1.3.4. In contrast, the crystallization rate in the beginning is almost equal and growing differences appear in the later stages, resulting in lower fitting values for n.

We summarize that the binary phase diagram does not include any signals that readily prove our measured effects. The absolute temperature may explain the earlier onset of crystallization with statistical cluster formation for low o-D_2 and more effective evaporative cooling for low p-H_2 mixtures. However, although qualitatively in agreement, the temperature clearly is not the main reason for the longer crystallization times and other mechanisms have to be responsible.

6.1.6.2 Local structures in the liquid

A deeper and more profound explanation for our findings evolves around the concept of local structures in the liquid phase. As stated in the basics chapter 2.5 local geometries, that are already close to the shape of an fcc or hcp lattice, could favor the formation of critical nucleation embryos initiating the crystal growth. On the other hand local geometric orders like the icosahedron may be energetically more stable than the crystal lattice, yet are incompatible with a three-dimensional periodic arrangement. Such structures may therefore be the reason for a so-called frustration of crystallization in the sense that the time it takes the system to solidify is enhanced or even infinite, eventually leading to a glassy state.

The probability as well as the range of variations of local structures are increased when the liquid is constituted of more than one substance [57]. Reasons for this are that the interaction between the particles is altered and/or different sizes of particles make certain arrangements more favorable. In the case of p-H_2 and o-D_2 the interaction potential is the same, yet due to the stronger zero-point vibrations of hydrogen the radius ratio of the isotopes is $r_{oD2}/r_{pH2} \approx 0.95$. Based on this size ratio, the local order approach is an interesting candidate to explain the earlier and longer crystallization of our mixtures.

To evaluate the possible connection of local structures in the liquid and our observed results, a collaborating group of theoreticians in Milano[6] carried out path integral Monte Carlo (PIMC) simulations of the supercooled liquid systems consisting of the same mol fractions as used in our experiments. The details of simulation are extensively discussed elsewhere [89, and ref. therein] and we are only interested in the qualitative results of these calculations. In a single sentence, this method reveals positional configurations of particles in a (supercooled) liquid state, while obeying the delocalization based on their quantum character. It is important to notice that only static properties of the liquid are retrieved, yet not the dynamics like diffusion or even the transition to the crystal.

One main output are the partial radial pair distribution functions, which for the mixture containing 10% o-D_2 are illustrated exemplary in fig.80. The plot yields information about the correlation between the respective pairs, i.e. a probability of finding adjacent molecules as a function of their intermolecular distance in Å= 10^{-10}m).
We find that the first maximum of the correlation function for o-D_2—o-D_2 (orange) is higher and slightly shifted towards lower distances than the corresponding p-H_2—p-H_2 interaction (green). This is an expression of the difference in the higher quantumness λ of the lighter isotope, which ultimately leads to a greater delocalization of the p-H_2

---

6 Filippo Tramonto and Davide E. Galli, Laboratorio di Calcolo Parallelo e di Simulazioni di Materia Condensata, Dipartimento di Fisica, Universita degli Studi di Milano, Via Celoria 16, 20133, Milano, Italy

wavefunction (see chapter 2.4.1). Hence, this approach approves that we can treat our mixtures as constituted of particles with two different effective sizes.

The fact that the correlation function p-H$_2$-o-D$_2$ (olive) lies in between the ones for the same species in height as well as position of the maxima, tells us that the interaction between the isotopes is equal to the interaction to themselves, as expected from the same intermolecular potential. A preferential clustering of e.g. same-species molecules would express itself in a decrease of this p-H$_2$-o-D$_2$ correlation function relative to the other two. We deduce that according to the simulation the isotopes have different effective sizes, yet their supercooled mixtures are completely miscible.
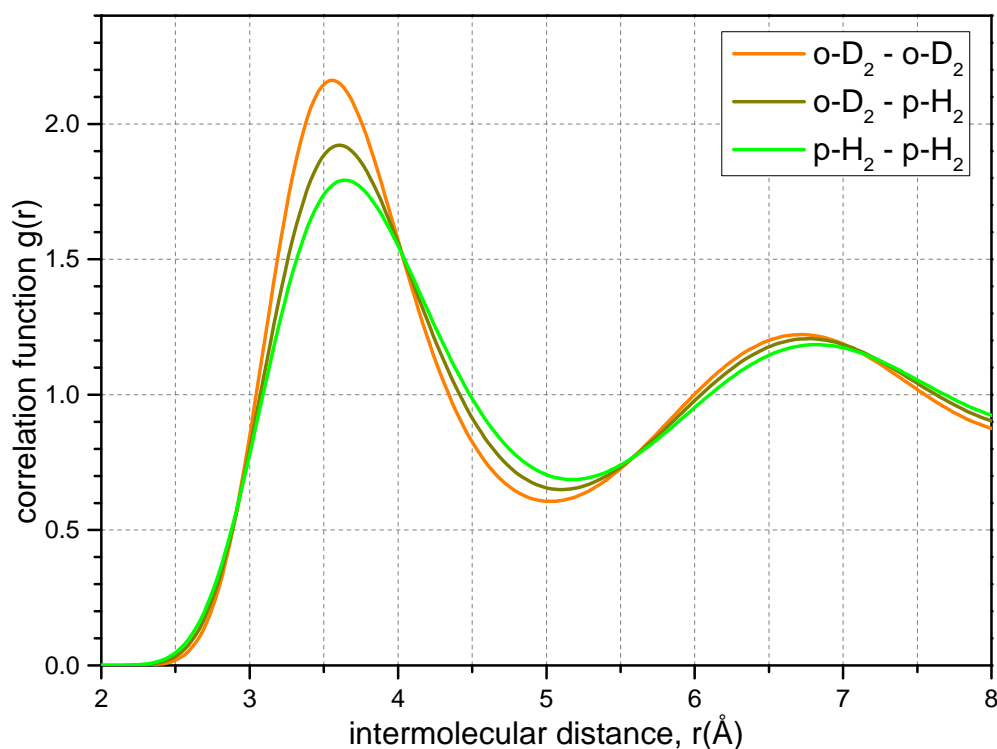

Figure 80: Correlation functions g(r) from PIMC simulations for a liquid mixture with 10% o-D$_2$ molecules.

Furthermore, the simulated data can be treated by the *local bond order* method [90], which gives insights into the geometric environment around particles to search for local structures. Again we spare the details and are satisfied with the core idea that this analysis spits out certain parameter values, we here refer to us *structure parameters*, which indicate if the adjacent particles around a central one resemble more an icosahedral, fcc or hcp etc. structure. The mathematics can be applied to p-H$_2$ and o-D$_2$ molecules separately to reveal differences in the surroundings of the isotopes.

A first important revelation of the bond order analysis for the simulated mixtures is that the structure parameters for both pure substances remain almost completely unchanged upon the insertion of impurities of the opposite isotope, when the temperature is held constant. This means that the average surrounding neither of p-H$_2$ nor o-D$_2$ changes significantly when some of the adjacent molecules are substituted by the opposite one. However, small differences exist between the structure parameters of p-H$_2$ compared to o-D$_2$. In this regard ortho-deuterium reveals a slightly higher trend towards icosahedral

ordering, which is the main candidate responsible for frustration of crystallization. Additionally the structure parameters for both isotopes exhibit minor increases of icosahedral-like order, when the temperature is lowered. This is in agreement with previous findings that lower energies favor the formation of local orders [6].

We now apply the above simulation results to our experimental data. Following above results, the addition of o-D_2 molecules to a p-H_2 liquid leads to an overall increase in the number of molecules which are situated in an icosahedral-like environment. Following Tanaka [57], this may lead to a frustration of the crystallization, which is in qualitative agreement with our stark incline in the crystallization time observed at increasing o-D_2 fractions (left side in fig.77 on p.168).
In the opposite case, admixing p-H_2 into o-D_2 would result in a decrease in icosahedral-like configurations. However, higher para-hydrogen amounts are also accompanied by a decrease of the mean temperature of these liquid mixtures, as evidenced by fig.70 on p.158. According to the simulations, lower temperatures favor the formation of icosahedrons, which may compensate the decrease of o-D_2 and even cause more molecules to build structures frustrating crystallization. This would concur with the less pronounced increase in crystallization time for the right flank in the previous fig.77.

Yet, there exist strong counterarguments against the local structure hypothesis being the valid explanation for our enhanced crystallization times. At first we want to point out that the framework for local structures in the liquid originally is developed to assess the complete prohibition of nucleation, rather than a slowing down in the crystallization process, what we observe in our experiment.
Despite this deviating initial purpose, inconsistencies to our data occur. One part of above argument is that lower temperatures entail a greater degree of frustration against crystallization due to a higher probability of local structures. Considering the crystal growth models, this is counterintuitive, because we expect liquids which are supercooled more extensively to exhibit faster crystallization rates (compare fig.36 on p.89). In agreement with the latter, our measurements of the 1.9 μm nozzle in section 6.1.5.6 prove that lower temperatures result in even larger crystallization rates, in pure substances as well as in mixtures of the hydrogen isotopes. Furthermore, the analysis of the two 48-52 mixtures signals that the constitution of the liquid is more important than its temperature. This is a clear contradiction to the prediction of the local order approach that lower temperatures lead to longer crystallization times. The observed increase in the crystallization times upon the insertion of para-hydrogen into ortho-deuterium, i.e. the right half of fig.77, therefore is not explainable by this framework.
To rescue the hypothesis of local structures in the liquid being responsible for the delay in the crystallization times, one may argue that other orders than the favorite icosa-hedron may form, when the two isotopes are mixed. Though, as stated, the structure parameters used in the present analysis do not indicate any major changes and behave as in the pure cases.
Further criticism is that the simulations only govern the static supercooled liquid phase, but not the dynamics in the liquid-solid interface. As we will see in the following sections, the relationship of diffusion and the velocity of the interface may play a crucial role. Considering the diffusion in the liquid later on, it is questionable, if the lifetime of local structures, which are limited by diffusion, is sufficient to have any impact onto the actual growth of the solid in our case.
Based on the above qualitative disagreement between the proposed effects of local struc-

tures and our experimental findings, we conclude that this approach probably cannot explain the enhanced crystallization rates in mixtures of the hydrogen isotopes.

However, our observed earlier freezing times in mixtures may be related to the formation of local structures in the liquid, since this also is the environment the approach was intended for. It is possible that certain geometric and/or compositional configurations favor the creation of crystallites by creating precursors of the crystal structure [57] or lowering the energy barrier for nucleation.
Although the PIMC simulations do not reveal any significant changes in the structure of p-H_2 and o-D_2, the larger amount of possible geometric arrangements due to the size difference of the isotopes makes it likely that certain configurations favor the formation of nucleation embryos in terms of their energy. Such structures may contain a greater number of particles than just the nearest neighbors covered by the simulation and would therefore remain undetected by the current analysis. This approach is quite similar to the previous argument of statistical compositional fluctuations in the previous section 6.1.6.1 and extends it by taking into account geometric arrangement.

6.1.6.3 Fractionation

An alternative approach to explain our observed phenomena evolves around the concept of phase segregation or fractionation. The basic idea is that o-D_2 and p-H_2 may have different tendencies to join the solid phase, which could influence the growth velocity of the interface.
Mainly for the purpose of investigating the behaviour of metallic alloys, Jackson et al. [5] have proposed an empirical kinetic model, which was introduced shortly at the end of chapter 2.5.2. Although it is questionable, if the analysis are applicable to the very different particle-interaction of our system (chemical vs. van der Waals bindings), we want to elucidate some of the parameters here.

At first we take a look at the equilibrium segregation coefficient k_e for each isotope, which is defined in formula 2.24 on p.36. To recap, k_e represents the ratio of concentrations of the solid divided by the liquid, if the interface was stationary. Hence, values $k_e > 1$ for an isotope indicate a tendency to join the solid, whereas $k_e < 1$ stands for increased amounts in the liquid phase.
From the thermodynamic properties the values for this segregation coefficient are calculated and illustrated in the left panel of fig.81 for p-H_2 (green) and o-D_2 (orange). Both curves cross the equilibrium value $k_e = 1$ at their respective normal melting points of the isotopes. For values below the melting point each curve exhibits $k_e > 1$, which of course signals the tendency to join the solid phase. It is clearly visible that o-D_2 has greater values than p-H_2 across the whole temperature range. In the interval of temperatures which according to eq.6.2 on p.155 are associated with the mean liquid temperatures of the liquid in our mixtures (blue dashed lines), we see that ortho-deuterium always is $k_e > 1$. In contrast to this, para-hydrogen even shows $k_e < 1$ for mixtures with high o-D_2 content, which have a temperature closer to the right dashed border. Although absolute values should not be trusted, this diagram signals that at least for a stationary liquid-solid interface the isotopes would have different concentrations in the solid and liquid phase.
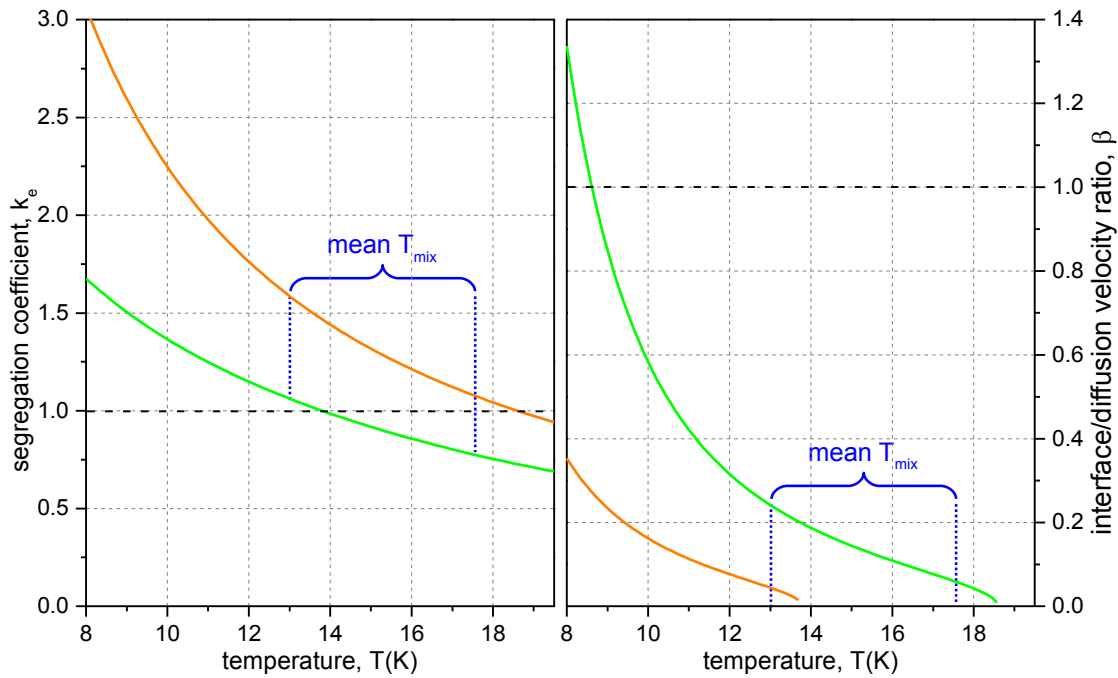
Figure 81: Equilibrium segregation coefficient k_e (left panel) and ratio of interface to diffusion velocity β (right panel) calculated for p-H_2 (green) and o-D_2 (orange). The blue dashed lines mark the interval of the estimated mean temperatures of our mixtures according to eq.6.2 on p.155.

Yet, in reality, the interface is moving with the velocity or crystallization rate u, which we roughly estimate from our experiments as $u = \frac{r}{t_{ll-fs}} \approx 0.1 - 0.3\,\text{m/s}$, depending on the mixture. Hence, since the above segregation requires time based on its dependency on diffusion, the growing solid may be fast enough to capture all particles regardless of their segregation tendency, which is referred to as solute trapping [62].

To estimate, if this is happening in our case, we calculate the parameter β defined in eq.2.25 on p.36, which is an indicator for the ratio of the growth velocity u divided by the ability of particles to escape it by diffusion. The corresponding plot is presented in the right panel of fig.81 for the pure substances p-H_2 (green) and o-D_2 (orange) with our maximum value $u = 0.28\,\text{m/s}$ for pure p-H_2, so that the presented curves correspond to an upper limit. For $\beta \geqslant 1$ the interface velocity u is greater than the diffusion velocity and all particles are devoured and do not have the ability to diffuse away.

In the temperature interval relevant for our cases, o-D_2 always is below $\beta < 0.3$ and further decreases the higher the temperature or o-D_2 content of the mixture, respectively, is. Based on the lower mass and related higher diffusion of p-H_2 its values are roughly a factor of 10 below that of o-D_2. Note that both plots are only valid for the pure substances and the diffusion within the mixtures result in curves in between those two according to [91]. Yet, one has to be careful because they were measured in the liquid at equilibrium and the dynamics could slow down in the supercooled phase.

The plot reveals that for all mixtures p-H_2 as well as o-D_2 molecules are able to diffuse away from the growing interface, whereas this capability is far more pronounced for the former. Combining this statement with the plot in the left panel, we conclude that

in our mixtures molecules are likely to build up a different concentration in the liquid and solid phases at the progressing interface with o-D_2 having a higher tendency to join the crystal.

This estimation is backed up by our experimental findings. For one, the discrepancy between the solid fractions of the two isotopes discussed in fig.75 on p.166 are a strong indication for fractionation at the interface. Especially the mixtures containing low concentrations of o-D_2 reveal a persistent advance of the o-D_2 solid fraction, which means a higher fraction of these molecules in the solid and is consistent with our numerical discussion above with the highest values for k_e for o-D_2. In mixtures with equimolar and high o-D_2 mol fraction the unpredictable cross overs of the solid fraction curves may be related to p-H_2 molecules not being supercooled respective to their normal melting point, as visible by $k_e < 1$ for p-H_2 in the left panel of fig.81.

Additional proof for the phase segregation is also provided by the solid fraction of p-H_2 at low contents not reaching the value $s_f = 1$ (compare fig.76 on p.167). This also is in agreement with the molecules being able to separate at the relative to diffusion slow moving interface so that towards the end of solidification increased amounts of p-H_2 in the liquid phase remain, which are unable to crystallize, since they are not at conditions below their respective melting point ($k_e < 1$).

Up to now we only have stated an agreement between the Jackson model and our experimental results, signaling that we in fact have fractionation during our crystallization process. Now we want to elucidate, if this effect is able to influence our observed increase in the crystallization time for the mixtures. For an estimation we take a qualitative look at formula 2.28 on p.37, which gives the growth rate dominated by substance A at low dilutions with substance B:

$$u_{mix} \approx u_A = u_A^0 \left[C_A^L - C_A^S \exp\left(-\frac{(1-P)\Delta G_A^0 + P\Delta G_{mix}^0}{k_B T} \right) \right] \qquad (6.3)$$

In this equation the thermodynamic quantities can be calculated, but the parameters $P = \{0...1\}$ as well as C_A^L and C_A^S, which mark the concentrations of the main substance at the liquid-solid interface, are unknown. Nevertheless, regardless of the value of P and for all mixtures, the expression in the exponent is close to zero, so that the exponent of that yields values in the range 0.9-1.0. Hence, in a rough approximation and for the sake of the following arguments the formula reduces to

$$u_{mix} \approx u_A^0 \left[C_A^L - C_A^S \right] \qquad (6.4)$$

This means that the growth velocity of the mixture u_{mix} is very sensitive to the actual concentration difference at the interface. Unfortunately, these concentrations are not accessible and probably depend on temperature as well as composition.

Nonetheless, the previous analysis of k_e indicates that the phase segregation in fact could influence the growth of the solid in our mixtures. In a qualitative picture, inserting o-D_2 into p-H_2 would result in an increase of C_{pH2}^L and a decrease of C_{pH2}^S, reducing u_{mix} in eq.6.3 in agreement with the experiment. In the opposite case o-D_2 diluted with p-H_2 would tend to elevate u_{mix}, which opposes our experimental results. Yet in defense, this is a highly dynamic process and all parameters are likely to vary during the whole crystallization process. In the latter case one could argue that the presence of p-H_2 molecules in the liquid phase, which effectively are not undercooled, may not be negligible as assumed by above approximation and could add to the

total crystallization growth rate and ultimately increase it. Although this is highly speculative, the asymmetry in plot 77 on p.168 exhibiting a smaller effect for diluting o-D_2 compared to p-H_2 at least matches with this qualitative assertion.

As another hypothesis, the concentrations in above equation could consequently change towards worse conditions with regards to the crystal growth. In detail, the crystal would be built up always with the most favorable fractions of the particles, resulting in the fractionation. As the process of crystallization progresses close to its completion, the remaining liquid consists of increasingly less favorable constitutions, progressively hampering the further growth. This approach would be in agreement with our previous figure 78 on p.170, which revealed that in the beginning the crystallization rate of all measurements is similar, yet severely slows down for mixtures towards the end. Also the analysis with Avrami fits in section 6.1.5.2 signals that the growth rate is not constant.

We conclude that no reliable estimation of the behaviour of the crystallization rate can be deduced from Jackson's model. There are too many unknowns and parameters, which potentially alter the qualitative outcome, so that this model can be neither endorsed nor rejected as being responsible for longer crystallization times.

6.1.6.4 Further approaches and related works

There may even be bigger sources of influence on the crystallization rate than the parameters discussed in the previous section. The Jackson model in eq.6.3 contains the base growth velocity u_A^0, which is deduced solely from the pure substance. Yet it is questionable, if even this presumption is justifiable in mixtures.

For pure para-hydrogen we discovered that the collision-limited model is likely to apply to this system, since the diffusion-limited model yields values that are too low for our measured crystal growth rate (see chapter 4.1.3.3). Note that one model does not entirely rule out the other, yet it is possible that both participate to a certain degree to the growth of the crystal.

Aziz et al. [4] state that the growth mechanism itself may be altered in mixtures (compare chapter 2.5.2). For example, the process of fractionation that supposedly occurs in our mixtures is determined by the limits of diffusion of molecules. This circumstance may very well alter the mechanism of the crystal growth itself in favor of the diffusion-limited model. Since the growth velocities from the two models differ by 1.5 orders of magnitude, even a slight crossover towards the diffusion-limited model is able to change the crystallization times drastically. In this case the base growth rate u_A^0 in eq.6.3 would already be lower for mixtures compared to the pure substances. In a practical picture one can imagine that for segregation to happen, o-D_2 molecules need to travel to the solid and p-H_2 molecules the other way, which takes time and ultimately may slow down the progress of the interface. Unfortunately, there is no way to extract such information from our data.

The transition to other growth kinetics in connection with a retardation of crystallization has been experimentally observed in colloidal suspensions [87]. Further support that diffusion effects may influence the growth of the crystal are supplied by recent simulations of the interface of metallic alloys [63]. In this work two binary alloys with a similar size ratio are compared, yet one is experimentally known as a good glass

former exhibiting slow crystallization, whereas the other is not. For the former they detect a stronger ordering at the interface, in the sense that in between the liquid and the completely crystallized phase the molecules already arrange in a specific configuration to a greater spatial extent (compare fig.82). This process requires diffusion and, although not explicitly stated, could be similar to fractionation. Interestingly, they do not relate their observed slow down in the crystallization rate to a change in the growth mechanism, but rather to the unknown attachment factor f (see eq.2.21), which is another completely unknown parameter and also associated with the growth dynamics covering geometric aspects.

An ordering at the interface may also be connected with preferred arrangements of differently sized particles based on the mathematical problem of the densest packing efficiency [92]. As an allegory, one can imagine that it is simple to build a wall (i.e. the crystal), out of equally sized bricks (particles), but bricks of different sizes have to be stacked in the right order for a stable/efficient structure. Hence it takes time (slower crystallization rate) for the correct bricks (particles) to be transported (diffusion) to their designated positions.
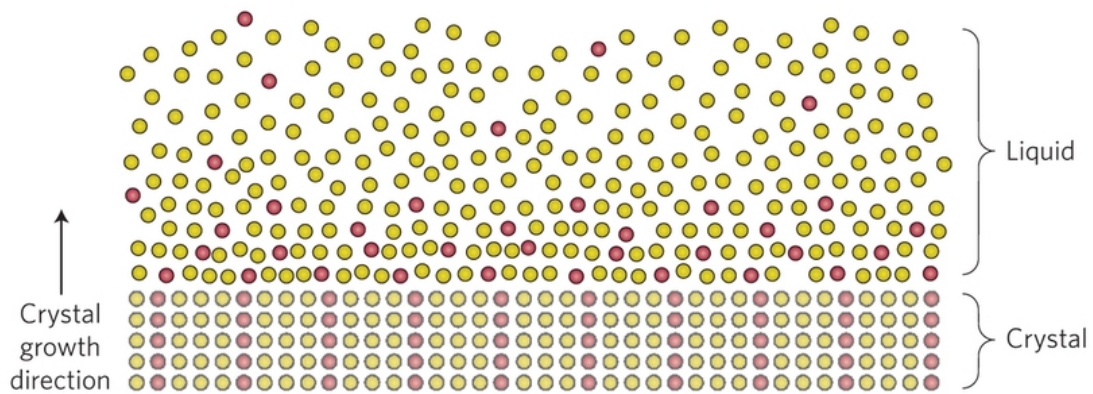

Figure 82: 2D schema of ordering of particles at the proceeding liquid-solid interface with a suggested increased tendency of the red particles to join the crystal (fig.1a from [93]).

Speaking of the crystal structure, also the number and size of voids and crystal defects may play a crucial rule. In the above metaphor of the wall, missing bricks/holes can make it harder to stack further. In the molecule picture such voids in the crystal represent gaps in the interaction potential between particles, so that an increased appearance of these may hinder the attachment of subsequent molecules due to the lack of attraction. In molecular dynamics simulations of binary metallic alloys [13], higher amounts of voids were detected in some compositions in which the crystallization was suppressed. In our case, the different sizes of the isotopes may promote the occurrence of defects in the crystal.

Furthermore, in above paper seeds are found that are particularly enriched in one species and already possess a crystalline structure [p.5], which may be preceded by fractionation [p.6] and are unable to grow. Their most interesting finding is that their longest crystallization times (infinite) are for mixtures with a 30-50% content of the smaller molecules. This is a similarity to our measurements, since according to fig.77 on p.168 our maximum crystallization times are also situated within this

region, considering o-D_2 is our small component. However we have to note that their interaction model bases on the Kob-Anderson type and is very different from our system, since their interaction between opposing particles is stronger than that between the same species. According to our correlation functions in fig.80 on p.176 this is not the case. Hence, it is questionable, if the qualitative agreement between our experiment and their simulation stems from a similar origin.

As a last related work Williams et al. [11] performed molecular dynamics simulations on a binary hard sphere mixture with a size ratio of 0.9, which is slightly lower than our value of 0.95. They found that mixtures with 50-70% content of the small component exhibit dramatically extended crystallization times, whereas in contrast in our case the largest times are found at above contents of the large p-H_2 molecules. Similar to the just discussed paper [13], in their mixtures crystallites with an increased amount of one species (here: large particles) are formed early one, but do not grow significantly larger and are long-lived. This may be a possible bridge to unite the usually separately treated phenomena of nucleation and crystal growth.
Although this hard sphere model also is very different from our real system, this work again highlights the importance of favorable compositional configurations, which can for one promote an early crystalline structure (i.e. nucleation), but are also capable of subsequently reducing the rate at which the liquid attaches to these crystals.

In conclusion we see that a broad variety of hypothesis and simulations exist, many of which relate to compositional effects at the liquid-solid interface being responsible for a slowdown in the crystallization rate. It seems likely that this interface plays a crucial role in the crystallization dynamics. Yet, since no theoretical or empirical framework is provided, we are just able to point out qualitative agreements with our experiment and cannot prove any validity of the approaches.
The key aspects probably are incorporated not in the exponential term related to the thermodynamics in eq.6.3, but in local geometric and kinetic parameters, which are incorporated in the relative concentrations $C_{A,B}^{L,S}$ as well as the basic growth rate u^0. In view of the novelty of above approaches and the connected general lack of knowledge, a theoretical quantitative description in the near future seems rather unlikely. Hence, for deeper insights into this relationship dynamic simulations of the interface on the basis of our measurements are the most promising candidate.

6.1.7 Summary: Solid fraction and interpretation

By gradually adding small amounts of o-D_2 into p-H_2 liquid filaments the crystallization process starts increasingly earlier and the total crystallization time rises significantly (fig.71 on p.161). Additionally, the solid fraction curves reveal a change in shape with a similarly fast increase in the beginning, yet a slowdown especially towards the end, indicating that the growth rate is not constant.
In the inverse mixtures of slightly diluted o-D_2 both above effects also appear, yet are less pronounced (fig.72 on p.162). Plotting the crystallization time against the composition results in an asymmetric, reversed-u shaped curve with the maximum between 30-50% o-D_2 content (see fig.77 on p.168).

Changing the starting temperature of an equimolar mixture leads to increased temperature of the liquid, however the solid fraction remains almost unchanged (fig.74 on p.164). When filaments are produced with a smaller nozzle, the crystallization rate increases uniformly for all compositions, confirming the reproducibility of the measurements.

Discrepancies in the separately extracted o-D_2 and p-H_2 solid fractions within each mixture signal that the isotopes exhibit different tendencies to join the solid. However, the trend is not univocal with o-D_2 always being ahead at small concentrations, yet an apparently arbitrary behaviour for high o-D_2 contents (see fig.75 on p.166). A (partial) fractionation becomes evident in mixtures, in which o-D_2 is the main component and completely solidifies, whereas small fractions of liquid p-H_2 persist beyond the observation time. This is explained in terms of temperature not being sufficiently low for the remaining liquid with strongly enhanced p-H_2 content to crystallize.

The earlier freezing time of mixtures with high p-H_2 contents is most likely explained by (statistically created) clusters o-D_2 being significantly supercooled below their normal melting point and serving as nucleation seeds. In o-D_2 dominated filaments, p-H_2 molecules experiencing comparably high temperatures may enhance the effectiveness of evaporative cooling and leave behind stronger supercooled o-D_2 on the surface with respect to pure o-D_2, initiating the crystallization. In addition, certain geometrical configurations may serve as precursors of nucleation embryos and could be more common in mixtures based on the two effective particle sizes revealed by the correlation function obtained from PIMC simulations of the supercooled liquids (fig.80 on p.176).

The microscopic mechanisms behind the longer crystallization times remain unsolved and several possible qualitative explanation exist. The simulations find a greater tendency for o-D_2 molecules to attain icosahedral-like configurations in the supercooled liquid state, which has been reported to frustrate crystallization. Though this is in agreement with the increase in crystallization time when o-D_2 is inserted into p-H_2, it does not correlate to the longer times observed in the opposite mixtures and therefore is unlikely to be the main factor.

A different framework based on kinetic effects indicates that differing concentrations in the liquid and solid at the crystallization interface can have a strong effect on the growth rate. Simple thermodynamic estimation signal that such fractionation indeed can happen in our system, which is supported by the experimentally observed difference in the solid fractions as well as the remaining p-H_2 liquid in mixtures with high o-D_2 concentration.

Further approaches suggest a change in the growth mechanism, which in our case could be from the collision-limited model evidenced in pure p-H_2 (partially) to the diffusion-limited model. This may be reasoned either by fractionation or an ordering at the liquid-solid interface as observed in other molecular dynamics simulations, both relying on the diffusion of molecules. In any case the literature suggests that the liquid-solid interface in combination with the composition of the particles with different effective size seem to play a crucial role in the crystallization dynamics.

6.2 Rotational region

Likewise to the vibrational region of the mixtures, we probe the rotational excitation $S_0(0)$ of o-D_2 and p-H_2 separately, since they are situated in different energy regimes. Similar to the pure substances, the rotational regions exhibit a smooth transition from liquid to solid along the z-axis of the filament according to the solid fraction. Yet as band structures are too broad to fit and the transition does not yield further information, we will focus on the static features rather than the dynamics in this chapter.
We start with the discussion of the initial liquid bands of both isotopes prior to crystallization 6.2.1, proceed with the structure of the solid 6.2.2 and at last compare with with the measurements of the small nozzle 6.2.3.

6.2.1 Bands in the liquid phase

The $S_0(0)$ rotational excitations in the liquid phase are presented in fig.83 for o-D_2 (left panel) and p-H_2 (right panel) according to the color code from green to orange depending on their o-D_2 content. The traveling distances and therefore times at which the spectra are recorded vary between 50 to 200 µm, but since the rotational liquid band is rather independent of temperature and in neither of the shown spectra the crystallization has started yet, we are able to directly compare the measurements. The error bars in the wavenumber scale are higher for the p-H_2 region in the right panel due to the low intensity and therefore uncertainty of the plasma line it has been calibrated to. Also note that the intensity (y-scale) of p-H_2 is magnified by a factor 3.5 compared to the o-D_2 ones. All areas are normalized to 1.

The plots may seem a bit crowded, yet the spectra are purposely not stapled towards the top to put the focus onto the changes in position and width of the bands. Starting at pure para-hydrogen in the right panel in light green, we notice that upon inserting up to 9% o-D_2 (towards orange) the Lorentz-shaped excitation becomes broader, visible at the decline of the maximum. With further dilution (83-17) a shoulder towards higher wavenumbers appears, into which intensity is increasingly redistributed. When p-H_2 molecules are the minority $< 4\%$, the band is almost symmetric again, yet at $\approx +1.5\,\mathrm{cm}^{-1}$ higher wavenumber and even slightly sharper than in the pure case. Its position is close to that of the gas line, which by the way is much sharper and within spectrometer resolution.
Pure ortho-deuterium in the left panel in orange produces a broader Lorentz peak (FWHM = $2.6\,\mathrm{cm}^{-1}$) than pure para-hydrogen (FWHM = $1.4\,\mathrm{cm}^{-1}$). With greater amounts of p-H_2 impurities (towards green), it also becomes broader and develops a shoulder at higher wavenumber, that grows stronger. At the lowest mol fractions it is surprisingly sharp, close to the spectrometer resolution (FWHM = $0.6\,\mathrm{cm}^{-1}$), and its position is also in good agreement with the gas line position. The small line width, however, is in stark contrast to the behaviour of p-H_2 (FWHM = $1.0\,\mathrm{cm}^{-1}$) at high dilutions.

The origin of the shift of both isotopes towards higher wavenumbers is the same as for the shift observed in the vibrational regions in chapter 6.1.1.1. The reason why the rotational excitations in the pure liquids is below the energy of the gas phase at all is
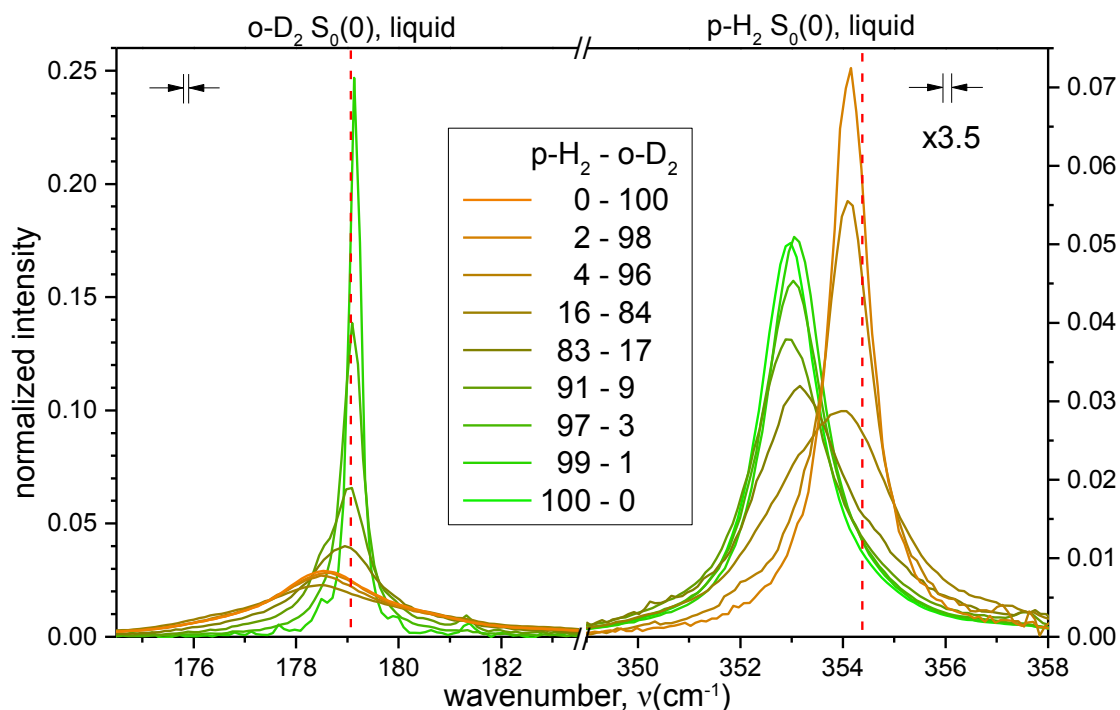
Figure 83: $S_0(0)$ excitation of o-D_2 (left panel) and p-H_2 (right panel, magnified x3.5) in the liquid state. The red vertical lines mark the positions of the corresponding excitations in the gas phase [36], the black arrow interval denotes the error bars in the wavenumber scale.

grounded in the capability of rotons, i.e. the pendant to vibrons, to travel to adjacent same species partners. Substituting molecules with impurities with a very different excitation energy reduces the hopping options for rotons and therefore increases their energy. Molecules with fewer number of same-species partner are the reason for the growing shoulder towards higher wavenumbers both found in diluting p-H_2 as well as o-D_2. For mixtures, in which one isotopic species is heavily underrepresented, a majority of such molecules does not have any adjacent same species partners. Since the hydrogen isotopes have the unique quantum property that the rotational excitation is a good quantum number (compare chapter 2.3.2), such isolated molecules can rotate almost freely and their according $S_0(0)$ energy corresponds to the value of the gas phase.

The observation that the excitations of highly diluted o-D_2 is much sharper than for p-H_2, however, is surprising and not entirely clear. Several possible explanations shall be presented and evaluated in the following.

The first candidate is based on the mechanics of rotons or Raman spectroscopy, respectively. When we look at the absolute values of the excitation energies, i.e. the wavenumber scales, of o-D_2 and p-H_2, we see that the value of the latter is close to twice of that of the former due to half the mass. This is different from the vibrational region, in which the energy of the two excitations differs by a factor of $\sqrt{2} \approx 1.4$.

For a closer view the two rotational excitation of the isotopes are plotted for the mixtures 2-98 (left panel) and 99-1 (right panel) in fig.84. This time the areas of the bands correspond to their actual content of the isotopes in the liquid and the wavenumber of
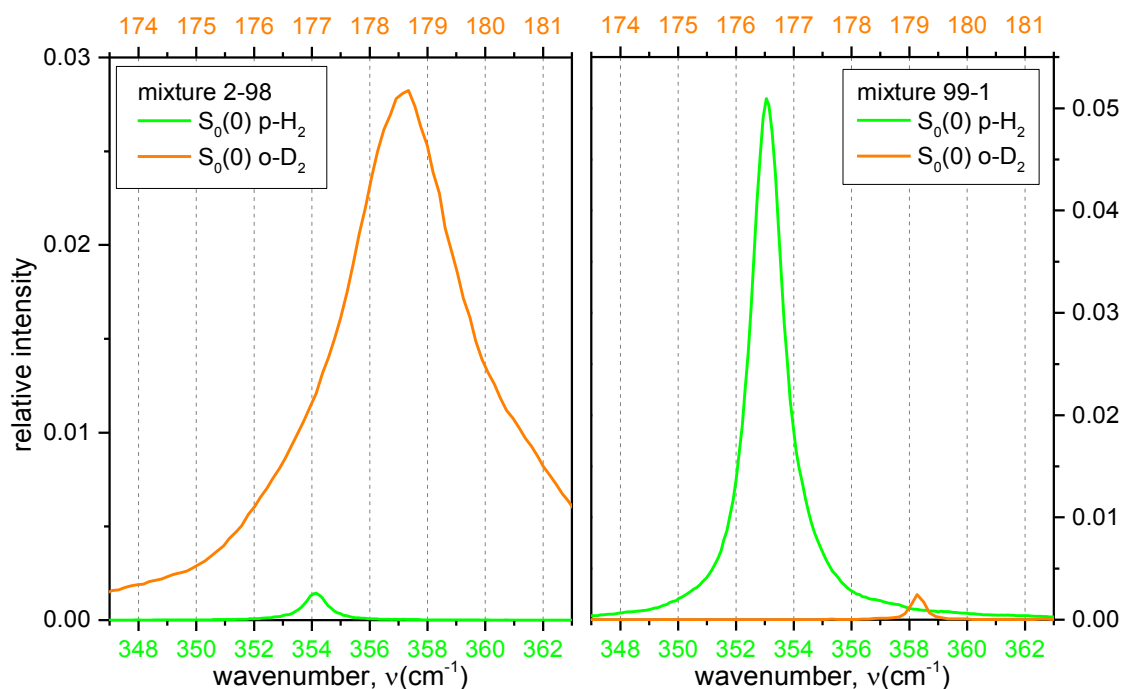
Figure 84: $S_0(0)$ excitation for p-H$_2$ (green) and o-D$_2$ (orange) with actual intensity ratio for mixtures 2-98 (left panel) and 99-1 (right panel). The wavenumbers (bottom and top) are scaled by a factor of 2 to point out the overlap of bands.

o-D$_2$ on the top is scaled by a factor of 2 with respect to p-H$_2$ at the bottom. Note that consequently all o-D$_2$ bands misleadingly appear twice as wide. For the 2-98 mixture in the left panel, we find that at this scaling ratio there is a significant overlap of the bands of the two isotopes. The impurity p-H$_2$ peak is at a position, at which the much more intense o-D$_2$ peak is still at almost half the value of its maximum. In the opposite case in the right panel, the impurity o-D$_2$ peak is situated in the right tail of the main p-H$_2$ peak that exhibits less than 2% of its maximum height there. Hence the overlap of bands at this scaling for p-H$_2$ impurities in o-D$_2$ is considerably greater than in the opposite case.

This discrepancy in the overlap may have following implications. Since in the 2-98 mixture the $S_0(0)$ excitation of p-H$_2$ is inside the energy range times two of the o-D$_2$ band, it could be able to induce resonance effects in the form of (two) traveling rotons onto the surrounding o-D$_2$ molecules, similar to how usually rotons hop onto adjacent partners. As in the liquid phase the environment is disordered, such rotons would not have a clearly defined energy and produce a broad band of p-H$_2$, which is the same effect as in the liquid phase of a pure substance.

In the opposite mixture 99-1, the rotational energy of an o-D$_2$ molecule is not sufficient to induce $S_0(0)$ rotons onto the p-H$_2$ band, as its energy is only half of the latter. Yet, we recall that the $S_0(0)$ band actually corresponds to a double excited rotational state (compare chapter 2.3.2), so that a resonance with the first excited rotational state of p-H$_2$ could still be possible. However, as discussed above, the overlap of the isotopic bands in the 99-1 mixture is negligible, considerably limiting the magnitude of a possible resonance effect. Hence, the lack of interaction of isolated o-D$_2$ molecules with the p-H$_2$ environment would yield an undisturbed, sharp energy, which is in agreement

with our spectra.

In conclusion, we see that such a resonance effect is indeed able to qualitatively reproduce the observed behaviour of bands. However, we cannot provide support from calculations, if such a mechanism is feasible at all. Additionally, such overtone excitations usually have a weak effectiveness, so that it is questionable if it is quantitatively sufficient to explain the discrepancy in the width of diluted p-H_2 and o-D_2.

Another explanation for the smaller line width of o-D_2 compared to p-H_2 for isolated impurities is rooted in the difference in their quantum character. We have discussed that due to their smaller mass para-hydrogen molecules possess more pronounced zero point vibrations, which is noticeable in the greater effective size compared to ortho-deuterium. Hence, para-hydrogen molecules can be considered as less localized. In the condensed phases, this could express itself as hydrogen molecules experiencing a higher degree of the repulsive core of the interaction potential of surrounding molecules and therefore losing the phase of their rotation easier, ultimately leading to a broader Raman band [94]. Ortho-deuterium on the other hand is more localized and interacts little with its environment resulting in a sharper line. Unfortunately, there is also no direct proof for this hypothesis either.

As a last option, the ≈ 12.5 times higher $J = 1$ content in converted deuterium with regard to converted hydrogen could also play role. In the pure substances o-D_2 produces an already broader liquid band compared to p-H_2, which probably is due to the presence of $J = 1$. This is in agreement with measurements of isomeric mixtures [95], in which the $S_0(0)$ line of p-H_2 has been found to broaden upon the dilution with o-H_2 and the mechanism is expected to also apply to deuterium.

In our highly diluted mixtures, p-H_2 molecules as impurities in an ortho-deuterium liquid have a significantly higher chance of having an adjacent $J = 1$ molecule than in the inverse mixtures, the numbers being $\approx 25\%$ compared to 2.5%, respectively, assuming 12 nearest neighbors (see appendix B.3). Through the stronger quadrupolar component, $J = 1$ molecules could interact with the impurities and therefore disturb their free rotation and broaden their energy bands, which should occur 10 times more often for the p-H_2 impurity according to above estimation.

Since it is the least speculative, this approach seems to be the most likely explanation for the broader p-H_2 impurity band in the liquid phase. We will gather more information in the discussion of the solid in the following chapter.

6.2.2 Structure of the solid

We now turn to the $S_0(0)$ lines of the completely solidified filaments. In fig.85 the rotational spectra of both o-D_2 (left panel) and p-H_2 (right panel) are displayed with increasing amount of the former towards the top. The spectra may be recorded at different traveling distances or times, respectively, yet after complete solidification, the structure does not considerably change anymore.
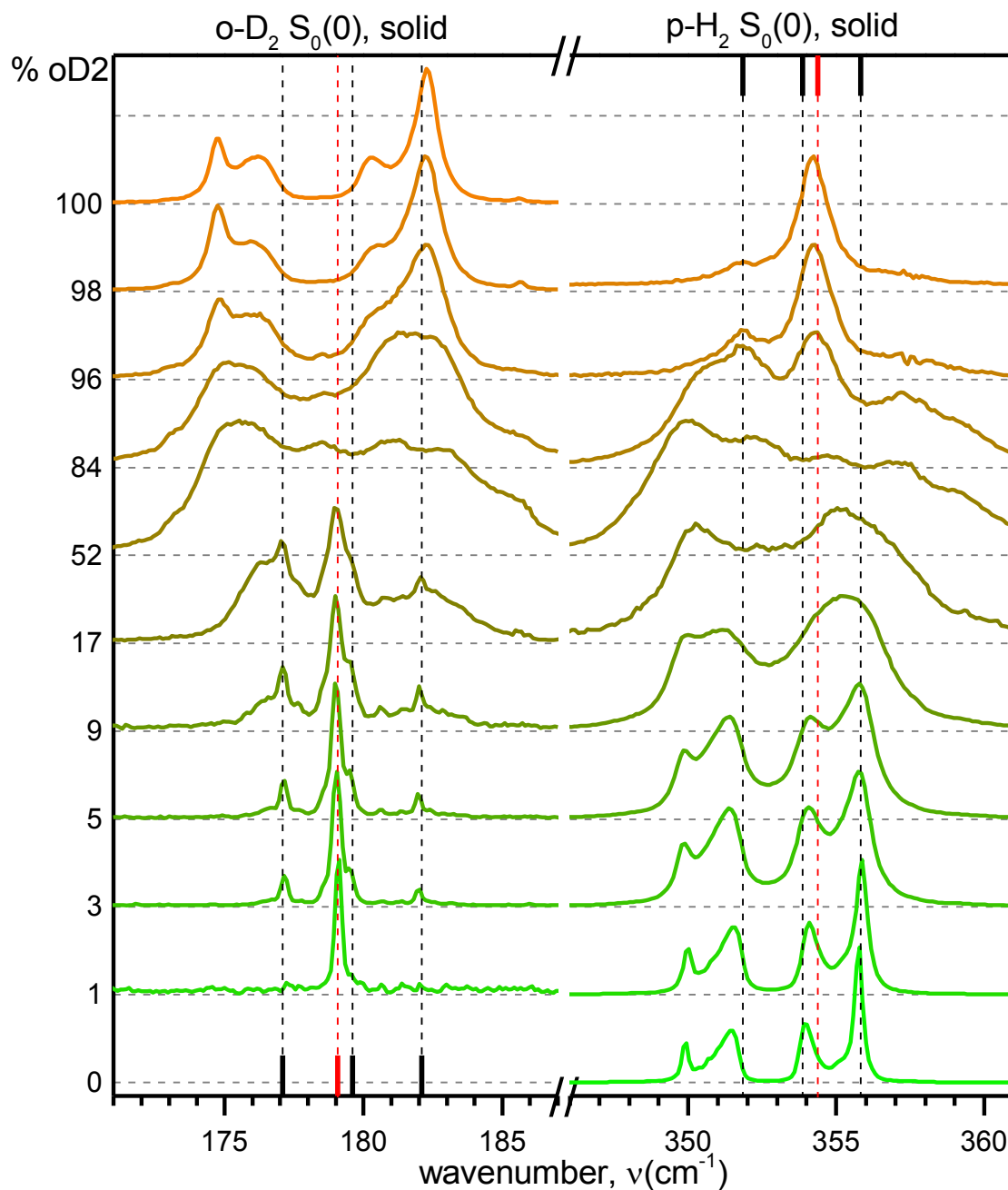
Figure 85: $S_0(0)$ excitation of o-D_2 (left panel) and p-H_2 (right panel) in the solid phase. The measurements are normalized to their maximum intensity value $= 1$ and stapled according to their o-D_2 content labeled on the left. Vertical red dashed lines indicate the position of the gas line [36], black lines the position of the equilibrium hcp crystal of the pure substances [31].

6.2.2.1 Solid ortho–deuterium

We start at pure ortho-deuterium in orange at the top left. When 2% p-H_2 is inserted (spectrum below), all lines appear broader. Additionally, we detect that the amount of o-D_2 molecules situated in a neat hcp lattice diminishes, noticeable from the lower intensity as well as further shift apart of the two stand-alone hcp peaks $m = \pm 1$ and $m = \pm 2$ located close the two left vertical black dashed lines that mark the position of the equilibrium hcp crystal (for orientation: peaks (2) and (3) fig.60 on p.135). As expected, the decrease of hcp is in favor of the clear fcc peak on the very left as well as the regions in between hcp and fcc associated with intermediate rhcp structures.
Upon further dilutions, the band structure of o-D_2 becomes increasingly blurred and no separate lines can be identified until at the 48-52 mixture a broad band yet still containing some intensity variation represents the turning point of this behaviour. Beyond this, when o-D_2 increasingly is the minority substance, the structure becomes clearer again and in the 83-17 mixture reveals a broader underground yet with several sharp peaks on top. These peaks have a width close to the spectrometer resolution and correlate very well with the positions of gas and equilibrium hcp lines indicated by the vertical dashed red and black lines, respectively. At even lower o-D_2 fractions the broad background diminishes and only these sharp peaks remain, so that in the mixtures 95-5 and 97-3 they contain almost the entire signal. In the most extreme measurement with only 1% o-D_2 even the peaks associated with hcp disappear except that one single peak, that corresponds to the gas line and exhibits a similar width and position as in the liquid phase.

Parts of the behaviour described above has been measured before [31], yet with higher total J = 1 content of < 5%, so that our measurements are less blurred and reveal more details. The initial broadening and merging of bands is typical for inserting impurities, because the symmetry of the crystal is progressively broken (compare para-hydrogen chapter 4.2.1.2) and the bands of our intermediate (20-80%) mixture look similar to those of the cited paper [31, fig.2].
However, a major difference is that our crystal is grown far off-equilibrium resulting in the obvious presence of fcc (and rhcp) for pure o-D_2 and at small dilutions. Our observation that 2% addition of p-H_2 molecules increases the amount of these metastable lattice configurations signals that, following Ostwald's rule, these arrangements are easier accessible from the energy point of view. This is in agreement with other measurements, that suggest that impurities are able to increase the energy barriers separating hcp and fcc [74, p.104] and therefore may stabilize the latter.

Another peculiarity of our spectra not visible to this extent in [31] is the sharp line structure of highly diluted o-D_2. For a closer view, the $S_0(0)$ spectrum of o-D_2 is plotted for the 97-3 mixture again in fig.86 in blue. The spectrum can decently be reconstructed (red) with 5 Gauss peaks labeled as (I) to (V) in green all exhibiting a width close to the spectrometer resolution. We find that peaks (I), (IV) and (V) match very well with the equilibrium hcp crystal as well as (III) with the position of the gas line. Peak (II) up to now remains unassigned. Note that the baseline of the fits is slightly above zero to account for the increased underground, which also belongs to the $S_0(0)$ signal.
The first feature to notice is that the Gauss shape of these lines is different from that of the liquid phase, which resembles more a Lorentz curve (compare fig.84 on p.187). This indicates that the energies of these peaks in the solid are sharp, i.e. do not vary.
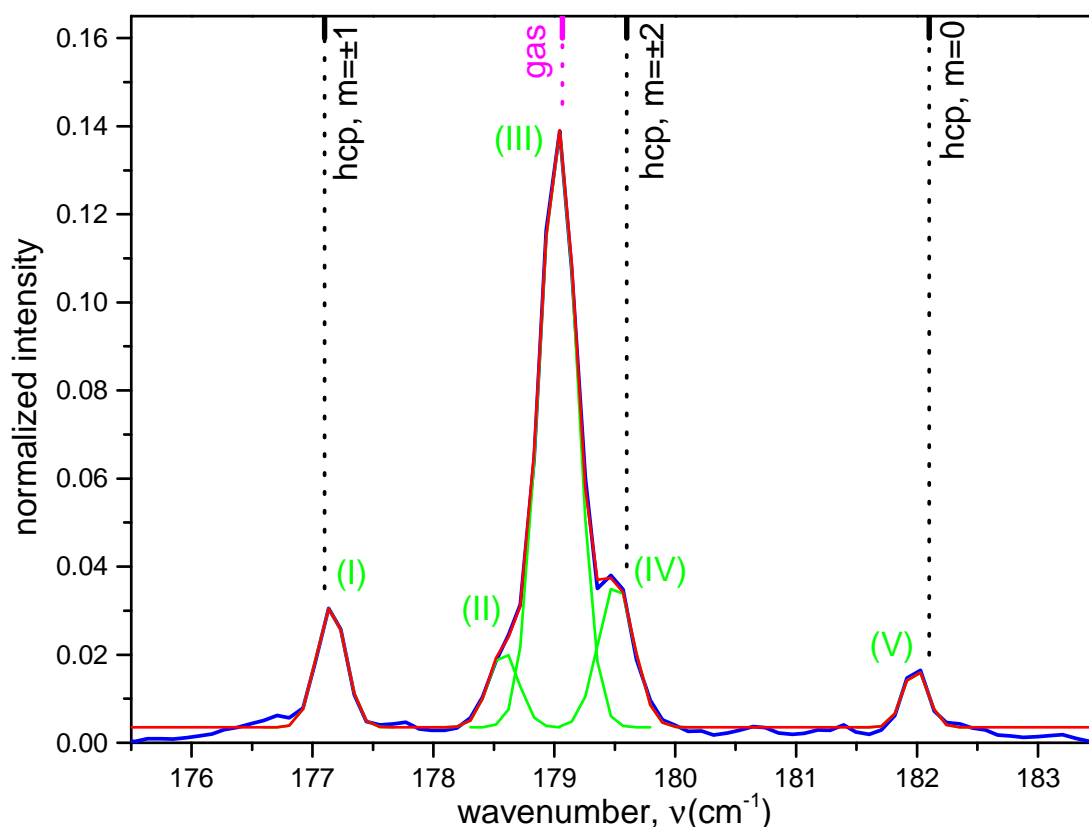
Figure 86: Peak structure in $S_0(0)$ spectrum of o-D_2 (blue) of mixture 97-3 fitted with Gauss-curves (green) labeled with (I) to (V) and the reconstructed cumulative spectrum (red). Ticks at the top mark the positions of the gas line (magenta, [36]) and the equilibrium hcp crystal (black, [31]).

The high intensity peak corresponding to the gas line is interpreted as Raman scattered light from isolated o-D_2 molecules (monomers), i.e. do not have any adjacent same-species as well as J = 1 molecules. In this case, the roton is undisturbed and not able to travel so that the energy always yields the same value. The fact that it coincides perfectly with the energy of the gas line again is due to the unique quantum properties of the p-H_2 allowing for free rotation also in the crystalline phase. The relative intensity of the band agrees decently with that of the $nn = 0$ band in the solid vibrational in fig.66 on p.150 for each mixture with o-D_2 as the minority.

Considering the high dilution, it is unlikely that the 3 lines coinciding with the energy of hcp really correspond to an extended hcp lattice of o-D_2 molecules. A more reasonable explanation is that the signal comes from isolated pairs (dimers) of o-D_2 molecules with no further o-D_2 or J = 1 molecules attached. The imaginary line connecting the centers of the two molecules defines a preferred axis, based on which it is possible that the usually degenerated magnetic sub-states are split up and produce the well-known hcp triplet [94]. The degree of this splitting depends on the intermolecular distance of the molecules. Yet, due to the ordered lattice structure enforced by the surrounding p-H_2 molecules, such o-D_2 dimers should always have a very similar intermolecular distance, in contrast to a dimer in the gas phase. Hence the energy levels between such pairs are always identical and the resulting Raman lines are sharp.

The observation that the distance in between the outer peaks $m = \pm 1$ to $m = 0$ is slightly smaller than the literature value could be related to the lattice constant. Whereas in a pure $o\text{-}D_2$ crystal the intermolecular distance at $4\,K$ is at 3.605 Å, in the $p\text{-}H_2$ crystal it is larger with 3.789 Å[31, p.7]. The splitting of hcp decreases with decreasing number density, because the EQQ interaction becomes weaker [81]. Following this argumentation, the hcp splitting of $o\text{-}D_2$ pairs in a $p\text{-}H_2$ crystal is expected to be less, which is in agreement with what we observe.

Finally, bigger agglomerations (trimers and beyond) of $o\text{-}D_2$ molecules as well as adjacent $J = 1$ components probably make up the increased background around the above sharp lines. The sum of its intensity plus that of the hcp lines above is roughly in agreement with what we see as the $nn = 1 + nn \geqslant 2$ band in the vibrational fig.66.

The remaining, unassigned peak (II) is on top of a (weak) plasma line from the Ar^+ laser and therefore could not entirely belong to the $S_0(0)$ line of $o\text{-}D_2$. Yet the fact that it disappears along with the hcp peaks in the mixture 99-1 proves that it also contains real signal. Most likely its origin could be $o\text{-}D_2$ molecules that are neighbors with molecules carrying $J = 1$, as this was found in infrared studies to change the energy of its rotation [96].

If we assume that the $o\text{-}D_2$ molecules are randomly distributed in the crystal, we can make a simple estimation, how often singles and paired molecules occur based on the fact that each molecules is adjacent to 12 partners in a hcp or fcc crystal (details in appendix B.3). From the fits to the spectra we can extract the relative intensity of single molecules (associated with gas line) and pairs (sum of hcp lines). The results for the calculation and the experimental values are summarized in table 9.

	calculated			experimental		
% o-D_2	% single	% pairs	% rest	% single	% pairs	% rest
1.0 ± 0.1	89	10	1	(100)	(0)	(0)
3.2 ± 0.4	67 ± 3	21 ± 1	11 ± 2	50	22	28
4.6 ± 0.6	57 ± 4	23 ± 1	20 ± 4	41	21	38
9.1 ± 1.2	32 ± 5	20 ± 3	49 ± 7	20	18	62
16.7 ± 0.8	11 ± 2	7 ± 1	81 ± 2	10	6	84

Table 9: Calculated and experimental number of isolated, paired and bigger cluster o-D_2 molecules. In the 1% mixture fits are not feasible due to low signal-to-noise ratio. Calculation details in appendix B.3

The number of molecules situated in a dimer configuration is in good agreement. Yet, we find that for mixtures below 10% o-D_2 the calculation yields a greater number of isolated o-D_2 molecules in comparison to the experiment. This may indicate that o-D_2 tends to form clusters in the crystal, since accordingly the amount of molecules in higher order configurations is increased. However keep in mind that the experimental fit probably is prone to systematical errors based on the underground and the unknown assignment of peak (II). Also, the calculation does not account for further effects, like $J = 1$ molecules and possible defects of the crystal, so that an accurate conclusion cannot be drawn.

6.2.2.2 Solid para–hydrogen

For the discussion of the $S_0(0)$ excitation of para-hydrogen we start at the bottom right spectra (green) in fig.85 on p.189. As expected, diluting pure para-hydrogen (towards top) broadens the peaks, yet in contrast to ortho-deuterium the fcc-hcp ratio may change slightly in favor of hcp detectable at the fcc and hcp peak on the left (for orientation: peak (1) and (2) in fig.45 on p.106), though the variations are not as evident. Above $\approx 9\%$ o-D_2 content the peak structure is increasingly blurred and looks similar to o-D_2 at similar dilutions, particularly visible in the mixture 48-52.

When p-H_2 is the minority substance (16-84), a broad underground triplet structure appears, yet in comparison to o-D_2 in the inverse measurement 83-17 the band is even broader and does not exhibit the sharp peaks on top of it. At even higher dilutions the background diminishes and a broad main Lorentz-shaped peak with a small side peak of similar width at lower wavenumbers remain in 4-96. The main peak is situated close to the position of the gas line (vertical red dashed line) and its shape is almost identical to the corresponding liquid phase. The location of the small one matches well with the lowest excitation line of the equilibrium hcp phase (left black dashed line) and at 2% p-H_2 content it carries less intensity. It is interesting to note that there seems to be no corresponding peak for the highest hcp energy and the main line does not exhibit a shoulder that would agree with the medium hcp energy (right and middle black dashed lines)[7].

The circumstance that small o-D_2 impurities added to p-H_2 may favor the formation of hcp over fcc probably is related to different sizes of the two isotopes. There is no literature available to shed light on this converse behaviour compared to o-D_2. In this regard, it would be enlightening to have calculations for the lattice energies for the given size ratios and compositions to make a definite statement.

In mixtures, in which p-H_2 is in the minority, the main peak in agreement with the gas line likewise to deuterium is interpreted as signal from isolated molecules. The small side peak at the position of an equilibrium hcp energy line probably is produced by paired p-H_2 molecules, yet the missing other two hcp lines is puzzling. For this unexpected behaviour and the broader lines, several explanations from the previous chapter 6.2.1 discussing the liquid phase shall be stressed.

The first hypothesis, stating that p-H_2 is able to induce rotons in an o-D_2 environment yet not the other way around, may still be viable. In particular, it would not only deliver an explanation, why the p-H_2 lines are broader, but also why there is no clear hcp peak structure present in the minority p-H_2 spectra. In the case that p-H_2 rotons interacted with adjacent o-D_2 molecules, dimers of p-H_2 would not perform the splitting of the energy sub-levels to a similar extent, as this is based on isolation from the environment. The small side peak visible in our spectra may be a product of p-H_2 pairs disturbed by the surrounding o-D_2 molecules.

The second possibility roots in the stronger delocalization based on the higher zero-point vibration of p-H_2. In this scenario we would expect to still see the hcp line

---

7   There is a plasma line of the Ar^+ laser overlapping at $357.6\,cm^{-1}$, which has been fitted with area restrictions determined by the intensity ratio of all other plasma lines and afterward subtracted from the spectrum. The remaining residuum is still visible, yet the decent match with the underground signals that there is no real peak belonging to the $S_0(0)$ excitation at this location.

structure of pairs, just with broader bands. However, the greater particle size may additionally come into play, because the p-H_2 molecules are forced into the o-D_2 lattice with a smaller lattice constant, what could in some way disturb the energy splitting.

Although we cannot exclude contributions from above approaches, the statement utilizing the higher $J = 1$ content of deuterium still is the most plausible one. If we assume a random distribution of particles and 12 nearest neighbors, the chance of finding a $J = 1$ molecule beside an isolated impurity molecule is the same for the liquid as for the solid, i.e. $\approx 25\%$ in the deuterium environment compared to 2.5% for hydrogen (compare last paragraph in chapter 6.2.1). This explains why the main peak, which is associated with such isolated molecules, has a larger width for diluted p-H_2 compared to diluted o-D_2. Additionally, increased amounts of $J = 1$ tend to change the shape of the $J = 0$ peaks towards Lorentz curves (compare fig.46 on p.108), which suits that highly diluted o-D_2 exhibits Gauss peaks, whereas the corresponding p-H_2 possesses extending tails.

For the hcp splitting a dimer is necessary, which in total has $12 + 7 = 19$ nearest neighbors in an hcp or fcc lattice structure (see appendix B.3). Therefore the chance of having an adjacent $J = 1$ molecule beside such a dimer is increased to 38% in a deuterium environment compared to 4% in hydrogen. The disturbance from the $J = 1$ is likely to destroy the symmetry of the dimer so that they do not yield three sharp hcp lines.

However, turning this argument upside down, we expect 62% of p-H_2 pairs to be not in contact with $J = 1$, so that at least they should produce the typical 3 line hcp structure. We conclude that the p-H_2 peak structure still remains puzzling and should be further addressed.

6.2.3 Comparison: Nozzle diameter

As the last step we compare the rotational spectra of the small ($d_0 = 1.9\,\mu m$) and big ($d_0 = 5.3\,\mu m$) nozzle recorded in the solid phase, which are presented in fig.87 in red and black, respectively. In previous chapters we have already discussed the pure substance at the bottom and top, so only the mixtures in the middle remain to be looked at.

Disregarding the increased noise in the small nozzle data based on the worse signal-to-noise ratio, we barely detect any differences neither in the 83-17 nor in the 48-52 spectrum. Since the temperature of the liquid prior to crystallization is smaller for all measurements of the $1.9\,\mu m$ filaments, we conclude that temperature has a negligible effect on the lattice structure of the (faster) growing crystal.

These rotational measurements prove the reproducibility of our measurements in a beautiful way.

6.2.4 Impact on the crystallization rate

The analysis of the rotational regions does not deliver any direct evidence to support explanations for the longer crystallization times in mixtures. As a matter of fact, we
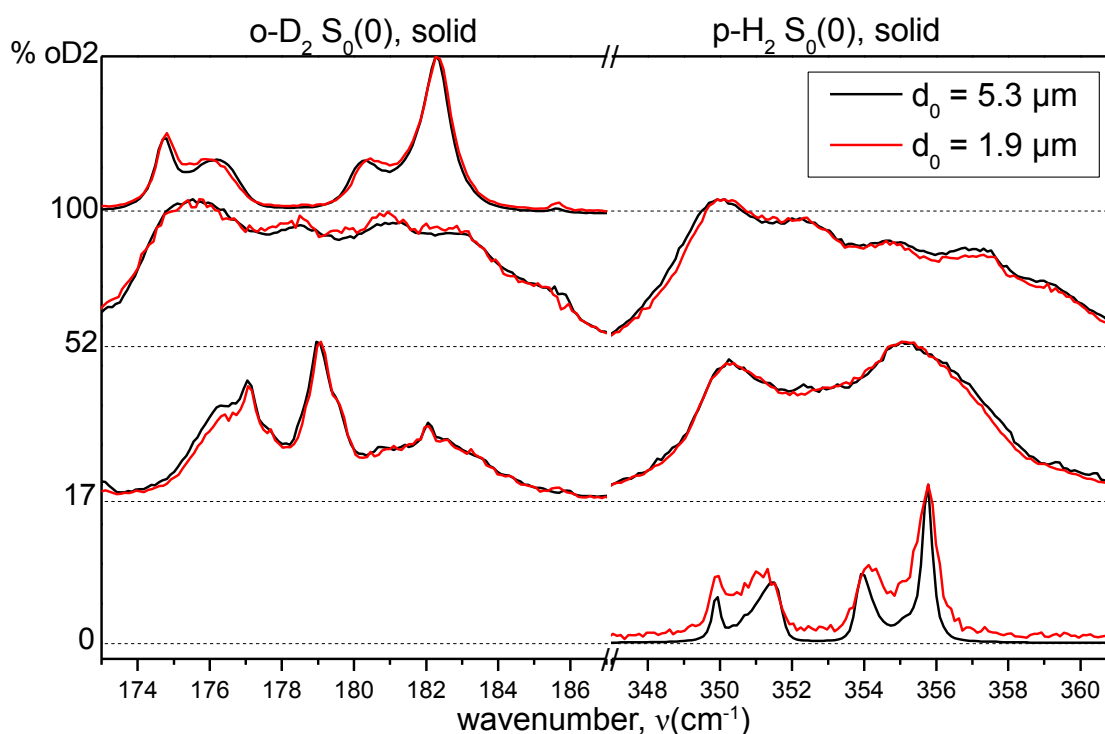
Figure 87: Comparison of the $S_0(0)$ line in the completely solidified 5.3 μm (black) and 1.9 μm (red) filaments.

detect differences in the contributions of lattice configurations in the spectra of the main component when small impurities of the other isotope are added. Yet, from the information that o-D_2 slightly changes in favor of fcc and p-H_2 towards hcp, we are unable to conclude, why the latter case should result in far greater percentage crystallization times compared to the pure substance than the other.

More promising, the difference in the structure of the rotational excitation for the very diluted mixtures may be linked to increased crystallization times, depending on the valid interpretation. In detail, the higher J = 1 content as well as the resonance effect causing the discrepancies would not have an influence, whereas the stronger delocalization of p-H_2 may indeed be connected to the crystal growth rate. The good agreement of the data from the small nozzle with the big one correlates nicely with the decent overlap in the plot of the crystallization times in fig.79 on p.172 and again proves that the temperature does not have a significant influence on the increase of crystallization duration compared to the pure substances.

6.2.5 Summary: rotational region

The broad, Lorentz-shaped $S_0(0)$ excitation in the liquid phase of both pure p-H_2 and pure o-D_2 shifts towards higher wavenumbers upon dilution (fig.83 on p.186), which is grounded in the reduction of traveling options of the rotons. For the highly diluted substances the peak position agrees with the value in the gas phase, which we interpret as impurity molecules that in majority are isolated from same-species partners and able

to rotate freely and undisturbed from the environment due to the quantum nature of the hydrogen isotopes.

In contrast to o-D_2, p-H_2 at low contents exhibits a significantly greater line width, which probably is due to the inevitably higher amount of $J = 1$ molecules present in deuterium and therefore higher probability to be located adjacent to impurities and disturbing their free rotation. However, possible overtone resonance effects based on the factor of 2 difference in the $S_0(0)$ excitation energy or the stronger delocalization rooted in the enhanced zero point vibrations of para-hydrogen could also play a role.

In the $S_0(0)$ excitation of the completely solidified filament, small dilutions of the main substances reveal an increase of molecules in fcc and rhcp lattice environments for o-D_2, yet a decrease in the same for p-H_2 (fig.85 on p.189). At intermediate mixtures the structure for both isotopes looks similar, in agreement with the literature.

At small mol fractions, o-D_2 features several sharp Gauss-shaped peaks, the main one being located at the value for the gas phase, which probably is associated with isolated molecules. Three further sharp peaks agree with the position of the equilibrium hcp crystal, which is interpreted as signal originating from isolated pairs of o-D_2 molecules. On the other hand, highly diluted p-H_2 produces a main broad Lorentz-shaped peak that matches with the gas phase line and a small side peak with similar width coinciding with the lowest energy of the equilibrium hcp excitation. The discrepancy to o-D_2 again probably is related to the greater amount of $J = 1$ molecules present in the deuterium environment, yet other explanations may also be viable.

7 | MIXTURES OF PARA-HYDROGEN/ ORTHO-DEUTERIUM WITH NEON

For further investigations of the crystallization behaviour of hydrogen isotopes with impurities, we measured samples of p-H_2 with Ne and o-D_2 with Ne, which are summarized in table 10. Due to the strong deviations of the melting points of hydrogen and deuterium compared to neon (compare fig.7 on p.23) and the complicated binary phase diagrams for intermediate compositions (fig.9 on p.27), we chose only to introduce small dilutions of up to 5% Neon, for which the components are completely miscible [48, 49]. For higher contents phase separation may occur in the liquid and we noticed that the stability of the filament suffered or the nozzle eventually froze.

Note that all noble gases atoms do not exhibit rotational and vibrational excitation, so that we are unable to obtain Raman spectra of the Ne component. We refrained from recording inverse mixtures with low hydrogen amounts due to unstable Neon filaments and lack of time.

One main peculiarity of our mixtures is the mass density. Due to the immense value of Neon with $1250 \, \text{kg/m}^3$ in the equilibrium liquid phase at 24.5 K , i.e. close to the melting line, compared to hydrogen with $76 \, \text{kg/m}^3$ or deuterium with $176 \, \text{kg/m}^3$, even small admixtures of Neon in the hydrogen isotopes increase the total mass density significantly. For example, the mixture 98H_2-2Ne already has a calculated value of $100 \, \text{kg/m}^3$.

name, #	date	temp2 (K)	P_0 (bar)	v_0 (m/s)	% Ne
100H_2-0Ne or #4	25/11/11	16	8.5	142	0.0
99.7H_2-0.3Ne	26/10/12	17	9.4	147	0.3
99H_2-1Ne	26/10/12	17.5	11.2	153	1.0
98H_2-2Ne	26/10/12	18	10.8	137	2.0
0Ne-100D_2 or #A	30/11/11	19.6	13.0	115	0.0
1Ne-99D_2	30/10/12	20	16.0	125	1.0
2Ne-98D_2	25/10/12	20	17.0	123	2.0
5Ne-95D_2	30/10/12	20	11.8	95	5.0

Table 10: Measurements with mixtures of p-H_2 with neon (upper half) and o-D_2 with Neon (lower half) using nozzle XVII-06 with $d_0 = 5.3 \, \mu\text{m}$. The content of neon is deduced from the set ratio of the flow controllers.

As usual, this chapter is divided into the main excitation regions vibrational 7.1 and rotational 7.2. Within the sections, the two data sets H_2-Ne and Ne-D_2 are discussed one after another, the latter referred to always in reverse order to avoid confusion. For

easier recognition, the color code light green for p-H_2 and orange for o-D_2 will be kept and increasing contents of neon are colored towards dark blue.

7.1 Vibrational region

As mentioned, only the hydrogen isotopes are Raman active and yield spectra. All vibrational series evidence the transition from the liquid to the solid band. Due to only small dilutions with Neon, the spectra series of p-H_2 with Ne and o-D_2 with Ne qualitatively do not differ from those of the pure substances or mixtures of p-H_2 and o-D_2 at small impurity contents, so that they are not shown here.
This chapter covers the temperature of the liquid (7.1.1) and the solid fraction (7.1.2).

7.1.1 Temperature of the liquid

Due to only small amounts of neon added to p-H_2 and o-D_2, respectively, the temperature of the liquid should not be altered much in the view of thermodynamics. The temperature of our filament is determined by evaporative cooling and heat conductivity towards the core. Inserting neon into the hydrogen isotopes barely changes the vapor pressure, since the partial pressure of Ne is negligible at such low starting temperatures compared to its melting point. Evaporative cooling should have the same effectiveness as in the pure hydrogen isotope filaments.
The thermal conductivity of pure Ne is roughly twice that of para-hydrogen at their respective melting points and the difference possibly increases at lower temperatures [97]. However the small contributions added to the liquids should not have an exceptional impact.

In fig.88 for all H_2-Ne measurements the extracted mean position of the liquid vibrational p-H_2 band is plotted against traveling time, representing the temperature evolution of filaments. With higher dilution of Ne (towards blue) the curves start at higher wavenumber, what is related to the continuously higher initial temperatures of the nozzle stated in the previous table 10 to avoid freezing of the nozzle and account for stable filaments. A comparison of the wavenumber position of the last liquid on the very right side, which has been a good indicator for similar final temperatures (compare fig.30 on p.79), reveals that the values for the mixtures are only slightly higher than for the pure substance, which roots in the reduced traveling options of vibrons due to the impurities (compare p-H_2—o-D_2 mixtures in chapter 6.1.3.2). We conclude that the translation wavenumber $\leftrightarrow$ temperature is basically equal for all cases and the graphs reflect actual temperature differences of the measurements.
For an estimation of evaporative cooling, we compare the slope of pure p-H_2 data (light green) with that containing 0.3% Ne (darker green) up to $\approx 2\,\mu s$, after which the latter starts to freeze (later chapter 7.1.2.1). The decline is almost parallel and since the data points describe the mean temperature, this signals that evaporative cooling as well as heat conductivity have to be similar in both cases as expected in above discussion of the thermodynamics. However, the slope of the mixtures containing 1 and 2% Ne is
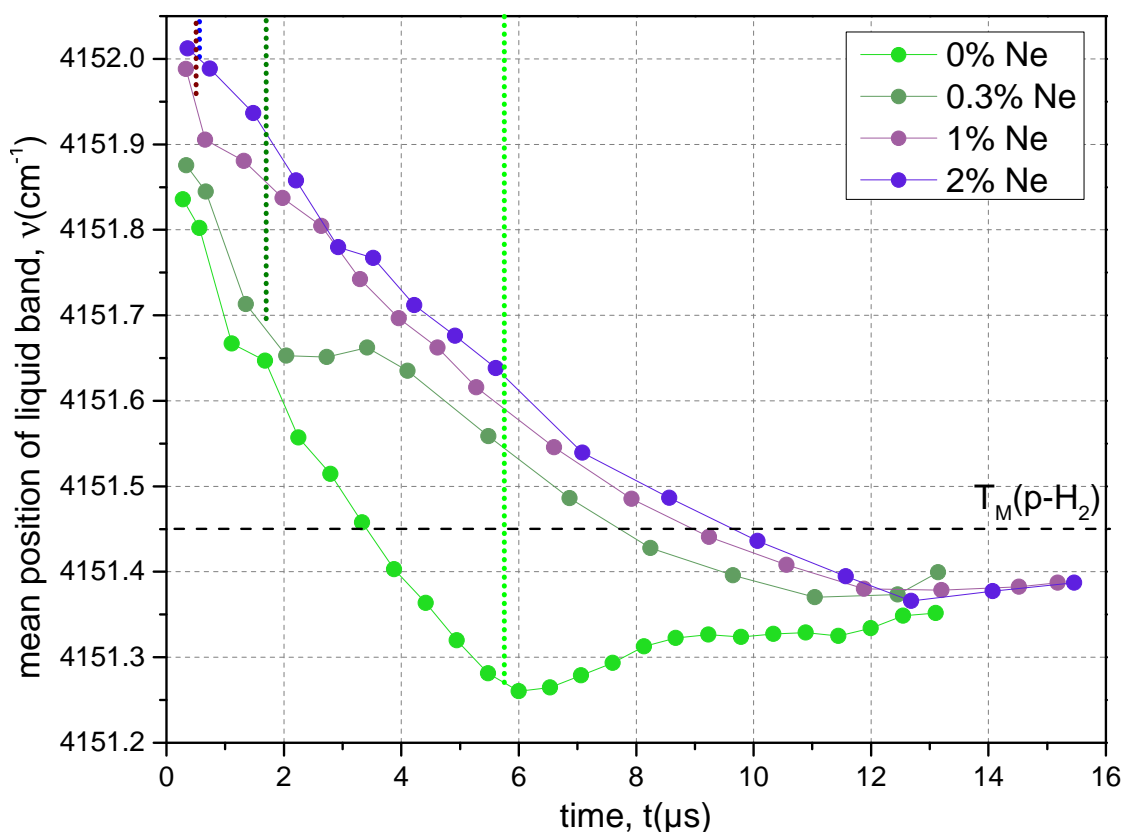
Figure 88: Mean wavenumber of the liquid vibrational p-H$_2$ band for increasing admixtures of neon (towards blue). The horizontal black dashed line marks the wavenumber corresponding to the melting temperature T$_M$ of pure p-H$_2$ according to the changed formula discussed in 4.1.1.1. Dotted vertical lines represent the onset of crystallization.

less steep, because the crystallization starts already at the beginning and the according heat released partially counters the effect of evaporative cooling.

The higher values for all mixtures compared to the pure case in the time interval 2-12 μs in plot 88 imply that throughout solidification the mean temperatures are significantly higher. It seems that for a major fraction of the crystallization process the mean temperature may be even above the melting line of pure p-H$_2$, which is indicated by the horizontal black dashed line according to the changed Vilesov formula of chapter 4.1.1.1. Note that the melting temperatures for the mixtures probably slightly vary, yet due to the lack of a accurate binary phase diagram, we cannot tell in which way.

To further assess the temperature during solidification, we plot the wavenumber gradient of the mixture 98H$_2$-2Ne (blue) compared to 100H$_2$-0Ne (green) in fig.89. The most interesting curve is the respective bottom curve, which corresponds to the lowest temperatures. We find that for the 2% Ne mixture the temperature does not decrease but rather increases due to the heat released by the early crystallization, which has already started at the second time step. In the further process, the wavenumber (=temperature) remains even slightly above the final temperature of the last liquid and very close to the melting temperature of pure para-hydrogen. According to our

isotropic model, the temperature gradient is warmer towards the core of the filament, which is also the direction in which the crystallization growth proceeds. Hence, it seems that only that small part of the liquid which is also the one currently transforming to the solid is actually below the melting temperature.
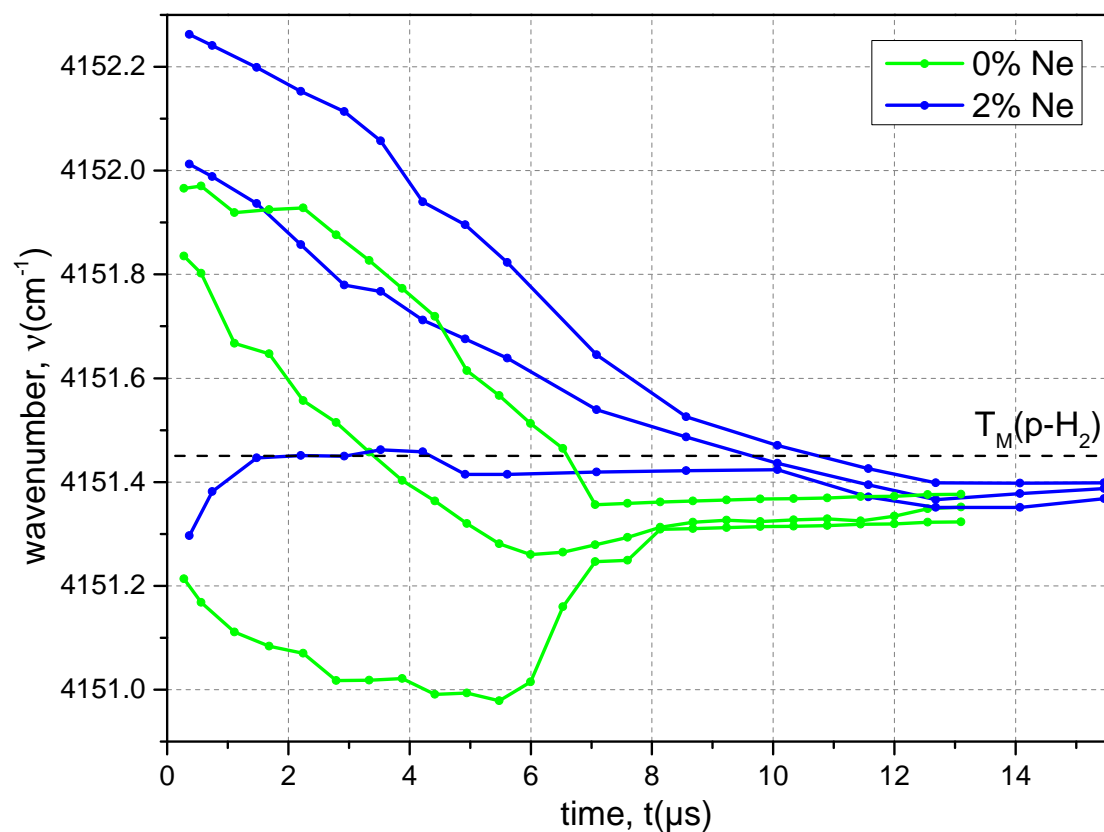

Figure 89: Wavenumber gradient of the liquid vibrational band of pure p-H_2 (green) and with the admixture of 2% neon (blue). Top, middle and bottom line correspond to highest, mean and lowest wavenumber according to the inflection point method described in chapter 4.1.1.1.

For Ne-D_2 mixtures no comparison of the liquid band of deuterium is possible due to the overlap of the $J = 1$ and $J = 0$ bands in connection with the change of the intensity enhancement due to the introduction of impurities. Yet, following above argumentation, effects of small contents of neon onto the effectiveness of evaporative cooling of the filament should be negligible. This is even more valid for the measurements of Ne-D_2 as all have the basically the same initial temperature of the nozzle (see previous table 10). Hence, only an earlier freezing of the filament discussed later on may increase the overall temperature of the filament.

7.1.2 Solid fraction

As for mixtures of p-H_2 with o-D_2, this section contains the most interesting data. It will start with a separate investigation of hydrogen-neon (7.1.2.1) and deuterium-

neon mixtures (7.1.2.2), proceed with the combination of both and a comparison with the previous p-H$_2$–o-D$_2$ data (7.1.2.3) and is finally analyzed on microscopic scales utilizing the previous discussion of the hydrogen mixtures (7.1.3).

7.1.2.1 Hydrogen–neon mixtures

The solid fractions of the para-hydrogen filaments at corresponding admixtures of neon are presented in fig.90 from green to blue. Introducing merely 0.3% of Neon results in an enormously earlier start of the crystallization compared to the pure substance. Additionally, the increase is rather abrupt compared to the gradual slope on pure p-H$_2$, but continuously becomes more shallow towards the end of solidification. Due to this early start, the total crystallization time is significantly larger, yet the curve is similarly smooth to the pure case.
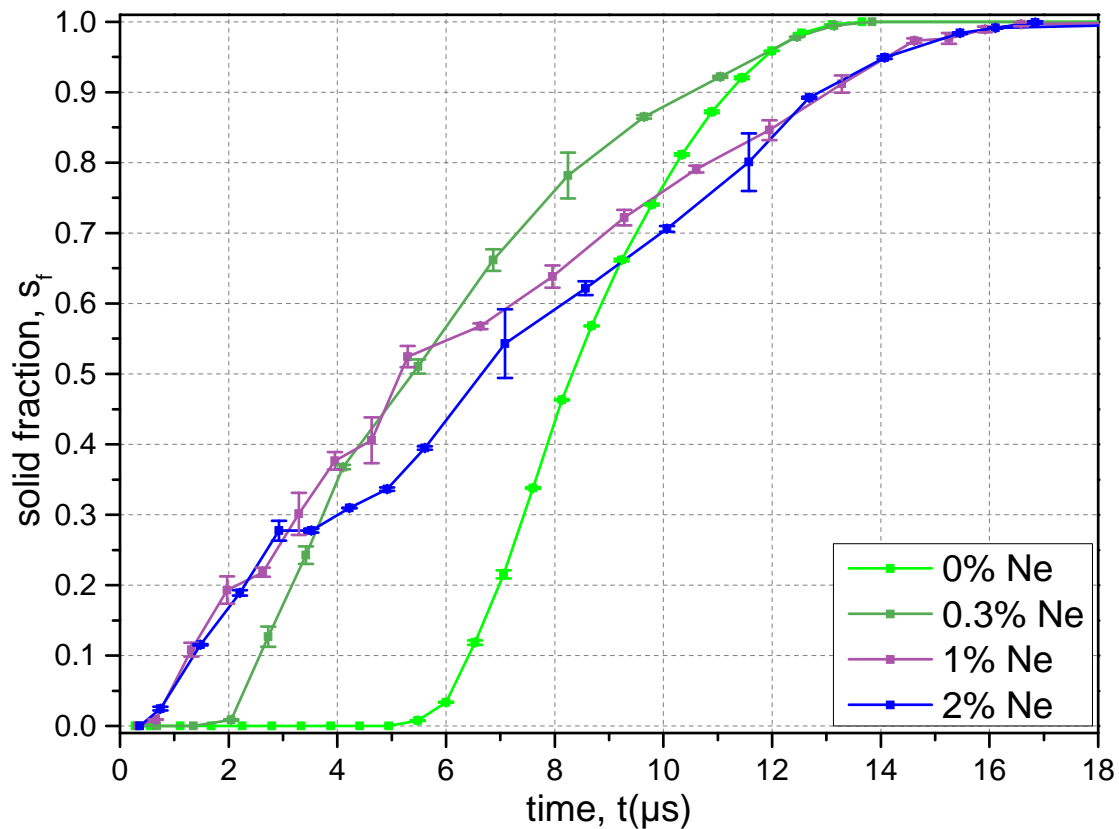

Figure 90: Solid fractions of p-H$_2$ (green) with small dilutions of Ne (towards blue).

Higher amounts of neon lead to an even earlier appearance of the solid, already at the second recorded distance and also with an instantly steep inclination. Both 1 and 2% solid fraction plots exhibit stark variations in their increases throughout the crystallization process, so that the curvature is not smooth. Despite the early start, the solidification lasts even longer than for the data with 0.3% Ne content.

All measurements with neon contributions show greater statistical error bars. In the raw spectra, this emerges as slight variations in the relative intensities of the liquid and solid bands in subsequently recorded spectra at the same z position. To stress

the reproducibility, the 1 and 2% mixtures have been remeasured with similar source conditions on different days for data points around the start and end of solidification. The remeasured data reveals an unchanged start of the solidification, yet differences in the last liquid (shown later in section 7.1.2.3), what signals that small admixtures of neon make para-hydrogen filaments sensitive to slight changes in conditions, eventually leading to variations in the growth dynamics.

In this regard, it would be interesting to look at a detailed binary phase diagram to determine, if already at equilibrium conditions phase related phenomena occur. Unfortunately, up to now no p-H_2−Ne phase diagram exists and the only available n-H_2−Ne diagram, applying to hydrogen with high $J = 1$ content, lacks a detailed view in the region, which our mixtures occupy (see right panel in fig.9 on p.27).

Considering the temperature gradient in fig.89 on p.200, the discussed low temperature curve may relate to the current growth rate of the solid fraction. For instance, while the solid fraction of the 2% Ne mixture stagnates between 3 and 4 µs, the corresponding lowest temperature curve in fig.89 in this time interval exhibits the highest values slightly above the melting line T_M of pure p-H_2. Hence, due to the early onset of freezing for the p-H_2−Ne mixtures the crystallization proceeds from a barely supercooled liquid, which may contribute to the subsequent extended crystal growth.
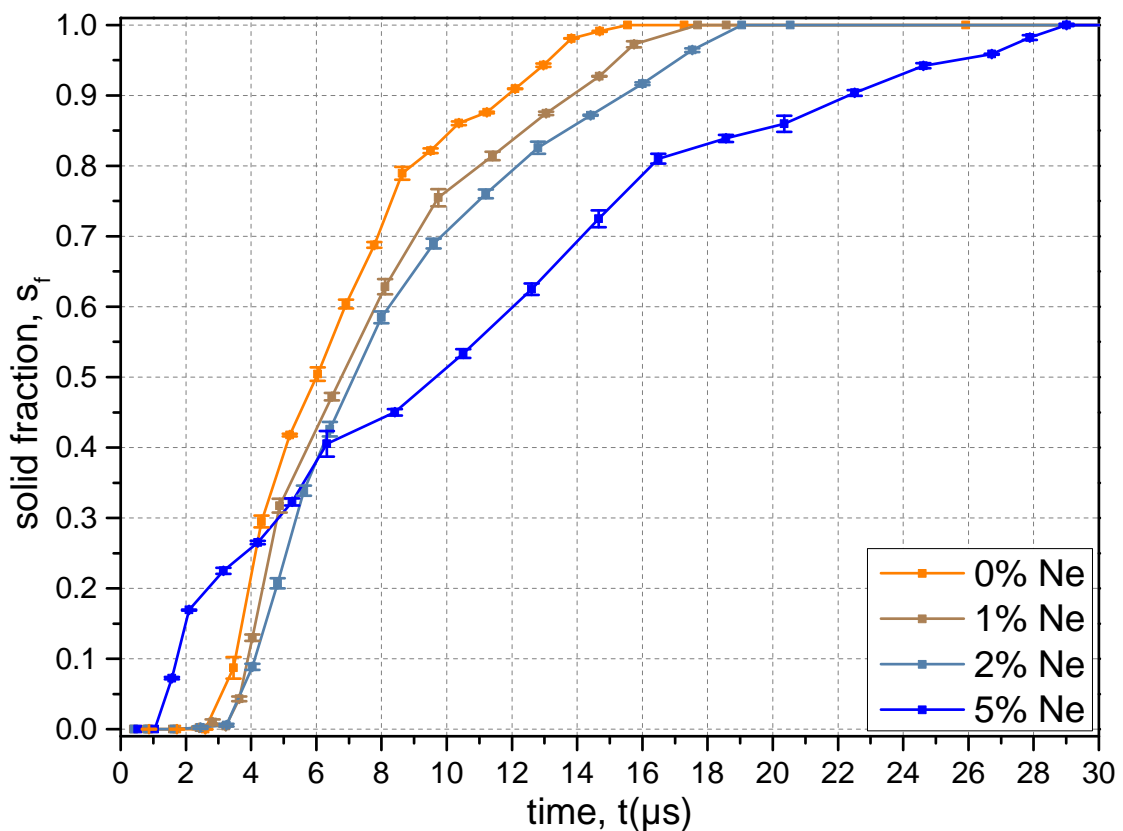
7.1.2.2 Deuterium–neon mixtures

Figure 91: Solid fractions of o-D_2 (orange) with small dilutions of Ne (towards blue).

The solid fractions of o-D$_2$ with small admixtures of Ne (towards blue) are presented in fig.91. One extremely interesting observation is that inserting 1 and 2% of neon leads to a later appearance of the first solid, which is in stark contrast to how all other mixtures behave. Although slight changes in the filaments condition, as discussed for pure para-hydrogen in chapter 4.1.3.5, may also play a role, there is also a physical explanation for this peculiarity. When we take a look at the corresponding binary phase diagram in the left panel of fig.9 on p.27, we find that for small additions of neon < 4% the melting line actually declines to lower temperatures, particularly visible in the magnified inset in the middle. This means the temperature of the liquid filament has to reach lower values to be similarly undercooled to the pure o-D$_2$ case, which could also lower the nucleation rate. For our measurement with 5% neon, the crystalline phase appears significantly earlier, which is in agreement with a higher respective melting point even than the pure phase according to this phase diagram.
However, two immediate restrictions have to be made with this explanation. For one, the available phase diagram applies to the case of n-D$_2$ with 33% J $= 1$ content rather than o-D$_2$ with 2.5%, which may introduce deviations. And secondly, although the relative undercooling may change due to the respective melting point, this does not necessarily have the same influence onto the nucleation rate, which is likely to vary based on the kind of impurities and is the key feature for the appearance of the solid that we measure.

Although we do not have estimations of the temperature, the later freezing indicates that the temperatures of the liquid filament for the 1 and 2% mixture are similar or even slightly below those of the pure o-D$_2$ case. Nonetheless, the solid fractions reveal that the crystallization process takes longer for increasing neon content. The 5% mixture, which is likely at higher temperatures, yields even the longest crystallization times of all measurements in this work.
The statistical error bars of the measurements are comparable with pure ortho-deuterium and do not vary that much as in the mixtures of p-H$_2$ with Ne. This indicates that mixtures of neon with the heavier hydrogen isotope are more stable in terms of the crystallization progress at the same z position.

7.1.2.3 First solid and solidification time

Likewise to hydrogen-deuterium mixtures it is insightful to reduce the solid fractions to the time for the start of crystallization t_{fs} and its duration t_{ll-fs}. As stated previously, these two observables have been remeasured for some data points to test reproducibility. The data for t_{fs} (stars) and t_{ll-fs} (circles) for mixtures containing neon are presented in blue in fig.92.

We first focus on the left panel having para-hydrogen as the main component. The remeasurements for 1% neon content deliver the same values for both the start and duration of solidification within error bars, the latter being almost double the value of pure p-H$_2$. The 2% data shows the same starting times, yet significant differences in the total crystallization time of $\approx 15\%$.
In the left panel also the data of p-H$_2$ with small dilution of o-D$_2$ from the previous chapter are plotted in green. The same trends, i.e. earlier starts of crystallization and longer durations, are visible for both the blue and the green curve, yet the magnitude is
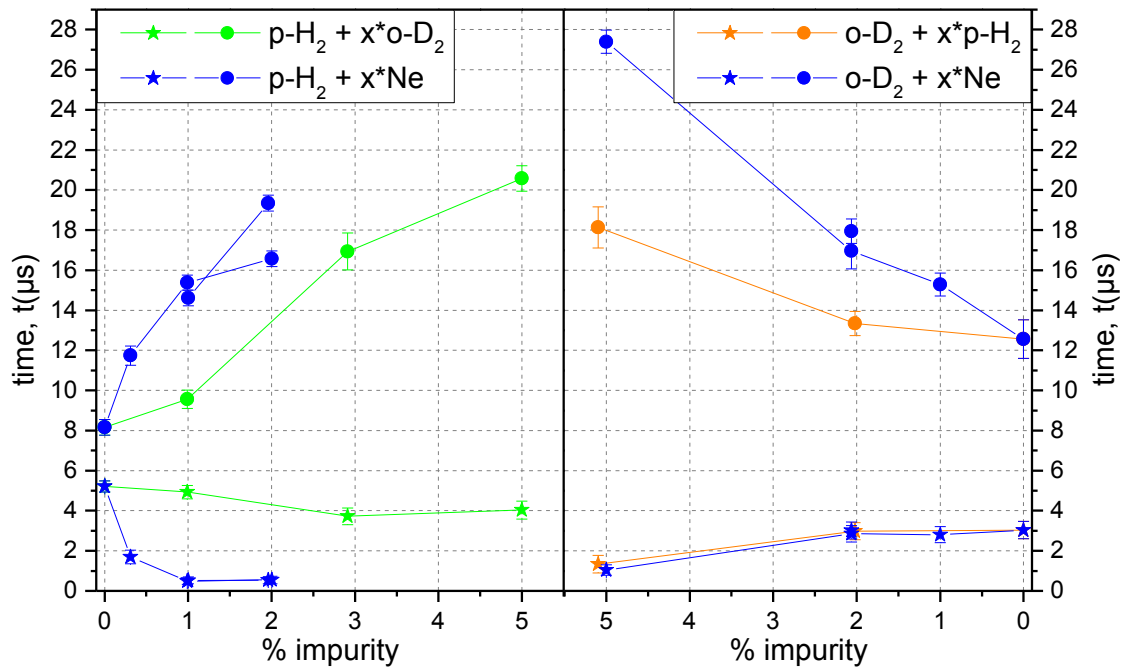
Figure 92: Left panel: Time for first solid t_{fs} (stars) and complete solidification t_{ll-fs} (circles) of p-H_2 with small dilutions of Ne (blue) and o-D_2 (green). Right panel: o-D_2 with small dilutions of Ne (blue) and o-D_2 (orange).

much more pronounced for mixtures with neon freezing significantly earlier and longer. However one has to take care that due to the early freezing the temperature of the liquid is higher, probably influencing the crystallization duration (see next section).

In the right panel, o-D_2 is the main component with neon and para-hydrogen impurities in blue and orange, respectively. Remeasuring the mixture with 2% neon content yields the same values for t_{fs} and t_{ll-fs}. In the comparison with small additions of p-H_2 as an impurity, we find that the starting times for the neon mixtures match quite decently and even the slight delay for the 2% impurity content is present in both measurements. The crystallization durations, however, are enhanced for all neon mixtures with twice the pure o-D_2 time for 5% Ne mol fraction compared to only 40% increase for 5% p-H_2 impurities.

7.1.3 Interpretation

This section is dedicated to the interpretation of the observations retrieved from the solid fractions in the previous sections, particularly in the light of the different hypothesis that were already introduced in mixtures of p-H_2 and o-D_2.

At first we want to have a short review of the most important features of the species. To recap chapter 2.4, p-H_2, o-D_2 and Ne exhibit a spherically symmetric interaction potential, which is crucial for simplifying further analysis. However, their sizes differ significantly and the ratios are summarized in table 11. We see that neon in p-H_2 represents even smaller particles than o-D_2 does. On the other hand, p-H_2 in an o-D_2

environment is a larger species, whereas Ne occupies less space. Additionally, Ne is 20 and 10 times heavier than p-H_2 and o-D_2, respectively.

We conclude that with para-hydrogen as the main component, neon, with its smaller size and its higher mass, can be considered a more extreme version of ortho-deuterium. In contrast, for ortho-deuterium impurities of neon are heavier and smaller and therefore qualitatively the opposite to the lighter and bigger para-hydrogen molecules.

impurity...	...in	p-H_2	o-D_2
p-H_2		-	1.05
o-D_2		0.95	-
Ne		0.84	0.88

Table 11: Size ratios of the different impurities in the hydrogen isotopes.

7.1.3.1 Temperature related effects

Regarding the start of crystallization, the information we gather from the mixtures with neon is ambiguous. For p-H_2 the very early onset of freezing can be argued in terms of the extremely undercooled neon agglomerations serving as nucleation embryos. It seems unlikely that with only 1% neon content large enough clusters statistically form, yet we do not have information, if phase separation, possibly even prior to the expansion through the nozzle, may happen in our system.

On the other hand, with o-D_2 as the main medium we find even a slight increase in the starting time for solidification at 1 and 2% Ne impurities, although it still heavily supercooled, yet slightly less than in the p-H_2 liquid. This indicates that either no phase separation occurs for o-D_2 or that geometric effects on microscopic scales have an impact (discussed later).

Based on the similar appearance of the solid and therefore equal temperature of the liquid at this point, the longer crystallization times are clearly not explicable by temperature effects for Ne in o-D_2.

For p-H_2 diluted with neon we see that temperatures of the liquid are considerably higher during solidification even in the coldest layer, which supposedly is the currently transforming one (compare fig.89 on p.200). Hence, part of the longer crystallization times may be related to the warmer temperatures, as for both crystal growth models this results in slower crystallization rates (compare fig.36 on p.89).

7.1.3.2 Local structures in the liquid

Simulations of the collaborating group in Milano show that for small amounts of Ne in p-H_2 as well in o-D_2 the correlation function of Ne-Ne has its first maximum at smaller intermolecular distances (compare fig.93), which is in agreement with the smaller size of Ne atoms discussed in the beginning.

The structure parameters obtained from the bond orientational order analysis reveal a higher tendency towards icosahedral ordering for neon compared to both hydrogen isotopes. Additionally, the magnitude of this is slightly larger for neon within the p-H_2 environment, since the absolute temperatures are lower than for o-D_2, which favors such local formations. Since the icosahedron is one main candidate responsible for the frustration of crystallization (compare chapter 6.1.6.2) and the number of particles in such configurations increases with higher admixtures of neon to the hydrogen liquids, the simulation results qualitatively correlate with our observed increased crystallization times. Furthermore, even the greater percentage increase for p-H_2 liquids compared to o-D_2 at same dilutions coincides with neon forming more icosahedral order at lower temperatures.

However, we recall that the simulations for p-H_2−o-D_2 mixtures at lower temperatures predict an increase in the total number of icosahedral structures in the liquid, yet our measurements identified rather a decrease in the crystallization times for this instance, leading to a contradiction. The conclusion was that local structures in the liquid alone are unable to account for our observed longer crystallization durations in p-H_2−o-D_2 mixtures. Despite the qualitative agreement for neon in the hydrogen isotopes pointed out above, it is therefore unlikely that the local structure approach applies in this case of neon.
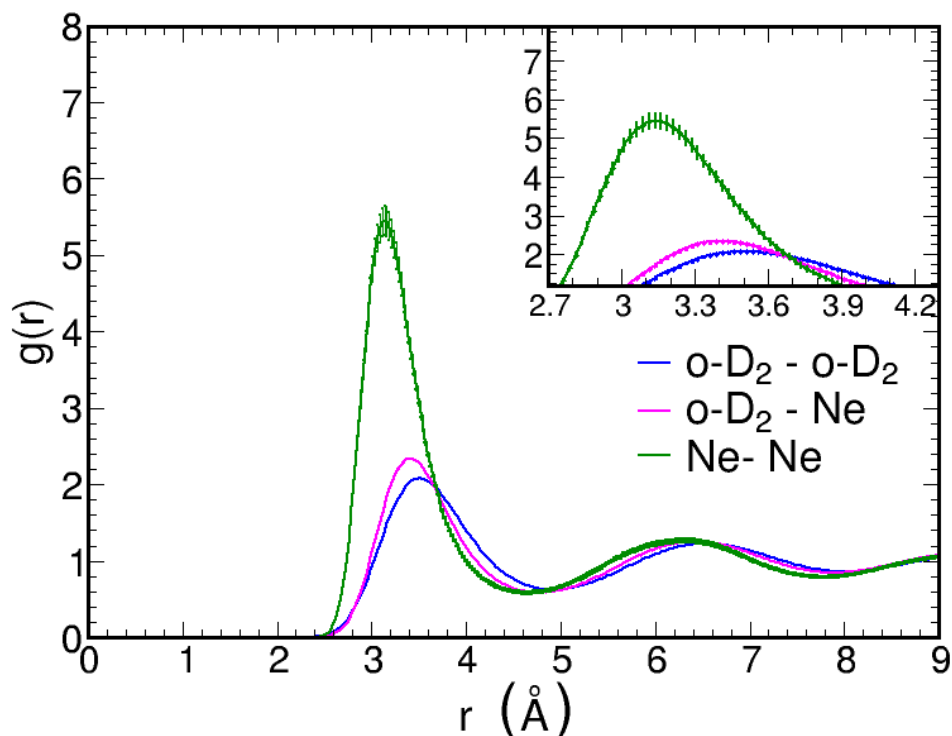

Figure 93: Correlation functions g(r) from PIMC simulations for an o-D_2 liquid diluted with 3% Ne. The inset shows a magnified detail of the first maximum.

In view of the earlier starts of crystallization it is quite probable that certain geometric structures induced by the smaller neon atoms in para-hydrogen promote the formation of nucleation embryos, e.g. by lowering the energy barrier or reducing the number

of particles necessary, which both drastically alter the nucleation rate. This may go hand in hand with the statement of the previous section that neon experiences strong supercooling in hydrogen.

The local order approach additionally offers a hypothesis for the slightly later appearance of the solid in liquid deuterium doted with neon. This may indeed be related to a frustration of nucleation, as the nucleation energy may be increased for certain geometric formations. In this regard the size ratio of the particles probably plays a crucial role. However, for further insights, simulations of the actual dynamics and/or energy calculations are mandatory.

7.1.3.3 Fractionation and interface effects

For the system p-H_2—o-D_2 effects at the liquid-solid interface seemed to be the most promising approach, yet – and partially because – a lack of quantitative as well as even qualitative estimations disables a detailed analysis and only comparisons with simulations and colloidal systems are available.

Regarding Jackson's kinetic model, for neon we cannot calculate the equilibrium segregation coefficient k_e of eq.2.24 on p.36 like for the hydrogen isotopes, because the thermodynamic properties of the liquid phase are not accessible at such strong supercoolings. However, due to this supercooling, k_e has to be strongly in favor of the solid phase. Backup for this is provided by simulated values for the chemical potential difference [98, fig.1], for which extrapolated values are used to estimate k_e, plotted in blue in fig.94 compared to the calculated k_e for p-H_2 (green) and o-D_2 (orange). The neon values have to be taken with care, especially towards lower temperatures, but it is clear that the curve is always higher than that those the hydrogen isotopes. Hence, Ne atoms probably have a higher tendency to join the crystalline phase in comparison to the respective hydrogen isotope in a mixture.

The diffusivity of neon in liquid hydrogen has been measured to be similar in its order of magnitude and, interestingly, even higher than for ortho-deuterium in para-hydrogen [91]. Since our measured crystallization rates in mixtures with neon are even lower, it follows that, similar to the p-H_2—o-D_2 system (compare right panel of fig.81 on p.179), the particles are able to diffuse away from the growing crystal interface and are able to build up different concentrations in the liquid and solid phase, i.e. perform fractionation. Due to the supposedly higher segregation coefficient k_e above, the effect of fractionation is expected to be stronger for mixtures of hydrogen isotopes with neon. Compared to the differences in the solid fractions curves of p-H_2—o-D_2 mixtures (compare fig.75 on p.166), this should manifest in even more pronounced discrepancies in favor of neon compared to its mixing partner. In this regard it is very unfortunate that neon does not offer Raman activity, which would be a strong test of this statement. In view of the calculation of the growth rate in Jackson's model in formula 6.3 on p.180, the relative concentration of the main components hydrogen or deuterium, respectively, should be higher in the liquid than in the solid phase, what potentially increases the crystallization rate in contrast to our experimental findings. However, the exponential term may have a higher impact based on the higher excess energy of neon mixed with hydrogen [47] and deuterium [99], which may counter the effect.

We conclude that due to the many unknown parameters the model is unable to propose an effect onto the crystallization times of mixtures with neon.
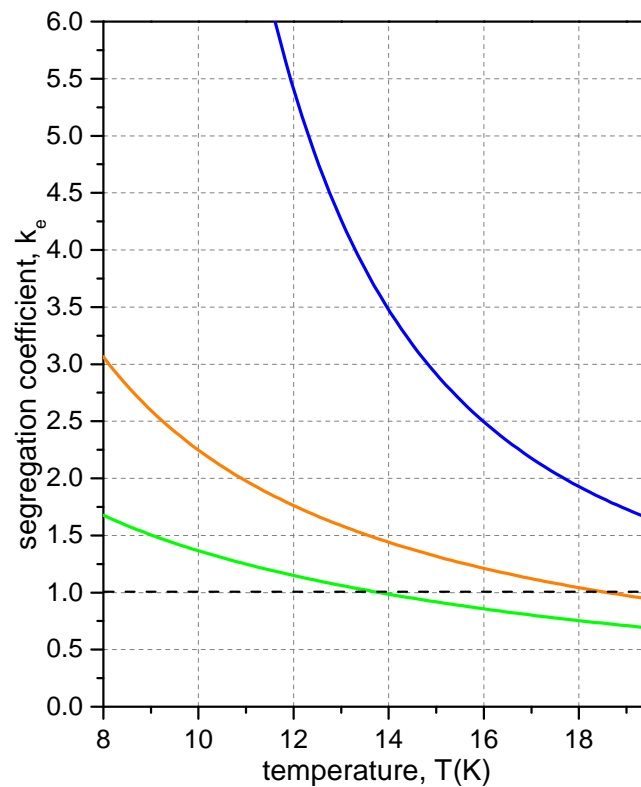
Figure 94: Calculated segregation coefficient k_e (eq.2.24 on p.36) for p-H$_2$ (green) and o-D$_2$ (orange) as well as the estimation for Ne (blue) extrapolated from [98].

Yet, the indications that fractionation at the liquid-solid interface probably is present and even stronger than in the hydrogen isotopic mixtures, opens up the basis for all further explanations, which have already been utilized for the mixtures of hydrogen isotopes. For one, the (partial) transition from the collision-limited to the diffusion-limited model [4] is still a viable approach and could be more pronounced, since with neon phase segregation is grounded on a stronger driving force. The influence of such fractionation effects likely is also dynamical throughout the whole crystallization phase, since the temperature at the surface towards the core in any case is increasing, yet also the compositions at the liquid-solid interface can vary.

Alternatively or additionally, the greater size ratio stated in the previous table 11 may also play a crucial role with regard to the ordering at the interface [63]. The more extreme difference in the sizes could make it harder to stack the particles efficiently into a crystalline lattice structure. Our observation that for o-D$_2$ adding significantly smaller particles (Ne) have a greater effect on the crystallization time than slightly larger ones (p-H$_2$) support this statement. However, also the slower thermal velocity based on the higher mass of neon could have an influence onto the behaviour.

As a new item on the long list of possible influences, we want to add the conflict between the lattice configurations of the crystal. Whereas the pure phases of the hydrogen isotopes arrange in hcp at equilibrium conditions, the instance that neon rather prefers fcc can also have an impeding effect on the crystallization rate in terms of minimization of the lattice energy. More information to this will follow in the rotational section 7.2.

The conclusion of this confusing and unsatisfying wilderness of ideas is that our experimental data alone is not able to find solutions for the observed effects. As the common way, theoretical work is mandatory to interpret the physical background of experimental findings. This theoretical contribution can for example be in the form of simulations of the dynamics of the liquid as well as the liquid-solid interface in our measured system. Particularly, such calculations have to take into account the diffusion as well as the arrangement of particles at the interface.

7.1.4 Summary: vibrational region

Analysis of the temperature gradient from the liquid p-H$_2$ band at small dilutions with Ne indicates that evaporative cooling as well as thermal conductivity are not influenced by the impurity, which is in agreement with thermodynamic considerations and probably applies to o-D$_2$$-$Ne mixtures as well. Yet, the temperature of the liquid during solidification is increased for small dilutions of p-H$_2$ compared to the pure case due to a very early appearance of the solid phase.

Already 0.3% Ne content result in a significantly earlier and longer crystallization of p-H$_2$ (fig.90 on p.201). Both effects are enhanced for 1 and 2% content.
In contrast, the onset of crystallization for o-D$_2$ doped with similar amounts of Ne is slightly later than for the pure substance, yet the crystallization durations are also increased (fig.7.1.2.2 on p.202). At 5% neon impurities solidification starts earlier and lasts even longer.
Compared to p-H$_2$$-$o-D$_2$ mixtures, for small dilutions of p-H$_2$ the behaviour is similar, yet both start and duration of crystallization are more pronounced. With Ne diluted o-D$_2$ filaments begin to crystallize at the same times as with similar dilutions of p-H$_2$, yet also here the duration is longer (fig.92 on p.204).

An explanation for the more extreme effects of hydrogen isotopes doped with neon probably are related to the greater size ratio of the constituents of the mixtures. Estimations of the segregation effect indicate that the tendency of neon to join the solid may be greater, which is comprehensible considering its strong relative undercooling. However, a microscopic mechanism for the earlier and longer crystallization process remains open.

7.2 Rotational region

In this chapter the $S_0(0)$ excitation of the hydrogen isotopes at low neon dilutions will only be discussed for the crystalline phase. The spectra obtained from the entirely liquid states are omitted, since they do not expose any differences due to the small amount of impurities.

7.2.1 Structure of the solid

7.2.1.1 Hydrogen-neon mixtures

The rotational spectra of the completely solidified filaments of p-H_2 with increasing amounts of Ne impurities are presented in fig.95 and reveal immense differences in the crystalline structure. Starting at pure p-H_2 (light green), adding only 0.3% neon (dark green) reduces the intensity of peaks (2) and (3), which are associated with an hcp lattice, to approximately half their previous value. Although the maximum heights of (1) and (4) are lower, the peaks actually gained signal as they are broader than for the pure case, so that we deduce that the amount of molecules in an fcc lattice structure is increased[1]. Additionally, intensity is redistributed into the regions in between (1)-(2) and (3)-(4), representing mixed rhcp configurations.

For the mixture containing 1% neon (purple) the hcp peaks (2) and (3) shrink further and shift apart, which is interpreted as structures increasingly resembling rhcp rather than a neat hcp lattice. This reduction in signal is compensated by a further increase of fcc configurations. For the highest measured dilution of 2%, this trend continues and most of the particles are arranged in fcc lattices accompanied by only small rhcp regions. The vanishingly small intensity at $352\,\mathrm{cm}^{-1}$ and $354\,\mathrm{cm}^{-1}$ indicates that almost no neat hcp lattice structures exist.

In dilutions of p-H_2 with o-D_2 the crystal structure changed only marginally in favor of hcp, so that the behaviour of neon not only is more extreme but also qualitatively different. Also, the peaks for the neon treatment are sharper, which probably can be related to the fact that Ne does not introduce any interfering $J = 1$ particles blurring the spectra.

The change from hcp towards fcc likely is attributed to the instance that fcc is the equilibrium lattice configuration of pure neon. As the starting time of crystallization happens at increasingly earlier times upon dilution, we may argue that Ne already predetermines the crystalline structure by forming the first nucleation seeds. Yet also during the growth of the crystal the placement of the noble gas atoms probably repeatedly prescribe the lattice configuration. The higher temperature of the liquid, however, seems to not a have a dominant influence on the structure as we will see for o-D_2 in the next section.

After complete solidification we do not notice any changes in the crystalline structure, so that no evidence is provided that this lattice configuration is influenced by Ostwald's rule of stages and therefore metastable. Yet, the lattice structure may still be metastable,

---

1   Likewise to p-H_2—o-D_2 mixtures, the broadening of all bands is grounded in the breaking of lattice symmetry due to impurities.
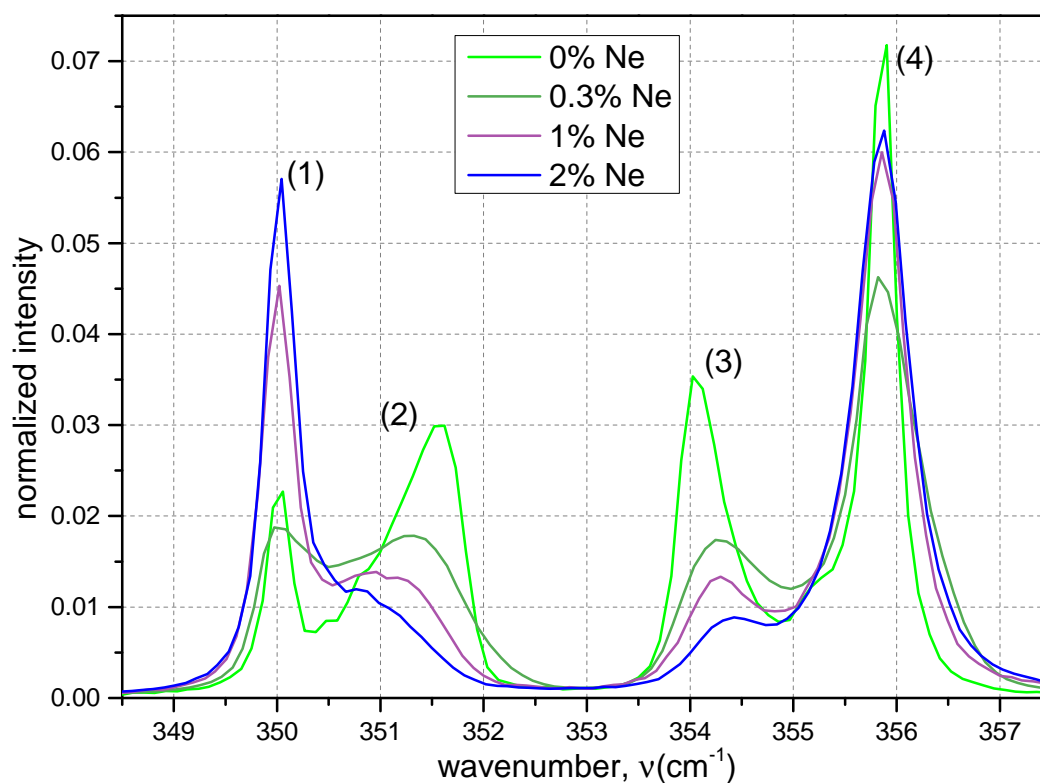
Figure 95: $S_0(0)$ excitation after complete crystallization of p-H$_2$ filaments doped with neon. The main peaks are enumerated from left to right.

because the addition of impurities can stabilize the lattice by increasing the amount of energy barriers separating fcc from hcp [74].

In view of the longer crystallization times, this lattice structure forced onto the p-H$_2$ molecules may indeed slow down the growth of the crystal. Reasons may be ordering at the liquid-solid interface or a less favorable arrangement in terms of local energy minimization. However, it is unlikely that this is the main effect responsible for the longer crystallization duration, since mixtures of p-H$_2$ with o-D$_2$ did not show significant changes in the crystalline structure despite having higher solidification times.

7.2.1.2 Deuterium–neon mixtures

The corresponding rotational spectra for o-D$_2$ with Ne impurities are plotted in fig.96. Similar to the p-H$_2$ case, peaks (2) and (3), again associated with hcp, are reduced, when pure o-D$_2$ (orange) is diluted with neon (towards blue). Additionally, these peaks shift apart, indicating that the lattice structure resembles more a mixed crystalline rhcp structure rather than clean hcp. The main part of the signal is redistributed into the fcc peak, so that at the highest content of 5% Ne, almost all intensity is united in the fcc peaks (1) and (4). The initial overall more blurred peaks originate from the higher $J = 1$ content serving as perturbations for the traveling of rotons. The further broadening comes from the neon impurities.
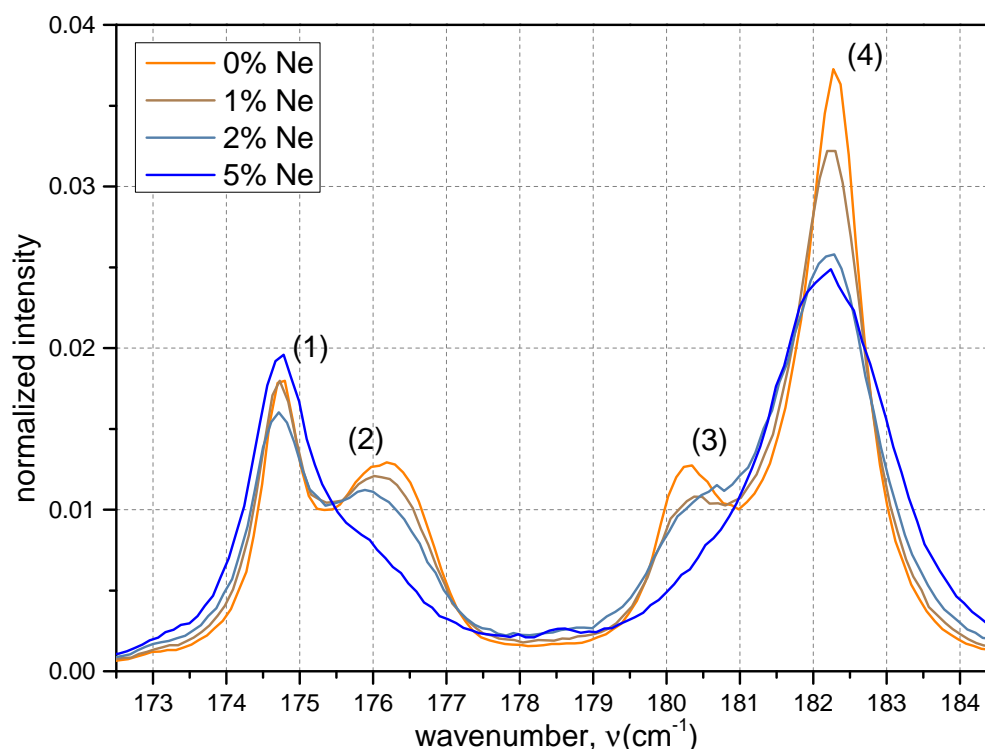
Figure 96: $S_0(0)$ excitation after complete crystallization of o-D_2 filaments doped with neon. The main peaks are enumerated from left to right.

We recall that inserting p-H_2 impurities into the o-D_2 lattice structure already signaled a slight trend in favor of fcc lattice configurations. However, in the spectra shown here this effect is much more pronounced. The similarity to neon introduced into p-H_2 in the preceding section strongly suggests that it is indeed the neon impurities that force their natural fcc lattice structure onto the hydrogen isotopes. Since the temperature of the o-D_2 liquid, from which the crystal forms, is similar for the pure and slightly neon doped mixtures, it can at most have a minor influence onto the lattice that forms.

After complete solidification no change in the peak intensities and, hence, no signs for metastability are found. As for the case of p-H_2 diluted with neon, the increased amounts of fcc lattice configurations may retard the growth of the crystal.

7.2.2 Summary: Rotational region

Inserting small ($\leqslant 2\%$) amounts of neon into p-H_2 changes the lattice structure significantly from hcp in favor of fcc (fig.95 on p.211). The remaining hcp peaks are shifted towards the strong fcc peaks, signaling that they resemble more randomly packed rhcp rather than neat hcp configurations. o-D_2 doped with up to 5% Ne exhibits a similar behaviour, yet with broader peaks due to the higher J = 1 content (fig.96 on p.212). Since fcc is the natural lattice configuration of pure neon, impurities of it probably force this configuration onto the structure of the hydrogen isotopes. This effect may contribute to the observed slower crystallization rates.

8 | RECAP AND CLOSURE

8.1 Summary

Novel experimental technique

This work presents a novel method to access the crystallization behaviour of super-cooled liquids on $10\,\text{ns}$ time scales. The core component is a liquid microjet, which is injected into vacuum through a glass pipette with a μm-sized orifice and propagates as a continuous cylindrical filament at velocities of $\approx 100\,\text{m/s}$. By evaporation at the vacuum exposed surface, the liquid filament cools down rapidly to a supercooled state, which eventually transforms into the crystalline phase. The high directional stability in combination with the self-replenishing nature of the jet allows to translate the traveling distance into a time axis fixed in space. By means of Raman spectroscopy with high spatial resolution, we are able to probe the evolution of the liquid filament as well as the transition to the crystalline phase along this axis.

New nozzle construction

To prove the feasibility of this principle, in this work hydrogen isotopes are used as the main sample, requiring a continuous flow cryostat to attain the initial liquid state. A new nozzle construction is designed, in which the nozzle is thermally coupled to the cryostat via a flexible copper strap and mounted onto a three-axis manipulator to enable positioning with sub-μm accuracy. By displacing the nozzle, series of Raman spectra of the vibrational $Q_1(0)$ as well as rotational $S_0(0)$ excitation are recorded from $2\,\mu\text{m}$ slices of the filament at several distances along the traveling axis. Preparatory to experiments, the hydrogen isotopes are converted at $20\,\text{K}$ to their spherically symmetric $J = 0$ ground state yielding para-hydrogen (p-H_2) with 99.8% and ortho-deuterium (o-D_2) with 97.5% purity, whereas the residuals are represented by the respective $J = 1$ isomers.

Supercooling and crystallization of para–hydrogen

The Raman series of the vibrational excitation of pure p-H_2 reveal a broad liquid band that gradually shifts towards lower wavenumber, i.e. energy, values with increasing traveling distance of the filament. Utilizing a relation between wavenumber and temperature from the literature, this behaviour is identified as a temperature gradient radially across the filament. In a model, the cross section of the filament is divided into 100 concentric layers, allowing for evaporative cooling of the outermost layer and governing the temperature exchange to the inner layers by heat conductivity. Numerical calculations of this model along the time axis agree qualitatively with the experimental findings

and also quantitatively, if the parameters of the wavenumber-temperature correlation are altered within their stated error bars. The outer layer reaches temperatures as low as 9-9.5 K, which corresponds to an undercooling of 30% below the normal melting point within $\approx 5\,\mu s$.

After this period the filament starts to freeze, evidenced in the Raman spectra by the appearance of a sharp peak, into which intensity continuously is redistributed from the liquid band, the percentage share being defined as the solid fraction. Due to the heat of solidification, the onset of crystallization is accompanied by an increase in the temperature of the liquid mainly in the coldest parts, so that we conclude that nucleation happens only at the cold surface, in agreement with the strong temperature dependence of classical nucleation theory. As the Raman spectra are recorded over periods orders of magnitude longer than the time scales of the filament dynamics and therefore yield averaged values, we propose that the crystal growth proceeds isotropically towards the core within the filament cross section model. By dividing the filament radius by the total crystallization time, we roughly estimate the growth velocity to be $\approx 0.3\,m/s$. By comparing this value with the predictions of two competing crystal growth methods we exclude the diffusion-limited model and confirm the collision-limited model to be valid for our case.

Nozzle and filament characterization

Filaments produced by smaller nozzles exhibit a similar temperature evolution of the outer layer in the first μs, since evaporative cooling mainly depends on the vapor pressure according to the current temperature. The core as well as mean temperature cool down faster compared to bigger filaments due to shorter heat transfer distances and match well with the numerical calculations. Based on these lower temperatures, the onset of crystallization occurs earlier and the crystal growth is higher, in agreement with classical nucleation theory and the collision-limited model. These findings apply to all filaments investigated regardless of their particle constitution.

Repetitive measurements of the same nozzle yield slight variations in the appearance time for the first solid for which no correlations to changes in the source parameters are detected. These seemingly arbitrary effects are probably rooted in deviations from ideal flow conditions, an isotropic surface and/or partial freezing of the nozzle orifice. However, the crystal growth rate remains largely uninfluenced by this.

Lattice structure of para–hydrogen

In the rotational Raman spectra we identify that the crystalline structure is constituted of a mixture of fcc, hcp and intermediate rhcp lattices. Since at equilibrium conditions bulk liquid para-hydrogen is exclusively found to freeze into a pure hcp arrangement, our observed structure probably is metastable and the result of Ostwald's rule of stages, which states that the initially formed crystal does not necessarily have to be the most stable configuration. This statement is supported by evidenced changes in the crystalline structure in favor of hcp during and even after complete solidification of the filament on time scales of μs, indicating a martensitic, i.e. a diffusionless transition. Available literature confirms that at temperatures of the solid of $\approx 8\,K$ present in our measurements a complete transformation to hcp should occur within minutes.

Crystallization and lattice structure of ortho–deuterium

Although no temperature gradient of liquid o-D_2 filaments can be extracted from the data, its mean wavenumber correlates well with our numerical calculations of the temperature gradient, in which similar relative supercoolings to the p-H_2 case with regard to their normal melting points are achieved. The solid fraction curve reveals that the crystallization of o-D_2 starts earlier and takes longer compared to p-H_2. Since the isotopes differ by a factor $\approx 1.4 \approx \sqrt{2}$ in both times, the origin probably is mass related, which is in agreement with the collision-limited model for the crystal growth.
Similarly to p-H_2, the lattice structure of o-D_2 consists of hcp, fcc and rhcp regions, yet the fcc amount is higher.

Crystallization of mixed para–hydrogen ortho–deuterium filaments

The admixture of $< 10\%$ o-D_2 molecules to p-H_2 results in an earlier onset and a longer duration for crystallization compared to the pure case. For the inverse mixtures both these behaviors are qualitatively similar, yet to a lesser extent. The earliest as well as longest crystallization times are found in mixtures with an o-D_2 content between 20 and 50%. Repeated measurements show that the temperature of the liquid cannot be the main reason for the lower crystallization rates in mixtures and the overall behaviour is qualitatively reproduced with measurements using a smaller nozzles.
The separately acquired solid fractions for p-H_2 and o-D_2 in each mixture reveal differences in their relative progress, indicating that phase segregation may happen during crystallization. Further support for this statement is provided by a persisting p-H_2 liquid peak in mixtures with high o-D_2 content which is interpreted as a bulk liquid enriched in p-H_2 remaining above its melting temperature in the core of the filament. Microscopic explanations for the increased crystallization times remain unclear and probably are related to ordering or fractionation processes requiring diffusion at the liquid-solid interface.

Upon small dilution with the other isotope, the lattice structure of o-D_2 changes slightly in favor of fcc, whereas in the opposite composition p-H_2 yields marginally more hcp. As the impurity $< 10\%$, o-D_2 exhibits a sharp line structure in the crystalline phase, in which the main peak coincides with the gas line and is interpreted as o-D_2 molecules isolated from same-species partners. The others lines match with hcp energies and probably originate from isolated pairs of o-D_2, the intensity agreeing with amount of pairs expected in a random distribution of particles.
In the minority, p-H_2 in the solid phase exhibits a significantly broader band at the position of the gas line without clear indications for hcp lines. This contrast to highly diluted o-D_2 probably is related to the increased $J = 1$ content of the surrounding o-D_2 bulk and/or higher delocalization due to more pronounced quantum effects of p-H_2.

Crystallization of hydrogen isotopes diluted with neon

Filaments of p-H_2 doped with $\leqslant 2\%$ neon show an almost immediate onset of crystallization as well as significantly longer periods for complete solidification. Compared to the same admixtures of o-D_2 both effects are more extreme. o-D_2 filaments with

up to 5% neon content reveal an unchanged start of solidification, yet increased durations. The appearance of the solid is similar to equal additions of p-H$_2$, but the total crystallization time increased. Since neon is severely supercooled and also smaller than the hydrogen isotopes, the cause of the reduced crystallization rates may be rooted in fractionation and/or geometric effects.

The crystal structure reveals a strong preference for fcc upon small additions of Ne in both p-H$_2$ and o-D$_2$ which probably is related to fcc being the equilibrium lattice structure for pure neon.

8.2 Conclusion

The original idea for this experiment, i.e. combining liquid microjets with Raman spectroscopy, was proposed around a decade ago to investigate the superfluid phase of hydrogen. Though this initial intention has not been achieved yet with the current setup we are confident to say that the experiments realized up to this point have indeed surpassed the expectations.

To begin with, several new technical concepts have been successfully proven to satisfy our requirements. The positioning of the nozzle via 3D linear stages in combination with the thermal coupling with the copper strap enables higher accuracy while maintaining sufficient cooling power. This setup now represents the new standard for experiments in which the jets are probed along the filament axis.

Furthermore, the requirement for stable filaments has been a major driving force for the development and refinement of the current nozzle design utilizing glass pipettes. In view of the immense effort for producing and cleaning nozzles it is astounding that in none of the actual experiments in Madrid clogging of nozzles has been a major obstacle – even with the record-holding smallest diameter of $\approx 2\,\mu m$. In fact, the three beam campaigns performed within this work are a convincing proof for the long time stability of filaments, i.e. the fundamental qualification for any experiment.

Beside the technical developments in our group this work marks an important milestone for the feasibility of probing filaments by Raman spectroscopy along their propagation axis. In advance it was not clear how the overlap between laser focus and filament could be found in a reasonable period and if the filament would be influenced by the intense continuous radiation.

Most importantly it has been proven that the linear relationship between the distance z and time traveled t can indeed be employed to map the temporal evolution of the filaments. This correlation is a key feature for this and further experiments.

Furthermore, the discovery of the temperature gradient across the filament has lead to the enhancement of the evaporative cooling calculations into the layered model, which captures the details more accurately. The characterization of filaments with different diameters and at different source conditions yields important information about reproducibility and limitations.

Hence, in addition to technical developments the proof of principal and enhancement of the model for probing liquid jets with scattering techniques is another major contribution of this work.

As the second main pillar the data itself provides unique revelations from the physical point of view. Over the course of three measurement campaigns in 3 years several interesting questions have been proposed or raised by the data and investigated.

For the first time the crystallization process of para-hydrogen has been observed, the crystallization rate for strong supercoolings determined and the suitable growth model identified. The measurements of the rotational region present one of the rare occasions in which Ostwald's rule of stages is spotted in action, producing a metastable lattice on short time scales that transforms in the long run. Similarly, the crystallization dynamics for ortho-deuterium is new and provides the important information for subsequent measurements that both isotopes behave quite similar and the scalings mainly are mass dependent.

The measurement of mixtures probably offer the highest physical value. The result that small additions of isotopic impurities increase the crystallization times by large amounts simply due to the mass and the entailed quantum effects is astounding. Although the data does not reveal the microscopic details and therefore interpretations remain fairly vague, these measurements demonstrate the potential to elucidate fundamental crystallization concepts that up to now have not been experimentally accessible.

The admixtures of neon to the hydrogen isotopes further highlight the influence of particle sizes and composition on crystallization. Additionally, they reveal a way to manipulate the lattice structure of the main component, which may also be of great interest for further theoretical and experimental studies.

All combined, it is the technical development, the proof of principle and characterization as well as the insights deduced from the data that represent the advances and the success of this thesis.

8.3 Outlook

Since this work successfully proves the functionality of a novel experimental method, this opens up a broad variety of further possible investigations. In general, the time evolution and phase changes of any liquid that is expanded as a microjet, can be studied by a suitable scattering technique on sub-μm time scales.

On the basis of this work, it would be interesting to further analyze the crystallization process of the hydrogen isotopes with varied parameters, as the details – especially in mixtures – are not yet fully understood. In this regard, manipulating the temperature of the filament is a key aspect. This is made possible by utilizing a small, temperature controlled cell filled with a buffer gas with which even deeper supercoolings may be accessed, possibly opening up pathways to the superfluid phase of hydrogen [10]. Furthermore, the filament temperature can be kept close to the melting temperature for varied crystal growth conditions or even above it to melt the solidified filament and investigate the reverse phase transition. Such cells are currently developed and tested in our group in Frankfurt and experiments with other liquids will be done in the near future.

Closely related to this work it would be interesting to probe trinary mixtures, e.g. p-H_2 + o-D_2 + Ne, which are more complicated, yet are especially appealing since crystallization may be even more suppressed possibly creating a link to glass formation.

A changed Raman setup also opens up the possibility to use a different excitation region, e.g. the low energy Brillouin scattering, from which completely new information may be obtained and in which also Raman inactive noble gases like neon yield signal. This, however, is not yet on the current schedule.

In the near future experiments will be done on different substances. Utilizing Raman scattering a very promising system will be water, since the supercooled liquid as well as the crystallization are an extremely important topic at the present time. Additionally, the equilibrium phases have been investigated extensively, so that from Raman spectra the temperature of the (supercooled) liquid can be deduced. Later investigations will focus on changing the temperature with a cell, which has already been tested successfully in our group [100]. With such a setup it will be possible to achieve deep undercoolings and explore the so called *no man's land* of water [101], which is expected to reveal fundamental properties of water. Also, impurities and liquid solutions enable sheer unlimited possibilities to influence crystallization processes.

The next big field of study is using other scattering techniques. Within the next years x-ray scattering will increasingly be exploited to directly access the structure factor of the phases. With this parameter it may be possible to obtain information about the crucial nucleation process, which is principally inaccessible in this work. A chamber already has been designed for experiments at *DESY* in Hamburg and Argon will be the first candidate to test the feasibility of this technique. If successful, later on other substances and maybe also the hydrogen system, which exhibits a low cross section for x-rays, will be investigated.

The experimental results in this work as well as above future plans provide a unique fundament for theoretical frameworks and simulations. These measurements of real systems represent the ultimate test for theories evolving around nucleation and crystal growth as well as the influence of quantum behaviour during these processes. As the quantum character presents a major obstacle and complicates the interaction in simulations, these models have to be optimized to account for higher particle numbers and particularly to be able to reconstruct the actual dynamics. Collaborating groups of theoreticians already have evinced interest in such studies.

Based on this overview this experimental technique is promising to investigate nucleation, crystallization and other phase change processes and potentially able to shed light onto some of the deepest questions of our times. The future looks bright!

Part III

APPENDIX

A ADDITIONAL MEASUREMENTS

This chapter provides two complementary measurements to support statements from the previous chapters. For one, the influence of the $J = 1$ content onto the solid fraction is analyzed in section A.1 and secondly, we have a look into the raw data of Raman spectra in section A.2.

A.1 Isomeric mixtures

Regarding the solid fraction and especially the longer crystallization times for mixtures, we want to determine the influence on the amount of $J = 1$ molecules in H_2 and D_2 filaments, respectively. For hydrogen, filaments with different amount of the $J = 1$ component ortho-hydrogen were prepared by mixing fully converted p-H_2 with a negligible 0.2% $J = 1$ content and unconverted n-H_2 exhibiting 75% by means of the mass flow controllers.

name, #	date	temp2 (K)	P_0 (bar)	v_0 (m/s)	% J = 1
99.8-0.2 H_2	25/11/11	16	8.5	142	0.2
90-10 H_2	25/11/11	16	9.8	153	10.0
80-20 H_2	25/11/11	16	9.8	153	20.0
97.5-2.5 D_2	30/11/11	19.6	13.0	115	2.5
67-33 D_2	30/11/11	19.6	13.0	115	33

Table 12: Measurements of hydrogen and deuterium with varying $J = 1$ contents.

The measurements are summarized in the upper part of table 12 and their corresponding total solid fractions displayed in the left panel of fig97. Since the first solid in all three measurement series appears at the same time and evaporative cooling is insensitive to the isomeric constitution, we consider the temperature of the liquid phase to be equal in all cases.

The two curves with increased o-H_2 amounts (red and yellow) basically are identical. In comparison, the pure p-H_2 plot overlaps very well for $s_f < 0.3$ and afterward is slightly ahead. This may be related to the slightly lower pressure P_0 and therefore calculated velocity of this measurement. Nevertheless, the difference between the curves is very small and the total solidification time t_{ll-fs} equal within error bar so that we conclude that for hydrogen increased amounts of $J = 1$ do not alter the crystallization

process significantly. Additionally, the individual solid fractions of the $J = 0$ and $J = 1$ component of each measurement do not differ from one another, so that both isomers seem to have the same tendency to join the solid phase.
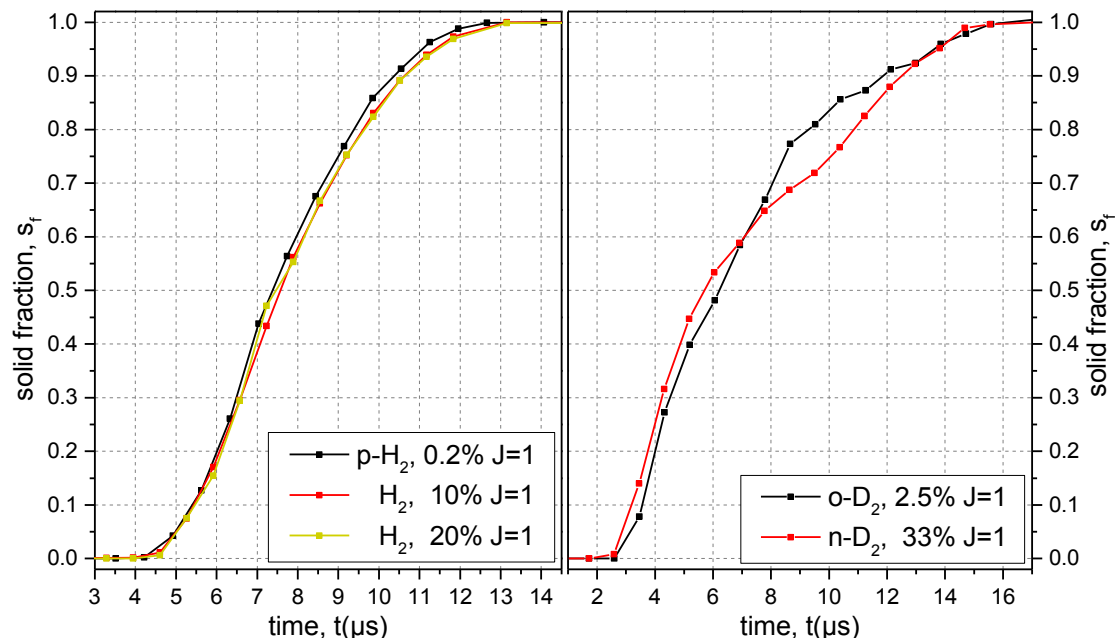

Figure 97: $S_0(0)$ excitation after complete crystallization of deuterium filaments doped with neon. The main peaks are enumerated from left to right.

For deuterium, the solid fractions for the fully converted o-D_2 and the natural n-D_2, listed in the lower half of table 12, are compared in the right panel of fig.97. Again, the temperature of the liquid filaments is assumed to be the same as solidification starts simultaneously, maybe with a slight headstart of n-D_2. We find that during the growth process there are considerable differences in the advances of crystallization. Whereas n-D_2 in the beginning takes the lead, o-D_2 passes at $s_f \approx 0.6$. This structure in the solid fraction, which seems to be typical for D_2 filaments (compare chapter 5.1.2) indicates that intervals with varying crystal growth exist. Yet, the total time for crystallization does not differ in between the two measurements.

We summarize that although the solid fraction may be altered slightly for H_2 and greater for D_2, the total crystallization time remains uninfluenced from the isomeric constitution. Although we have no direct measurements, it is unlikely that this behaviour changes in mixtures of the isotopes, particularly when we consider that the total $J = 1$ amount in these mixtures is very small.

A.2 Raman raw data

In chapter 3.4.2 it was stated that the raw Raman data actually consists of 10 simultaneously recorded single spectra at the same wavenumber interval. In the analysis up to this point we have only covered the accumulated data, i.e. the intensity of these 10 raw
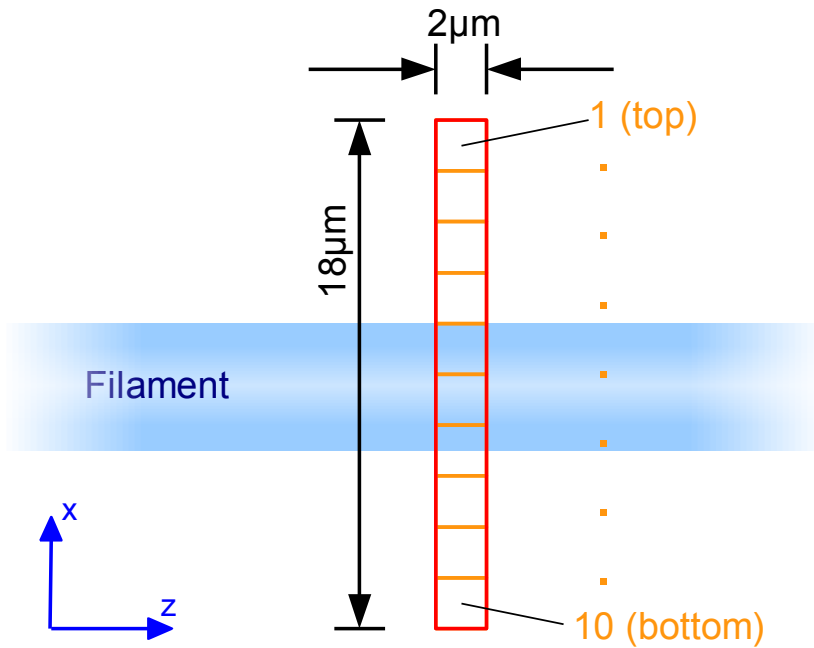
Figure 98: Schema of the filament zone seen by the spectrometer (red rectangle) in the ideal case. For the raw Raman data this projection is divided into 10 sub-regions/stripes (orange) with dimensions $2 \cdot 1.8 \, \mu m^2$ each, enumerated from top to bottom.

files simply added up.

Fig.98 illustrates, what the raw spectra are associated with. Based on the optics and slit geometry, the projection of the spectrometer CCD onto the interaction region in the vacuum chamber corresponds to a vertical strip of $2 \, \mu m$ width, marked in the figure as a thick red rectangle (for details, see chapter 3.4.2). This region contains a whole cylindrical section of the filament and the resulting Raman spectrum represents, what was analyzed throughout this work. This rectangle is divided into 10 sub-regions (orange), we refer to as stripes as they correspond to adjacent horizontal pixel rows on the spectrometer CCD and are readout in parallel. Hence, this raw data contains different parts of the filament, so that theoretically we are able to extract information from the surface and the core of the filament separately.

Yet, in practice several constraints limit the validity of this idealized assumption. As a main source of error, the desired spatial resolution is close to the limit of what the optics and the spectrometer are able to spectrally resolve based on the wavelength of the light of $\approx 0.5 \, \mu m$. Taking into account deviations from diverse aberrations (e.g. spherical, chromatic,...) in addition to the alignment and focusing for all optical elements, in reality the projection of the filament onto the spectrometer CCD is blurred. Small fluctuations in the position of the filament additionally increase the statistical error of this method. This manifests in the Raman signal from the filament not occupying just $5.3 \, \mu m / 1.8 \, \mu m \approx 3$ stripes, but rather $6 - 8$ stripes, depending on the focusing.

Furthermore, the aberrations of the system may not simply blur the projection, but also introduce systematical errors, so that the correspondence between the region of the filament (top, core, bottom) and the image on the CCD (top, middle, bottom pixel

rows) does not necessarily have to be valid at all. One can think even deeper and claim that the illumination of the filament by the Ar^+ laser may not be homogeneous, since its cylindrical shape with a refraction index [102, p.20] of $n \approx 1.1$ acts as a micro-lens. Stripes may therefore carry intensities, that are not proportional to the actual number of molecules situated within it, what distorts the subsequent interpretation.

Keeping in mind above caveats, we finally take a look at the information extractable from the raw spectra, exemplary from the pure p-H_2 data with conditions #4 in table 3 on p.68. To reduce the huge amount of data, we extract the mean wavenumber (i.e. temperature) of the liquid as well as the solid fraction of the vibrational excitation for each of the 10 raw spectra and at different distances z along the filament axis. As a further parameter, we plot the intensity of each of the 10 stripes as an indicator for the profile or quality of focusing, respectively.

These three quantities are presented in black, red and green, respectively, in fig.99. The x-axis in this plot is different from previous ones. It is divided into intervals (blue vertical lines), that contain the data from each of the 10 stripes recorded at one z position labeled at the bottom. In each interval the data points from left to right correspond to stripes 1 to 10, i.e. the filament scanned from top to bottom (compare fig.98). The error bars are the standard derivative calculated from the 3-4 subsequent recordings at each z position.

Before we analyze the plots, it is is worth thinking about what we would expect from the raw data. Assuming that the aberration effects of the optical elements simply blur rather than distort the image on the CCD, the stripes in an interval from left to right should still correlate from a scan from top to bottom through the filament. The intensity profile (green) would be broader than the ideal 3 stripes, but still be symmetric. If we assume our isotropic cooling/freezing model for the filament, the mean temperature of the liquid (black) should exhibit a reverse-u shape with the highest temperatures in the core (middle) and the lowest at the surface (top and bottom). As in this model solidification starts at this surface and proceeds towards the core, the solid fraction (red) in this plot would be u-shaped in each z interval.

Now let us look into the actual plots. Starting at the intensity profile at the bottom part in green, we indeed find a symmetric peak with most intensity in the center stripes and a FWHM of 5-6 stripes for all distances z. For all measurements in this work, it is not possible to focus the same total signal into less stripes, so that this seems to be the limit resolution as discussed above. However, the shape of this profile varies from day to day and can even be strongly asymmetric, depending on the focus of the individual optical elements.

The black plot of the mean wavenumber of the liquid, as a measure of the temperature, reveals a strong asymmetric behaviour. At the first position $z = 100\,\mu m$, there seem to prevail significantly lower temperatures at one side, which is associated with the bottom part of the filament. This characteristic is more pronounced at $z = 200\,\mu m$, but paradoxically yields even lower values for the bottom part as for the subsequent $300\,\mu m$ measurement. The asymmetric trend continues up to $600\,\mu m$, yet becomes gradually more homogeneous.

The growing solid fraction in red also reveals an asymmetry up to $900\,\mu m$, yet with higher values at the opposite (top) side. At further distances, the other (bottom) side catches up, so that the minimum value of s_f from this point on is situated in a more centered stripe.
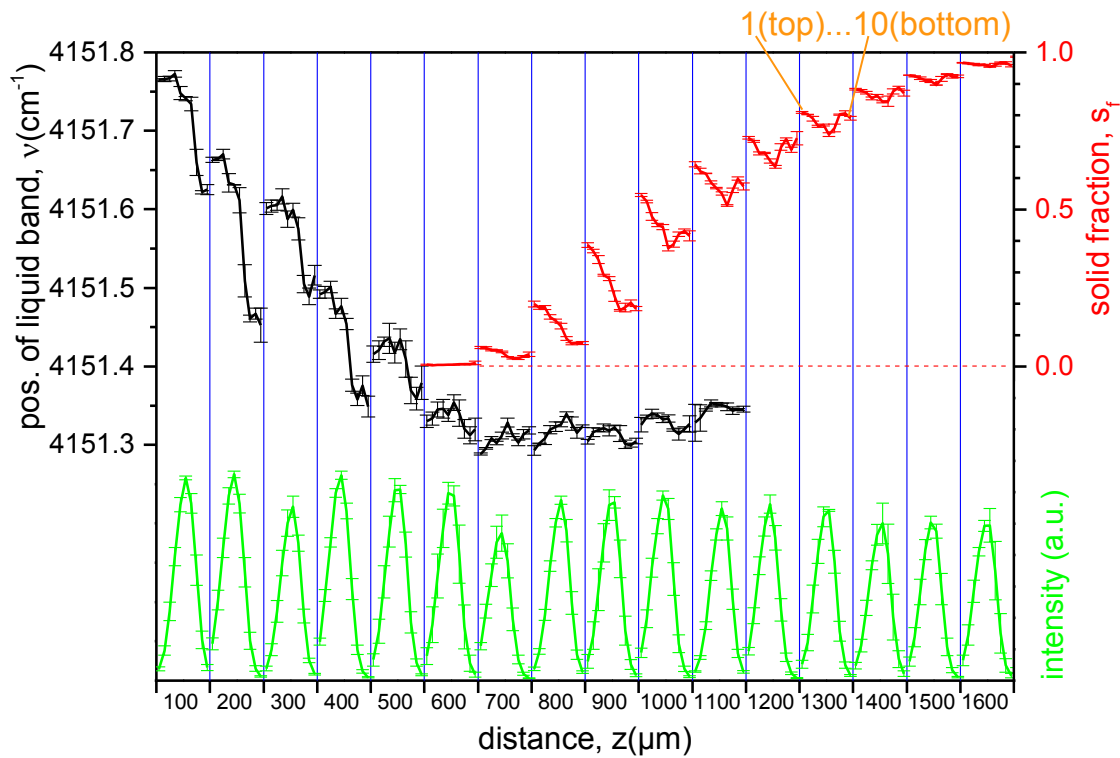
Figure 99: Mean wavenumber (i.e. temperature) of the liquid (black), solid fraction
(red) and intensity (green) of the raw data of the pure p-H_2 filament with
conditions #4 in table 3 on p.68. Data points in between the blue vertical
lines correspond to the 10 stripes from top to bottom at each z position
(bottom scale), exemplary indicated at the top for $z = 1300\,\mu m$.

The result that one side of the filament should be at significantly lower temperatures
than the other is incomprehensible, since evaporative cooling affects any surface of the
filament that is exposed to vacuum. Even if the filament deviated significantly from a
cylindrical shape, both top and bottom signals should still be at lower temperatures
than the core and produce an (asymmetric) reverse-u shaped plot. The almost steadily
decreasing temperature from top to bottom in our plot therefore casts severe doubt
onto the assertion that the series of 10 raw Raman spectra de facto correspond to a
vertical scan across the filament.

The asymmetry in the solid fraction may be physically reasonable, as it can be in-
terpreted as deviations from the isotropic growth model. Due to disturbances in the
filament induced by e.g. imperfections in the nozzle orifice (compare chapter 3.3.1),
one side of the filament could start to freeze earlier and therefore have more advanced
values for s_f. However, the black curve suggests that the lowest temperatures prevail
just at the opposite side of where the solid first appears, which is in contrast to what
we expect based on the strong temperature dependency of the nucleation rate.

The behaviour shown in this exemplary measurement, i.e. lower temperatures at bottom
and higher initial solid fraction at top side, is present in most other recorded raw data
with similar focusing or intensity profile, respectively. It remains unaffected by the par-
ticle constitution in mixtures and other parameters like the velocity of the filament and,
most importantly, throughout measurements in different beam campaigns, in which the

nozzle is mounted at a different angle. This strongly suggests that the observed effects, particularly for the temperature profile, are artifacts of systematical errors based on the focusing and aberrations of the optical elements.

We conclude that the raw data is not a reliable source for extracting information about different regions of the filament.

B CALCULATIONS

B.1 Evaporative cooling model

The model for the temperature gradient of liquid filaments is based on calculations of evaporative cooling published previously in [23]. The approach developed for this work is an enhanced version to account for the finite thermal conductivity from the surface of the filament to its core.
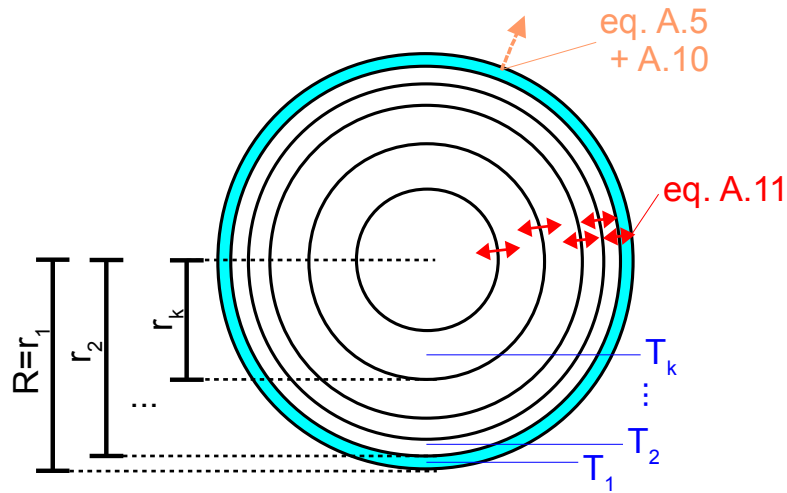
Figure 100: Schematic cross section of the liquid filament divided into concentric rings with equal area. Evaporative cooling (orange) is governed by eq.B.5 and B.10, thermal conductivity to inner layers (red) by eq.B.11.

The cross section of the filament with radius R is divided into $n = 100$ concentric rings with equal volume (per unit length) $V_k = \pi R^2/100(\cdot dz)$ or mass, respectively, depicted in fig.100.

The cooling effect through evaporation in general is described by the energy balance equation [23, p.542]:

$$V \rho c_p \, dT = \rho L \, dV \, , \tag{B.1}$$

whereas V and dV are the Volume and its change, respectively, dT the change in temperature of this volume, ρ the mass density of the substance, c_p the specific heat capacity and L the heat of evaporation. Physically this means that the (negative) change in temperature of the volume is linked to a loss in volume through the evaporation of particles.

To account for a possible heating effect of the warm chamber onto the filament, one can append the term [103]

$$-\epsilon_0 \, A_1 \, \sigma \, (T_1^4 - T_{ch}^4) \, dt \tag{B.2}$$

to the right side of eq.B.1. This formula applies to an infinite cylinder at temperature T_1 and surface (per unit length) $A_1 = 2\pi\,R$ surrounded by (vacuum chamber) walls at $T_{ch} \approx 300\,\mathrm{K}$ with σ the Stefan-Boltzmann constant and $\epsilon_0 = 1$ the maximal emissivity of liquid hydrogen. Yet, its effect has been empirically tested to be orders of magnitude below the two other terms and therefore subsequently is neglected.

Since in our model evaporative cooling only applies to the surface layer (light blue in fig.100), its volume per unit length, and change (derivative), respectively are given by

$$V = V_k = \pi(R^2 - r_2^2) \tag{B.3}$$
$$dV = 2\pi\,R\,dR \,, \tag{B.4}$$

with $R = r_1$ being the (current) radius of the filament and r_2 the radius of the first layer beneath.
Inserting B.4 into B.1 and solving yields

$$dT = \frac{2\pi\,L\,R(T)}{V_k\,c_p(T)}\,dR(T) \,, \tag{B.5}$$

which is the first differential equation for evaporative cooling with $T = T_1$ the temperature of the surface layer.

For the second equation we write the number of particles lost through evaporation per time step as [23, p.542]

$$dN = -A_1 \frac{p_{sat}(T)}{\sqrt{2\pi\,m\,k_B\,T}}\,dt \,, \tag{B.6}$$

with the saturated vapor pressure p_{sat} at the current temperature $T = T_1$ of the surface layer, the particle mass m and k_B the Boltzmann constant.
The total number of molecules (per unit length) of this surface layer and its change on radius is also given by

$$N = \frac{\pi(R^2 - r_2^2)\,\rho}{m} \Rightarrow \tag{B.7}$$
$$dN = \frac{2\pi\,R\,\rho}{m}\,dR \,. \tag{B.8}$$

Our fundamental correspondence of the filament between distance traveled z and time t connected by the velocity v_0 in infinitesimal form is

$$dt = \frac{dz}{v_0} \,. \tag{B.9}$$

Utilizing this correspondence we insert B.8 into B.6 and solve for

$$dR = -\frac{p_{sat}(T)}{\rho\,v_0}\sqrt{\frac{m}{2\pi\,k_B\,T}}\,dz \,, \tag{B.10}$$

which is the second differential term for calculating evaporative cooling of the surface layer with $T = T_1$.

The temperature exchange towards the center of the filament is governed by the thermal conductivity λ. The exchange of heat between two adjacent layers k and $k+1$ in a time step dt is given by the energy balance

$$V \rho c_p \, dT_k = \frac{\lambda A_{k+1} \cdot (T_k - T_{k+1})}{l_{k+1}} \, dt \, , \tag{B.11}$$

which is solved for

$$dT_k = dT_{k+1} = \frac{\lambda A_{k+1} \cdot (T_k - T_{k+1})}{l_{k+1} \, V \rho c_p} \, dt \, . \tag{B.12}$$

To account for the equal masses of the layers, their corresponding radii are calculated consecutively by

$$r_{k+1} = \sqrt{r_k^2 - R^2/100} \, , \tag{B.13}$$

so that the (heat conducting) surface A_{k+1} (per unit length) and the distance l_{k+1} the heat has to travel are

$$A_{k+1} = 2\pi r_{k+1} \tag{B.14}$$
$$l_{k+1} = r_k - r_{k+1} \, . \tag{B.15}$$

In the actual algorithm, at first the temperature of the surface layer T_1 is numerically approximated by using the common fourth-order Runge-Kutta method onto both eq.B.5 and B.10. Afterward the temperature exchange dT_k is calculated and added/subtracted to/from the two participating layers in a consecutive manner towards the center of the filament using eq.B.12.
The iteration steps are chosen to be $dz = 10^{-10}$ (meter), since for greater steps the evaporative cooling formulas change too fast to be approximated satisfactorily. It is important to note that since the total radius R progressively decreases slightly ($\approx 5\%$), all radii r_k are recalculated in each step.
To reduce the output data, only values in steps of $\Delta z = 10^{-6} = 1 \, \mu m$ are written into a textfile, which contains the distance z in the first column and in the following columns the current temperature of each of the 100 layers.

All parameters for hydrogen and deuterium are summarized in table 13, except for the fits for the vapor pressure, which for hydrogen reads [109, p.50]

$$p_{sat}(T) = \exp(15.46688 - 101.3778/T + 0.05432 \cdot T - 0.00011056 \cdot T^2) \tag{B.16}$$

and for deuterium [110]

$$p_{sat}(T) = 133.3 \cdot \exp(2.30259 \cdot (5.8404 - 70.044/T + 0.000459 \cdot (T - 23)^2) \, . \tag{B.17}$$

Note that no data is available in the literature for the supercooled liquid states, which prevail within most of the calculation. All fits and constants in the table are extrapolations to values $T < T_m$.

parameter	hydrogen	deuterium
m [kg], molecular mass	$2 \cdot 1.66e^{-27}$	$4 \cdot 1.66e^{-27}$
L [J kg^{-1}], latent heat of vaporization	$4.5e^5$ [104]	$3.0e^5$ [104]
ρ [kg m^{-3}], mass density	76	176
$c_p(T)$ [J kg^{-1} K^{-1}], specific heat capacity	$466 \cdot T$ fit to [105]	$266 \cdot T$ fit to [106]
$\lambda(T)$ [W m^{-1} K^{-1}], thermal conductivity	$6.14e^{-2} + 1.76e^{-3} \cdot T$ fit to [107]	$8.46e^{-2} + 2.08e^{-3} \cdot T$ fit to [108]
$p_{sat}(T)$ [Pa], saturated vapor pressure	see eq.B.16 [109, p.50]	see eq.B.17 [110]

Table 13: Parameters used in the evaporative cooling model.

B.2 Calculated thermodynamic properties

For the estimation of the two crystal growth models in chapter 4.1.3.3 we need the Gibbs free energy difference between the liquid L and the solid S, i.e. the energetic driving force for crystallization in eq.2.21 on p.34:

$$\Delta g = g^L - g^S \tag{B.18}$$

Both energies can be expressed as

$$g^{L,S} = h^{L,S} - T \, s^{L,S} \, , \tag{B.19}$$

with $h^{L,S}$ and $s^{L,S}$ being the enthalpy and entropy per unit mass, respectively. Furthermore, it is

$$s(T) = \int_T^{T_M} \frac{c_p(T')}{T'} \, dT' \tag{B.20}$$

and

$$c_p(T) = \left(\frac{\partial h}{\partial T} \right)_p \Rightarrow \tag{B.21}$$

$$h(T) = h(T_M) - \int_T^{T_M} c_p(T') \, dT' \, , \tag{B.22}$$

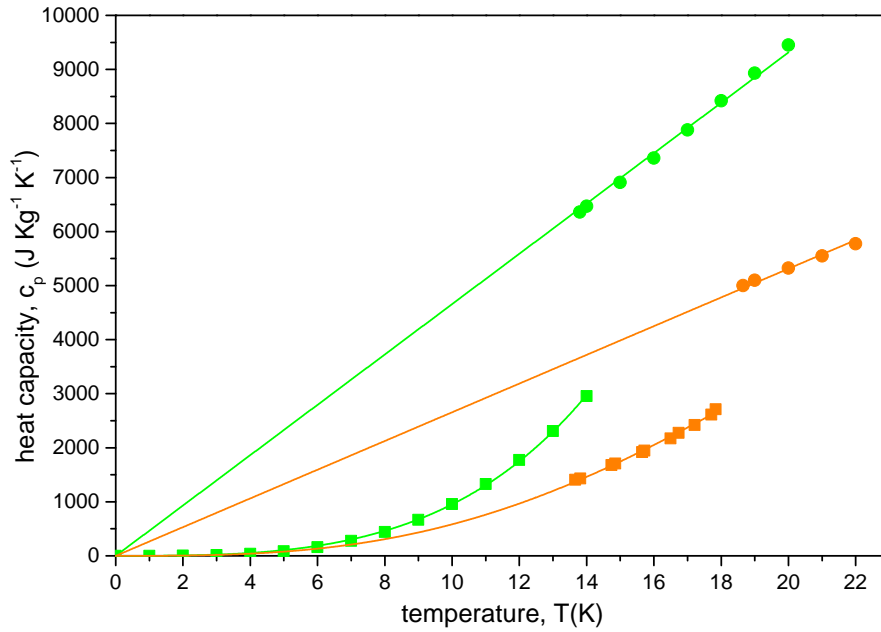with the melting point T_M and the specific heat capacity c_p.

Figure 101: Experimental heat capacities of hydrogen (green) and deuterium (orange) for the liquid (circles) and the solid (squares) and the fits according to eq.B.23 and B.24 with coefficients and sources in table 14.

Experimental values for the specific heat capacity in the liquid and the solid $c_p^{L,S}$ are available at equilibrium conditions. c_p^S is simply fitted to the data and c_p^L fitted and extrapolated to values $T < T_M$ with the empirical equations

$$c_p^L(T) = A \cdot T \tag{B.23}$$

$$c_p^S(T) = B \cdot T^3 + C \cdot T^5 \ . \tag{B.24}$$

The fitting curves are presented in fig.101 for hydrogen and deuterium.

Utilizing eq.B.20 and B.22, we can calculate from above fits the Gibbs energies for the liquid and the solid in eq.B.19 to

$$g^L(T) = -\frac{A}{2}(T - T_M)^2 + h^L(T_M) - T\, s^L(T_M) \tag{B.25}$$

$$g^S(T) = -\frac{B}{12}(T^4 + 3T_M^4 - 4t_M^3 T) - \frac{C}{30}(T^6 + 5T_M^6 - 6T_M^5 T) + h^S(T_M) - T\, s^S(T_M) \ . \tag{B.26}$$

Inserting both into the starting eq.B.18 yields

$$\Delta g(T) = -\frac{A}{2}(T - T_M)^2 + \frac{B}{12}(T^4 + 3T_M^4 - 4t_M^3 T) + \frac{C}{30}(T^6 + 5T_M^6 - 6T_M^5 T) \\ + \Delta h(T_M) - T\Delta s(T_M) \ , \tag{B.27}$$

with similarly defined $\Delta h = h^L - h^S$ and $\Delta s = s^L - s^S$.
Since at T_M it is $g^L(T_M) = g^S(T_M)$, we get the expression

$$\Delta g(T_M) = 0 = \Delta h(T_M) - T_M \Delta s(T_M) \Leftrightarrow \tag{B.28}$$

$$\Delta s(T_M) = \Delta h(T_M)/T_M \ , \tag{B.29}$$

Inserting B.29 into B.27 finally leads to

$$\Delta g(T) = -\frac{A}{2}(T - T_M)^2 + \frac{B}{12}(T^4 + 3T_M^4 - 4T_M^3 T) + \frac{C}{30}(T^6 + 5T_M^6 - 6T_M^5 T)$$
$$+ \Delta h(T_M)\frac{T_M - T}{T_M} , \quad \text{(B.30)}$$

which exclusively contains known parameters, which are listed in table 14 for hydrogen and deuterium.

In mixtures of hydrogen and deuterium the Gibbs energy difference can be written as

$$\Delta g_{mix}(T) = (1-x)\frac{m_{H2}}{m_{mean}}\Delta g_{H2}(T) + x\frac{m_{D2}}{m_{mean}}\Delta g_{D2}(T) + x(1-x)\frac{\Delta\alpha}{N_A\, m_{mean}} , \quad \text{(B.31)}$$

whereas x is the mol fraction of deuterium, N_A the Avogadro number and $m_{mean} = (1-x)m_{H2} + x\, m_{D2}$ the mean mass of particles.

In the last term, $\Delta\alpha$ represents the excess energy of mixing, which has been determined to be $\Delta\alpha = 27 - 49\, J\,mol^{-1}$ [43, 111].

parameter	hydrogen	deuterium
T_M [K], melting point	13.8	18.7
Δh [J kg^{-1}], enthalpy of fusion	5.86e^4 [112]	4.93e^4 [106]
A [J kg^{-1} K^{-2}], coefficient in eq.B.23	466 fit to [105]	266 fit to [106]
B [J kg^{-1} K^{-4}], coefficient in eq.B.24	0.815 fit to [113]	0.636 fit to [106]
C [J kg^{-1} K^{-6}], coefficient in eq.B.24	1.37e$-$3 fit to [113]	$-$5.3e$-$4 fit to [106]

Table 14: Parameters used in the calculation for the Gibbs energy difference B.30.

B.3 Nearest neighbor calculations

In isotopic and/or isomeric mixtures of hydrogen, it is interesting for the condensed phases to estimate the number of impurity molecules that are isolated, paired or of higher order with respect to their same species partners. These are here referred to as monomers, dimers and trimers or higher.

In the crystalline fcc and hcp phases a particle is surrounded by $nn = 12$ nearest neighbors, assuming there are no voids and defects in the lattice present. For the liquid phase

the estimation of adjacent particles is more complicated due to its disordered nature and therefore definition of nn, but we estimate that the number remains unchanged with $nn = 12$.

From the conversion efficiency or mass flow meters of the gases we know the actual mol fraction x of this impurity, e.g. $x = 2.5\%$ p-D_2 within converted o-D_2 or $x = 1\%$ o-D_2 diluted into p-H_2. For above estimation we imagine to locate an impurity molecule and consider its environment for a completely homogeneous or miscible, respectively, distribution of molecules in the bulk phase.

The probability that an arbitrary adjacent partner is not an impurity is $P_{nn=1,x}(nn_{imp} = 0) = 1 - x$. The probability that none of the 12 partners is an impurity molecule is

$$P_{nn=12,x}(nn_{imp} = 0) = (1 - x)^{12} \,, \tag{B.32}$$

which corresponds to the probability of the impurity being a monomer. The probability that 1 nn is an impurity and none of the others is $P_{nn=12,x}(nn_{imp} = 1) = 12 \cdot x \cdot (1 - x)^{12}$, since any of the 12 neighbors may be the impurity.

Hence, the number of adjacent impurity molecules nn_{imp} is given by the Binomial distribution

$$P_{nn,x}(nn_{imp} = k) = \binom{nn}{k} x^k (1 - x)^{nn-k} \tag{B.33}$$

As the traveling of vibrons and rotons on same-species molecules reaches beyond nn molecules and influences the excitation energy, it is important to take into account same-species molecules adjacent to the same species nearest neighbors nn_{imp} of the central particle, we refer to as nearest nearest neighbors nnn_{imp}.

Since the number and possibilities of structural configurations get complicated quite fast, we only consider the one particular case, in which the central (impurity) particle exhibits $nn_{imp} = 1$, but no further ones beyond, $nnn_{imp} = 0$, i.e. a dimer. In the crystalline phases, the two particles constituting the dimer share $nn = 5$, so that the non-shared are $nnn = 7$. We assume the liquid phased to be statistically similar.

In this scenario the probability is given by

$$P_{nn=12,x}(nn_{imp} = 1) \cdot P_{nnn=7,x}(nnn_{imp} = 0) \tag{B.34}$$

The numbers of monomers (eq.B.32), dimers (eq.B.34) and other configurations are presented for all important values for x in this work in table 15. Note that x can represent isotopic as well as isomeric contents.

In chapter 6.2.2.2 we also estimate the probability that an isotopic dimer of the highly diluted sample is adjacent to a $J = 1$ molecule. A dimer exhibits $nn = 12 + 7 = 19$ nearest neighbors and we can utilize the same eq.B.33 with x the mol fraction of $J = 1$ molecules in the condensed phase. The results are summarized in table 16.

measurement	% x	% monomers	% dimers	% rest
o-D$_2$ in p-H$_2$	1	89	10	1
	3.2	67	21	11
	4.6	57	23	20
	9.1	32	20	49
	16.7	11	7	81
p-H$_2$ in o-D$_2$	2.4	75	18	7
	4.3	59	23	18
	16	12	8	80
Ne in p-H$_2$	0.3	96	3	< 1
	1	89	10	1
	2	78	17	5
Ne in o-D$_2$	1	89	10	1
	2	78	17	5
	5	54	24	22
o-H$_2$ in p-H$_2$	0.2	98	2	< 1
	10	28	18	54
	20	7	4	89
p-D$_2$ in o-D$_2$	2.5	74	19	7
	33	1	< 1	99

Table 15: Calculation of same-species nearest neighbors with $nn = 12$ and $nnn = 7$ for dimers.

measurement	% x	% $nn_{J=1} = 0$	% $nn_{J=1} \geqslant 1$
J = 1 nn to p-H$_2$ dimer	2.5	62	38
J = 1 nn to o-D$_2$ dimer	0.2	96	4

Table 16: Calculation of J = 1 molecules adjacent to impurity dimers in the diluted isotopic mixtures with $nn = 19$.

BIBLIOGRAPHY

[1] David W. Oxtoby (1990). *New perspectives on freezing and melting*. Nature, **347** (6295), 725–730. URL http://dx.doi.org/10.1038/347725a0. (cited on page 3.)

[2] Kenneth F. Kelton (2013). *Crystal Nucleation in Supercooled Liquid Metals*. Int. J. Microgravity Sci. Appl., **30/1**, 11–18. (cited on pages 3 and 32.)

[3] David Turnbull (1969). *Under what conditions can a glass be formed?* Contemporary Physics, **10**(5), 473–488. URL http://www.tandfonline.com/doi/abs/10.1080/00107516908204405. (cited on page 3.)

[4] MJ Aziz and WJ Boettinger (1994). *On the transition from short-range diffusion-limited to collision-limited growth in alloy solidification*. Acta metallurgica et materialia, **42** (2), 527–537. (cited on pages 3, 34, 35, 181 and 208.)

[5] Kenneth A. Jackson, Kirk M. Beatty, and Katherine A. Gudgel (2004). *An analytical model for non-equilibrium segregation during crystallization*. Journal of Crystal Growth, **271**(3-4), 481–494. ISSN 0022-0248. URL http://www.sciencedirect.com/science/article/pii/S0022024804009200. (cited on pages 3, 36, 87 and 178.)

[6] Hiroshi Shintani and Hajime Tanaka (2006). *Frustration on the way to crystallization in glass*. Nat Phys, **2**(3), 200–206. ISSN 1745-2473. URL http://dx.doi.org/10.1038/nphys235. (cited on pages 3 and 177.)

[7] Frans Spaepen (1987). *The Art and Science of Microstructural Control*. Science, **235** (4792), 1010–1014. URL http://www.sciencemag.org/content/235/4792/1010.abstract. (cited on page 3.)

[8] J. Bernstein (2002). *Polymorphism in Molecular Crystals*. IUCr monographs on crystallography. Clarendon Press. ISBN 9780198506058. URL http://books.google.de/books?id=Rg97h45jtIkC. (cited on page 4.)

[9] Marco Zoppi (2003). *Microscopic structure of liquid hydrogen*. Journal of Physics: Condensed Matter, **15**(23), R1047. URL http://stacks.iop.org/0953-8984/15/i=23/a=202. (cited on page 4.)

[10] H.J. Maris, G.M. Seidel, and T.E. Huber (1983). *Supercooling of liquid H_2 and the possible production of superfluid H_2*. Journal of Low Temperature Physics, **51**(5-6), 471–487. ISSN 0022-2291. URL http://dx.doi.org/10.1007/BF00683224. (cited on pages 4, 19, 30, 31, 32 and 217.)

[11] Stephen R. Williams, C. Patrick Royall, and Gary Bryant (2008). *Crystallization of Dense Binary Hard-Sphere Mixtures with Marginal Size Ratio*. Phys. Rev. Lett., **100**, 225502. URL http://link.aps.org/doi/10.1103/PhysRevLett.100.225502. (cited on pages 4 and 183.)

[12] J. Q. Broughton, G. H. Gilmer, and K. A. Jackson (1982). *Crystallization Rates of a Lennard-Jones Liquid*. Phys. Rev. Lett., **49**, 1496–1500. URL `http://link.aps.org/doi/10.1103/PhysRevLett.49.1496`. (cited on pages 4 and 35.)

[13] L.-C. Valdes, F. Affouard, M. Descamps, and J. Habasaki (2009). *Mixing effects in glass-forming Lennard-Jones mixtures*. The Journal of Chemical Physics, **130** (15), 154505. URL `http://scitation.aip.org/content/aip/journal/jcp/130/15/10.1063/1.3106759`. (cited on pages 4, 182 and 183.)

[14] Wai-Lun Chan, Robert S. Averback, David G. Cahill, and Yinon Ashkenazy (2009). *Solidification Velocities in Deeply Undercooled Silver*. Phys. Rev. Lett., **102**, 095701. URL `http://link.aps.org/doi/10.1103/PhysRevLett.102.095701`. (cited on page 4.)

[15] Zhengdong Cheng, Jixiang Zhu, William B. Russel, William V. Meyer, and Paul M. Chaikin (2001). *Colloidal Hard-Sphere Crystallization Kinetics in Microgravity and Normal Gravity*. Appl. Opt., **40**(24), 4146–4151. URL `http://dx.doi.org/10.1364/ao.40.004146`. (cited on page 4.)

[16] Hans Joachim Schöpe, Gary Bryant, and William van Megen (2007). *Effect of polydispersity on the crystallization kinetics of suspensions of colloidal hard spheres when approaching the glass transition*. The Journal of Chemical Physics, 127(8): 084505. URL `http://scitation.aip.org/content/aip/journal/jcp/127/8/10.1063/1.2760207`. (cited on page 4.)

[17] John Russo, Anthony C. Maggs, Daniel Bonn, and Hajime Tanaka (2013). *The interplay of sedimentation and crystallization in hard-sphere suspensions*. Soft Matter, **9**, 7369–7383. URL `http://dx.doi.org/10.1039/C3SM50980J`. (cited on page 4.)

[18] R. A. Costa Fraga, A. Kalinin, M. Kühnel, D. C. Hochhaus, A. Schottelius, J. Polz, M. C. Kaluza, P. Neumayer, and R. E. Grisenti (2012). *Compact cryogenic source of periodic hydrogen and argon droplet beams for relativistic laser-plasma generation*. Review of Scientific Instruments, **83**(2), 025102. URL `http://link.aip.org/link/?RSI/83/025102/1`. (cited on pages 5, 10, 45 and 48.)

[19] G. Tejeda, J. M. Fernández, S. Montero, D. Blume, and J. P. Toennies (2004). *Raman Spectroscopy of Small Para-*H_2* Clusters Formed in Cryogenic Free Jets*. Phys. Rev. Lett., **92**, 223401. URL `http://link.aps.org/doi/10.1103/PhysRevLett.92.223401`. (cited on pages 5 and 56.)

[20] Kerstin Avila, David Moxey, Alberto de Lozar, Marc Avila, Dwight Barkley, and Björn Hof (2011). *The Onset of Turbulence in Pipe Flow*. Science, **333**(6039), 192–196. URL `http://www.sciencemag.org/content/333/6039/192.abstract`. (cited on page 8.)

[21] M. Kühnel (2009). *Entwicklung einer kryogenen Cluster- und Tröpfchenquelle als internes Target am Experimentierspeicherring ESR*. Diplomarbeit, Johann Wolfgang Goethe-Universität Frankfurt am Main. (cited on pages 8, 10 and 47.)

[22] Robert E. Grisenti and J. Peter Toennies (2003). *Cryogenic Microjet Source for Orthotropic Beams of Ultralarge Superfluid Helium Droplets*. Phys. Rev. Lett.,

90, 234501. URL `http://link.aps.org/doi/10.1103/PhysRevLett.90.234501`. (cited on page 8.)

[23] R. E. Grisenti, R. A. Costa Fraga, N. Petridis, R. Dörner, and J. Deppe (2006). *Cryogenic microjet for exploration of superfluidity in highly supercooled molecular hydrogen*. EPL (Europhysics Letters), **73**(4), 540. URL `http://stacks.iop.org/0295-5075/73/i=4/a=540`. (cited on pages 8, 10, 73, 227 and 228.)

[24] Derek A. Long. *Quantum Mechanical Theory of Rayleigh and Raman Scattering*, pages 49–84. John Wiley & Sons, Ltd (2002). ISBN 9780470845769. URL `http://dx.doi.org/10.1002/0470845767.ch4`. (cited on pages 12, 13 and 14.)

[25] Jan Van Kranendonk (1983). *Solid Hydrogen*. Springer US. (cited on pages 12, 16, 18, 19, 21, 105, 106 and 109.)

[26] Wikipedia (2013). URL `http://en.wikipedia.org/wiki/File:Ramanscattering.svg`. (cited on page 13.)

[27] Isaac F. Silvera (1980). *The solid molecular hydrogens in the condensed phase: Fundamentals and static properties*. Rev. Mod. Phys., **52**, 393–452. URL `http://link.aps.org/doi/10.1103/RevModPhys.52.393`. (cited on pages 16, 17, 22, 23, 24, 106 and 139.)

[28] R.D. McCarty, J. Hord, and H.M. Roder (1981). *Selected Properties of Hydrogen (engineering Design Data)*. U.S. Department of Commerce, National Bureau of Standards. URL `http://books.google.de/books?id=pw5RAAAAMAAJ`. (cited on page 17.)

[29] J. van Kranendonk and G. Karl (1968). *Theory of the Rotational and Vibrational Excitations in Solid Parahydrogen, and Frequency Analysis of the Infrared and Raman Spectra*. Rev. Mod. Phys., **40**, 531–555. URL `http://link.aps.org/doi/10.1103/RevModPhys.40.531`. (cited on pages 18 and 95.)

[30] Russell Sliter and Andrey F. Vilesov (2009). *Temperature dependence of the Raman spectra of liquid parahydrogen*. The Journal of Chemical Physics, **131**(7), 074502. URL `http://link.aip.org/link/?JCP/131/074502/1`. (cited on pages 18, 68, 72 and 100.)

[31] B. J. Kozioziemski and G. W. Collins (2003). *Raman spectra of solid isotopic hydrogen mixtures*. Phys. Rev. B, **67**, 174101. URL `http://link.aps.org/doi/10.1103/PhysRevB.67.174101`. (cited on pages 19, 23, 24, 101, 134, 135, 144, 145, 146, 189, 190, 191 and 192.)

[32] Izo I. Abram, Robin M. Hochstrasser, James E. Kohl, Myron G. Semack, and David White (1980). *Decay of vibrational coherence in ortho-para mixtures of solid hydrogen*. Chemical Physics Letters, **71**(3), 405–408. ISSN 0009-2614. URL `http://www.sciencedirect.com/science/article/pii/0009261480801928`. (cited on page 19.)

[33] J. De Kinder, A. Bouwen, D. Schoemaker, A. Boukahil, and D. L. Huber (1994). *Near-resonance scattering of the para-H_2 vibrons in (ortho-H_2)$_x$(para-H_2)$_{1-x}$ mixed*

crystals. Phys. Rev. B, **49**, 12754–12761. URL `http://link.aps.org/doi/10.1103/PhysRevB.49.12754`. (cited on page 19.)

[34] Hubert M. James and J. Van Kranendonk (1967). *Theory of the Anomalous Intensities in the Vibrational Raman Spectra of Solid Hydrogen and Deuterium*. Phys. Rev., **164**, 1159–1168. URL `http://link.aps.org/doi/10.1103/PhysRev.164.1159`. (cited on pages 20, 22, 101, 102, 103, 119 and 120.)

[35] A. H. Mckague Rosevear, G. Whiting, and Elizabeth J. Allin (1967). *An intensity anomaly in the Raman spectra of solid and liquid hydrogen and deuterium*. Canadian Journal of Physics, **45**(11), 3589–3595. URL `http://www.nrcresearchpress.com/doi/abs/10.1139/p67-302`. (cited on pages 20, 67 and 103.)

[36] S. S. Bhatnagar, Elizabeth J. Allin, and H. L. Welsh (1962). *The Raman spectra of liquid and solid H_2, D_2 and HD at high resolution*. Canadian Journal of Physics, **40**(1), 9–23. URL `http://www.nrcresearchpress.com/doi/abs/10.1139/p62-002`. (cited on pages 20, 104, 106, 133, 134, 186, 189 and 191.)

[37] G. M. Murphy and Helen Johnston (1934). *The Nuclear Spin of Deuterium*. Phys. Rev., **46**, 95–98. URL `http://link.aps.org/doi/10.1103/PhysRev.46.95`. (cited on page 22.)

[38] KnowledgeDoor (2013). URL `http://www.knowledgedoor.com/`. (cited on page 23.)

[39] V. G. Belan, N. N. Gal'tsov, A. I. Prokhvatilov, and M. A. Strzhemechnyǐ (2005). *Solid solutions Ne–nD_2. Diagram of phase equilibrium*. Low Temperature Physics, **31**(11), 947–950. URL `http://link.aip.org/link/?LTP/31/947/1`. (cited on pages 23, 26 and 27.)

[40] W. Kolos and L. Wolniewicz (1968). *Improved Theoretical Ground-State Energy of the Hydrogen Molecule*. The Journal of Chemical Physics, **49**(1), 404–410. URL `http://link.aip.org/link/?JCP/49/404/1`. (cited on page 23.)

[41] S.N. Ishmaev, I.P. Sadikov, A.A. Chernyshov, and et al. (1992). *Possibility of isotopic separation in H_2-D_2 solutions*. Journal of Experimental and Theoretical Physics, **75/2**, 382. (cited on pages 24 and 25.)

[42] M.A. Strzhemechny, A.I. Prokhvatilov, G.N. Shcherbakov, and N.N. Galtsov (1999). *Phase separation in nH_2-nD_2 alloys*. Journal of Low Temperature Physics, **115**(3-4), 109–126. ISSN 0022-2291. URL `http://dx.doi.org/10.1007/BF02876016`. (cited on pages 24 and 25.)

[43] M. Lambert (1960). *Excess Properties of H_2-D_2 Liquid Mixtures*. Phys. Rev. Lett., **4**, 555–556. URL `http://link.aps.org/doi/10.1103/PhysRevLett.4.555`. (cited on pages 24 and 232.)

[44] Francesco Operetto and Francesco Pederiva (2007). *Distortion effects and clustering of isotopic impurities in solid molecular para-hydrogen from variational Monte Carlo simulations with shadow wave functions*. Phys. Rev. B, **76**, 174517. URL `http://link.aps.org/doi/10.1103/PhysRevB.76.174517`. (cited on pages 25 and 146.)

[45] David White and J. R. Gaines (1965). *Liquid-Solid Phase Equilibria in the Hydrogen–Deuterium System*. The Journal of Chemical Physics, **42**(12), 4152–4158. URL `http://link.aip.org/link/?JCP/42/4152/1`. (cited on pages 25 and 142.)

[46] H. Föll (2013). URL `http://www.tf.uni-kiel.de/matwis/amat/mw1_ge/kap_5/backbone/r5_4_1.html`. (cited on page 26.)

[47] J.P. Brouwer, C.J.N. Van Den Meijdenberg, and J.J.M. Beenakker (1970). *Specific heat of the liquid mixtures of neon and hydrogen isotopes in the phase-separation region: I. The system Ne-H_2*. Physica, **50**(1), 93–124. ISSN 0031-8914. URL `http://www.sciencedirect.com/science/article/pii/003189147090056X`. (cited on pages 27 and 207.)

[48] M. Simon (1963). *On the phase separation in the liquid system Ne-pH_2*. Physics Letters, **5**(5), 319+. ISSN 0031-9163. URL `http://www.sciencedirect.com/science/article/pii/S0375960163942312`. (cited on pages 26 and 197.)

[49] J.P. Brouwer, L.J.F. Hermans, H.F.P. Knaap, and J.J.M. Beenakker (1964). *Phase separation in the liquid mixture of neon and deuterium*. Physica, **30**(7), 1409–1420. ISSN 0031-8914. URL `http://www.sciencedirect.com/science/article/pii/0031891464900898`. (cited on pages 26 and 197.)

[50] Youtube (2013). URL `http://youtu.be/ph8xusY3GTM`. (cited on page 29.)

[51] David Turnbull (1952). *Kinetics of Solidification of Supercooled Liquid Mercury Droplets*. The Journal of Chemical Physics, **20**(3), 411–424. URL `http://link.aip.org/link/?JCP/20/411/1`. (cited on page 29.)

[52] Santi Prestipino, Alessandro Laio, and Erio Tosatti (2012). *Systematic Improvement of Classical Nucleation Theory*. Phys. Rev. Lett., **108**, 225701. URL `http://link.aps.org/doi/10.1103/PhysRevLett.108.225701`. (cited on pages 29, 30 and 32.)

[53] Vitaly A. Shneidman (1995). *Theory of time-dependent nucleation and growth during a rapid quench*. The Journal of Chemical Physics, **103**(22), 9772–9781. URL `http://link.aip.org/link/?JCP/103/9772/1`. (cited on page 32.)

[54] E. Cini, B. Vinet, and P. J. Desré (2000). *A thermodynamic approach to homogeneous nucleation via fluctuations of concentration in binary liquid alloys*. Philosophical Magazine A, **80**(4), 955–966. URL `http://www.tandfonline.com/doi/abs/10.1080/01418610008212092`. (cited on page 32.)

[55] P.J. Desré, E. Cini, and B. Vinet (2001). *Homophase-fluctuation-mediated mechanism of nucleation in multicomponent liquid alloys and glass-forming ability*. Journal of Non-Crystalline Solids, **288**(1-3), 210–217. ISSN 0022-3093. URL `http://www.sciencedirect.com/science/article/pii/S0022309301005221`. (cited on page 32.)

[56] M. Baus (1987). *Statistical mechanical theories of freezing: An overview*. Journal of Statistical Physics, **48**(5-6), 1129–1146. ISSN 0022-4715. URL `http://dx.doi.org/10.1007/BF01009537`. (cited on page 32.)

[57] John Russo and Hajime Tanaka (2012). *The microscopic pathway to crystallization in supercooled liquids*. Scientific Reports, **2**, 505+. ISSN 2045-2322. URL http://dx.doi.org/10.1038/srep00505. (cited on pages 32, 36, 38, 175, 177 and 178.)

[58] Jürn W. P. Schmelzer, Vladimir M. Fokin, Alexander S. Abyzov, Edgar D. Zanotto, and Ivan Gutzow (2010). *How Do Crystals Form and Grow in Glass-Forming Liquids: Ostwald's Rule of Stages and Beyond*. International Journal of Applied Glass Science, **1**(1), 16–26. ISSN 2041-1294. URL http://dx.doi.org/10.1111/j.2041-1294.2010.00003.x. (cited on pages 32 and 107.)

[59] V. Erukhimovitch and J. Baram (1994). *Crystallization kinetics*. Phys. Rev. B, **50**, 5854–5856. URL http://link.aps.org/doi/10.1103/PhysRevB.50.5854. (cited on pages 33, 34 and 90.)

[60] C. Michaelsen, M. Dahms, and M. Pfuff (1996). *Comment on "Crystallization kinetics"*. Phys. Rev. B, **53**, 11877–11877. URL http://link.aps.org/doi/10.1103/PhysRevB.53.11877. (cited on page 34.)

[61] R. A. Clemente and A. M. Saleh (2002). *Crystallization kinetics: A solution for geometrical impingement*. Phys. Rev. B, **65**, 132102. URL http://link.aps.org/doi/10.1103/PhysRevB.65.132102. (cited on page 34.)

[62] S.L. Sobolev (2012). *An analytical model for complete solute trapping during rapid solidification of binary alloys*. Materials Letters, **89**(0), 191–194. ISSN 0167-577X. URL http://www.sciencedirect.com/science/article/pii/S0167577X12011846. (cited on pages 37 and 179.)

[63] Chunguang Tang and Peter Harrowell (2013). *Anomalously slow crystal growth of the glass-forming alloy CuZr*. Nat Mater, **12**(6), 507–511. ISSN 1476-1122. (cited on pages 37, 181 and 208.)

[64] Ludovic Berthier and Giulio Biroli (2011). *Theoretical perspective on the glass transition and amorphous materials*. Rev. Mod. Phys., **83**, 587–645. URL http://link.aps.org/doi/10.1103/RevModPhys.83.587. (cited on pages 37 and 38.)

[65] V. Kokotin and H. Hermann (2009). *Geometrical aspects of the glass-forming ability of dense binary hard-sphere mixtures*. Scripta Materialia, **61**(3), 261–264. ISSN 1359-6462. URL http://www.sciencedirect.com/science/article/pii/S135964620900253X. (cited on page 38.)

[66] M. Kühnel, N. Petridis, D.F.A. Winters, U. Popp, R. Dörner, Th. Stöhlker, and R.E. Grisenti (2009). *Low-z internal target from a cryogenically cooled liquid microjet source*. Nuclear Instruments and Methods in Physics Research Section A: Accelerators, Spectrometers, Detectors and Associated Equipment, **602**(2), 311–314. ISSN 0168-9002. URL http://www.sciencedirect.com/science/article/pii/S016890020802127X. (cited on page 45.)

[67] L.J. Salerno, P. Kittel, and A.L. Spivak (1994). *Thermal conductance of pressed metallic contacts augmented with indium foil or Apiezon grease at liquid helium temperatures*. Cryogenics, **34**(8), 649–654. ISSN 0011-2275. URL http://www.sciencedirect.com/science/article/pii/0011227594901422. (cited on page 51.)

[68] R. Berman and D. K. C. MacDonald (1952). *The Thermal and Electrical Conductivity of Copper at Low Temperatures*. Proceedings of the Royal Society of London. Series A. Mathematical and Physical Sciences, **211**(1104), 122–128. URL `http://rspa.royalsocietypublishing.org/content/211/1104/122.abstract`. (cited on page 54.)

[69] S. Montero, J. H. Morilla, G. Tejeda, and J. M. Fernández (2009). *Experiments on small $(H_2)_N$ clusters*. The European Physical Journal D, **52**(1-3), 31–34. ISSN 1434-6060. URL `http://dx.doi.org/10.1140/epjd/e2009-00031-y`. (cited on page 56.)

[70] J. H. Morilla, J. M. Fernandez, G. Tejeda, and S. Montero (2010). *The onset of molecular condensation: hydrogen*. Phys. Chem. Chem. Phys., **12**, 12060–12064. URL `http://dx.doi.org/10.1039/C003376F`. (cited on page 56.)

[71] G. Tejeda, J. M. Fernández-Sánchez, and S. Montero (1997). *High-Performance Dual Raman Spectrometer*. Appl. Spectrosc., **51**(2), 265–276. URL `http://as.osa.org/abstract.cfm?URI=as-51-2-265`. (cited on page 58.)

[72] NIST (2013). URL `http://physics.nist.gov/PhysRefData/ASD/ionEnergy.html`. (cited on pages 62 and 64.)

[73] Matthias Kühnel, José M. Fernández, Guzmán Tejeda, Anton Kalinin, Salvador Montero, and Robert E. Grisenti (2011). *Time-resolved study of crystallization in deeply cooled liquid parahydrogen*. Phys. Rev. Lett., **106**, 245301. URL `http://link.aps.org/doi/10.1103/PhysRevLett.106.245301`. (cited on page 67.)

[74] G. W. Collins, W. G. Unites, E. R. Mapoles, and T. P. Bernat (1996). *Metastable structures of solid hydrogen*. Phys. Rev. B, **53**, 102–106. URL `http://link.aps.org/doi/10.1103/PhysRevB.53.102`. (cited on pages 106, 110, 113, 115, 116, 117, 134, 135, 136, 138, 190 and 211.)

[75] Mario E. Fajardo and Simon Tam (1998). *Rapid vapor deposition of millimeters thick optically transparent parahydrogen solids for matrix isolation spectroscopy*. The Journal of Chemical Physics, **108**(10), 4237–4241. URL `http://link.aip.org/link/?JCP/108/4237/1`. (cited on page 106.)

[76] Kirill Kuyanov-Prozument and Andrey F. Vilesov (2008). *Hydrogen Clusters that Remain Fluid at Low Temperature*. Phys. Rev. Lett., **101**, 205301. URL `http://link.aps.org/doi/10.1103/PhysRevLett.101.205301`. (cited on page 106.)

[77] Stefan Auer and Daan Frenkel (2001). *Prediction of absolute crystal-nucleation rate in hard-sphere colloids*. Nature, **409**(6823), 1020–1023. (cited on page 107.)

[78] Allin, E.J., M, A.H., Soots, V., and Welsh, H.L. (1965). *The Raman spectrum of solid hydrogen*. J. Phys. France, **26**(11), 615–620. URL `http://dx.doi.org/10.1051/jphys:019650026011061500`. (cited on pages 108, 144, 145, 146 and 149.)

[79] U. Buontempo, S. Cunsolo, P. Dore, and L. Nencini (1983). *The $S(0)$ line in solid H_2*. Canadian Journal of Physics, **61**(10), 1401–1404. URL `http://www.nrcresearchpress.com/doi/abs/10.1139/p83-179`. (cited on page 108.)

[80] Xi Qin and Horst Meyer (1991). *Martensitic transition in solid* H_2 *under pressure studied via ultrasound propagation*. Phys. Rev. B, **44**, 4165–4169. URL `http://link.aps.org/doi/10.1103/PhysRevB.44.4165`. (cited on page 115.)

[81] Massimo Moraldi, Mario Santoro, Lorenzo Ulivi, and Marco Zoppi (1998). *Rotational and vibrational excitations in solid parahydrogen*. Phys. Rev. B, **58**, 234–241. URL `http://link.aps.org/doi/10.1103/PhysRevB.58.234`. (cited on pages 135 and 192.)

[82] S. C. Durana and J. P. McTague (1973). *Density-Dependent Phase Transition and Anisotropic Interactions in Solid Parahydrogen and Orthodeuterium*. Phys. Rev. Lett., **31**, 990–993. URL `http://link.aps.org/doi/10.1103/PhysRevLett.31.990`. (cited on page 138.)

[83] J. R. Gaines, P. A. Fedders, G. W. Collins, J. D. Sater, and P. C. Souers (1995). *Diffusion of atoms and molecules in the solid hydrogens*. Phys. Rev. B, **52**, 7243–7251. URL `http://link.aps.org/doi/10.1103/PhysRevB.52.7243`. (cited on page 139.)

[84] M. Celli, D. Colognesi, M. Zoppi, and A. J. Ramirez-Cuesta (2005). *Microscopic self dynamics in liquid hydrogen and in its mixtures with deuterium and neon: a neutron scattering study*. Journal of Low Temperature Physics, **138**(3-4), 887–892. ISSN 0022-2291. URL `http://dx.doi.org/10.1007/s10909-005-2320-1`. (cited on page 142.)

[85] Kazuko Motizuki and Takeo Nagamiya (1956). *Theory of the Ortho-Para Conversion in Solid Hydrogen*. Journal of the Physical Society of Japan, **11**(2), 93–104. URL `http://jpsj.ipap.jp/link?JPSJ/11/93/`. (cited on page 147.)

[86] Yu.Ya. Milenko, R.M. Sibileva, and M.A. Strzhemechny (1997). *Natural ortho-para conversion rate in liquid and gaseous hydrogen*. Journal of Low Temperature Physics, **107**(1-2), 77–92. ISSN 0022-2291. URL `http://dx.doi.org/10.1007/BF02396837`. (cited on page 147.)

[87] S. I. Henderson and W. van Megen (1998). *Metastability and Crystallization in Suspensions of Mixtures of Hard Spheres*. Phys. Rev. Lett., **80**, 877–880. URL `http://link.aps.org/doi/10.1103/PhysRevLett.80.877`. (cited on pages 165 and 181.)

[88] H. J. Maris, G. M. Seidel, and F. I. B. Williams (1987). *Experiments with supercooled liquid hydrogen*. Phys. Rev. B, **36**, 6799–6810. URL `http://link.aps.org/doi/10.1103/PhysRevB.36.6799`. (cited on page 173.)

[89] O. N. Osychenko, R. Rota, and J. Boronat (2012). *Superfluidity of metastable glassy bulk para-hydrogen at low temperature*. Phys. Rev. B, **85**, 224513. URL `http://link.aps.org/doi/10.1103/PhysRevB.85.224513`. (cited on page 175.)

[90] Paul J. Steinhardt, David R. Nelson, and Marco Ronchetti (1983). *Bond-orientational order in liquids and glasses*. Phys. Rev. B, **28**, 784–805. URL `http://link.aps.org/doi/10.1103/PhysRevB.28.784`. (cited on page 176.)

[91] G. Cini-Castagnoli, A. Giardini-Guidoni, and F. P. Ricci (1961). *Diffusion of Neon, HT, and Deuterium in Liquid Hydrogen*. Phys. Rev., **123**, 404–406. URL `http://link.aps.org/doi/10.1103/PhysRev.123.404`. (cited on pages 179 and 207.)

[92] Adam B. Hopkins, Frank H. Stillinger, and Salvatore Torquato (2012). *Densest binary sphere packings*. Phys. Rev. E, **85**, 021130. URL `http://link.aps.org/doi/10.1103/PhysRevE.85.021130`. (cited on page 182.)

[93] K. F. Kelton. Glass-forming alloys: Order at the interface (2013). URL `http://www.nature.com/nmat/journal/v12/n6/full/nmat3662.html`. (cited on page 182.)

[94] Personal correspondence with Jose Ma. Fernandez (2013). (cited on pages 188 and 191.)

[95] P. A. Fleury and J. P. McTague (1975). *Molecular interactions in the condensed phases of ortho-para hydrogen mixtures*. Phys. Rev. A, **12**, 317–326. URL `http://link.aps.org/doi/10.1103/PhysRevA.12.317`. (cited on page 188.)

[96] David P. Weliky, Karen E. Kerr, Teresa J. Byers, Yu Zhang, Takamasa Momose, and Takeshi Oka (1996). *High resolution infrared spectroscopy of isotopic impurity $Q_1(0)$ transitions in solid parahydrogen*. The Journal of Chemical Physics, **105** (11), 4461–4481. URL `http://scitation.aip.org/content/aip/journal/jcp/105/11/10.1063/1.472298`. (cited on page 192.)

[97] NIST (2013). URL `http://webbook.nist.gov/chemistry/fluid/`. (cited on page 198.)

[98] R. Ramírez and C. P. Herrero (2008). *Quantum path-integral study of the phase diagram and isotope effects of neon*. The Journal of Chemical Physics, **129**(20), –. URL `http://scitation.aip.org/content/aip/journal/jcp/129/20/10.1063/1.3023036`. (cited on pages 207 and 208.)

[99] J.P. Brouwer, A.M. Vossepoel, C.J.N. Van Den Meijdenberg, and J.J.M. Beenakker (1970). *Specific heat of the liquid mixtures of neon and hydrogen isotopes in the phase-separation region: II. The system Ne-D_2*. Physica, **50**(1), 125–148. ISSN 0031-8914. URL `http://www.sciencedirect.com/science/article/pii/0031891470900571`. (cited on page 207.)

[100] Alexander Schottelius (2013). *Auf dem Weg ins Niemandsland des Wassers*. Master's thesis, Johann Wolfgang Goethe-Universität Frankfurt am Main. (cited on page 218.)

[101] Emily B. Moore and Valeria Molinero (2010). *Ice crystallization in water's "no-man's land"*. The Journal of Chemical Physics, 132(24):244504. URL `http://scitation.aip.org/content/aip/journal/jcp/132/24/10.1063/1.3451112`. (cited on page 218.)

[102] R.D. McCarty, L.A. Weber, United States. National Bureau of Standards, and Institute for Basic Standards (U.S.). Cryogenics Division (1972). *Thermophysical properties of parahydrogen from the freezing liquid line to 5000 R for pressures to 10,000 psia*. U.S. Dept. of Commerce, National Bureau of Standards. URL `http://books.google.de/books?id=AxmF8RrHnJ0C`. (cited on page 224.)

[103] John R. Howell Robert Siegel (2001). *Thermal radiation heat transfer.* New York : Taylor & Francis, 4th ed edition. ISBN 1560328398. (cited on page 228.)

[104] David White, Jih-Heng Hu, and Herrick L. Johnston (1959). *The Heats of Vaporization of Para-hydrogen and Ortho-deuterium from their Boiling Points to their Critical Temperatures.* The Journal of Physical Chemistry, **63**(7), 1181–1183. URL `http://pubs.acs.org/doi/abs/10.1021/j150577a038`. (cited on page 230.)

[105] B.I. Verkin, T.B. Selover, and J.I. Ghojel (1991). *Handbook of Properties of Condensed Phases of Hydrogen and Oxygen.* Hemisphere Publishing Corporation. ISBN 9780891167143. URL `http://books.google.de/books?id=aCJ2QgAACAAJ`. (cited on pages 230 and 232.)

[106] Eugene C. Kerr, Elis B. Rifkin, Herrick L. Johnston, and John T. Clarke (1951). *Condensed Gas Calorimetry. II. Heat Capacity of Ortho-deuterium between 13.1 and 23.6°K., Melting and Boiling Points, Heats of Fusion and Vaporization. Vapor Pressures of Liquid Ortho-deuterium.* Journal of the American Chemical Society, **73**(1), 282–284. URL `http://pubs.acs.org/doi/abs/10.1021/ja01145a093`. (cited on pages 230 and 232.)

[107] H. M. Roder and D. E. Diller (1970). *Thermal Conductivity of Gaseous and Liquid Hydrogen.* The Journal of Chemical Physics, **52**(11), 5928–5949. URL `http://scitation.aip.org/content/aip/journal/jcp/52/11/10.1063/1.1672877`. (cited on page 230.)

[108] Robert W. Powers, Robert W. Mattox, and Herrick L. Johnston (1954). *Thermal Conductivity of Condensed Gases. III. The Thermal Conductivity of Liquid Deuterium from 19 to 29°K.* Journal of the American Chemical Society, **76**(23), 5974–5974. URL `http://pubs.acs.org/doi/abs/10.1021/ja01652a022`. (cited on page 230.)

[109] P.C. Souers (1986). *Hydrogen Properties for Fusion Energy.* University of California Press. ISBN 9780520055001. URL `http://books.google.de/books?id=I2K6DKA1IMwC`. (cited on pages 229 and 230.)

[110] E. R. Grilly (1951). *The Vapor Pressures of Hydrogen, Deuterium and Tritium up to Three Atmospheres.* Journal of the American Chemical Society, **73**(2), 843–846. URL `http://pubs.acs.org/doi/abs/10.1021/ja01146a103`. (cited on pages 229 and 230.)

[111] M. Simon and A. Bellemans (1960). *On the excess thermodynamic properties of ^{3}He-^{4}He and H_2-D_2 liquid mixtures.* Physica, **26**(3), 191–197. ISSN 0031-8914. URL `http://www.sciencedirect.com/science/article/pii/003189146090015X`. (cited on page 232.)

[112] J.A. Dean and N.A. Lange (1999). *Lange's Handbook of Chemistry.* Number 15. McGraw-Hill. ISBN 9780070163843. URL `http://books.google.de/books?id=56KPMQEACAAJ`. (cited on page 232.)

[113] Guenter Ahlers (1964). *Lattice Heat Capacity of Solid Hydrogen.* The Journal of Chemical Physics, **41**(1), 86–94. URL `http://scitation.aip.org/content/aip/journal/jcp/41/1/10.1063/1.1725656`. (cited on page 232.)

ACKNOWLEDGEMENTS

ZUSAMMENFASSUNG

Einführung einer neuen Experimentiertechnik

Das Fundament dieser Arbeit stellt das Konzept einer neuartigen experimentellen Methode dar, mit der die Kristallisationsdynamik von stark unterkühlten Flüssigkeiten untersucht werden kann. Derzeitig etablierte Verfahren haben entweder den Nachteil, an levitierenden Metalltröpfchen Veränderungen lediglich auf Zeitskalen von Sekunden festzustellen oder in Kolloidsystemen mit stark beeinflussenden Störeffekten wie Sedimentierung, Partikel-Solvens-Interaktion, etc. behaftet zu sein. Die hier präsentierte Technik vereint Mikro-Flüssigkeitsstrahlen mit linearer Raman-Spektroskopie und ermöglicht die Analyse der Evolution von molekularen Flüssigkeiten mit einer zeitlichen Auflösung von $\approx 10\,\text{ns}$. Dies eröffnet den Zugang zur Untersuchung der Kristallisationsdynamik in realen Systemen.

Das zu untersuchende Gas, hier zunächst Wasserstoff, wird dazu bei Temperaturen von $\approx 20\,\text{K}$ verflüssigt und durch eine Düse mit einem Durchmesser von ca. $5\,\mu\text{m}$ in eine Vakuumkammer expandiert (siehe (1) in Abbildung auf S.248). Der flüssige Strahl tritt als zylinderförmiges Filament aus der Düse aus und propagiert geradlinig mit konstanter Geschwindigkeit $v_0 \approx 100\,\text{m/s}$. Aufgrund des Dampfdrucks der Vakuumexponierten Oberfläche kühlt die Flüssigkeit rapide unterhalb des Schmelzpunktes ab, bis sie schließlich gefriert.
Die hohe Richtungsstabilität des Filaments resultiert in einem proportionalem Zusammenhang zwischen Distanz z, die das Filament zurückgelegt hat, und Zeit t über $t = \frac{v_0}{z}$, welche den ersten Schlüsselaspekt für die genaue Zeitauflösung darstellt. Das zweite maßgebende Charakteristikum wird durch die hohe räumliche Auflösung des Raman-Spektrometers erreicht (siehe (2) in Abbildung auf S.248). Über die Projektion der Optiken können Raman-Spektren eines Ausschnitts des Filaments von $\Delta z = 2\,\mu\text{m}$ entlang der Filamentachse z aufgenommen werden.

Anhand von flüssigen Filamenten der Wasserstoff-Isotope wird die erfolgreiche Funktionsfähigkeit dieses Ansatzes bewiesen. Alle Experimente finden im Rahmen einer Kollaboration am *Instituto de Estructura de la Materia, CSIC* in Madrid statt.

Entwicklung der Düsenkonstruktion

Für das Gelingen des beschriebenen Vorgehens sind diverse Veränderungen des typisch verwendeten Aufbaus unserer Arbeitsgruppe notwendig. Die essentielle Richtungsstabilität der Filamente wird durch neuartige Glas-Pipetten als Düsen erreicht, die im Rahmen dieser Arbeit mitentwickelt wurden. Um Störungen durch den Raman-Laser bei der Aufnahme von Spektren nah am Düsenausgang zu vermeiden, wird speziell für dieses Experiment die Spitze dieser Pipetten mit einer eigens entwickelten Schleifkonstruktion auf $\approx 500\,\mu\text{m}$ reduziert.
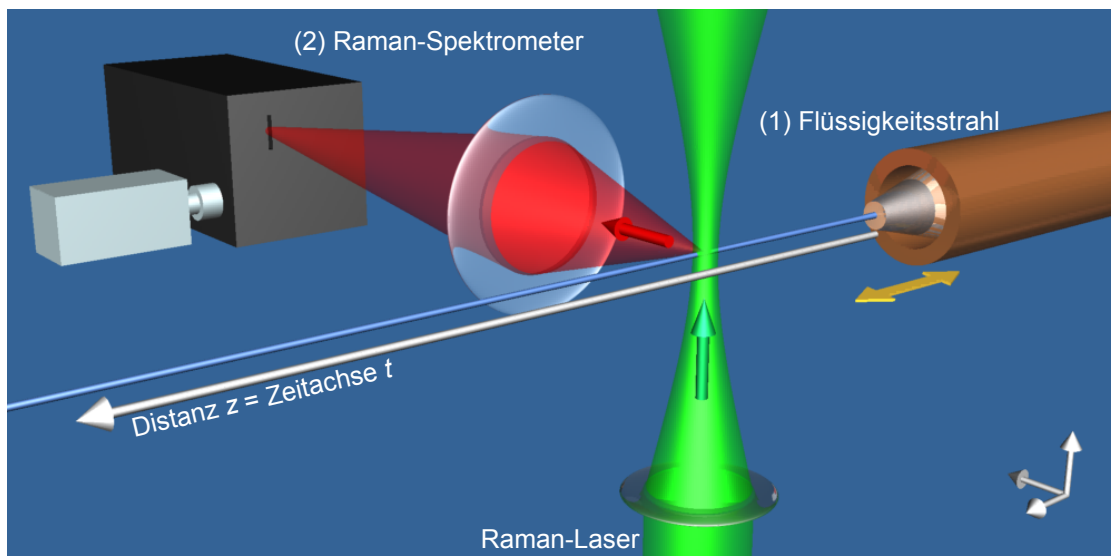
Schematische Darstellung der wichtigsten Komponenten des experimentellen Aufbaus.

Die Aufnahme von Spektren entlang der Filamentachse verlangt nach einer präzisen Positionierung der Düsenkonstruktion, die durch 3 motorgesteuerte, senkrechte Linearachsen mit sub-µm Genauigkeit realisiert ist. Für die benötigten kryogenen Temperaturen ist die Düse erstmalig nicht direkt, sondern über 2 flexible Kupferlitzen thermisch an einen stationären Durchfluss-Kryostaten gekoppelt.

Durch Raman-Messungen und Vergleich von verschiedenen Pipetten-Düsen können Charakteristiken, Abhängigkeiten und Limitierung der neuen Düsenart identifiziert werden. So wird in den folgenden Experimenten unter anderem festgestellt, dass der Startzeitpunkt der Kristallisation lediglich einen geringen Einfluss auf dessen Gesamtdauer hat.

Kristallisationsverhalten von Wasserstoff

Das erste mit diesem Aufbau untersuchte System ist Wasserstoff, welches mittels eines Katalysators vorab zu 99.8% in den kugelsymmetrischen Grundzustand $J = 0$ para-Wasserstoff umgewandelt wird. Serien von Raman-Spektren werden entlang der Filament-Achse (vgl. Abbildung auf S.248) im Vibrations- $Q_1(0)$ und Rotations-Regime $S_0(0)$ aufgenommen.

Vibrationsspektren nahe am Düsenausgang weisen ein breites, asymmetrisches Band auf, welches sich mit zunehmendem Abstand zur Düse z zu kleineren Wellenzahlen (=Energien) verschiebt. Mit Hilfe einer Korrelation zwischen Wellenzahl und Temperatur aus der Literatur wird dieses Band als der flüssigen Phase zugehörig und dessen Breite als Temperaturverteilung des Filaments identifiziert.

Zur weiteren Temperatur-Analyse wird ein Model des Filaments erstellt, bei dem dessen Querschnitt in 100 zylindrische, konzentrische Schichten aufgeteilt wird. In einer eigens erweiterten numerischen Simulation kühlt lediglich die Vakuum-exponierte Oberfläche auf Grundlage des aktuellen Dampfdrucks durch Verdampfung ab, während die inneren Schichten dem Temperaturaustausch über Wärmeleitung unterliegen. Ein Vergleich der zeitlichen Entwicklung der Temperatur der Oberflächenschicht, des Kerns

und der mittleren Temperatur mit den aus den Raman-Spektren extrahierten Werten weist quantitative Übereinstimmung auf, so dass das beobachtete Verhalten als ein radialer Temperaturgradient im Filament interpretiert wird. Die Oberfläche des Filaments erreicht dabei minimale Temperaturen von 9-9.5 K nach 5 μs, was einer Unterkühlung von ca. 30% entspricht.

Ab diesem Zeitpunkt erscheint ein neuer wachsender Peak in den Vibrations-Raman-Spektren, dessen Position mit der kristallinen Phase übereinstimmt. Der Fortschritt der Kristallisation zu jedem Zeitschritt entlang der Filamentachse wird mittels des Intensitätsanteils dieses Peaks am Gesamtspektrum ermittelt und dauert ca. 8 μs bis zum vollständigen Verschwinden der flüssigen Phase an.

Das Wachstum der festen Phase geht aufgrund der Kristallisationswärme mit einer Zunahme der Temperatur der verbleibenden flüssigen Phase einher. Aus dem stärksten Temperaturanstieg der kältesten Teile der Flüssigkeit lässt sich schlussfolgern, dass der Start der Kristallisation an der Oberfläche des Filaments stattfindet, was zudem durch die starke Temperaturabhängigkeit der klassischen Nukleationstheorie bestätigt wird. Mit Bezug auf das oben beschriebene konzentrische Schichtenmodell findet die Kristallisation isotrop und radial in Richtung Kern des Filaments statt. Die mittlere Kristallisationsgeschwindigkeit für Wasserstoff bei einer mittleren Temperatur von 12.5 K wird durch das Verhältnis von Filamentradius zu Gesamtkristallisationszeit ermittelt zu $\approx 0.3\,\mathrm{m/s}$. Dieser Wert befürwortet ein Wachstumsmodell, welches auf der kinetischen anstatt der Diffusions-Geschwindigkeit der Teilchen beruht.

Messungen der Rotationsanregung $S_0(0)$ zeigen, dass die kristalline Struktur hcp, fcc und Gitter ohne feste Symmetrien (rhcp) beinhaltet. Da laut Literatur bei langsamen Gefrieren unter Gleichgewichtsbedingung reine hcp Strukturen entstehen, deutet unsere Messungen auf eine metastabile Struktur hin. Eine wahrscheinliche Erklärung beruft sich auf die *Ostwaldsche Stufenregel*, welche bei der initialen Phasenumwandlung metastabile Zwischenstufen vorhersagt.

Eine Analyse der zeitlichen Intensitätsveränderung der entsprechenden fcc und rhcp Peaks bestätigt, dass selbst nach vollständig abgeschlossener Kristallisation deren relativer Intensitätsanteil innerhalb der beobachteten Zeiträume von μs abnimmt. Dies deckt sich mit Literatur, die ein Verschwinden von fcc Strukturen innerhalb von Minuten bei den bei uns vorherrschenden Temperaturen von $\approx 8\,\mathrm{K}$ feststellt.

Kristallisationsverhalten von Deuterium

Als zweites reines System werden flüssige Filamente aus zu 97.5% konvertiertem ortho-Deuterium untersucht, welche das Pendant zu kugelsymmetrischem para-Wasserstoff darstellt. Aufgrund von überlappenden Anregungsbändern und fehlender Wellenzahl-Temperatur Korrelation in der Literatur können keine direkten Temperaturen aus den Raman-Daten extrahiert werden. Jedoch zeigt die für Deuterium adaptierte numerische Simulation des Temperaturgradienten einen qualitativ ähnlichen Verlauf zu Wasserstoff, so dass die Temperaturverteilung des Filaments sowie die Unterkühlung relativ zum Schmelzpunkt im Vergleich zu Wasserstoff als nahezu identisch angenommen wird. Der Kristallisationsprozess von Deuterium im Vergleich zu Wasserstoff startet früher und hält länger an, wobei der Faktor zwischen den Isotopen für diese beiden Zeiten bei jeweils $1.4 \approx \sqrt{2}$ liegt. Dieser Unterschied legt nahe, dass die doppelte Masse von Deuterium hierbei der Haupteinflussfaktor ist, was sich mit dem für das Kristallwachs-

tum zuständigen kinetischen Modell deckt.

Die Kristallstruktur aus den Rotationsdaten weist ebenfalls ein Mischung aus fcc, hcp und rhcp Gitterkomponenten auf, jedoch mit einem höheren Anteil an fcc.

Mischungen von para–Wasserstoff und ortho–Deuterium

Die Beimengung von bis zu 10% ortho-Deuterium zu para-Wasserstoff lässt den Abkühlungsprozess des flüssigen Filamentes unbeeinflusst. Die Kristallisation setzt früher ein und dauert deutlich länger im Vergleich zu reinen Wasserstoff-Filamenten. Inverse Mischungen mit Deuterium als Hauptkomponente zeigen einen qualitativ ähnlichen Trend bezüglich Kristallisationsbeginn und -dauer zur reinen Substanz auf, jedoch mit geringerem Ausmaß. Die längsten Kristallisationszeiten treten für Mischungen mit $20-50\%$ ortho-Deuterium auf und liegen mit mehr als einem Faktor 3 über dem Wert von reinem Wasserstoff.

Der Kristallisationsfortschritt kann separat für die Isotope gemessen werden und zeigt zeitweise Unterschiede von bis zu 10 Prozentpunkten. Dies deutet auf eine teilweise Trennung der Isotope während des Kristallisationsprozesses hin. Weitere Hinweise hierauf sind bei Mischungen mit geringem Anteil an para-Wasserstoff zu finden, bei denen nach vollständiger Kristallisation von Deuterium ein kleiner Teil ($\approx 1\%$) der Wasserstoffmoleküle in der flüssigen Phase verbleibt und sich auch bei längeren Messzeiten von μs nicht mehr verändert.

Reproduktionsmessungen mit veränderten Parametern bezüglich Starttemperatur und Düsendurchmesser bestätigen, dass die Temperatur der flüssigen Filaments nicht die Hauptgrund für die beobachteten längeren Kristallisationszeiten von Mischungen sein kann. Obwohl alle Wasserstoff-Isotope im Grundzustand durch das selbe intermolekulare Interaktiospotential beschrieben werden, besitzen sie unterschiedliche effektive Größen, was auf die stärkeren Nullpunktsschwingungen der geringen Masse bedingt ist. Aufgrund dieser Größenunterschiede könnten geometrische bzw. Diffusionseffekte an der flüssig-fest-Grenzfläche das Kristallwachstum verlangsamen.

Durch das Hinzufügen von Wasserstoff zu Deuterium ändert sich dessen kristalline Struktur leicht zugunsten von fcc, während im umgekehrten Fall ein marginaler Anstieg der hcp Intensitäten beobachtet wird. Als Minderheitskomponente in Mischungen zeigt Deuterium eine scharfe Linienstruktur, deren Positionen mit reinem hcp im Gleichgewichtszustand sowie der Gaslinie übereinstimmen, was als gepaarte bzw. isolierte ortho-Deuterium Moleküle interpretiert wird. Die Schärfe dieser Peaks beruht auf dem Quantencharakter von para-Wasserstoff-Kristallen, welche eine freie Rotation von eingepflanzten Molekülen erlaubt.

Im umgekehrten Fall weist Wasserstoff in der Minderheit eine breitere Struktur mit keiner klaren Indikation für hcp-Linien auf, was auf weniger ausgeprägte Quanteneigenschaften vom Deuterium Hauptgitter und einen erhöhten Anteil an Molekülen, die sich nicht im Grundzustand befinden, zurückzuführen ist.

Mischungen von Wassersoff–Isotopen mit Neon

Beimengungen von $< 2\%$ Neon zu para-Wasserstoff Filamenten resultieren in einem nahezu sofortigen Beginn der Kristallisation, die deutlich länger anhält. Im Vergleich zu ähnlichen Beimischungen von ortho-Deuterium sind beide Effekte stärker ausgeprägt.

Das Hinzufügen von < 5% Neon zu ortho-Deuterium verändert den Zeitpunkt des Kristallisationsstarts kaum, verlängert jedoch die Dauer der Kristallisation erheblich stärker als ähnliche Beimengungen von para-Wasserstoff.
Neon-Atome besitzen eine geringere Größe als Moleküle der Wasserstoffisotope. Daher sind die beobachteten erhöhten Kristallisationszeiten wahrscheinlich ebenso auf Effekte an der flüssig-fest-Grenzfläche zurückzuführen.

Bei diesen bereits kleinen Anteilen von Neon ändert sich die kristalline Struktur der Wasserstoff-Isotope stark zugunsten von fcc. Dies lässt sich damit begründen, dass für reines Neon fcc die stabile Gitterstruktur unter Gleichgewichtsbedingungen ist.

Mehrwert der Arbeit

Die Entwicklung und das erfolgreiche Testen des Düsensystems mit Glas-Pipetten, die über Kupferlitzen thermisch an den Kryostaten gekoppelt sind, legen den neuen Standard für Experimente fest, bei denen der Flüssigkeitsstrahl selbst untersucht werden soll.
Der Beweis der Funktionalität der hier vorgestellten Methode eröffnet eine Vielzahl an darauf aufbauenden Experimenten. Zum einen können andere Flüssigkeiten, wie beispielsweise Wasser, mit Raman-Spektroskopie untersucht werden. Weiterhin werden Messungen mit anderen Photonenquellen, vorzugsweise Röntgenstrahlen, Erkenntnisse auf mikroskopischen Größenskalen liefern.

Wohingegen in der Literatur bisher lediglich die flüssige und feste Phase im Gleichgewicht betrachtet wurden, liefern die hier vorgestellten Ergebnisse Details zum Kristallisationsverhalten an sich. Erstmalig wird die Kristallwachstumsgeschwindigkeit von stark unterkühltem Wasserstoff und Deuterium sowie deren Wachstumsmechanismus bestimmt. Die Messungen stellen einen Beleg für die Gültigkeit der Ostwaldschen Stufenregel für Wasserstoff dar, die mit anderen Techniken bisher nicht beobachtet werden konnte.
Die Untersuchungen der Mischungen zeigt enorme Auswirkungen auf das Kristallisationsverhalten, welche wahrscheinlich auf Quanteneffekten basieren. Da die Kristallisationsdynamik im Allgemeinen durch Experimente nur begrenzt zugänglich ist, stellen die Daten ein neues System für den Test theoretischer Vorhersagen dar. Auf Grundlage der Ergebnisse lassen sich Quanten-Simulationen entwickeln, die Details zu den mikroskopischen Effekten der flüssig-fest-Grenzfläche eröffnen können.

Curriculum Vitae

Angaben zur Person

Name:	Kühnel, Matthias
Anschrift:	Kirchhainer Str. 23
	60433 Frankfurt
Geburtsdatum:	19.10.1984 in Hanau
Nationalität:	Deutsch
Familienstand:	Ledig

Universitäre und schulische Bildung

06/2004	Abitur an der Hohen Landesschule (Hanau), Note *1,0* Leistungskurse: Mathematik, Physik
2004 – 2009	Studium der Physik an der Goethe-Universität Frankfurt
09/2006	Vordiplom, Note *sehr gut*
09/2009	Abschluss: Physik (Diplom), Note *sehr gut (mit Auszeichnung)* Thema: „Entwicklung einer kryogenen Cluster- und Tröpfchenquelle als internes Target am Experimentierspeicherung ESR"
seit 09/2009	Promotion in Physik am Institut für Kernphysik Frankfurt an der Goethe-Universität Frankfurt Thema: „Time-resolved crystallization of deeply cooled liquid hydrogen isotopes"

Forschungsaufenthalte

11/2007 (1 Woche)	BESSY II, Berlin
04/2008 (1 Woche)	FLASH, Hamburg
08/2008 (2 Wochen)	LBNL ALS, Berkeley, USA
09/2009 (1 Woche)	SPARC-Meeting, Lissabon
11/2009 (4 Wochen)	CSIC, Madrid
04/2010 (9 Wochen)	CSIC, Madrid
12/2010 (1 Woche)	CSIC, Madrid
11/2011 (4 Wochen)	CSIC, Madrid
10/2012 (4 Wochen)	CSIC, Madrid

Veröffentlichungen

1. M. Kühnel, J. M. Fernández, F. Tramonto, G. Tejeda, E. Moreno, A. Kalinin, M. Nava, D. E. Galli, S. Montero, and R. E. Grisenti (2014). *Observation of crystallization slowdown in supercooled para-hydrogen and ortho-deuterium quantum liquid mixtures.* (to be published)

2. M. Kühnel, J. M. Fernández, G. Tejeda, A. Kalinin, S. Montero, and R. E. Grisenti (2011). *Time-resolved study of crystallization in deeply cooled liquid parahydrogen.* Phys. Rev. Lett., **106**, 245301.
   DOI: http://link.aps.org/doi/10.1103/PhysRevLett.106.245301

3. M. Kühnel, N. Petridis, D.F.A. Winters, U. Popp, R. Dörner, Th. Stöhlker, R.E. Grisenti (2009). *Low-Z internal target from a cryogenically cooled liquid microjet source.* Nucl. Instr. and Meth. in Phys. Res. A, **602** 311-314.
   DOI: dx.doi.org/10.1016/j.nima.2008.12.212

4. T. Havermeier, T. Jahnke, K. Kreidi, R. Wallauer, S. Voss, M. Schöffler, S. Schössler, L. Foucar, N. Neumann, J. Titze, H. Sann, M. Kühnel, J. Voigtsberger, A. Malakzadeh, N. Sisourat, W. Schöllkopf, H. Schmidt-Böcking, R. E. Grisenti, and R. Dörner (2010). *Single Photon Double Ionization of the Helium Dimer.* Physical Review Letters, **104**, 153401. DOI: dx.doi.org/10.1103/PhysRevLett.104.153401

5. T. Havermeier, T. Jahnke, K. Kreidi, R. Wallauer, S. Voss, M. Schöffler, S. Schössler, L. Foucar, N. Neumann, J. Titze, H. Sann, M. Kühnel, J. Voigtsberger, J. H. Morilla, W. Schöllkopf, H. Schmidt-Böcking, R. E. Grisenti, and R. Dörner (2010). *Inter-atomic Coulombic Decay following Photoionization of the Helium Dimer: Observation of Vibrational Structure.* Physical Review Letters, **104**, 133401.
   DOI: dx.doi.org/10.1103/PhysRevLett.104.133401

6. T. Havermeier, K. Kreidi, R. Wallauer, S. Voss, M. Schöffler, S. Schössler, L. Foucar, N. Neumann, J. Titze, H. Sann, M. Kühnel, J. Voigtsberger, N. Sisourat, W. Schöllkopf, H. Schmidt-Böcking, R. E. Grisenti, R. Dörner and T. Jahnke (2010). *Angular distributions of photoelectrons and interatomic-Coulombic-decay electrons from helium dimers: Strong dependence on the internuclear distance.* Physical Review A, **82**, 063405. DOI: dx.doi.org/10.1103/PhysRevA.82.063405

7. T. Osipov, Th. Weber, T. N. Rescigno, S. Y. Lee, A. E. Orel, M. Schöffler, F. P. Sturm, S. Schössler, U. Lenz, T. Havermeier, M. Kühnel, T. Jahnke, J. B. Williams, D. Ray, A. Landers, R. Dörner and A. Belkacem (2010). *Formation of inner-shell autoionizing CO+ states below the CO2+ threshold.* Physical Review A, **81**, 011402.
   DOI: dx.doi.org/10.1103/PhysRevA.81.011402

Akademische Lehrer

Prof. Dr. Harald Appelshäuser
Prof. Dr. Wolf Aßmus
Prof. Dr. Johann Baumeister
Prof. Dr. Christoph Blume
PD Dr. Harald Bräuning
Prof. Dr. Reinhard Dörner
Prof. Dr. Carsten Greiner
PD Dr. Robert Grisenti
Prof. Dr. Claudius Gros
Prof. Dr. Frank Grünwald
Prof. Dr. Walter Hofstetter
Prof. Dr. Michael Huth
Prof. Dr. Joachim Jacoby
PD Dr. Till Jahnke
Prof. Dr. Bernd Kolbesen
Prof. Dr. Peter Kopietz
Prof. Dr. Cornelius Krellner
Prof. Dr. Michael Lang
Prof. Dr. Joachim Maruhn
Prof. Dr. Salvador Montero Martín
Prof. Dr. Jens Müller
Prof. Dr. Ulrich Ratzinger
Prof. Dr. Hartmut Roskos
Prof. Dr. Alwin Schempp
Prof. Dr. Horst Schmidt-Böcking
Prof. Dr. Horst Stöcker
Prof. Dr. Thomas Stöhlker
Prof. Dr. Herbert Ströbele
Prof. Dr. Matthias Wagner
Prof. Dr. Joachim Weidmann

Frankfurt am Main, 13th February 2014